



The
University
Of
Sheffield.

Conceptual Design of Jet Transport Aircraft with Energy Harvesting Structure

By:

Mahesa Akbar

Supervisors:

Dr. Jose Luis Curiel-Sosa

Dr. Anton Krynkin

A thesis submitted in partial fulfilment of the requirements
for the degree of Doctor of Philosophy

March 2019

Abstract

Piezoelectric material has been utilised to construct a small scale (μW order) power generator devices in recent years. In the case of aerial vehicles, some works have presented its implementation on small unmanned aerial vehicles (UAV). However, an application on larger aircraft structure has not yet been investigated. The present work aimed to seek insight into the potential energy that could be harvested from a large aircraft structure, i.e., wing. The alternative energy support may reduce fuel consumption and improve flight performance. However, the computational procedure fit for design purposes of an aircraft with energy harvesting capability also has not yet been developed. Thus, the development of computational methods for energy harvesting from an aircraft structure is also aimed in the present work.

As the first part of the present work, a novel hybrid mathematical/computational scheme is built to evaluate the energy harvested by a mechanical system. The governing voltage differential equations of the piezoelectric composite beam can be coupled with the output from a numerical method, e.g. the Finite Element Method (FEM). The scheme can evaluate various excitation forms concerning bending deformation including dynamic force and base excitation. In this report, the capabilities and robustness of the scheme are compared with results from the literature. Implementation to the simulation of a notional jet aircraft wingbox with a piezoelectric skin layer is shown in some detail. The results pointed out that the electrical power generated can be as much as 39.13 kW for a 14.5 m wingspan.

The second part of the present work focused on the evaluation of alternative composite material, namely the multiphase composite with active structural fiber. The active structural fiber constructed of carbon fiber as a core with a piezoelectric shell as the coating can be flexibly optimised in terms of weight and electromechanical coupling. Hence, it may provide a lightweight benefit compared to the bulk piezoelectric material. In the present work, for the first time, the multiphase composite is implemented for energy harvesting purpose. An application to a notional jet aircraft wingbox is evaluated. An analysis of the trade-off between the energy harvested, the weight reduction and the fuel saving of the aircraft is shown in some detail.

Lastly, the third part of the present work is the development of a novel iterative FEM for piezoelectric energy harvesting. The application of the present iterative FEM to evaluate the piezoelectric energy harvesting of lifting structures under an aeroelastic condition, i.e., gust load, is shown in some details. Furthermore, energy harvesting potential from a transport aircraft wingbox is also investigated. The results pointed out that the wingbox is still in a safe condition even when it is subjected to a 30 m/s gust amplitude while harvesting 51 kW power. In addition, for the first time, stress and failure analyses of the structure with an active energy harvesting layer are performed.

Acknowledgment

The author gratefully acknowledges Dr Jose Luis Curiel-Sosa and Dr Anton Krynkin for their continuous support and the fruitful discussions. The author also acknowledges the funding from Indonesia Endowment Fund for Education (LPDP).

The author also would like to thank Indonesia National Institute of Aeronautics and Space (LAPAN), in particular, Mr Nanda Wirawan for the support in the engineering analysis works. Lastly, I want to dedicate my deepest gratitude to my family and friends.

List of Publications

During his PhD study, the author has published several journal articles in which some of them are based on the works done for his PhD thesis. The main articles published and submitted by the author during his PhD study are listed below:

Main publications

1. **M. Akbar** and J.L. Curiel-Sosa, "Piezoelectric energy harvester composite under dynamic bending with implementation to aircraft wingbox structure" *Composite Structures*, vol. 153, pp. 193-203, 2016.
2. **M. Akbar** and J.L. Curiel-Sosa, "Evaluation of piezoelectric energy harvester under dynamic bending by means of hybrid mathematical/isogeometric analysis" *International Journal of Mechanics and Materials in Design*, vol. 14(4), pp. 647-667, 2018.
3. **M. Akbar** and J.L. Curiel-Sosa, "Implementation of multiphase piezoelectric composites energy harvester on aircraft wingbox structure with fuel saving evaluation" *Composite Structures*, vol. 202, pp. 1000-1020, 2018.
4. **M. Akbar** and J.L. Curiel-Sosa, "An iterative finite element method for piezoelectric energy harvesting composite with implementation to lifting structures under gust load conditions", *Composite Structures*, vol. 219, pp. 97-110, 2019.
5. **M. Akbar** and J.L. Curiel-Sosa, "An iterative finite element method for piezoelectric energy harvester and actuator with implementation to jet aircraft wing" submitted to *Composite Structures*.

Meanwhile, other publications of the author are:

Other publications

1. N.A. Abdullah, J.L. Curiel-Sosa and **M. Akbar**, "Aeroelastic assessment of cracked composite plate by means of fully coupled finite element and Doublet Lattice Method" *Composite Structures*, vol. 202, pp. 151-161, 2018.
2. M.I.M Ahmad, J.L. Curiel-Sosa, **M. Akbar** and N.A. Abdullah, "Numerical inspection based on quasi-static analysis using Rousselier damage model for aluminium wingbox aircraft structure" *Journal of Physics: Conference Series*, vol. 1106, pp. 012013, 2018.

-
3. N. Wirawan, N.A. Abdullah, **M. Akbar** and J.L. Curiel-Sosa, "Analysis on cracked commuter aircraft wing under dynamic cruise load by means of XFEM" *Journal of Physics: Conference Series*, vol. 1106, pp. 012014, 2018.
 4. N.A. Abdullah, J.L. Curiel-Sosa and **M. Akbar**, "Structural integrity investigation on cracked composites under aeroelastic condition by means of XFEM" accepted for publication in *Composite Structures*, 2019.
 5. N.A. Abdullah, J.L. Curiel-Sosa and **M. Akbar**, "Structural integrity investigation of commuter aircraft wing under discrete gust loads by means of XFEM" submitted to *AIAA Journal*.

Letter of Statement on The Use of Published Works

I the undersigned,

Name: Jose Luis Curiel-Sosa

Position: Lecturer

Affiliation: The University of Sheffield.

Hereby testify that I am the PhD supervisor of Mr Mahesa Akbar and a contributing author for his published works in

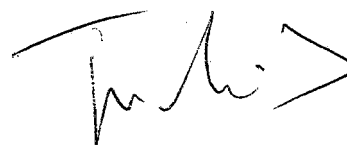
Akbar M, Curiel-Sosa JL. Piezoelectric Energy Harvester Composite Under Dynamic Bending with Implementation to Aircraft Wingbox Structure. *Composite Structures* 2016; 153: 193– 203.

Akbar M, Curiel-Sosa JL. Evaluation of Piezoelectric Energy Harvester Under Dynamic Bending by means of Hybrid Mathematical/ Isogeometric Analysis. *International Journal of Mechanics and Materials in Design* 2018; 14 (4): 647-667.

Akbar M, Curiel-Sosa JL. Implementation of Multiphase Piezoelectric Composites Energy Harvester on Aircraft Wingbox Structure with Fuel Saving Evaluation. *Composite Structures* 2018; 202, 1000-1020.

Mr Mahesa Akbar as the main author of those articles has contributed to the writing of the articles and performed the works on engineering analysis. I have supervised and reviewed his works before these articles submitted to the journals. Therefore, I acknowledged and approved the use of our published works in his PhD Thesis.

Sheffield, United Kingdom, 2019



Jose Luis Curiel-Sosa

Contents

Abstract	i
Acknowledgment	ii
List of Publications	iii
Table of Contents	vi
List of Figures	ix
List of Tables	xv
1 Introduction	1
1.1 Background and motivations	1
1.2 Research objectives	3
1.3 Research work plan	3
1.4 Thesis outline	5
2 Literature Review	6
2.1 Piezoelectric energy harvesting from lifting structure vibration	6
2.2 Computational analysis of piezoaeroelastic energy harvesting	9
2.3 Multiphase composites with active structural fiber	15
3 Hybrid Analytical/ Computational Scheme for Piezoelectric Energy Harvesting	18
3.1 Mathematical model	18
3.2 Code algorithm	24
3.3 Validation against analytical solution	26
3.4 Validation against experimental result	29
3.5 Validation against electro-mechanically coupled FEM	32
3.6 Investigation by higher-order elements	38
3.7 Summary	42
4 Implementation of The Hybrid Scheme on A Jet Aircraft Wingbox	44
4.1 Wingbox FEM analysis	44
4.2 Wingbox energy harvesting simulation	48
4.3 Summary	52

5	Multiphase Piezoelectric Composites with Active Structural Fiber	54
5.1	The Double-Inclusion model	54
5.2	Evaluation procedure of the multiphase composite effective electro-elastic properties	58
5.3	Case study and validation: Multiphase composite electro-elastic properties estimation	60
5.3.1	Electro-elastic properties comparison against analytical model and experimental results	60
5.3.2	Electro-elastic properties comparison against finite element model	66
5.3.3	Highlights on the effective electro-elastic properties concerning energy harvesting analysis	74
5.4	Summary	76
6	Application of The Multiphase Composites on A Jet Aircraft Wingbox	77
6.1	Aircraft weight breakdown in conceptual design	77
6.2	Evaluation procedure on the trade-off between aircraft weight and energy harvested	79
6.3	Wingbox energy harvesting simulation with the multiphase composite .	81
6.4	Aircraft fuel saving evaluation	85
6.5	Summary	88
7	Iterative Finite Element Method for Piezoelectric Energy Harvesting	90
7.1	The coupled electro-mechanical equations	91
7.2	Computational scheme	93
7.3	Unimorph plate under base excitation	97
7.4	Discrete 1-cosine gust and unsteady aerodynamic loads	101
7.5	Bimorph plate under gust load conditions	103
7.6	UAV wingbox under gust load conditions	109
7.7	Summary	115
8	Iterative Finite Element Method with Implementation to An Aircraft Wingbox	116
8.1	Jet aircraft wingbox under Gust Load Condition	116
8.2	Discussion on the power density and the flight performance	128
8.3	Summary	134
9	Conclusion	136
9.1	On the hybrid piezoelectric energy harvester model	139
9.2	On the multiphase piezoelectric composite	139

9.3	On the iterative FEM for piezoelectric energy harvesting	140
9.4	Future work	142
	Bibliography	143
	APPENDIX A	155
	APPENDIX B	157
	APPENDIX C	160
	APPENDIX D	168
	APPENDIX E	181
	APPENDIX F	187
	APPENDIX G	193
	APPENDIX H	195
	APPENDIX I	197
	APPENDIX J	199
	APPENDIX K	202
	APPENDIX L	208

List of Figures

1.1	The research flow diagram	4
2.1	2-DoF airfoil aeroelastic model	9
2.2	2-DoF airfoil piezoaeroelastic model	10
3.1	Specimen loaded by voltage, V	19
3.2	Specimen loaded by force, F	20
3.3	A cantilevered multilayer beam with piezoelectric layer	21
3.4	A cantilever beam loaded by bending moment, M	21
3.5	A cantilever beam with piezoelectric layer loaded by voltage, V	22
3.6	A cantilever beam with uniform cross-section	22
3.7	A cantilevered piezoelectric energy harvester exerted by mechanical and electrical loads	25
3.8	Schematic diagram of the energy harvesting system evaluation process	25
3.9	Bimorph 1 - Variation of the voltage amplitude with the resistance load	28
3.10	Bimorph 1 - Variation of the power amplitude with the resistance load	29
3.11	Bimorph 2 - Variation of the voltage amplitude with the resistance load	30
3.12	Bimorph 2 - Variation of the power amplitude with the resistance load	31
3.13	Variation of the thickness ratio, h^* , with the length ratio, L^* , of the spar	33
3.14	Variation of the (a) natural frequency, (b) critical damping ratio with the length ratio of the spar	34
3.15	Variation of the (a) maximum power amplitude and (b) optimum resistance load with the length ratio of the spar	35
3.16	Variation of the power amplitude with the resistance load for various length ratio of the spar	35
3.17	Investigation by IGA: Voltage amplitude vs resistance	39
3.18	Investigation by IGA: Power amplitude vs resistance	40
3.19	Variation of the (a) tip displacement and (b) tip angle with the thickness ratio, h_0/h	41
3.20	Variation of the reverse piezoelectric parameter with the thickness ratio, h_0/h	41

3.21	Bimorph 1 with $h_0/h = 10^{3.75}$ - Variation of the (a) voltage amplitude and (b) power amplitude with the resistance load	42
3.22	Bimorph 1 with $h_0/h = 10^4$ - Variation of the (a) voltage amplitude and (b) power amplitude with the resistance load	43
4.1	Wingbox vertical stiffness distribution	45
4.2	Wingbox topside view layout	45
4.3	Wingbox model for finite element analysis	46
4.4	Sketch of the lift coefficient distribution on the wing	48
4.5	Wingbox dynamic response amplitude along the span	48
4.6	Wingbox voltage amplitude vs resistance	49
4.7	Wingbox power amplitude vs resistance	50
4.8	Wingbox voltage amplitude vs resistance, loglog scale	50
4.9	Wingbox power amplitude vs resistance, loglog scale	51
5.1	Multiphase composite with active structural fiber (ASF)	56
5.2	Cross-section of energy harvester beam with multiphase composite as an active layer	58
5.3	(a) Stiffness, C_{33} , (b) Piezoelectric Constant, e_{33} , (c) Compliance, S_{31} , and (d) Charge Constant, d_{31} , vs ASF Volume Fraction of PZT-7A - Carbon Fiber - Epoxy Composites	63
5.4	(a) Density, ρ , (b) Charge Constant, d_{33} , (c) Compliance, $S_{11} + S_{12}$, and (d) Dielectric Permittivity Ratio, $\frac{\epsilon_{33}^T}{\epsilon_0}$, vs ASF Volume Fraction of PZT-7A-Carbon Fiber-Epoxy Composites	64
5.5	Charge Constant Ratio, $d_{31}^{\text{comp}}/d_{31}^{\text{bulk}}$, vs ASF Volume Fraction of BaTiO ₃ - SiC - LaRC-SI Composites	65
5.6	(a) Modulus Young, E_3 , (b) Relative Permittivity, $\epsilon_{33}^S/\epsilon_0$, (c) Modulus Young, E_1 , and (d) Relative Permittivity, $\epsilon_{11}^S/\epsilon_0$, vs ASF Volume Fraction of PZT-7A - Carbon Fiber - LaRC-SI Composites	67
5.7	Charge Constant Ratio $d_{31}^{\text{comp}}/d_{31}^{\text{bulk}}$ & $d_{33}^{\text{comp}}/d_{33}^{\text{bulk}}$, vs Aspect Ratio of PZT-7A - Glass - Epoxy Composites	69
5.8	Natural Frequency Comparison of PZT-5A - Carbon - LaRC-SI Composites for (a) Different Aspect Ratio at 50% Volume Fraction (b) Different Volume Fraction at 0.3 Aspect Ratio	70
5.9	(a) Detailed 3D FE eigenvector (structural mode shape), (b) Homogenisation FE eigenvector (structural mode shape), (c) Detailed 3D FE eigenvector (voltage mode shape), and (d) Homogenisation FE eigenvector (voltage mode shape) of the first bending mode, PZT-5A - Carbon Fiber - LaRC-SI composites with Vf 50% and AR 0.3	71

5.10	(a) Detailed 3D FE displacement, (b) Homogenisation FE displacement, (c) Detailed 3D FE voltage, and (d) Homogenisation FE voltage of the static bending response, PZT-5A - Carbon Fiber - LaRC-SI unimorph beam with Vf 50% - AR 0.3 and aluminium substrate	72
5.11	(a) Detailed 3D FE displacement, (b) Homogenisation FE displacement, (c) Detailed 3D FE voltage, and (d) Homogenisation FE voltage of the dynamic bending response at 0.6 frequency ratio, PZT-5A - Carbon Fiber - LaRC-SI unimorph beam with Vf 50% - AR 0.3 and aluminium substrate	73
6.1	Schematic diagram of the weight change calculation	80
6.2	Schematic diagram of the fuel saving evaluation	81
6.3	Variation of voltage amplitude to the resistance load for wingboxes with multiphase composite skin, AR 0.2, 0.4 & 0.6 at Vf 50%, and bulk PZT skin	85
6.4	Variation of power amplitude to the resistance load for wingboxes with multiphase composite skin, AR 0.2, 0.4 & 0.6 at Vf 50%, and bulk PZT skin	86
6.5	Variation of power amplitude to the resistance load for wingboxes with multiphase composite skin, Vf 50%, 60% & 70% at AR 0.2 and bulk PZT skin	87
7.1	Illustration of the iterative FEM process	93
7.2	The algorithm of the iterative FEM for a time domain problem	94
7.3	The algorithm of the iterative FEM for a frequency domain problem	95
7.4	The iteration histories of (a) voltage and (b) relative tip displacement amplitudes of the unimorph modelled by solid elements	99
7.5	The iteration histories of (a) voltage and (b) relative tip displacement amplitudes of the unimorph modelled by shell elements	99
7.6	The voltage output time history of the unimorph modelled by solid elements	100
7.7	Illustration of a lifting surface exposed to a freestream flow with airspeed V_∞ and 1-cosine gust with maximum gust speed V_{g_0}	101
7.8	Configuration of the bimorph	103
7.9	(a) Damping vs Airspeed, and (b) Frequency vs Airspeed graphs of the bimorph	104
7.10	Illustration of a lifting surface exposed to a freestream flow with airspeed V_∞ and an impulse gust with maximum gust speed V_{g_0}	106

7.11	Time histories of the power output of the bimorph at 10 m/s airspeed for different gust period	107
7.12	Time histories of (a) the tip displacement and (b) the power output of the bimorph at 10 m/s airspeed	107
7.13	Time histories of (a) the tip displacement and (b) the power output of the bimorph 30 m/s airspeed	108
7.14	Displacement contours at $t_g = 0.175$ s of the bimorph with airspeeds (a) 10 m/s and (b) 30 m/s (displacement unit in mm)	109
7.15	Topside view of the UAV wingbox configuration: Wingbox only - Structural model (top), Wingbox and wing surface - Structural model and aerodynamic panels (bottom)	110
7.16	(a) Damping vs Airspeed, and (b) Frequency vs Airspeed graphs of the UAV wingbox	111
7.17	Time histories of (a) the tip displacement and (b) the voltage output of the UAV wingbox under 1-cosine gust	112
7.18	The power output time history	113
7.19	Displacement contour of the UAV wingbox at $t_g = 0.0285$ s (displacement unit in mm)	113
7.20	Voltage contour of the piezoelectric layer of the UAV wingbox at $t_g = 0.0285$ s (voltage unit in μV)	114
7.21	The voltage output time histories at different iteration steps	114
8.1	Topside view of the aircraft wingbox configuration: Wingbox only - Structural model (left), Wingbox and wing surface - Structural model and aerodynamic panels (right)	117
8.2	Mode shapes the aircraft wingbox	118
8.3	(a) Airspeed vs Damping ($V-g$), and (b) Airspeed vs Frequency ($V-f$) graphs of the aircraft wingbox	119
8.4	The time histories of (a) vertical tip displacement and (b) voltage output of the aircraft wingbox for different gust gradient distances with gust velocity 15 m/s	120
8.5	The power output time history of the aircraft wingbox for different gust gradient distance with gust velocity 15 m/s	120
8.6	The voltage output time history of the aircraft wingbox with gust gradient distance 12.5 MAC at different iteration step	121
8.7	The time histories of (a) vertical tip displacement and (b) voltage output of the aircraft wingbox for different gust velocities with gust gradient distance 12.5 MAC	122

8.8	The power output time history of the aircraft wingbox for different gust velocity with gust gradient distance 12.5 MAC	123
8.9	Displacement contours of the aircraft wingbox for 12.5 MAC gust gradient distance with (a) 15 m/s and (b) 30 m/s gust velocities at $t_g = 0.3$ s (displacement unit: mm)	124
8.10	The stress contours with (a) $V_{g0} = 15$ m/s, (b) $V_{g0} = 30$ m/s of the aircraft wingbox for $H_g = 12.5$ MAC at $t_g = 0.3$ s (stress unit: kPa) . .	125
8.11	The failure indices with (a) $V_{g0} = 15$ m/s, (b) $V_{g0} = 30$ m/s of the aircraft wingbox for $H_g = 12.5$ MAC at $t_g = 0.3$ s	126
8.12	The time histories of (a) voltage output and (b) power output of the aircraft wingbox with multiphase composite for different time step . . .	127
8.13	The time histories of (a) voltage output and (b) power output of the aircraft wingbox with multiphase composite for different gust velocities (Up gust) with gust gradient distance 12.5 MAC	127
8.14	The time histories of (a) voltage output and (b) power output of the aircraft wingbox with multiphase composite for different gust velocities (Down gust) with gust gradient distance 12.5 MAC	128
8.15	Mission profile of a typical jet transport aircraft	131
8.16	Mission profile with energy harvesting system and extended cruise range using the fuel saved	132
8.17	(a) The number of gust occurrence per flight, and (b) Total energy generated per flight as functions of the gust amplitude (V_{g0})	132
G.1	The first bending mode of the jet aircraft wingbox with PZT-5A as upper skin material	193
G.2	The dynamic response at 0.5 frequency ratio of the jet aircraft wingbox with PZT-5A as upper skin material (displacement unit: inch)	193
G.3	The dynamic response at 0.7 frequency ratio of the jet aircraft wingbox with PZT-5A as upper skin material (displacement unit: inch)	194
G.4	The dynamic response at 0.9 frequency ratio of the jet aircraft wingbox with PZT-5A as upper skin material (displacement unit: inch)	194
H.1	The dynamic response at 0.9 frequency ratio of the jet aircraft wingbox with multiphase composite at Vf 50% and AR 0.2 (displacement unit: inch)	195
H.2	The dynamic response at 0.9 frequency ratio of the jet aircraft wingbox with multiphase composite at Vf 50% and AR 0.6 (displacement unit: inch)	195

H.3	The dynamic response at 0.9 frequency ratio of the jet aircraft wingbox with multiphase composite at V_f 60% and AR 0.2 (displacement unit: inch)	196
H.4	The dynamic response at 0.9 frequency ratio of the jet aircraft wingbox with multiphase composite at V_f 70% and AR 0.2 (displacement unit: inch)	196
I.1	The flutter response of Xiang et al. UAV wingbox associated with the third bending eigenvector at airspeed 150 m/s and frequency 174 Hz . .	197
I.2	The flutter response of Xiang et al. UAV wingbox associated with the first torsion eigenvector at airspeed 150 m/s and frequency 207 Hz . . .	197
I.3	The flutter response of Xiang et al. UAV wingbox associated with the fourth bending eigenvector at airspeed 150 m/s and frequency 336 Hz .	198
I.4	The flutter response of Xiang et al. UAV wingbox associated with the mixed eigenvector (bending and torsion modes already coalesced) at airspeed 210 m/s and frequency 90 Hz	198
J.1	Displacement contour of the aircraft wingbox for 12.5 MAC gust gradient distance with gust velocities at $t_g = 0.225$ s (displacement unit: mm) .	199
J.2	Displacement contour of the aircraft wingbox for 12.5 MAC gust gradient distance with gust velocities at $t_g = 0.275$ s (displacement unit: mm) .	199
J.3	Displacement contour of the aircraft wingbox for 12.5 MAC gust gradient distance with gust velocities at $t_g = 0.325$ s (displacement unit: mm) .	200
J.4	Displacement contour of the aircraft wingbox for 12.5 MAC gust gradient distance with gust velocities at $t_g = 0.375$ s (displacement unit: mm) .	200
J.5	Displacement contour of the aircraft wingbox for 12.5 MAC gust gradient distance with gust velocities at $t_g = 0.525$ s (displacement unit: mm) . .	200
J.6	Displacement contour of the aircraft wingbox for 12.5 MAC gust gradient distance with gust velocities at $t_g = 0.225$ s (displacement unit: mm) .	201
J.7	Displacement contour of the aircraft wingbox for 12.5 MAC gust gradient distance with gust velocities at $t_g = 1.275$ s (displacement unit: mm) .	201
J.8	Displacement contour of the aircraft wingbox for 12.5 MAC gust gradient distance with gust velocities at $t_g = 1.475$ s (displacement unit: mm) .	201

List of Tables

2.1	Power Density Comparison from Different Case Studies	17
3.1	Bimorph 1 - Material properties and configuration	26
3.2	Bimorph 1 - Natural frequency comparison	27
3.3	Bimorph 1 - Relative tip displacement & tip angle comparison	27
3.4	Bimorph 1 - Electrical parameters comparison	29
3.5	Bimorph 2 - Material properties and configuration	30
3.6	Bimorph 2 - Electrical parameters comparison at $R = 6.7 \text{ k}\Omega$	31
3.7	Material properties and geometry of the bimorph UAV wingspar	32
3.8	Natural frequency and maximum power comparison of De Marqui Jr. et al - FEM and Present Model (FEM)	36
3.9	Simulation time comparison	37
3.10	Electrical Parameters Comparison with $h_0/h = 10^4$	42
4.1	Weight and tip displacement, Z_{tip} , original model vs model A	47
4.2	Natural frequency comparison, model A vs model B	47
4.3	Simulation time comparison for the wingbox model	52
5.1	Material Properties of Piezoelectric Materials	60
5.2	Material Properties of Core Fiber Materials	61
5.3	Material Properties of Matrix Materials	62
5.4	Comparison of The Present Model and Lin-Sodano Model against The Experimental Results	66
5.5	Charge Constant Ratio Comparison: The Present Model vs XFEM - Koutsawa et al.	70
5.6	Natural Frequency Comparison for Different Volume Fraction at 0.3 Aspect Ratio of PZT-5A - Carbon - LaRC-SI Composites, Detailed 3D Finite Element vs Finite Element with Homogenization Properties	74
5.7	Natural Frequency Comparison of homogenised FE for Different Volume Fraction at 50% Volume Fraction of PZT-5A - Carbon - LaRC-SI Composites, Pure Mechanical Effect vs Activated Electro-mechanical Coupling	75

5.8	Natural Frequency Comparison for The Unimorph Beam, Detailed 3D Finite Element vs Finite Element with Homogenization Properties . . .	75
6.1	Wingbox Weight: Different Upper Skin Material	82
6.2	Wingbox Weight: Multiphase Composites Upper Skin, PZT-5A - Carbon - LaRC-SI 50% Volume Fraction	82
6.3	Wingbox Weight: Multiphase Composites Upper Skin, PZT-5A - Carbon - LaRC-SI 0.2 Aspect Ratio	82
6.4	Aircraft Empty Weight and Take-Off Weight: Different Wingbox Upper Skin Material	83
6.5	Aircraft Empty Weight and Take-Off Weight: Multiphase Composite Wingbox Upper Skin, PZT-5A - Carbon - LaRC-SI 50% Volume Fraction	83
6.6	Aircraft Empty Weight and Take-Off Weight: Multiphase Composite Wingbox Upper Skin, PZT-5A - Carbon - LaRC-SI 0.2 Aspect Ratio .	83
6.7	1st Bending Natural Frequency of The Wingbox for Different Multiphase Composite Composition	84
6.8	Maximum Power Amplitude and Resistance Load at Maximum Power of The Wingbox for Different Multiphase Composite Composition with 0.9 Frequency Ratio Excitation	88
6.9	Aircraft Fuel Saving Evaluation: Wingbox with Bulk PZT-5A Upper Skin	88
6.10	Aircraft Fuel Saving Evaluation: Wingbox with PZT-5A - Carbon - LaRC-SI Composite Upper Skin	89
7.1	Natural frequency comparison of the unimorph	98
7.2	Voltage amplitude for each iteration of the unimorph modelled by solid elements	100
7.3	Tip displacement amplitude for each iteration of the unimorph modelled by solid elements	100
7.4	Voltage and relative tip displacement amplitudes comparison of the unimorph	101
7.5	Natural frequency comparison of the bimorph	104
7.6	Electrical energy comparison of the bimorph	108
7.7	Electrical energy output of the UAV wingbox on each iteration step . .	115
8.1	Electrical energy output of the aircraft wingbox for different gust gradient distance with gust velocity 15 m/s	121
8.2	Electrical energy output of the aircraft wingbox on each iteration step .	122
8.3	Power Density Comparison from Different Case Studies	129

Chapter 1

Introduction

1.1 Background and motivations

The interest in the implementation of the multifunctional structure has grown significantly in the past decade. The terms multifunctional structures or defined as Multifunctional Material Systems by Christodoulou and Venables [1] possess not only load-bearing capability but also other non-structural functions. The type of multifunctional structure classified in the structural power system [1], or so-called the energy-storing/harvesting structure [2] is focused in the present work.

Despite numerous researches on small scale energy-storing/harvesting systems, only a few have made successful implementation on aerial vehicles. The Wasp UAV [3, 4] and a study by Anton and Inman [5] are amongst the few of them. The WASP UAV successfully implemented the concept of a multifunctional battery system. The structural-battery system is rechargeable before the flight, served as the energy storing system.

In contrast with the energy storing system of The WASP, Anton and Inman investigated in-flight energy harvesting capability of a remote control aircraft embedded with solar panels and piezoelectric patches [5]. During the flight test, both systems proven could harvest the energy and support the power sources of the aircraft. This work was followed by a series of analytical and experimental studies on the piezoelectric energy harvesting system for UAV. One of the most cited works in this field were the studies done by Erturk, Inman and colleagues [6, 7]. They successfully developed an analytical model of piezoelectric energy harvesting via structural vibration and validated it experimentally.

The implementation of piezoelectric materials for energy harvesting purpose on aerial vehicle shows the extended range of the multifunctional or smart structure applications. Targeted in the present work is the study of energy harvesting capabilities of piezoelectric embedded civil jet transport aircraft. Even though there has been

significant development on the topic of piezoelectric energy harvesting from lifting structures in the recent years [8], to the author's knowledge, there has not been any study concerning large aircraft structure.

In the present work, the focus on the transport aircraft structure is chosen due to the potential benefit that could be obtained for the flight operation. If proven that the energy harvested from the aircraft structure is promising to be used as alternative energy, fuel efficiency and flight performance may be increased. Hence, it will be profitable for the aircraft operator, i.e., airline.

The unique interaction between the aerodynamic loads and the structure in aircraft could be used as one of the sources for energy harvesting. The aerodynamic loads acting on aircraft are self-excited loads generated from the aircraft movement. These loads are heavily influenced by the shape of the structure, i.e., airfoil shape on wing structure. As the aircraft moves, the aerodynamic forces are generated; hence, the structure is deformed, and further, the aerodynamic load is reformed, and so on. These interactive coupling of aerodynamic and structure is called aeroelasticity phenomena [9].

The wing structure is focused as the primary object of investigation in the present work. During the flight operation, the aircraft wings generated the most substantial aerodynamic loads and their structures commonly exercised a significant amount of deformation. Therefore, in the present work, the first concern arises in how much energy could be harvested from this deformation.

De Marqui Jr. et al. in [10] provided one of the earliest models for energy harvesting via aeroelastic vibration. The studies on this topic have been evolved since, and numerous models have been developed [8]. However, there are only a few models [11–16] that are applicable for aircraft's normal flight operation. Moreover, those models are only verified for small scale and simple geometries, i.e., plates, UAV wings. Hence, in the present work, the second concern is how to evaluate the energy that is harvested from a larger and more complex wing structure, i.e., jet aircraft wing. Therefore, the development of computational methods to address this concern is an essential part of the present work.

In the first part of the present work, the development of a novel scheme to evaluate energy harvesting from an aircraft wing is conducted. A low computational cost scheme which aimed for early aircraft design stage is proposed. Further, a novel piezoelectric composite is also investigated in the present work. This new composite is purposed as an alternative to the bulk piezoelectric material; thus, better optimisation on the structural weight can be achieved. Lastly, the present work is focused on the development of a new finite element method for piezoelectric energy harvesting structure. This new finite element method is dedicated to a higher-fidelity investigation concerning a more realistic model on the aeroelastic vibration.

1.2 Research objectives

The research aims to provide a novel investigation on the energy harvesting potential from an aircraft wing exerted by aeroelastic loading. The present work will utilise existing commercial software augmented with computational coding as a means of evaluation. Hence, the present work embarks on the following objectives:

- Development of a new mathematical model or computational scheme concerning the utilisation of existing commercial software supported by computational code to perform aeroelastic simulation of an aircraft wing with energy harvesting capability;
- Modelling and analysis on a new piezoelectric composite for energy harvesting application;
- Investigation of piezoelectric energy harvesting feasibility on jet transport aircraft wing from aeroelastic vibration.

1.3 Research work plan

In the process of completing this research, a research flow diagram is made to highlight several essential processes as depicted in Figure 1.1.

The first part of this research focused on the study of a cantilevered piezoelectric energy harvester model under dynamic bending excitation. A cantilevered beam model is chosen due to it could be used as a simplified representation of an aircraft wing. A new computational scheme for piezoelectric energy harvesting, so-called hybrid analytical/computational scheme, is developed in this first part. This model is implemented to estimate the energy harvested from an aircraft wingbox structure.

A novel multiphase piezoelectric composite is investigated in the second part of this research. For the first time, the evaluation of this composite for energy harvesting purpose is conducted. The hybrid scheme is also applied to investigate the aircraft wingbox with different multiphase composite configurations. An analysis of the trade-off between the structural weight and energy harvested from different composite configurations is conducted.

The last part of the research focused on the evaluation of the aircraft wingbox exerted by aeroelastic conditions, i.e., cruise and gust loads. A new computational scheme based on an iterative process involving finite element method (FEM) is developed. Analysis of the aircraft wingbox through this iterative FEM is conducted. Both bulk piezoelectric material and multiphase composite are applied.

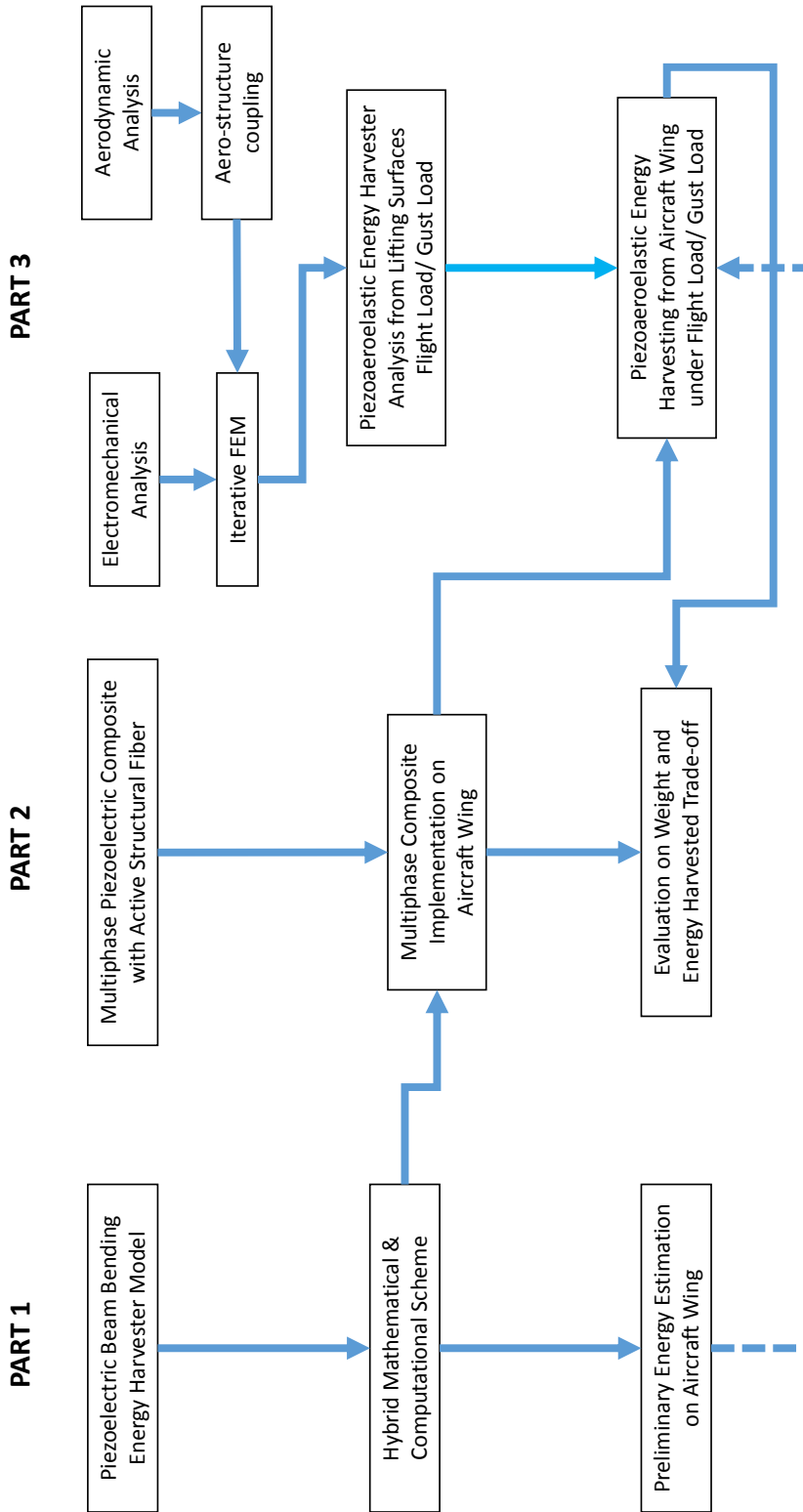


Figure 1.1: The research flow diagram

1.4 Thesis outline

This thesis presents the methods, results and discussions on the works conducted during the research.

Chapter 1 provides the backgrounds, motivations, objectives and the workflow of the current research.

Chapter 2 presents a detailed review of the significant researches on the piezoelectric energy harvesting, which influenced and provided valuable insights to the current research.

Chapter 3 depicts the derivation of the hybrid analytical/ computational scheme for piezoelectric energy harvesting under dynamic bending. A computational algorithm concerning this hybrid scheme is presented. Validations with the literature are discussed.

Chapter 4 shows the implementation of the hybrid scheme for energy harvesting evaluation of a notional jet aircraft wingbox. The results laid out the importance of the following parts of the current research.

Chapter 5 presents an extended Double-Inclusion method to model the multiphase piezoelectric composites. Validations with the results obtained by the previous researchers are discussed. Analyses of the electro-elastic properties of the composite comprised of carbon fiber, piezoceramic and epoxy are also shown in some details.

Chapter 6 discusses the implementation of the multiphase composite on the aircraft wingbox. An analysis of the structural weight, energy harvested and fuel saved from various composite configurations is presented.

Chapter 7 presents the derivation of the iterative FEM for piezoelectric energy harvesting structure. The algorithm of the computational work is explained. Investigations on lifting piezoelectric structures are discussed. Verifications with the literature are also shown in some details.

Chapter 8 discusses the evaluation of the aircraft wingbox exerted by aeroelastic loadings. The comparison of the power harvested with those from the literature is presented. An analysis of the flight performance with active energy harvesting is elaborated.

Chapter 9 concludes the findings and contributions of the current research in the field of piezoelectric energy harvesting. Some potential future works are also discussed.

Chapter 2

Literature Review

In this chapter, a review of the published works in relation to the current research is presented. The scope of the review is divided into three topics, as follows:

- The development of piezoelectric energy harvesting method with implementation to lifting structure;
- The advance on the piezoaeroelastic energy harvesting by means of computational analysis;
- The established works on piezoelectric composites and multiphase piezoelectric composites modelling.

2.1 Piezoelectric energy harvesting from lifting structure vibration

In the present work, the main interest is to study the potential of energy harvesting from civil transport aircraft. The initiation of this research came from an idea to convert structural vibration in aircraft to harvest the energy that can be utilised for aircraft flight. However, yet there has not been many studies involving large structure, especially transport aircraft. Numerous articles in energy harvesting topic have been published in the last few years. Despite this fact, based on the reviews in [17–19] most of the past researches only studied the level of power in microwatts to tens of watts.

In the case of a small-scale aerial vehicle, The Wasp UAV [3,4] is one of the successful application for multifunctional structure in a power system category. A structural-battery laminated wing skin reduced the weight and enhanced the endurance of the UAV. However, this structural-battery was focused on the energy storing capability rather than energy harvesting. Therefore, it was functioned to store the charged electrical energy when it was on the ground, connected to a power source.

Anton and Inman [5] performed one of the earliest and the most successful implementation of energy harvesting during flight operation. Solar panels and piezoelectric plates were embedded to a remote control aircraft's wings while a piezoelectric beam was put inside the fuselage. The piezoelectric plates in the wings were attached to the spars, harvesting energy via the wings' vibration whereas the piezoelectric beam was harvesting the energy from fuselage motion. They found that the piezoelectric-based energy harvesters were able to supply the internal capacitor up to 70%. It is important to remark that at their time, there has not been many established analytical model nor computational work on the piezoelectric energy harvesting from structural vibration.

Erturk and Inman established one of the first analytical models on the piezoelectric energy harvesting from vibration in [20]. They proposed a cantilevered piezoelectric energy harvester model under base excitation load. This model was then extended for the design of a so-called self-charging UAV wing spar in [6]. The self-charging system of this wing spar consisted of piezoelectric layers, and thin-film batteries functioned as energy harvesters and energy storage component. The design itself has been successfully tested experimentally [7].

The Erturk-Inman's base excitation model provided solutions for structural (displacement), and electrical (voltage and power) responses of the cantilever beam exerted by transverse dynamic motions [20]. The structural deformations are evaluated concerning the electromechanical coupling effect of the piezoelectric materials. Prior to this model, several modelling issues of piezoelectric energy harvesters were discussed by Erturk and Inman in [21].

Erturk and Inman stated that from the past researches, there had been a critical issue in the lack of reverse piezoelectric effect on the analytical models of the energy harvester. Based on [21], the absence of the reverse piezoelectric coupling from several studies leads to misleading results. The experiment by Erturk and Inman in [22] further confirmed the importance of the reverse piezoelectric effect. The inclusion of this effect on the mathematical model yields good comparisons with experimental results, whereas the model without the reverse effect overestimated the experimental results. This reverse effect is essential as it provides counterbalancing deformation to the deformation exerted by mechanical loads. In the present work, this reverse piezoelectric effect also becomes an important parameter as later discussed in Chapter 3 and Chapter 7.

Furthermore, the base excitation model has inspired several other studies. The piezoelectric energy harvester model via the vibration of two degrees of freedoms (2-DoF) airfoil under flutter condition was proposed by Erturk et al. in [23]. This model has also been successfully validated by wind tunnel testing. They also introduced the term "piezoaeroelastic" energy harvesting in [23]. This term is associated with

piezoelectric energy harvesting via the vibration of an aeroelastic system. Hence, in the piezoaeroelastic subject, involved not only the electrical and structural domains but also the fluid dynamic/ aerodynamic field.

In line with the 2-DoF flutter model of Erturk et al., other notable piezoaeroelastic models can be found [12, 24–26]. De Marqui Jr. et al. proposed a planar lifting surface model with the unsteady aerodynamic load modelled via Vortex Lattice Method in [24]. In addition, they also proposed a different model with unsteady aerodynamic calculation via Doublet Lattice Method in [25]. The main difference of both models is that the former is used in a time-domain analysis while the latter is applied in the frequency domain. Furthermore, a coupled model considering the electromagnetic field is proposed by [12]. Dias et al. in [26] extended the work of 2-DoF flutter model into a three degree of freedoms (3-DoF) concerning an additional degree of freedom from the control surface.

Detailed reviews on numerous studies of the piezoaeroelastic energy harvesting within the period of 2004-2017 are given in [8, 27–30]. One main concern that arises from those review articles is the lack of study on a more practical aerodynamic loading. Although significant attention was given to the piezoaeroelastic energy harvesting, mainly the studies focused on resonance and instability phenomenon, i.e., Vortex-Induced Vibration, flutter. To the author' knowledge, apart from the works done by De marqui et al. [11, 24], only a few articles [13–16] presented the evaluation of the lifting structure under a more practical aerodynamic loading condition, i.e., cruise and gust loads.

Flutter and other instability problems are never meant to be encountered during a typical flight of civil jet aircraft. The civil jet aircraft itself, based on the certification process refer to FAR 25, is designed to have flutter speed much higher than cruise speed. If an instability problem, i.e., flutter, is happened during a flight, it may lead to catastrophic behaviour. Hence, concerning energy harvesting from an aircraft structure, most of the available energy harvester models could not be implemented in the case of normal flight. Furthermore, the aircraft structure constructed from a more complicated configuration, i.e. skins, ribs and spars; thus, an airfoil model or a planar lifting surface model also could not be utilised. In more detail, the author further focused a review on the development of the computational and analytical model for piezoaeroelastic energy harvesting considering non-flutter or non-instability problem as presented in Section 2.2.

2.2 Computational analysis of piezoaeroelastic energy harvesting

The 2-DoF airfoil piezoaeroelastic model proposed by Erturk et al. in [23] laid a fundamental principle on the coupling between electrical response (voltage) and structural responses exerted by unsteady aerodynamic loads during critical flutter condition. An increase in the flutter instability limit due to additional damping in the system provided by the piezoelectric coupling effect, so-called shunt damping, was found from their investigation.

In their analytical model, Erturk et al. treated the voltage response as an additional degree of freedom to the 2-DoF aeroelastic system. The difference of a pure 2-DoF aeroelastic model and a piezoaeroelastic model can be seen in Equations (2.1)-(2.2) and Equations (2.3)-(2.5).

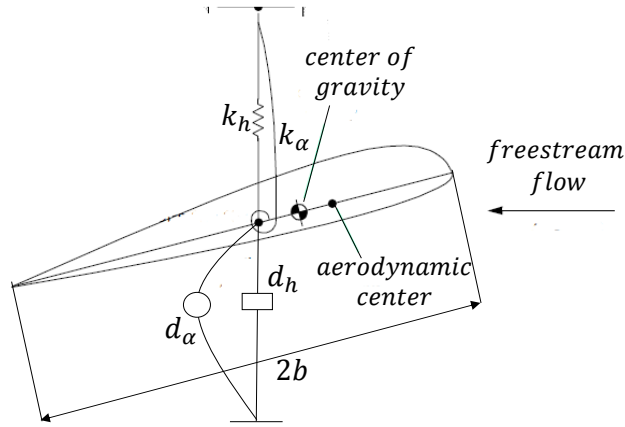


Figure 2.1: 2-DoF airfoil aeroelastic model

Equation (2.1) and Equation (2.2) define a set of equations for 2-DoF (airfoil) aeroelastic system [9]. The coupled degree of freedoms are heaving and pitching motions. These motions are denoted by h and α . The dot, $[\dot{\quad}]$, and double dots, $[\ddot{\quad}]$, define the first and second derivative to the time. Meanwhile, m and I are the mass per unit length and moment inertia per unit length of the airfoil. The terms b and x_α define the half-chord length and the dimensionless distance from the centroid to the elastic axis of the airfoil, respectively. The stiffness and damping parameters per unit length for both heaving and pitching motions are denoted by k_h , k_α , d_h and d_α . The aerodynamic lift and moment are represented by L and M , respectively.

$$m\ddot{h} + mx_\alpha b\ddot{\alpha} + d_h\dot{h} + k_h h = -L \quad (2.1)$$

$$mx_\alpha b\ddot{h} + I\ddot{\alpha} + d_\alpha\dot{\alpha} + k_\alpha\alpha = M \quad (2.2)$$

For flutter analysis, the 2-DoF aeroelastic system is commonly solved in the frequency domain, by assuming harmonic oscillation motions, i.e., $h = \bar{h}e^{i\omega t}$, $\alpha = \bar{\alpha}e^{i\omega t}$, $L = \bar{L}e^{i\omega t}$, $M = \bar{M}e^{i\omega t}$ where \bar{h} , $\bar{\alpha}$, \bar{L} and \bar{M} denote the amplitudes. The unsteady aerodynamic model based on the Theodorsen function [31] is often applied to find the aerodynamic coefficients. The airfoil movement influences the surrounding flow, and the aerodynamic loads affect the structural displacement; hence, the aerodynamic loads, \bar{L} and \bar{M} , can be modelled as the functions of motions, \bar{h} and $\bar{\alpha}$ [9]. In addition, based on the Theodorsen function, the aerodynamic coefficients are evaluated as functions of the reduced frequency, the ratio of the excitation frequency to the freestream airspeed times the airfoil's half-chord.

Concerning the aerodynamic loads as the functions of motions, the right-hand side terms of Equation (2.1) and Equation (2.2) can be moved to the left-hand side; hence, the right-hand side becomes zero. Therefore, this set of equations becomes a complex eigenvalue problem which is a function of the aerodynamic coefficients. This eigenvalue problem is solved via the classic flutter determinant approach for various airspeed and frequency or various reduced frequency [9]. The airspeed that makes the imaginary part of the respective eigenvalue branch equal to zero is determined as the critical flutter speed. At this speed, the damping of the aeroelastic system is zero. Physically, at this point, the aerodynamic load which equivalent to the damping force, so-called aerodynamic damping, eliminates the structural damping. Hence, further increasing the airspeed may lead to unstable behaviour, causing a catastrophic effect.

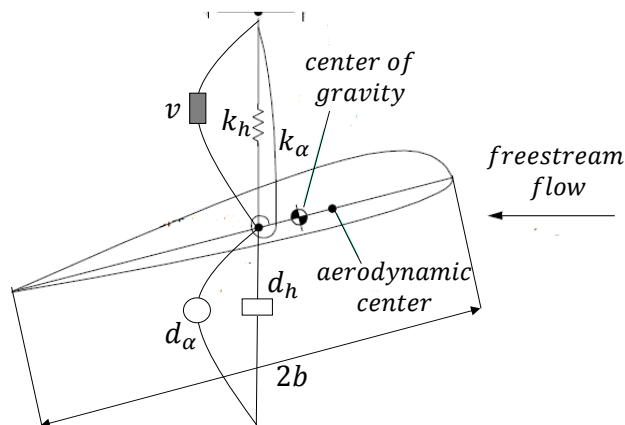


Figure 2.2: 2-DoF airfoil piezoaeroelastic model

Erturk et al. in [23] added the additional electrical degree of freedom to modify the 2-DoF aeroelastic system. The voltage degree of freedom, v , is coupled with the heaving motion, as shown in Equation (2.3) and Equation (2.5). Meanwhile, as the pitching motion is not coupled with the voltage, Equation (2.4) remains the same as

the 2-DoF aeroelastic system. The piezoelectric coupling term is defined by θ . The capacitance of the piezoelectric structure and the resistance load are denoted by C_p and R , respectively. It is important to note that in the 2-DoF aeroelastic system, the parameters, i.e., mass, distances, loads, are mostly defined per unit length to represent an airfoil, a two-dimensional object. However, as the electromechanical coupling term, θ , usually evaluated for a specific length [23], the effect of the span length of the piezoelectric plate, l , needs to be included as shown in Equation (2.3).

$$m\ddot{h} + mx_\alpha b\ddot{\alpha} + d_h\dot{h} + k_h h - \frac{\theta}{l}v = -L \quad (2.3)$$

$$mx_\alpha b\ddot{h} + I\ddot{\alpha} + d_\alpha\dot{\alpha} + k_\alpha\alpha = M \quad (2.4)$$

$$C_p\dot{v} + \frac{v}{R} + \theta\dot{h} = 0 \quad (2.5)$$

Erturk et al. proposed an iterative solution procedure to solve the complex eigenvalue problem of Equations (2.3)-(2.5). The basic idea of this iterative process is to solve the set of these three equations using a similar approach as the 2-DoF problem. Although the voltage function of Equation (2.5) can be substituted to Equation (2.3) to eliminate the voltage term, the complex eigenvalue problem could not be solved using classical flutter determinant approach. There is another ω term as part of the electromechanical coupling function in addition to the ω term in the eigenvalue term. Hence, an iterative process was proposed by Erturk et al. concerning the convergence of the voltage term in Equation (2.5) and Equation (2.3) [23].

An initial condition assuming the electromechanical coupling terms as zero in Equation (2.3) can be applied to start the iterative process. Then, Equations (2.3) and (2.4) can be solved using the flutter determinant approach. Once the eigenvectors \bar{h} and $\bar{\alpha}$ are known, the voltage eigenvector, \bar{v} , can be obtained from Equation (2.5). This value of \bar{v} then become input for the next iteration, in which the electromechanical coupling term in Equation (2.3) is not zero. The iteration is continued until the eigenvalue, and the eigenvectors are converged.

Even though the model of Erturk et al. in [23] was proposed for solving a piezoaeroelastic problem at the flutter boundary, this model provided important insights for the present work. First, the piezoaeroelastic system of Equations (2.3)-(2.5) strengthen the author's understanding of the reverse piezoelectric effect. A comparison of Equation (2.1) and Equation (2.3) shows that the voltage harvested will add equal force to the system which acts against the mechanical force, i.e., aerodynamic force.

Furthermore, theoretically, it is possible to extend the system defined by Equations (2.3)-(2.5) to a forced excitation problem by adding external mechanical forces or disturbance. Lastly, the iterative process introduced by Erturk et al. in [23] to solve the piezoaeroelastic system can be further developed for the more complex system, i.e., multi-degree of freedoms (MDOF) system.

The airfoil flutter model of Erturk et al. [23] was further developed to a lifting surface model in [11, 24, 25]. A preliminary model of the piezoaeroelastic planar lifting surface was proposed by De Marqui Jr. and Jose Maria in [11]. This model utilises the combination of an electromechanically coupled FEM and a time-domain unsteady aerodynamic model via the Vortex-Lattice Method (VLM) of Katz and Plotkin [32]. De Marqui Jr. et al. further elaborated this preliminary model in [24] to evaluate the energy harvesting potential of a plate-like wing under excitation of different airspeed condition.

De Marqui Jr. et al. in [24] extended the piezoaeroelastic system of Erturk et al. [23] by defining an external disturbance to the system, a sharp-edged gust. Hence, the system became a forced excitation problem. Furthermore, the gust was defined so that the plate had a small angle of attack to produce an additional lift. The gust load was given within a very short period at the beginning of the analysis. Moreover, De Marqui Jr. et al. utilised finite elements to model the structure of the plate, i.e., mass, damping and stiffness matrices. Thus, the piezoaeroelastic system comprised an MDOF structure. Equations (2.6)-(2.7) depict the piezoaeroelastic system proposed by De Marqui Jr. et al. in [24].

$$\mathbf{M}\ddot{\Psi} + \mathbf{G}\dot{\Psi} + \mathbf{K}\Psi - \Theta V = \mathbf{F} \quad (2.6)$$

$$\Theta^T \dot{\Psi} + C_p \dot{V} + \frac{V}{R} = 0 \quad (2.7)$$

The mechanical coordinates are represented by vector Ψ . The mass, structural damping and stiffness matrices are defined by \mathbf{M} , \mathbf{G} and \mathbf{K} , respectively. The electromechanical coupling vector is denoted by Θ . Meanwhile, V is the voltage generated across the structure, i.e., plate. The force vector, \mathbf{F} , represents the aerodynamic loads obtained via the VLM. The effect of aerodynamic damping on the system was discussed in [24]. They observed that by initially increasing the airspeed, the system reached a point of the maximum damping. At this point, the maximum aerodynamic damping occurred and supported the structural damping. However, as the airspeed was further increased, the aerodynamic damping decreased until it vanished and even became negative damping. At the critical flutter speed, the aerodynamic loads produced negative damping which eliminated the structural damping [24].

Concerning the energy harvesting case, the maximum aerodynamic damping gives a rapidly damped vibration as shown in [24]. Hence, the case of maximum damping is undesirable in the vibration-based energy harvesting, as the harvested energy will be minimum. In contrast, at the critical flutter boundary, De Marqui Jr. et al. expected a large deformation and sustained oscillation; thus, it gives the most benefit for the energy harvesting [24]. Abdelkefi also strengthens this conclusion in his review article [8].

He found that most of the studies in aeroelastic energy harvesting expected to gain sustained energy by imposing the structure at the flutter boundary.

However, as previously discussed in Section 2.1, flutter is a catastrophic phenomenon in the aircraft flight. Therefore, despite generating sustained deformation and energy, the aircraft structure will be collapsed if flutter happens. Hence, energy harvesting at the flutter condition is not an applicable practice for aircraft structure. Nevertheless, the study by De marchi Jr. et al. in [24] provided a good insight that an external disturbance, i.e., gust load, could be utilised to generate additional energy from a low airspeed. Despite a gust load is also an undesirable phenomenon in a flight, it is very likely to occur during a routine flight. Therefore, firstly, in the present work, the concern that arises is whether the electrical energy harvested at a regular flight operation, i.e., cruise with gust disturbance, will be sufficient to be considered as alternative energy to the aircraft.

De Marqui Jr et al. in [25] performed similar investigation to the plate-like wing in [24] via a frequency-domain analysis. The frequency-domain unsteady aerodynamic model, Doublet-Lattice Method (DLM) of Albano and Rodden [33], was used to perform the flutter analysis. In agreement with [23], they found that the shunt damping effect increased the critical flutter speed of the system.

The structural model in [11,24,25] utilised the laminated quadrilateral shell element developed by De Marqui Jr. et al. in [10]. Apart from the 3-DOF displacement, one vertical translation and two rotations, on each node, a voltage degree of freedom is added to each element. This model was further advanced for the analysis of energy harvesting from functionally graded piezoelectric materials (FGPMs) in [34,35]. The FGPMs were implemented in order to enhance the mechanical performance of the piezoelectric composites by avoiding stress concentration and crack propagation.

To the author's knowledge, to this date, the work by De Marqui Jr. et al. in [10] is one of the few that successfully modelled a plate-like energy harvester with three-dimensional motion via an electromechanically coupled finite element model. However, this shell model requires an effort in computational coding. Concerning large and complicated structure, i.e., jet aircraft wing, the computational effort will significantly increase. Geometry reconstruction and meshing considerably will need a high cost if a self-made computational program is used. Hence, in the present work, another concern also arises, whether an already established commercial software can be utilised to perform the energy harvesting evaluation with minimum addition or modification to complement the software.

In contrast with the finite element model of [10] which require numerical code development, some efforts have been made to utilise commercial finite element and computational fluid dynamic (CFD) software for the energy harvesting simulation such as

presented in [36–40]. Although those models have been experimentally well-validated, the analyses were only performed for short-circuit (no resistance load, $R \rightarrow 0$) or open-circuit ($R \rightarrow \infty$) problems. Thus, there was no variation to the resistance load.

An attempt of using 3D finite elements of commercial software to evaluate the effect of the resistance load variation is given in [41]. However, validation by other methods was not conducted in their investigation. Furthermore, the governing equation applied to their finite element model depicted the full effect of the electromechanical coupling and capacitance as the analogues of the stiffness. This approach is in contrast with the model in [10, 23], in which the capacitance and one part of electromechanical coupling are the analogues of damping and associated with the velocity as shown in Equation (2.5) and Equation (2.7).

Other efforts performed numerical investigation via the analogue of the piezoelectric energy harvester structure with the electrical circuit model. In [42], parameter identification on a finite element model was conducted to construct an equivalent circuit model which was simulated in an integrated circuit simulator software. In opposite, the investigation in [43] constructed the equivalent of the structural model from the electrical parameters, which was input to a commercial finite element software. Meanwhile, the investigation presented in [44] attempted to couple a finite element model with a circuit modeller software.

Recent studies by [45, 46] proposed beam elements which comprise 3D effects to model the piezoelectric energy harvester. Another use of beam element for fluid-structure interaction is presented in [47]. Iterative scheme between beam elements and aerodynamic loads modelled via the Reynolds-averaged Navier-stokes (RANS) was developed. However, their simulation also concerned a resonance case, not a forced excitation problem, where the wake of a cylinder exerted an energy harvester plate.

Xiang et al. [13] and Bruni et al. [14] investigated discrete gust loading conditions, i.e., 1-cosine and square gusts. Xiang et al. [13] modelled a UAV wingbox structure using beam elements with discrete masses and stiffnesses obtained from a step function. Whereas Bruni et al. [14] utilised lumped parameters to model the masses and stiffnesses of a slender wing. Both investigations applied the aerodynamic loading via the Strip theory. The unsteady aerodynamic model of Strip theory is the extension of the Theodorsen aerodynamic model for airfoil [9]. In the Strip theory, the wing is divided into panels in the spanwise direction, where the aerodynamic loads acting on each panel are based on the Theodorsen theory. Meanwhile, Tsushima and Su in [15] developed a model to evaluate random gust/ turbulence condition. Beam elements were also used to discretise the structure and coupled with a 2D airfoil unsteady aerodynamic model. In [16], this model was extended to include active control function. A highlight of these piezoaeroelastic studies concerning a flying structure is shown in

Table 2.1.

The entries in Table 2.1 depict a couple of experimental efforts in [5, 23]. Despite the fact that the models built in [11, 13–16, 24] provided the platforms to evaluate the energy harvesting potential from the lifting structure under cruise/gust loads, to the author’s knowledge, comparison of each method with other approaches have not yet been conducted.

The proposed new computational method, the iterative FEM, is utilised to reconstruct and to compare with some results depicted in Table 2.1. The detailed discussion is given in Chapter 7. Furthermore, Chapter 8 provides a more detailed comparison of the studies shown in Table 2.1 with some correlations to the present work.

2.3 Multiphase composites with active structural fiber

A highlight on the results presented later in Chapter 4 depicts that the weight increment due to the use of piezoelectric material in aircraft is massive compared to the power harvested. Thus, instead of benefits, it resulted in a loss due to weight increment. Hence, in the present work, an alternative to the bulk piezoelectric material is concerned. A so-called multiphase composite is evaluated to provide a lightweight energy harvesting structure.

Initially, Lin and Sodano in [48] introduced a concept of active structural fiber (ASF) constructed of a piezoelectric shell and a core fiber. The primary structural function, i.e., the load-bearing capability, is provided by the core fiber. In contrast, the piezoelectric shell provided electromechanical coupling effect, i.e., actuating and sensing. Lin and Sodano presented the fabrication methodology and the experimental test validation of the ASF in [49, 50]. Furthermore, the multiphase composite model was proposed by Lin and Sodano in [51]. The composite was depicted as the ASF with a surrounding matrix material.

Lin and Sodano proposed the Double-Inclusion model in [51] to estimate the effective electro-elastic properties of the multiphase composite. The FEM simulation was used to validate the model’s results. The Double-Inclusion model of the multiphase piezoelectric composite in [51] was based on the model proposed initially by Dunn and Ledbetter [52]. Hori and Nemat-Nasser in [53] initially derived the Double-Inclusion model. This model was generalised to a multi-inclusion model in [54]. However, both models in [52, 53] were applicable only to obtain effective elastic properties, non-piezoelectric material.

In order to incorporate the full electro-elastic properties, the piezoelectric analogue Eshelby’s tensor of [55] was introduced to the Double-Inclusion model in [51]. Eshelby’s

tensor [56] was initially established for an elastic material. The Eshelby tensor was further developed to the homogenisation scheme, i.e., effective medium approximation, by Hashin [57] and Mori-Tanaka [58]. Hashin and Mori-Tanaka methods provided transformations of the heterogeneous materials' microscopic properties to the macroscopic properties based on the averaging techniques, or so-called homogenisation. One of the most well-known and simplest homogenisation methods is the rule of mixture. The implementation of the Eshelby's tensor with the Mori-Tanaka method is more accurate to estimate the effective composite properties with large volume fraction than the rule of mixture [59].

Chan and Unsworth [60] derived one of the earliest analytical models to homogenise the properties of the single piezoelectric fiber composite. Dunn and Taya [61] implemented the piezoelectric Eshelby tensor with various homogenisation scheme, i.e., dilute model, Mori-Tanaka method, self-consistent model, to predict the effective electro-elastic properties of a single piezoelectric fiber composite. The model's results were compared with the experimental data of Chan and Unsworth [60]. It was found that the best comparison with the experiment's is provided by the Mori-Tanaka method. Odegard [62] compared the results of FEM simulation with the homogenisation schemes for the single inclusion piezoelectric composite. The Mori-Tanaka method was also given the closest comparison with the FEM results.

Other related works with the multiphase piezoelectric composite can be found in the development of the multi-inclusion piezoelectric composite models in [63–65] and the multiphase magneto-electro-elastic composite model in [66–68]. The interested reader is also referred to a review article in [69] which discussed various works on the inclusion model. Even though the multiphase piezoelectric provide multifunctional capability [51, 70], the implementation of energy harvesting structure is not found in the literature.

Table 2.1: Power Density Comparison from Different Case Studies

Case Study	Flight/ Load Condition	Aircraft/Wing Structure	Piezoelectric Structure	Power Density kW/m ³
Anton & Inman [5]	Flight test, 6 min cruise, V=12.5 m/s, h=30m	RC Aircraft, 1.8m span, 23cm chord	MFC & PFC patches: (102×16×0.3)mm ³ , (145×15×0.3)mm ³	0.001 (MFC) 0.008 (PFC)
Wang & Inman [71]	Numerical, V=15m/s, Assumed clear sky with 0.02g RMS vibration	Plate-like wing 700.5mm halfspan, 38mm chord	1 Packaged PZT-5A layer (45×25.4×0.5)mm ³	0.275
Tsushima & Su [16]	Numerical model, Dryden gust, Vg=30m/s, 10s, V=70m/s, h=15km	Tapered Wing, 200cm halfspan, 15cm meanchord	Piezo layers cover upper-lower surfaces, thickness=0.127mm	1.75
Erturk et al. [23]	Wind tunnel test, 25s flutter, V=9.3m/s (critical flutter speed)	2DoF Wing Section, 0.5m span, 25cm chord	Bimorph, Packaged PZT-5A 2×(45×25.4×0.5)mm ³	4.61
De Marqui Jr. et al. [24]	Numerical Model, 1.5s flutter, V=41m/s (critical flutter speed)	Plate-like wing, 1.2m halfspan 24cm meanchord	Bimorph, PZT-5A 2×(360×240×0.5)mm ³	8.68
Tsushima & Su [72]	Numerical model, LCO, V=89.25m/s (post-flutter speed)	Tapered Wing, 200cm halfspan, 15cm meanchord	Piezo layers cover upper-lower surfaces, thickness=0.127mm	75.62
Xiang et al. [13]	Numerical model, 1-cos gust, Vg=0.15V, 1.05s, V=9.3m/s, h=4km	Tapered Wing, 1m halfspan, 19cm meanchord	1 layer PZT-5H at upper skin (100×40×0.255)mm ³	251.77

Chapter 3

Hybrid Analytical/ Computational Scheme for Piezoelectric Energy Harvesting

In this chapter, the mathematical model for the energy harvesting of a piezoelectric cantilever beam under dynamic bending load is presented. The novel scheme to calculate energy harvested involving hybrid analytical and computational procedure is described. The governing voltage differential equations of the piezoelectric composite beam are coupled with the output from the computational method, i.e., finite element method.

This hybrid scheme is purposed to serve as a tool to evaluate energy harvesting potential for a more complicated structure which could not be solved analytically. The implementation of the hybrid scheme is aimed at a conceptual design level, to provide a fast and cheap computational procedure. This hybrid scheme is validated with the analytical method, numerical investigation, and experimental result from the literature. An investigation through coupling with an advanced computational method, higher-order elements, is also discussed in some details.

Some works and results presented in this chapter are parts of the author's published works in *Composite Structures*, Volume 153, 2016; and *International Journal of Mechanics and Materials in Design*, Volume 14(4), 2018.

3.1 Mathematical model

The constitutive relationship of piezoelectric material is constructed from both the electrical and mechanical domains. For an isotropic material, the description of the electrical and mechanical characteristics are shown in Figures 3.1 and 3.2.

In Figure 3.1, when a voltage load is supplied to an electrically active specimen,

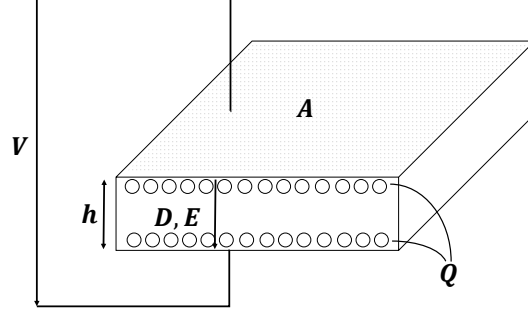


Figure 3.1: Specimen loaded by voltage, V

V , the electrical charges, Q (denoted by circles 'o'), accumulate. In relation to the voltage, an electrical field, E , is also created along the thickness of the specimen. The material's permittivity, ε^T , allows the movement of the electrical charges and generates the electrical displacement, D [73]. The transformations between these properties are expressed as

$$D = \frac{Q}{A} \quad (3.1)$$

$$Q = CV \quad (3.2)$$

$$C = \varepsilon^T \frac{A}{h} \quad (3.3)$$

$$D = \varepsilon^T E \quad (3.4)$$

where Q , C , V , D , and E are the electrical charges (Coulomb), capacitance (Farad), voltage (Volt), electrical displacement (Coulomb/m²) and electrical field (Volt/m); A and h are the surface area (m²) and thickness (m) of the specimen. Meanwhile, ε^T , is the permittivity at a constant stress field (Farad/m). This permittivity often represented as a relative permittivity as follows

$$\varepsilon^T = \varepsilon_r \varepsilon_0 \quad (3.5)$$

where ε_0 is the vacuum permittivity (8.85x10⁻¹² Farad/m) and ε_r is the relative permittivity. For a piezoelectric material, the expression in Equation (3.4) is called the strain-charge form. Another expression is defined as the stress-charge form where the permittivity at a constant strain field is used [74].

A specimen made of an isotropic material in Figure 3.2 is loaded by a mechanical force, F . This force exerted a deformation, δ (shown in the figure reducing the thickness). Hence, it creates a mechanical strain, S and stress, T [75]. The relationships between these quantities in a homogeneous, isotropic and linear-elastic material are written as

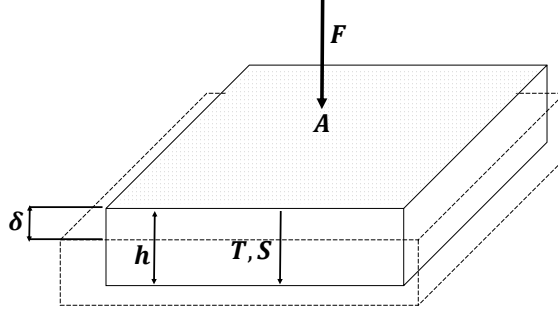


Figure 3.2: Specimen loaded by force, F

$$T = \frac{F}{A} \quad (3.6)$$

$$S = \frac{\delta}{h} \quad (3.7)$$

$$S = sT \quad (3.8)$$

In a piezoelectric material, the electrical and mechanical domains are coupled. Mechanical stress could generate an electrical displacement, and an electrical field could create a mechanical strain. In a strain-charge form, this coupling is defined by a piezoelectric charge constant, d . This charge constant relates the structural deformation generated by a unit of voltage; and vice versa [73]. Based on the IEEE Standard on Piezoelectricity [74], the constitutive relations in Equations (3.4) and (3.8) can be coupled as a set of electromechanical equations and can be expressed as

$$D = \varepsilon E + dT \quad (3.9)$$

$$S = dE + sT \quad (3.10)$$

Ballas [76] derived the mathematical models of a piezoelectric beam bending actuator exerted by static and dynamic bending loads. The composite beam made of substrate layers (host structure; non-piezoelectric material) and electrically active layers (piezoelectric material) is concerned in [76]. The illustration of this beam is shown in Figure 3.3.

The following assumptions were taken by Ballas in [76]:

1. The electrical field only generated in the thickness direction (poling direction)
 $E_2 = E_3 = 0$ & $E_1 \neq 0$;
2. Only one mechanical stress component generated in the longitudinal direction
 $T_1 = T_2 = T_4 = T_5 = T_6 = 0$ & $T_3 \neq 0$;
3. All active layers are driven by the same voltage along the poling direction, V_1 .

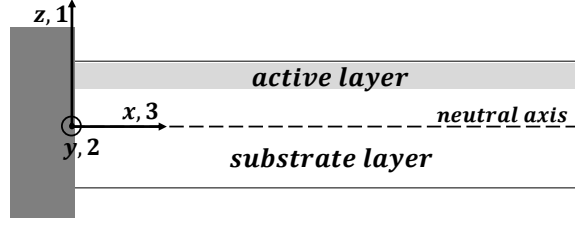


Figure 3.3: A cantilevered multilayer beam with piezoelectric layer

Hence, Equations (3.9) and (3.10) can be rewritten as

$$D_1 = \varepsilon_{11}^T E_1 + d_{31} T_3 \quad (3.11)$$

$$S_3 = d_{31} E_1 + s_{33} T_3 \quad (3.12)$$

In Figure 3.4, illustration of a mechanical load in the form of bending moment, M , acting on a cantilever beam is shown. Here, the bending deformation can be quantified by a transverse displacement, ζ , and a bending slope, θ . In addition, at an arbitrary point, P , located at a distance, z , from the neutral axis, a strain is generated.

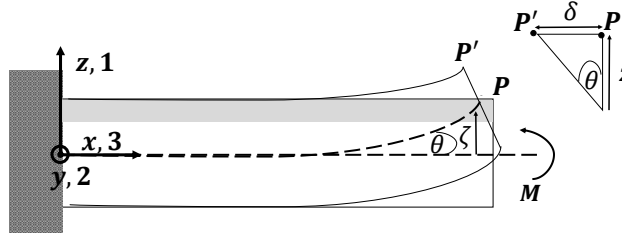


Figure 3.4: A cantilever beam loaded by bending moment, M

The mechanical strain at x-direction is written as

$$S_3 = -z \frac{\partial^2 \zeta}{\partial x^2} \quad (3.13)$$

In the active layer, the electrical voltage, V , creates an electrical field, E , as depicted in Figure 3.5.

$$V = \int_{h_l}^{h_u} E_1 dz \quad (3.14)$$

Incorporating Equations (3.13) and (3.14) into Equations (3.11) and (3.12), yields

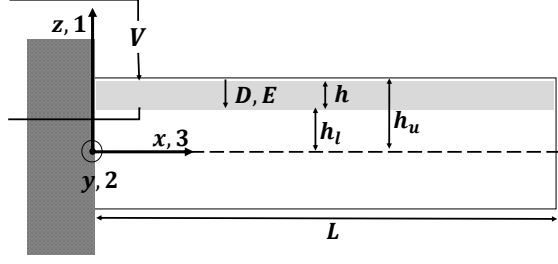


Figure 3.5: A cantilever beam with piezoelectric layer loaded by voltage, V

$$D_1 = \frac{V}{h} \left(\varepsilon_{11}^T - \frac{d_{31}^2}{s_{33}} \right) - \frac{d_{31}(h_u^2 - h_l^2)}{2s_{33}h} \frac{\partial^2 \zeta}{\partial x^2} \quad (3.15)$$

Moreover, the electrical charges at a certain point, Q , is evaluated through the Gauss's theorem over an area, A , as

$$Q = \oint D_1 dA \quad (3.16)$$

Thus, considering a uniform cross section depicted in Figure 3.6, the electrical charges, $Q(x)$, from the root until a certain point at length x , could be defined as

$$Q(x) = \frac{V(x)bx}{h} \left(\varepsilon_{11}^T - \frac{d_{31}^2}{s_{33}} \right) - \frac{d_{31}(h_u^2 - h_l^2)b}{2s_{33}h} \frac{\partial \zeta(x)}{\partial x} \quad (3.17)$$

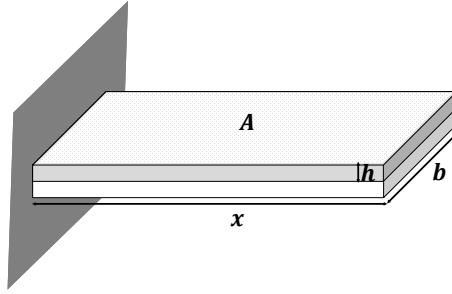


Figure 3.6: A cantilever beam with uniform cross-section

In the present work, two parameters are defined as

$$\Gamma_1 = \frac{bx}{h} \left(\varepsilon_{11}^T - \frac{d_{31}^2}{s_{33}} \right) \quad (3.18)$$

and,

$$\Gamma_2 = \frac{d_{31}(h_u^2 - h_l^2)b}{2s_{33}h} \quad (3.19)$$

For a time-dependant motion, Equation (3.17) becomes

$$Q(x, t) = \Gamma_1(x)V(x, t) - \Gamma_2(x)\frac{\partial\zeta(x, t)}{\partial x} \quad (3.20)$$

The parameter Γ_2 defines an internal bending moment, M_{piezo} , exerted by a unit of voltage, V .

$$M_{piezo} = \Gamma_2 V \quad (3.21)$$

The concept of M_{piezo} was applied by Ballas [76] to evaluate the static deformation of a voltage-driven piezoelectric beam actuator. This concept has been well validated experimentally [76].

In the present work, Equation (3.20) is further elaborated for the energy harvesting purpose. An electrical circuit connected to the piezoelectric beam is considered.

$$\frac{dQ(x, t)}{dt} = I(x, t) = \frac{V(x, t)}{R} \quad (3.22)$$

where, I is the electrical current (Ampere) and R is the resistance load (Ohm, Ω).

Incorporating Equation (3.20) to Equation (3.22), yields a differential equation in terms of V ,

$$\Gamma_1 \frac{dV(x, t)}{dt} - \Gamma_2 \frac{d}{dt} \left(\frac{\partial\zeta(x, t)}{\partial x} \right) = \frac{V(x, t)}{R} \quad (3.23)$$

Assumes a harmonic oscillation motion

$$\zeta(x, t) = Z(x)e^{i\omega t} \quad (3.24)$$

$$V(x, t) = \bar{V}(x)e^{i\omega t} \quad (3.25)$$

where Z is the transverse displacement amplitude (meter) and \bar{V} is the voltage amplitude.

Equation (3.23) becomes

$$i\omega\Gamma_1\bar{V} - i\omega\Gamma_2\frac{\partial Z(x)}{\partial x} = \frac{\bar{V}}{R} \quad (3.26)$$

Concerning the electromechanical coupling effect, it is critical to remark that the displacement, $Z(x)$, is comprised of the displacement exerted by a mechanical load, Z_{mech} , and an accumulated electrical load, Z_{elec} . Thus,

$$\frac{\partial Z}{\partial x} = \frac{\partial Z_{mech}}{\partial x} + \frac{\partial Z_{elec}}{\partial x} \quad (3.27)$$

The Z_{elec} is generated by the internal forces due to the reverse piezoelectric effect. By employing the concept of M_{piezo} , the bending slope due to the electrical load is defined as

$$\frac{\partial Z_{elec}}{\partial x} = H_{\alpha m} M_{piezo} \quad (3.28)$$

or,

$$\frac{\partial Z_{elec}}{\partial x} = H_{\alpha m} \Gamma_2 V \quad (3.29)$$

Here, $H_{\alpha m}$ is the admittance function (rad/Newton-meter) of the displacement slope (rad) due to a unit of moment applied at the tip. This admittance function can be obtained straightforwardly by analytical method [76] or via computational analysis.

As stated by Erturk and Inman in [20], early works in piezoelectric energy harvesting as can be found in [77, 78], were lacking this reverse effect. Hence, the responses were highly inaccurate and overestimated the experimental results.

As far as the author's knowledge, the concept of M_{piezo} had only been used for the actuator case. Therefore, for energy harvesting purpose it is a novel concept to evaluate the reverse piezoelectric effect.

Furthermore, incorporating Equations (3.27) and (3.29), then Equation (3.26) becomes

$$\bar{V}(x) = \frac{i\omega\Gamma_2(x)\frac{\partial Z_{mech}(x)}{\partial x}}{-\frac{1}{R} + i\omega\Gamma_1(x) - i\omega\Gamma_2(x)^2 H_{\alpha m}(x)} \quad (3.30)$$

Concerning the voltage along the length of the beam ($x = L$), Equation (3.30) is rewritten as

$$\bar{V}(L) = \frac{i\omega\Gamma_2(L)\frac{\partial Z_{mech}(L)}{\partial x}}{-\frac{1}{R} + i\omega\Gamma_1(L) - i\omega\Gamma_2(L)^2 H_{\alpha m}(L)} \quad (3.31)$$

The maximum electrical power, P_{max} (Watt), is given as

$$P_{max} = \frac{\bar{V}^2}{R} \quad (3.32)$$

Figure 3.7 illustrates a cantilevered piezoelectric energy harvester exerted by two types of loading. The bending moment, M , as the mechanical load and the resistance, R , as the electrical load.

3.2 Code algorithm

In the present work, a computational code is built using MATLAB[®] to estimate the voltage and power responses based on Equations (3.31) and (3.32). The algorithm of the present code is depicted in Figure 3.8.

Two key inputs for the present code are

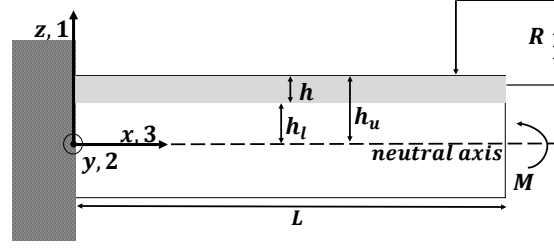


Figure 3.7: A cantilevered piezoelectric energy harvester exerted by mechanical and electrical loads

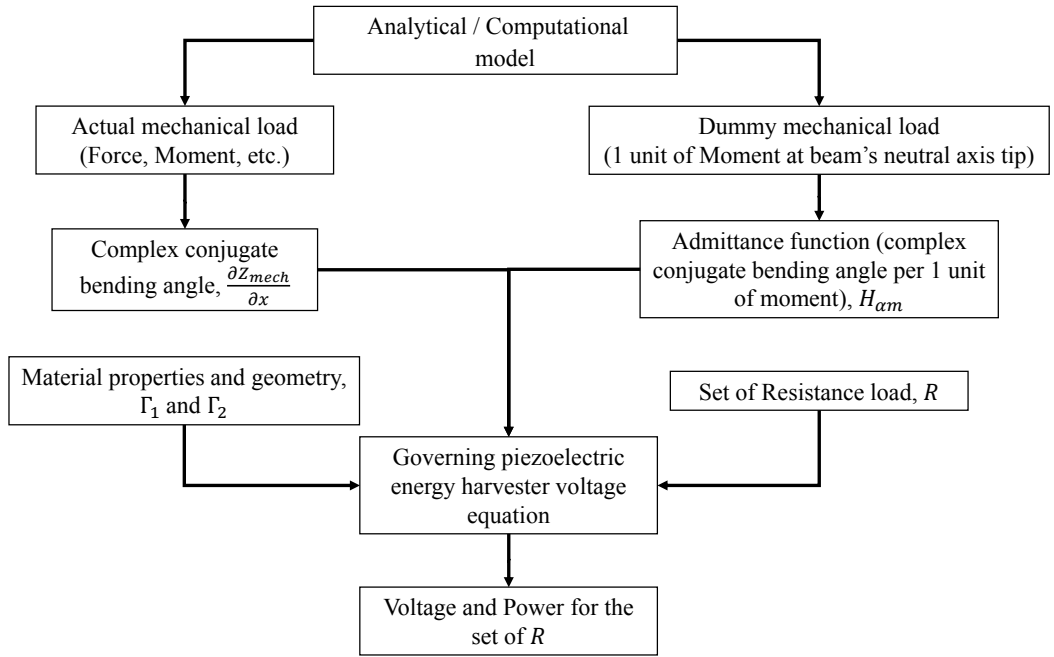


Figure 3.8: Schematic diagram of the energy harvesting system evaluation process

1. the displacement slope (bending angle) function due to the (actual) mechanical loading, $\frac{\partial Z_{mech}}{\partial x}$, and
2. the admittance function of bending angle due to a unit of moment, $H_{\alpha m}$.

The admittance function, $H_{\alpha m}$, can be obtained by applying a dummy load represented by one unit (i.e. 1 Nm) of moment at the neutral axis of the beam's tip.

In the current work, a computational method, i.e. finite element method (FEM), is applied to obtain both of these inputs. Dynamic analysis via FEM is concerned to evaluate a complex geometry. Hence, the scheme provided here is called a hybrid analytical/computational scheme. Hereafter, for simplification, this scheme will also be called the hybrid scheme. However, the hybrid is not limited to the inputs from

the computational method, analytical solution and experimental data may also be considered to obtain the structural responses.

Other inputs in the present code are the material properties and the geometrical information of the structure. To be noted that Equation (3.31) is derived based on a uniform cross-section beam. Hence, an approximation, i.e. polynomial function, may be required to define the geometrical distribution along the cantilever span ($hu(x)$, $hl(x)$, $b(x)$) for a not uniform beam, i.e., tapered beam. Lastly, the voltage and power amplitudes are calculated for a set of external resistance loads, R .

An example of computational code to evaluate the governing electromechanical equation is shown in Appendix C. This code is used to perform the analysis presented in Section 3.4. It can be seen in Appendix C, there are segments to input the material properties and beam configuration. There are also segments to evaluate the dynamic responses based on the analytical function and to input the experimental data for comparison purpose. The other essential segments are the inputs from commercial software in terms of tip displacement angles for the actual and dummy loads. Lastly, there are segments to calculate of voltage and power outputs based on Equation (3.31) and Equation (3.32).

3.3 Validation against analytical solution

In this section, validation for the proposed hybrid method with an analytical model is presented. The Erturk-Inman's analytical model [21] for the bimorph cantilevered energy harvester under base excitation is used as the benchmark. The material properties and the bimorph configuration are shown in Table 3.1.

Table 3.1: Bimorph 1 - Material properties and configuration

Properties	Piezoceramics	Substructure
Length, L (mm)	30	30
Width, b (mm)	5	5
Thickness, h (mm)	0.15(each)	0.05
Material	PZT-5A	Aluminium
Density, ρ (kg/m ³)	7750	2700
Elastic modulus, $1/S_{33}$ (GPa)	61	70
Piezoelectric constant, d_{31} (pm/V)	-171	-
Permittivity, ϵ_{11} (nF/m)	15.045	-

Erturk and Inman utilised the analytical approaches to evaluate both the structural dynamic response and the harvested energy [21]. Meanwhile, the hybrid model

can use both the structural dynamic responses based on the analytical solution and FEM simulation to estimate the harvested energy. An industrial finite element software [79] is used in the present work. Bi-linear quadrilateral elements and the direct frequency response module are applied. The meshes of 2 x 12 equal sized elements are implemented. A MATLAB[©] code is written to obtain the analytical solution of the structural dynamic response.

Table 3.2: Bimorph 1 - Natural frequency comparison

Mode Shape	Natural frequency (Hz)		
	Erturk - Inman [21]	Analytical - Present	FEM - Present
1 ST Bending	185.1	185.1	187
2 ND Bending	1159.8	1160.1	1162.3
3 RD Bending	3247.6	3248.3	3238.5

Table 3.3: Bimorph 1 - Relative tip displacement & tip angle comparison

Parameter	Erturk - Inman [21]	Analytical - Present	FEM - Present
Tip displacement (μm)	78.0	78.3	78.3
Tip angle (rad)	3.59e-3	3.60e-3	3.60e-3

Table 3.2 shows comparison of the natural frequencies for both the analytical solution and FEM results of the present work are in a good agreement with Erturk-Inman's results [21]. Meanwhile, Table 3.3 shows the comparison of the relative tip displacements and angles due to 1 μm base excitation amplitude at the resonance frequency of the first bending. The tip displacements and angles of all three procedures are also well agreed.

For comparison purpose, a separate code via MATLAB[©] is built to reconstruct Erturk and Inman's electromechanical model for a bimorph cantilevered piezoelectric energy harvester under base excitation [21]. Using the configuration from Table 3.1, the harvested energy with series connection is evaluated.

Figure 3.9 and Figure 3.10 show the voltage and amplitudes of the 3 different procedures at the first resonance's excitation frequency. Denoted by "Present Model (Analytical)" is the result of the present hybrid model combined with the analytical structural dynamic solutions. Meanwhile, the result via coupling with the FEM model is denoted by "Present Model (FEM)".

The figures are in logarithmic to logarithmic scale, where both the voltage and power are normalized per unit of g (9.81 m/s^2) and g^2 , following the way it is presented in [21]. Value of "V per g " is obtained from the voltage amplitude divided by the base

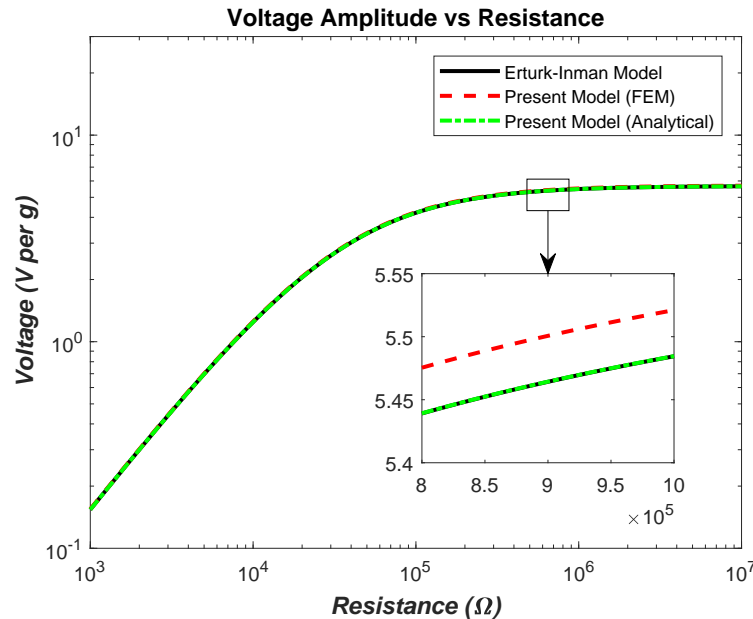


Figure 3.9: Bimorph 1 - Variation of the voltage amplitude with the resistance load

acceleration ratio to g , i.e. base amplitude $1 \mu\text{m}$ and 150 Hz excitation equal with 0.89 m/s^2 base acceleration or 0.09 acceleration ratio. Meanwhile, the electrical power is normalized per unit g^2 , or power divided by the square of the acceleration ratio.

Figure 3.9 and Figure 3.10 depict that the voltage and power amplitude for the 3 procedures are almost coincide. In the enlarged view, in a smaller range of resistance loads, it can be seen that the hybrid model results via FEM combination slightly overestimates the Erturk-Inman model's as shown in figures 3.9 and 3.10. Meanwhile, the hybrid model results via analytical structural response still coincide with the Erturk-Inman model's.

All the three procedures show the same trend of voltage and power functions. Initially, the voltage increases with the resistance load before it is going in asymptotic behaviour as displayed in Figure 3.9. Mathematically, it can be explained via Equation (3.30), as the resistance load is very large, close to the open circuit ($R \rightarrow \infty$), the effect of the resistance load will vanish. Hence, the voltage function will be reduced as only a function of material properties, configuration and displacements.

The power function, as a result of the voltage function's asymptotic behaviour, will initially increases with the resistance load until it reaches a maximum point. This maximum point, is the point before the voltage goes asymptotic. Thus, beyond this point, increasing the resistance load will only decrease the harvested power as the voltage is almost constant. As it can be seen from Equation (3.32), if the voltage is constant while the resistance load is getting closer to the open circuit ($R \rightarrow \infty$), the harvested power will be diminished ($P_{max} \rightarrow 0$).

Detailed comparison for the maximum voltage and power amplitude are given in

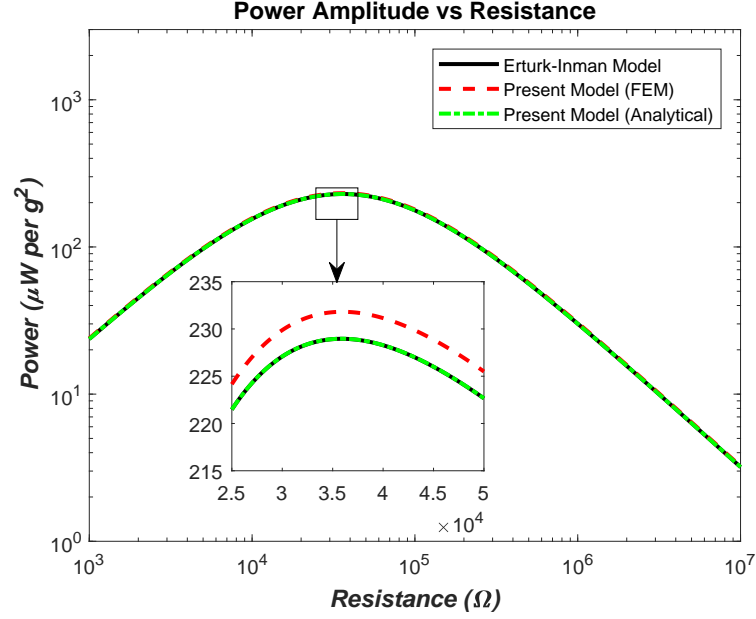


Figure 3.10: Bimorph 1 - Variation of the power amplitude with the resistance load

Table 3.4. It can be seen that the variances are insignificant (less than 2%).

Table 3.4: Bimorph 1 - Electrical parameters comparison

Electrical parameters	Erturk-Inman [80]	Present Model (Analytical)		Present Model (FEM)	
Max Voltage (mV)	782.10	782.10	$\Delta=0.0\%$	782.80	$\Delta=0.09\%$
Max Power (μ W)	4.35	4.35	$\Delta=0.0\%$	4.40	$\Delta=1.15\%$
R at Max Power (k Ω)	35.90	35.90	$\Delta=0.0\%$	35.96	$\Delta=0.17\%$

3.4 Validation against experimental result

This section presents the comparison of the results obtained via the present hybrid method and the experiment done by Erturk - Inman [22]. Table 3.5 depicts the material properties and the configuration of the investigated bimorph.

A case of 1 μ m base excitation amplitude is evaluated. The first resonance frequency is applied as the excitation frequency. The analytical and FEM model predicted 502.6 Hz as the fundamental first bending natural frequency. It is well agreed with the value of 502.5 Hz obtained from the experiment done by Erturk and Inman [22].

Figure 3.11 and Figure 3.12 show the variations of voltage and power amplitudes against the resistance loads for 4 different procedures. Both figures display the results from the Erturk-Inman analytical model, the present hybrid methods via analytical and FEM coupling, and lastly the experiment. The figures are also in logarithmic to

Table 3.5: Bimorph 2 - Material properties and configuration

Properties	Piezoceramics	Substructure
Length, L (mm)	24.53	24.53
Width, b (mm)	6.4	6.4
Thickness, h (mm)	0.265(each)	0.140
Material	PZT-5H	Brass
Density, ρ (kg/m ³)	7500	9000
Elastic modulus, $1/S_{33}$ (GPa)	60.6	105
Piezoelectric constant, d_{31} (pm/V)	-274	-
Permittivity, ϵ_{11} (nF/m)	30.09	-

logarithmic scale, where both the voltage and power are normalized per unit of g (9.81 m/s²) and g^2 .

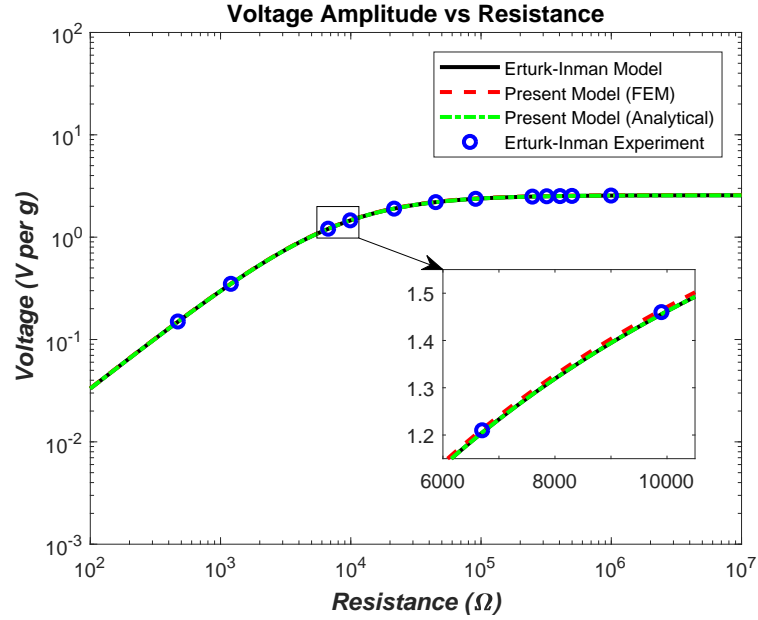


Figure 3.11: Bimorph 2 - Variation of the voltage amplitude with the resistance load

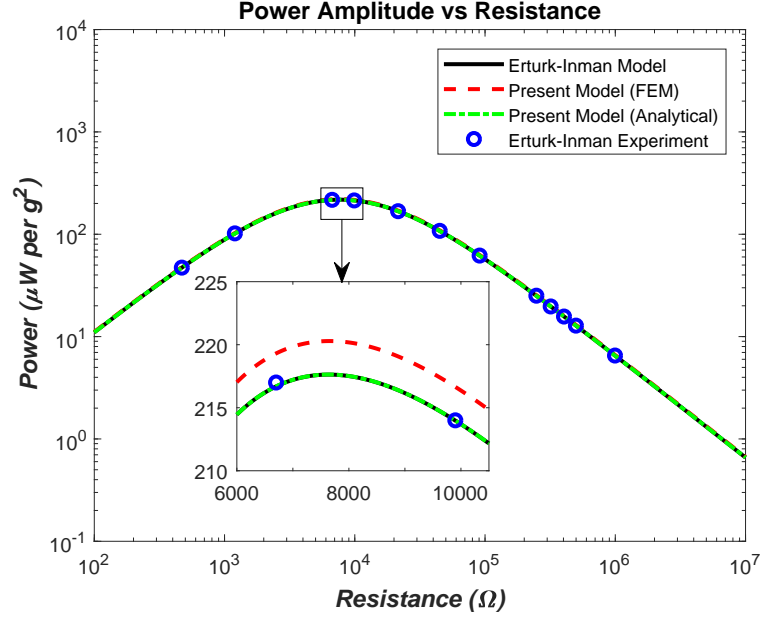


Figure 3.12: Bimorph 2 - Variation of the power amplitude with the resistance load

It can be seen that all 4 procedures are in a good agreement. In the enlarged view, it is shown that the results from the present hybrid method via FEM coupling just slightly overestimate the analytical and experimental results. Similar behaviours as presented in Section 3.3 are also captured in Figures 3.11 and 3.12. The voltage functions for all procedures go asymptotic towards the open circuit condition ($R \rightarrow \infty$). Meanwhile, the power functions achieved a maximum value before declining as the resistance going towards the open circuit.

All the models predicted the value of resistance load at the maximum power amplitude is 7.6 k Ω . The Erturk-Inman model estimates the maximum power of 224.89 μW . Meanwhile, the present hybrid model via FEM coupling predicts as much as 227.64 μW , overestimates Erturk-Inman model's by only 1.22 %. In addition, both procedures are also well agreed in the estimation of the maximum voltage, 2.62 V by Erturk-Inman's and 2.61 V via the present model (FEM), respectively. However, the resistance value of 7.6 k Ω was not used in the experiment. The nearest value used was 6.7 k Ω [22]. Therefore, the output parameters obtained by the models and the experiment for 6.7 k Ω are compared as displayed in Table 3.6.

Table 3.6: Bimorph 2 - Electrical parameters comparison at $R = 6.7 \text{ k}\Omega$

Electrical parameters	Erturk-Inman Model [22]	Erturk-Inman Experiment [22]		Present Model (FEM)	
Voltage (V)	1.225	1.230	$\Delta=0.41\%$	1.232	$\Delta=0.57\%$
Power (μW)	223.92	225.77	$\Delta=0.83\%$	226.63	$\Delta=1.21\%$

It can be seen in Table 3.6, the variances of the voltage and power amplitudes between the models' and the experiment's are insignificant. The maximum variance is only 1.21 %, coming from the power comparison between the present model via FEM coupling and the Erturk-Inman model.

3.5 Validation against electro-mechanically coupled FEM

In this subsection, the comparison of the present hybrid method and the electro-mechanically coupled FEM investigation of De Marqui Jr. et al. [10] is discussed. Energy harvested from a UAV wing spar is evaluated. The spar is a bimorph plate with the material properties and geometry as shown in Table 3.7. The piezoelectric layer is connected as series configuration, and the load source is the base excitation motion.

Table 3.7: Material properties and geometry of the bimorph UAV wingspar

Dimension of The Beam	
Total Length, L (mm)	300
Total Width, b (mm)	30
Total Thickness, h (mm)	12
Piezoceramics	
ρ (kg/m ³)	7800
c_{11}^E (GPa)	120.3
c_{12}^E (GPa)	75.2
c_{13}^E (GPa)	75.1
c_{33}^E (GPa)	110.9
c_{66}^E (GPa)	22.7
e_{31} (C/m ²)	-5.2
e_{33} (C/m ²)	15.9
ε_{11} (nF/m)	15.93
Host-structure (Aluminum)	
ρ (kg/m ³)	2750
E (GPa)	70

In Table 3.7, the piezoelectric properties are shown in 3D orthotropic of the stress-charge form [74]. The $c_{11}^E, c_{12}^E, \dots, c_{66}^E$ are the components of elastic stiffness of the mechanical constitutive relations. The e_{31}, e_{32}, e_{33} are the components of piezoelectric charge constant.

De Marqui Jr. et al. [10] adopted Kirchhoff plate theory to develop the electromechanically coupled finite element model of the piezoelectric energy harvester. The piezoceramic layer is assumed poled in the thickness direction; thus, align with the assumption used in Section 3.1. The piezoceramic layer is also assumed covered by a continuous electrode and perfectly bonded to the host-structure. It is assumed very thin and conductive electrode layers are on the top and bottom surfaces of the piezoceramic layers. Hence, it is assumed that all finite elements generate the same voltage output. Furthermore, one degree of freedom is used as the voltage output degree of freedom of each element. The reader is referred to [10] for the detail of their formulation.

Rayleigh mechanical damping is used in the finite element formulation. The damping is assumed proportional to the mass and stiffness matrices with the constant of proportionality α and β . Thus the critical damping ratio ζ is written as

$$\zeta = \frac{\alpha}{2\omega_n} + \frac{\omega_n\beta}{2} \quad (3.33)$$

where ω_n is the natural frequency of the structure. In the case presented in this subsection, $\alpha = 21.28$ rad/s and $\beta = 10^{-5}$ s/rad are used.

The configuration of the spar is limited to 10% additional mass of the full aluminum spar mass. Therefore, a restriction of length and thickness of the piezoelectric layer, $L^* \times h^* \leq 0.02723$, is applied. L^* is the ratio of piezoelectric length to the total length of the beam and h^* is the thickness ratio of one piezoelectric layer to the total thickness of the beam. The relationship of $L^* \times h^*$ boundary is shown in Figure 3.13.

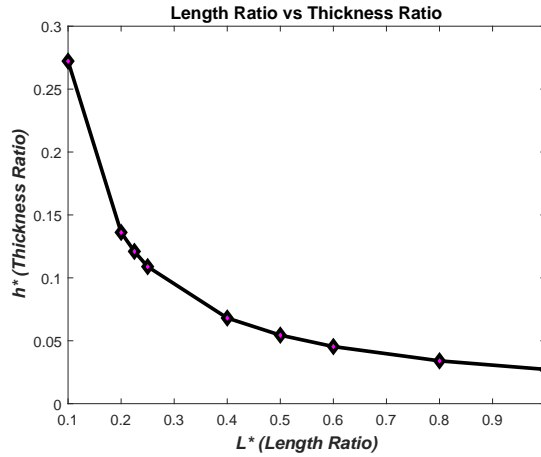


Figure 3.13: Variation of the thickness ratio, h^* , with the length ratio, L^* , of the spar

As the length and thickness of the piezoelectric layers and the aluminum layer are varied and not uniform along the span, thus, the analytical solution of [21] is not applicable. Thus, in this subsection, the comparison is only applied to the hybrid model with FEM combination. Figure 3.14 shows the variation of the 1st Bending natural frequency and the critical damping ratio for various length ratio, L^* .

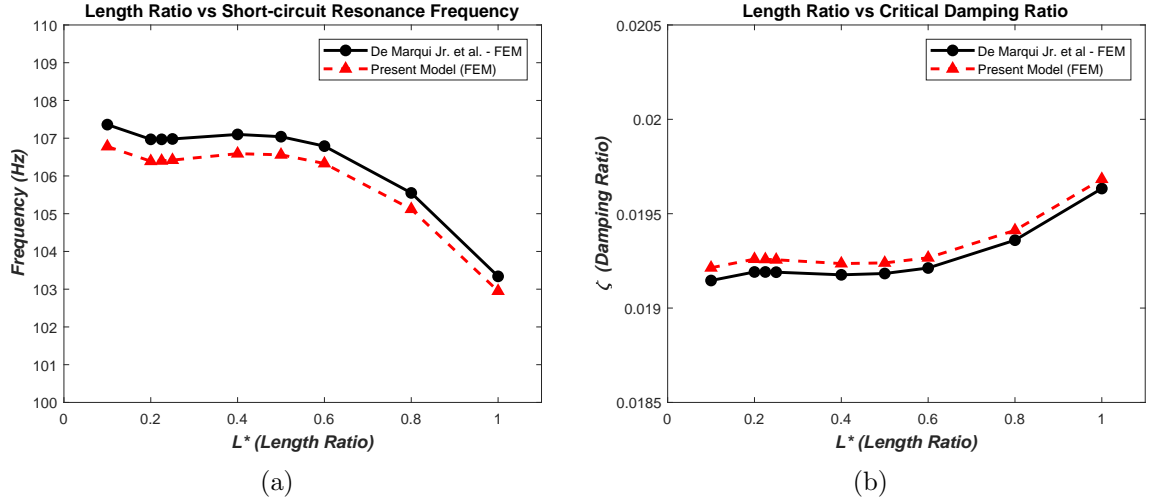


Figure 3.14: Variation of the (a) natural frequency, (b) critical damping ratio with the length ratio of the spar

It is seen from Figure 3.14 the trends of the natural frequency and damping ratio for all three procedures are all in good comparison. The total mass of the beam is fixed at $1.1 \times$ full aluminum mass, and the cross section shape is maintained. Therefore, the only variation that is affecting the change of the natural frequency is the composite material properties along the span.

In general, the natural frequency is decreasing from $L^* = 0.1$ to 1. However, from $L^* = 0.25$ to 0.4 a slight increment occurs, despite it is followed by a significant drop from $L^* = 0.8$ to 1. This trend is caused by a reduced stiffness of the piezo-aluminum composite beam as the piezoceramics layers approaches $L^* = 1$. In addition, for a benchmark, analytically the natural frequency of a full aluminum spar is 108.79 Hz.

The maximum power and the optimum resistance load for various length ratio are depicted in Figure 3.15a and Figure 3.15b. All of the three procedures are also in good agreement. The maximum power increased at first and reached its highest point at $L^* = 0.225$ before it significantly drops when L^* approach 1. In contrast, the optimum resistance load is decreased with the increment of L^* .

De Marqui Jr. et al. [10] concluded that for very thin piezoceramics, at $L^* > 0.5$, the effect of increased dynamic flexibility (decreased natural frequency, Figure 3.14a) is not able to overcome the increased structural damping as shown in Figure 3.14b. Therefore, although the flexibility is increased, the amplitude of the vibration is reduced. It resulted in the decrease of the power harvested as shown in Figure 3.15a. This behavior is aligned with Equation (3.30) in which the energy output is influenced by the displacement variation along the structural element.

Figure 3.16 depicts the variation of the power amplitude with the resistance load for different length ratio. The black cross "x" denoted $L^* = 1$ and the blue plus "+"

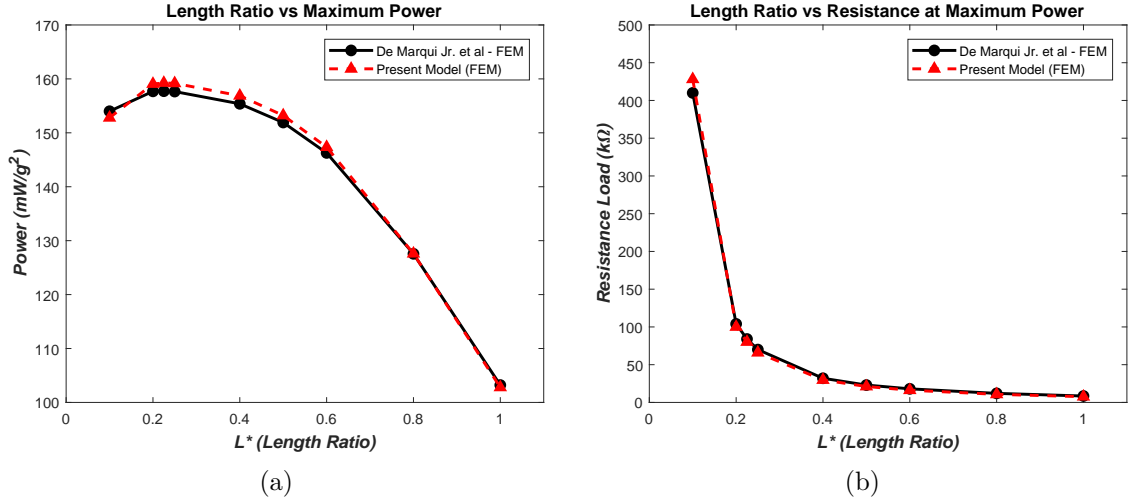


Figure 3.15: Variation of the (a) maximum power amplitude and (b) optimum resistance load with the length ratio of the spar

denoted $L^* = 0.1$. It can be seen that the Power-Resistance curve is shifting from left to right as the L^* decreases. In alignment with Equation (3.18), thinner and longer piezoelectric layer means Γ_1 parameter is increased. Thus, the voltage function reached the asymptotic behavior at smaller resistance load.

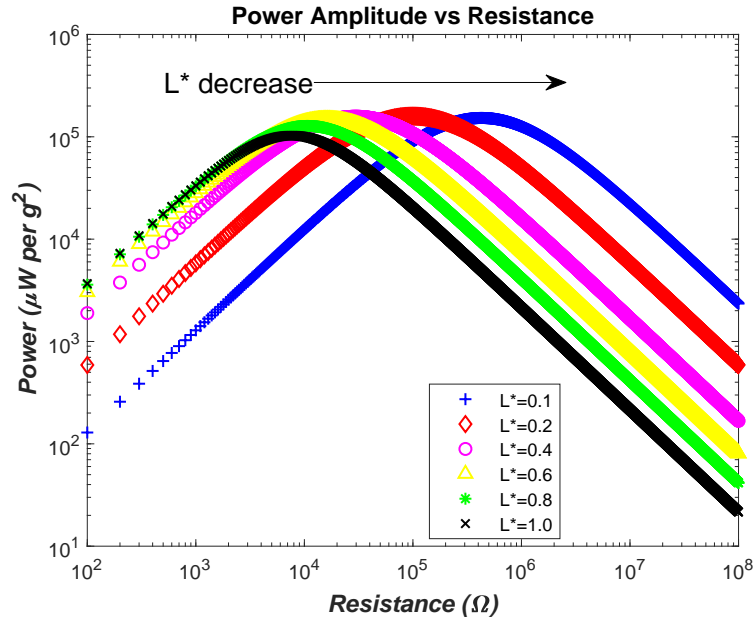


Figure 3.16: Variation of the power amplitude with the resistance load for various length ratio of the spar

In detail, the comparison of the natural frequency and maximum power obtained from the present hybrid model and the results of [10] is presented in Table 3.8. The 1st bending natural frequency is denoted by "F" and the maximum power is denoted by "P". The subscripts "DMJ" and "Present" represent the results of [10] and the ones

obtained via the present hybrid scheme. The Δ shows the variance of both procedures.

Table 3.8: Natural frequency and maximum power comparison of De Marqui Jr. et al - FEM and Present Model (FEM)

L^*	h^*	F_{DMJ} (Hz)	$F_{present}$ (Hz)	ΔF	P_{DMJ} (mW/g ²)	$P_{present}$ (mW/g ²)	ΔP
0.1	0.272	107.36	106.78	0.54%	154.00	152.79	0.79%
0.2	0.136	106.97	106.39	0.54%	157.69	159.06	0.87%
0.225	0.121	106.97	106.40	0.53%	157.72	159.24	0.97%
0.25	0.109	106.98	106.42	0.52%	157.65	159.18	0.97%
0.4	0.068	107.10	106.59	0.48%	155.38	156.88	0.96%
0.5	0.054	107.04	106.56	0.45%	151.90	153.22	0.86%
0.6	0.045	106.79	106.33	0.43%	146.27	147.33	0.74%
0.8	0.034	105.55	105.12	0.41%	127.56	127.59	0.02%
1.0	0.027	103.34	102.95	0.38%	103.22	102.79	0.41%

Table 3.8 shows that the natural frequencies and maximum power amplitude are all in good agreement with variances less than 1%. These results demonstrate the robustness of the present hybrid scheme, the capability to estimate energy harvested from a structure with non-uniform material properties and obtained a good level of accuracy similar to the electromechanically coupled finite element model.

A general illustration of the simulation time comparison between the hybrid scheme and fully coupled FEM is shown in Table 3.9. The simulation time of the UAV spar case with the full-length piezoelectric layer is observed. The fully coupled FEM follows [10] formulation, in which one additional voltage degree of freedom is added to each element. The configuration of 2 x 12 elements are used. For both procedures, computational codes are built and run via MATLAB[®]. The simulations are performed by a standard office laptop with Intel Core i7 2.4 GHz and 4 GB RAM.

In Table 3.9, "Hybrid - Present" denotes the present hybrid scheme, while the full electromechanically coupled FEM of [10] is denoted with "FEM - DMJ". As explained in Section 3.2 and Figure 3.8, the present hybrid scheme only requires three primary processes consisted of two numerical simulations for actual and dummy load, and one process to calculate voltage-power harvested. Step A denotes the non-coupled/purely mechanical loads numerical simulations performed via FEM configuration. Calculation of voltage (\bar{U}) and power (P_{max}) for N-number of resistance loads, R , is denoted by step B. Process of calculation in step B is also performed via a MATLAB[®] computational code.

For "FEM - DMJ" simulation, the only step used is step C, the full electromechanically coupled finite element simulation. In step C, the resistance load and the

Table 3.9: Simulation time comparison

Steps	Simulation Time (s)			
	100 no. of R		10000 no. of R	
	Hybrid-Present	FEM-DMJ	Hybrid-Present	FEM-DMJ
A. Non-coupled simulations	2 x 15	-	2 x 15	-
B. \bar{U} and P_{max} calculations	5	-	15	-
C. Fully coupled simulations	-	100 x 20	-	10000 x 20
TOTAL	35	2000	45	20000

mechanical load are both given as the excitation source on the finite elements, while both the structural deformation and voltage responses are obtained directly as the output of FEM simulation. It is assumed that for a set of N-numbers of R, N-times of simulations is required.

As shown in Table 3.9, step A shows fixed simulation time, 2 x 15 seconds. The elapsed time for the actual load (base excitation) and the dummy load (the moment at the tip) are around 15 seconds each and independent to the number of R. In step B, shows an increment of computing time as the number of resistance loads is increasing. For a set of 100 variances of R, the elapsed time is less than 5 seconds. While for 10000 numbers of R, around 15 seconds computing time is required. Therefore, in total, "Hybrid - Present" simulations require 35 seconds for 100 variances of R, and 45 seconds for 10000 numbers of R.

In contrast, the simulation time required for "FEM - DMJ", step C, is purely dependent on the number of R observed. For a simulation with one resistance load, it only requires less than 20 seconds. However, the simulation times are multiplied with N-number of R investigated. Therefore, if 100 number of R used, then 2000 seconds is required. Furthermore, if 10000 number of R used, then 200000 seconds or around 56 hours is required. Interesting to note that to produce a plot with the level of detail such as shown in Figure 3.16, a set of R from 10^2 to $10^8 \Omega$ with 100Ω step is used. Thus, to produce this plot utilizing the present hybrid scheme only need less than 1 minute, while with full electromechanically coupled FEM will require around 56 hours.

The independence on the number of simulations on the hybrid scheme is beneficial especially in a preliminary/conceptual design stage, in which a faster iterative design process to obtain an optimal harvester structural design and resistance load is achievable. However, despite the higher computational cost, a full electromechanically coupled FEM may provide more details for a particular area of interests, i.e., the region

near optimum resistance load. Thus, the hybrid scheme may build the fundamental sense of the best harvester design at the early design stage, while more detailed analysis may be provided by fully coupled FEM at the later design phase. Furthermore, an illustration is given in Chapter 4 to show the computational time of a larger structure, i.e, aircraft wingbox, via the present hybrid scheme.

3.6 Investigation by higher-order elements

In this section, the robustness of the present hybrid scheme with higher-order elements is elaborated to investigate very thin structural configurations. Isogeometric Analysis (IGA) is implemented to perform the structural analysis. IGA was first proposed by Hughes et al. [81]. They utilised Non-Uniform Rational B-Spline (NURBS) function to construct a so-called basis function of IGA elements, analogous to the shape function of finite element. The main attribute of NURBS-based IGA is the ability to establish numerical engineering analysis within the same model from the computational engineering design/drawing. Hence, decreasing the cost of numerical analysis-design interface and improving the accuracy compared to the standard finite element [81].

In the present work, another advantage of IGA is focused. In this section, the advantage of IGA against shear locking phenomena on a thin shells and its effect on the energy harvesting response is focused. Piezoelectric structures often manufactured as thin-walled structures; hence a problem of shear locking may occur on the numerical analysis. A study by Thai et al. [82] concluded that higher-order IGA elements hardly suffer from shear locking phenomena. The shear locking phenomena have been investigated since the early development of finite elements. It happens when the shear energy becomes very dominant compared to the bending energy as the thickness of the element is very small compared to its length [83]. A brief summary on the state-of-the-art of IGA for solid mechanics is given in Appendix A. To be noted here, the literature review on IGA is not given in this chapter nor Chapter 2 as the main focus of the work here is the piezoelectric energy harvesting while IGA is one of supporting the tools to provide the structural analysis similar to FEM.

In the present study, two different methods, i.e., analytical and numerical, are implemented to perform the structural dynamic analysis. Nine-noded bi-quadratic (Q9) and 25-noded bi-quartic (Q25) IGA shell elements are utilised. Full integration points, 3×3 for bi-quadratic and 5×5 for bi-quartic, are used. The same number of elements as mentioned in Section 3.3, 2×12 equal sized elements, is used. Computational codes are developed in MATLAB[®] to perform IGA structural dynamic analysis. The detail of the IGA elements construction can be found in Appendix B. To be noted as well, the IGA elements development is not discussed in this chapter to allow more focus on

the piezoelectric energy harvesting aspect.

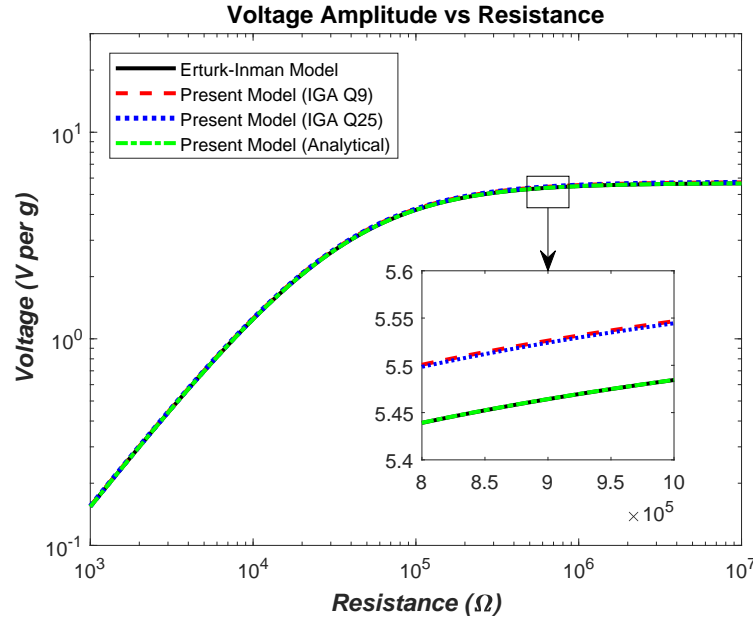


Figure 3.17: Investigation by IGA: Voltage amplitude vs resistance

The Bimorph 1 configuration from Table 3.1 is investigated. The energy harvesting analysis from base excitation case is evaluated. Figure 3.17 and Figure 3.18 show the generated voltage and maximum power amplitude for a set of resistance load obtained via Erturk-Inman's model and the present hybrid scheme. These figures are similar to those shown in Section 3.3 with the exception of IGA-based analyses replacing the FEM-based analysis.

It can be seen from Figure 3.17 and Figure 3.18, there is no significant difference between the results obtained by IGA Q9 and Q25. In order to investigate the effect of various thickness, the beam with the configuration on Table 3.1 is modified. The thickness of the beam is varied with h is the investigated thickness and h_0 is the original thickness on Table 3.1. Thus, a ratio of thickness, h_0/h is defined as the non-dimensional parameter.

The thickness ratio of the beam is varied from $h_0/h = 1$ to $h_0/h = 10^4$. The number of elements is kept the same. As the thickness ratio, h_0/h increases, the investigated thickness becomes smaller. At $h_0/h = 10^4$, the length per thickness ratio of the element is more than 7000 and considered as a very thin element. For comparison, eight-noded standard finite elements (FEM Q8) are also used for the analysis.

The numerical investigation results show that IGA Q9, Q25, and FEM Q8 elements are all maintained at a good level accuracy at small thickness ratio. In contrast, at the larger thickness ratio, shear locking effect started influenced the FEM Q8 elements. The variation of the tip displacement and tip angle with the thickness ratio are displayed in Figure 3.19.

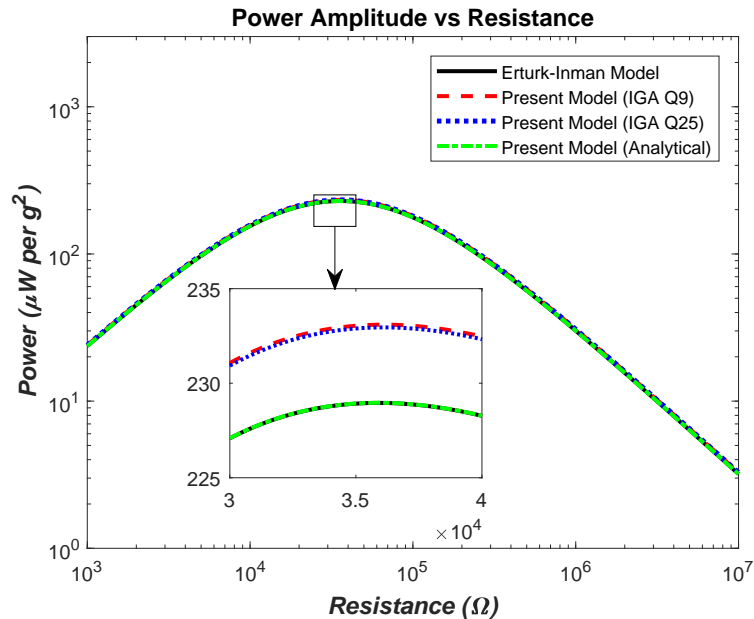


Figure 3.18: Investigation by IGA: Power amplitude vs resistance

In Figure 3.19, the black line, red diamond, blue circle and green square are denoted the analytical results, FEM Q8, IGA Q9 and IGA Q25 results. The results of FEM Q8 started deviating from the analytical results at $h_0/h = 10^{3.5}$ or $h_0/h = 3200$ and dropped significantly at thickness ratio 10^4 . While the IGA 9 and IGA 25 results just slightly deviated at thickness ratio 10^4 .

The results shown in Figure 3.19 are aligned with the trend shown by Thai et al. in [82]. For finite element results, the structural displacement is distorted further from the analytical results as the shear energy dominated within the element. At a particular thickness when the element becomes extremely thin, the plate/shell element behaves more like a plane stress element. Hence, the element is unable to be loaded by out-of-plane loading, i.e. bending load, and resulted in an unreliable response.

In Figure 3.20, the effect of shear locking as the element becomes thinner to the reverse piezoelectric parameter is shown. The magnitude of the reverse piezoelectric parameter, $|i\omega\Gamma_2^2 H_{am}|$, is referred to the part of Equation(3.30). In general, similar trend with Figure 3.19 is obtained. For finite element result, the magnitude of the reverse piezoelectric parameter, is dropped significantly towards $h_0/h = 10^4$. Figure 3.21 and Figure 3.22 show the voltage-resistance and power-resistance curves shifted from the reference value at very thin plate.

For the finite element results, at the very thin plates, the voltage response is underestimated at the range of resistance load close to short circuit ($R \rightarrow 0$). The geometrical configuration and material properties, Γ_1 & Γ_2 , unaffected by the numerical results. However, for the finite element results at very thin plates, the reverse piezoelectric effect is decreased, thus, at the range near short circuit, the reverse piezo-

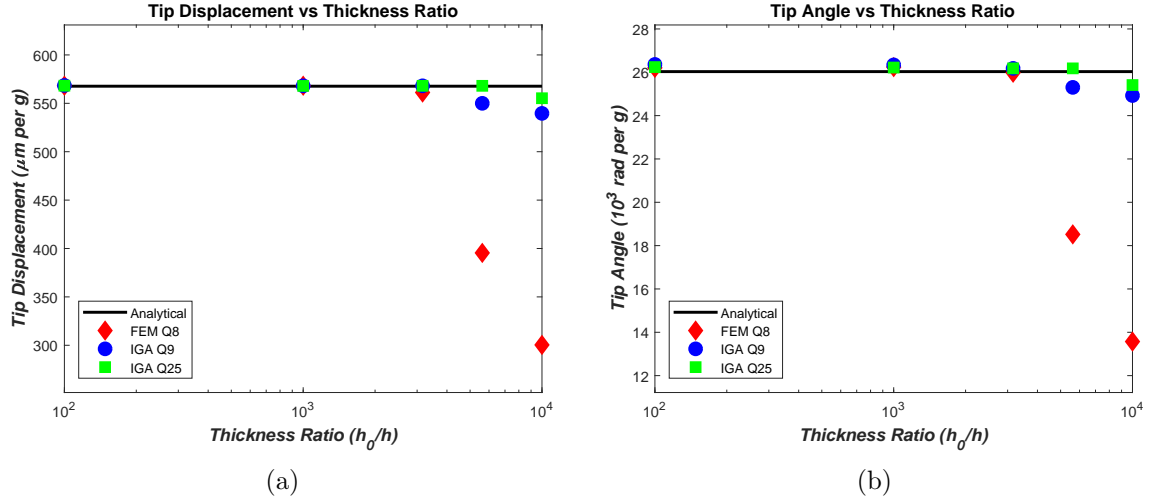


Figure 3.19: Variation of the (a) tip displacement and (b) tip angle with the thickness ratio, h_0/h

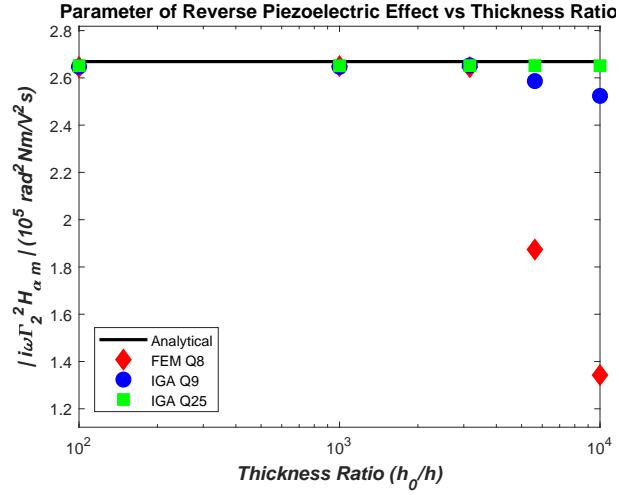


Figure 3.20: Variation of the reverse piezoelectric parameter with the thickness ratio, h_0/h

electric parameter unable to overcome the $1/R$ parameter. Moreover, with also smaller mechanical deformation, hence the voltage response is underestimated.

On the other side, as the resistance value is close to the open circuit ($R \rightarrow \infty$), the $1/R$ parameter is decreased. Furthermore, as for FEM result, the reverse piezoelectric also dropped at the very thin plate, it led to the overestimated voltage response.

Figure 3.21a and Figure 3.22a show the voltage response is shifted further from the analytical value as the thickness ratio changed from $10^{3.75}$ to 10^4 . The "FEM" refers to the results of FEM Q8 and "IGA" depicts the result of IGA Q25. The maximum voltage is greater overestimated at thickness ratio 10^4 . As the voltage responses are shifted, the power response are also shifted as shown in Figure 3.21b and Figure 3.22b. Despite the fact that the power-resistance curves of the finite element results similar

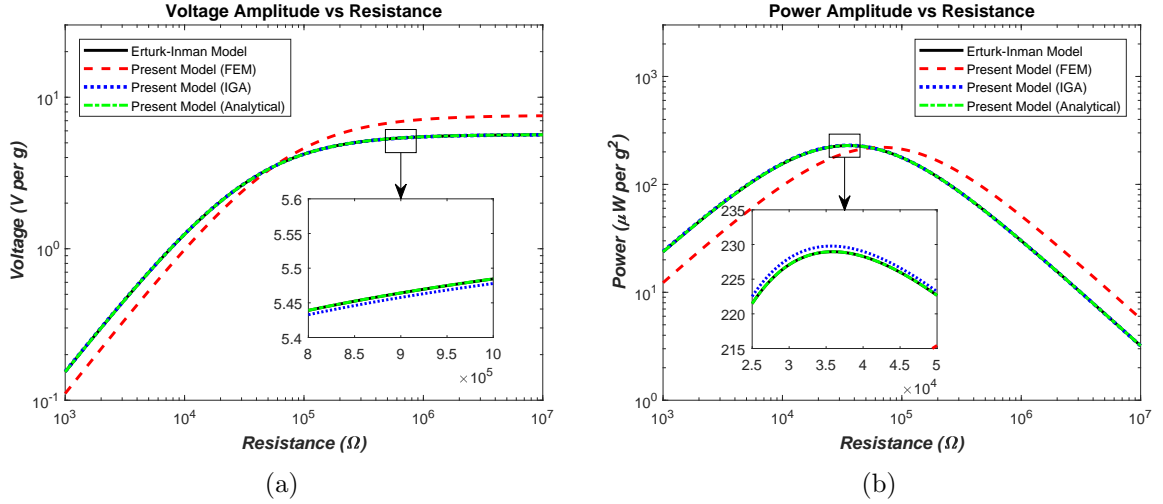


Figure 3.21: Bimorph 1 with $h_0/h = 10^{3.75}$ - Variation of the (a) voltage amplitude and (b) power amplitude with the resistance load

to the trend of the analytical, the resistance values are overestimated.

Table 3.10: Electrical Parameters Comparison with $h_0/h = 10^4$

Electrical Parameters Comparison				
Parameter	Erturk - Inman	Present (Analyt.)	Present (FEM)	Present (IGA)
Max Voltage (nV)	7.8	7.8	14.5	7.64
		$\Delta=0.0\%$	$\Delta=85.9\%$	$\Delta=2.0\%$
Max Power (pW)	4.35e-10	4.35e-10	4.55e-10	4.17e-10
		$\Delta=0.0\%$	$\Delta=4.6\%$	$\Delta=4.1\%$
R at Max	35.9	35.9	125.07	36.09
Power (kΩ)		$\Delta=0.0\%$	$\Delta=248\%$	$\Delta=0.5\%$

In detail, Table 3.10 presents the comparison of maximum voltage and maximum power amplitude with the resistance at maximum power for all procedures at $h_0/h = 10^4$. It can be seen that all of the methods are in good agreement except the one combined with FEM. Although the maximum power obtained with FEM combination is less than 5% variance (Δ), however the resistance value at the maximum power is overestimated by 2.5 times the analytical result.

3.7 Summary

A mathematical model and computational scheme to evaluate a cantilevered piezoelectric energy harvester under dynamic bending have been developed. The energy

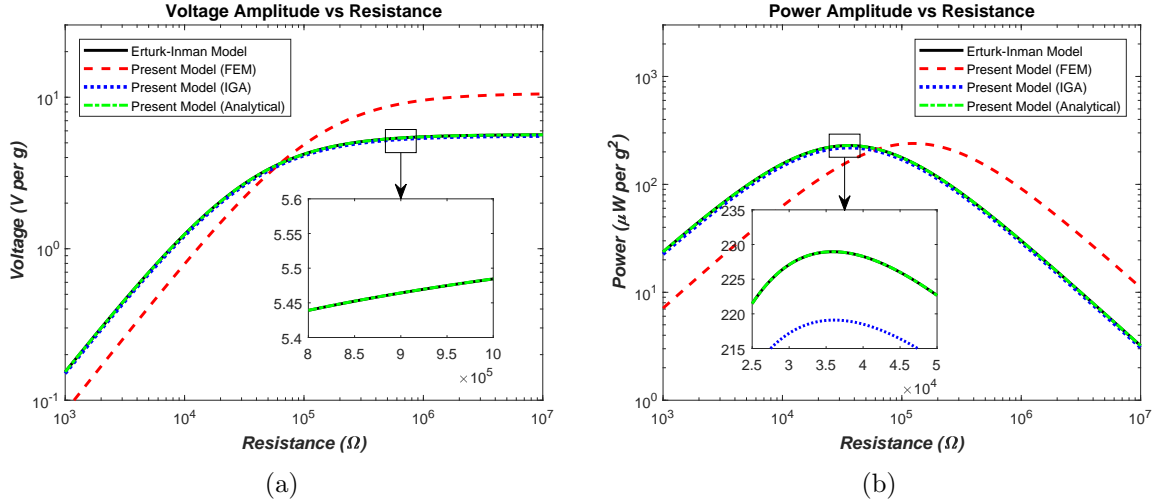


Figure 3.22: Bimorph 1 with $h_0/h = 10^4$ - Variation of the (a) voltage amplitude and (b) power amplitude with the resistance load

harvesting investigations by means of the hybrid analytical/ computational scheme have been discussed in this chapter. The capabilities and robustness of the scheme are shown by comparison with results from the literature.

The results obtained via the present hybrid scheme are well agreed with those obtained from analytical, numerical and experimental methods. It is shown in some details that the present hybrid scheme provided a faster computational time compared to an electro-mechanically coupled finite element method. Moreover, the hybrid scheme provided ease to utilise commercial software with minimum addition of computational coding for energy harvesting evaluation. By means of the hybrid scheme, the reverse piezoelectric effect was obtained from the dummy load structural simulation via a commercial software. Thus, full electromechanical coupling on the finite elements were not required. Hence, it can be used as an alternative tool during an early design stage to evaluate the harvester potential.

In relation to the aim of the present research to evaluate the energy harvesting potential of a large aircraft wing, the hybrid scheme is further implemented to investigate a jet aircraft wingbox in Chapter 4. The investigation presented in Chapter 4 will serve to give some insights on the power harvested and concerns on the addition of piezoelectric material concerning the aircraft structure.

Chapter 4

Implementation of The Hybrid Scheme on A Jet Aircraft Wingbox

In this chapter, the implementation of the novel hybrid scheme on a notional jet aircraft wingbox is presented. A typical long-ranged civil jet transport aircraft type is chosen. It is expected that with this type of wing structure, the order of power is much larger compared to those obtained from small lifting structure in the literature. A jet aircraft wingbox with 14.5 m half span is used for the energy harvesting evaluation. A piezoelectric material replaces the original upper skin's material of the wingbox. A dynamic cruise load is applied. The results pointed out that the electrical power generated can be as much as 39.13 kW.

Some works and results presented in this chapter are parts of the author's published works in Composite Structures, Volume 153, 2016.

4.1 Wingbox FEM analysis

A test case for a notional civil jet aircraft wingbox is simulated in the present work. The structural dynamic response is performed via FEM. A common practical case in the operational flight is considered. The dynamic excitation forces is equal with the cruise load. The excitation frequencies observed are around the 1st bending mode natural frequency.

An aircraft wingbox model [84] is taken as the reference for the present simulation. However due to some details of the wingbox are not given, the geometry is simplified based on the available data.

Figure 4.1 shows the wingbox vertical stiffness distribution. Due to the detail of the ribs cross section is not available from [84], it is assumed that the ribs are plates with rectangular cross section. Figure 4.2 shows the wingbox layout from topside view. The available data from [84] are the span length of the spar (570 in or 14.48 m), the

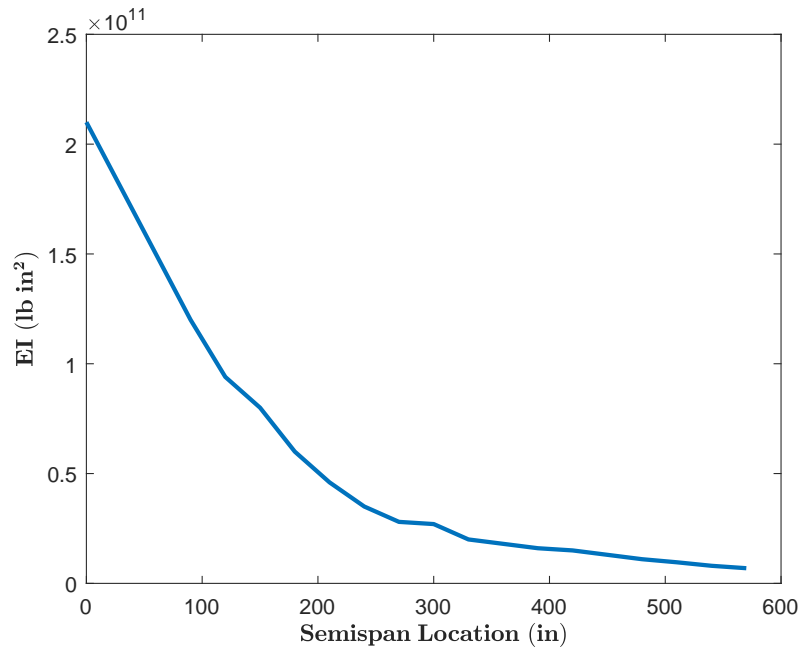


Figure 4.1: Wingbox vertical stiffness distribution

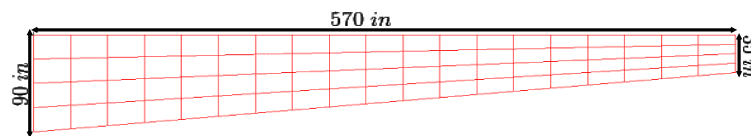


Figure 4.2: Wingbox topside view layout

distance between the front spar and the rear spar at the wing root (90 in or 2.29 m) and at the wing tip (35 in or 0.88 m). For simplification, the front spar length is assumed perpendicular to the ribs at the root and tip. The rear spar is assumed to be straight connecting the trailing edge of the root and tip ribs. The ribs spacing are assumed uniform. Hence, there are 20 ribs with 30 inches spacing in the simplified model.

Other simplifications made for the present simulation are

1. The skins, ribs and spars are assumed as rectangular plates with uniform thickness. The thickness for the skins is 0.24 inches and for the ribs and the spars is 0.29 inches. These are maximum thickness values of the original model [84].
2. The stringers and spar caps are not modelled for the present simulation.

3. The skins, ribs and spars are made of uniform plates with isotropic material, Al-2219. Later on, for energy harvesting purpose, the upper skin material is replaced by a piezoceramic material, PZT-5A.

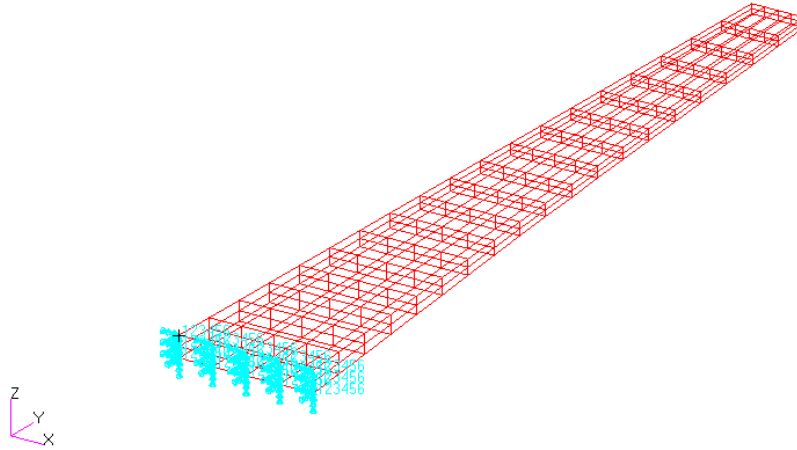


Figure 4.3: Wingbox model for finite element analysis

Figure 4.3 shows the wingbox model used for the finite element analysis. The skins, ribs and spars are modelled as quadrilateral shell elements with the thickness as mentioned earlier. The translations and rotations (for 3 directions) are fixed at the root and free at the tip. The different material configurations used for the simulation are

1. For the first wingbox model, its skins, ribs and spars are all modelled by Al-2219 with modulus of elasticity 73.1 GPa (10.6^6 lb-in²), poisson's ratio 0.33 and density 2840 kg/m³(0.1 lb/in³). This model is called model A, hereafter.
2. For the second model, its upper skin replaced with piezoceramic material, PZT-5A with modulus of elasticity 60.9 GPa (8.8×10^6 lb-in²), poisson's ratio 0.33 and density 7750 kg/m³(0.27 lb/in³). PZT-5A is chosen due to its high electromechanical coupling. This model is called model B, hereafter.

The data given in [84] shows that the original model is weighted 2742.5 lbs and the maximum tip displacement is around 30 inches during the ultimate load (2.5 g up gust and 50,000 lbs thrust load). The weight of the aircraft itself is 170,000 lbs and the 2.5 g up gust is equal with 425,000 lbs. The comparison of the original model [84] and model A is shown in Table 4.1.

Modal analyses are conducted to verify the structure of model B. The natural frequencies comparison between model A and B is shown in Table 4.2. The modification

Table 4.1: Weight and tip displacement, Z_{tip} , original model vs model A

	Weight (lbs)	Z_{tip} - ultimate (in)	Z_{tip} - cruise (in)
Original model	2472.5	30	-
Model A	2415	33.8	13.5

in model B resulted in a lower natural frequency than model A for the same mode shape. This characteristic mainly influenced by the weight increment from 2415 lbs (model A) to 3929 lbs (model B). Meanwhile the stiffness just slightly decreases from model A to model B as the PZT-5A only applied to the upper skin. The square root of the mass ratio between model B and A is found to be 1.27. This ratio is reasonably close to the frequency ratio (f_A/f_B) for the first 3 bending modes shapes shown in Table 4.2. It is important to note, a weight increment may result in a much more fuel to burn in an aircraft flight; hence, it will become a major challenge on the implementation of piezoelectric material in an aircraft. The significance of the weight increment is further discussed in Chapter 6.

Table 4.2: Natural frequency comparison, model A vs model B

Mode Shape	Natural frequency (Hz)		
	Model A	Model B	f_A/f_B
1st Bending	2.16	1.61	1.34
2nd Bending	9.01	6.74	1.34
3rd Bending	21.70	16.19	1.34

Moreover, for the energy harvesting purpose, Model B is analyzed by applying the frequency-dependent forced excitation via a FEM module [79]. The force amplitude is equal to the steady cruise lift, half of the aircraft weight (85,000 lbs). However, the detail of the airfoil is not available in [84], and the lift distribution is unknown. Therefore, the lift is simplified as a concentrated load acting on the wingbox.

An evaluation of the lift coefficient (Cl) distribution via Lifting Line Theory [85] is conducted to obtain the concentrated load point. A typical cambered NACA 6-series is assumed as the airfoil of the wing. To be noted, several configuration parameters of the wing are assumed, adopted the wing illustration given in [84]. Hence, as most of the inputs are based on assumptions, this Cl distribution may not be applied as a real load and herein only serve as a sketch to estimate the concentrated load point. The Cl distribution is depicted in Figure 4.4, the concentrated load point is estimated at around 6 m from the root. The excitation frequencies varied from 0.80, 1.31 to 1.45 Hz. These range of frequencies is close to the natural frequency of the 1st mode shape.

It is important to note that the assumption of harmonically oscillating cruise load

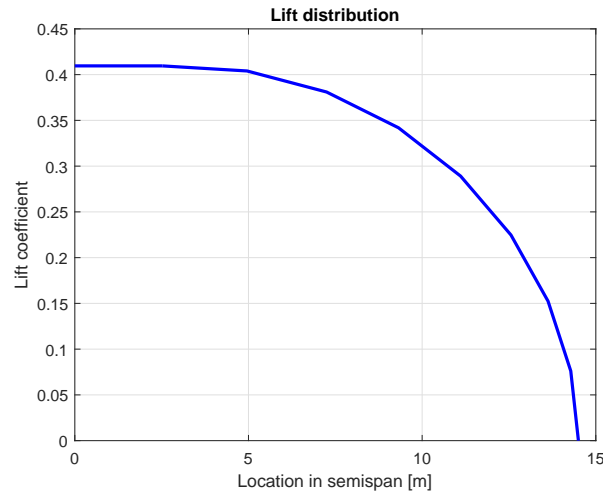


Figure 4.4: Sketch of the lift coefficient distribution on the wing

may provide unrealistic loading condition in comparison to a typical cruise flight. One of the main consequences that may need to be noted is the structural responses may be overestimated. This is due to the vibration amplitude directly applies the load equal to the aircraft weight and the excitation frequencies near the first bending mode. Moreover, a continuous vibration, i.e., harmonic oscillation, may not occur on a normal flight as the aeroelastic damping is sufficient to reduce the oscillation and stabilise the response exerted by external disturbance, i.e., gust wing. Thus, the following evaluation in Section 4.2 may only be interpreted as an extreme and rare case, serves as the upper benchmark on the energy harvesting estimation.

4.2 Wingbox energy harvesting simulation

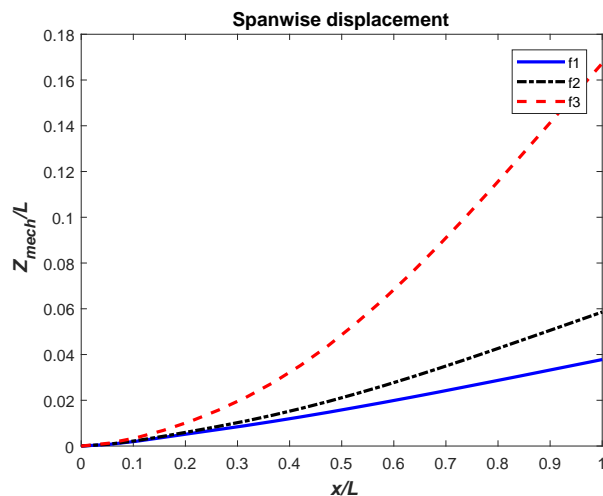


Figure 4.5: Wingbox dynamic response amplitude along the span

Figure 4.5 shows the plot of model B displacement functions obtained via the FEM

simulation. The plot shows the non-dimensionalised amplitude, Z_{mech}/L , with respect to the neutral axis. The excitation frequencies below the first bending mode is observed. The excitation frequencies applied, f_1 , f_2 and f_3 , are 0.80, 1.31 and 1.45 Hz. These values are 0.5, 0.7 and 0.9 times of the first bending frequency. It is shown in Figure 4.5 that all the displacement responses are mainly influenced by the first bending mode shape. The displacements are all shown increasing from the root to the tip. The excitation on 1.45 Hz provided the largest displacement as it is the closest to the resonance frequency. Appendix G displays the first bending mode shape and the displacements of the wing for different excitation frequencies.

The voltage amplitude responses are shown in Figure 4.6. It can be seen that the voltage amplitudes resemble the behaviour of the structural dynamic responses. At 1.45 Hz, the voltage amplitude is the largest amongst the other two frequencies. The voltage responses in Figure 4.6 also exhibit the similar behaviour with the results displayed in Chapter 3, Figure 3.9. The voltage responses at first are increasing with the resistance load until at a certain point it undergo an asymptotic behaviour. Hence, from this point, further increment of the resistance load is no more affecting the voltage responses.

Meanwhile, the power amplitude responses are shown in Figure 4.7. The responses are aligned with those of the voltage responses. The power amplitude at 1.45 Hz is the largest amongst the other two frequencies. The power responses in Figure 4.7 also exhibit similar behaviour with those previously shown for the base excitation model in Chapter 3, Figure 3.10. The power responses at first is increasing proportionally with the resistance load, but after reaching a certain point it is declining while the resistance increased. The resistance load that gives the maximum power response is the first resistance load before the voltage response goes asymptotic.

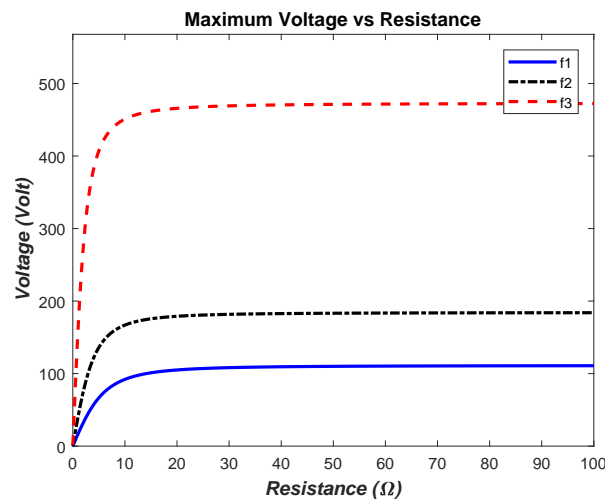


Figure 4.6: Wingbox voltage amplitude vs resistance

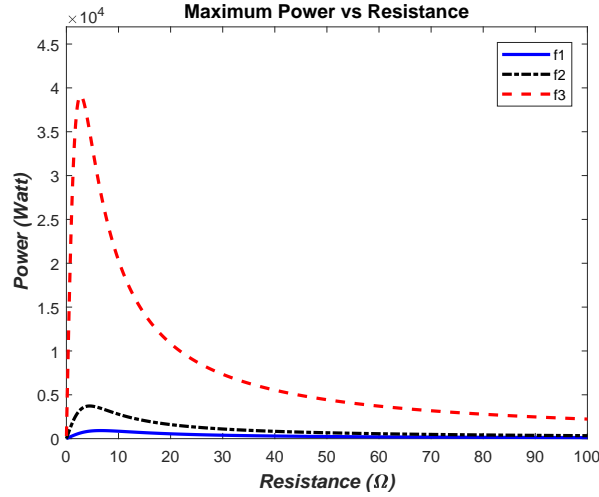


Figure 4.7: Wingbox power amplitude vs resistance

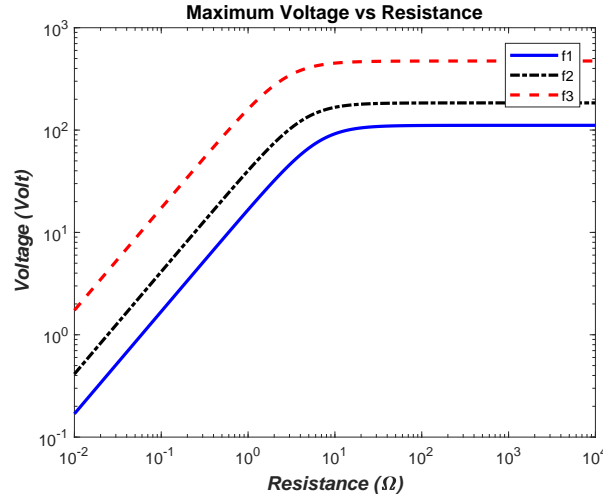


Figure 4.8: Wingbox voltage amplitude vs resistance, loglog scale

In a wider range of resistance loads, the voltage and power responses are plotted by logarithmic to logarithmic scale in Figure 4.8 and Figure 4.9 (the responses are not normalized to g such previously done for the base excitation model). In Figure 4.6 and Figure 4.7, the range of resistance loads used are between 0-10 Ω . The resistance loads at maximum power amplitude are around 6.59 Ω at 0.80 Hz, 4.46 Ω at 1.31 Hz and 2.73 Ω at 1.45 Hz. Figure 4.8 shows the voltage responses become asymptotic even until the order of $10^4 \Omega$.

Figure 4.9 shows the optimum power is achieved in a small range of resistance loads, around $10^{-1} \Omega$ to $10^1 \Omega$. Within this range, electrical power in order of 10^2 watts to 10^3 watts is achievable. However, the power is dropped significantly outside of this area. Therefore, the selection of the resistance loads is critical to design an optimum harvester configuration.

For the purpose to evaluate the speed of computation, a comparison between the

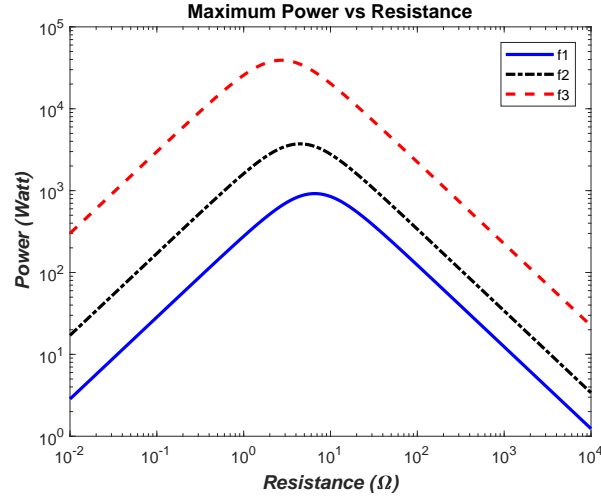


Figure 4.9: Wingbox power amplitude vs resistance, loglog scale

hybrid scheme and fully coupled FEM is shown in in Table 4.3. However, it is important to note that the fully coupled FEM developed in [10] is based on the 3-DoF quadrilateral planar shell element (1 vertical translation and 2 rotations degree-of-freedoms). Hence, it could not be used to construct the wingbox model as shown in Figure 4.3 as it requires 6-DoF shell element (3 translations and 3 rotations degree-of-freedoms). Therefore, for comparison purpose, the computational time of the fully coupled FEM is based on a rough estimation concerning the ratio to the non-coupled FEM.

In Table 3.9, it is shown that the simulation times for a standard non-coupled FEM and a fully coupled FEM are 15 seconds and 20 seconds, respectively. Hence, there is 33% additional time required to perform a fully coupled FEM simulation. In the present case, for the wingbox model, a non-coupled FEM simulation requires around 2 minutes. The simulations is performed by a standard office laptop with Intel Core i7 2.4 GHz and 4 GB RAM. Therefore, assuming 33% additional time, a fully coupled FEM simulation needs around 2 minutes and 40 seconds.

Table 4.3 displays the same computational steps shown in Table 3.9. Step A denotes the non-coupled FEM simulations for the actual and dummy loads performed via commercial software. Calculation of voltage (\bar{U}) and power (P_{max}) for N-number of resistance loads, R , is denoted by step B. The process in step B is also performed via a MATLAB[®] computational code. The only step used in the fully coupled FEM is step C. It is assumed that for a set of N-numbers of R , N-times of simulations is required.

As can be seen in Table 4.3, the computation times of voltage and power outputs in step B are the same with the ones shown in Table 3.9. Step B performs analytical calculation based on Equation (3.30) and Equation (3.32); hence, independent to the number of elements. Therefore, the gaps of simulation times between the hybrid scheme and fully coupled FEM are much larger. Simulations times for 100 and 10000 variances

Table 4.3: Simulation time comparison for the wingbox model

		Simulation Time (s)			
		100 no. of R		10000 no. of R	
Steps		Hybrid Scheme	Fully Coupled	Hybrid Scheme	Fully Coupled
		- Present	FEM	- Present	FEM
A.	Non-coupled simulations	2 x 120	-	2 x 120	-
B.	\bar{U} and P_{max} calculations	5	-	15	-
C.	Fully coupled simulations	-	100 x 160	-	10000 x 160
TOTAL		245	16000	255	1600000

of R via the hybrid scheme are less than 3 minutes. In contrast, by means of fully coupled FEM, simulation times for 100 and 10000 variances of R are more than 4 hours and 440 hours, respectively. Thus, for a large structure, the present hybrid scheme may provide significant benefit in terms of computational time.

4.3 Summary

In this chapter, a simulation for a notional civil jet aircraft wingbox with piezoelectric skin layer has been presented. Based on the simulation results, the voltage and power responses could attain a promising level, in the order of 10^1 to 10^2 Volts and 10^2 to 10^4 Watts.

However, concerning an aircraft design process and flight operation, there are still some issues to be addressed as follows:

1. One of the major issues is the weight increment on the aircraft structure due to the existence of piezoelectric material. The commercially available piezoelectric materials are three times heavier than the common aluminium alloy used in the aircraft structure, i.e. Al-2219, Al-7075.

It has been shown in this chapter, by replacing the upper skin with a piezoelectric material, the wingbox weight increased more than 60%. In a flight operation, more weight means more lift force to produce; hence, more drag force generated and more fuel is burnt. Therefore, this issue should be addressed in the design process to gain the optimum weight-power exchange.

2. It has been shown in this chapter that a jet aircraft wingbox structure potentially

could produce a promising electrical power. However, this amount of power may be difficult to be sustained during a practical flight. Moreover, an assumption of a dynamic cruise lift force requires further verification.

In a normal flight operation, i.e., cruise, the aircraft wing might not sustain a level of vibration near the bending resonance frequency during the whole flight mission. Furthermore, the wing structural response might be influenced by several main modes, i.e., bending and torsion. In addition, it is known that the aerodynamic load and the structural deformation are interactively coupled during the flight. Thus, aeroelasticity analysis is needed to validate the energy harvesting potential for a more realistic loading scenario.

3. Another issue yet to be observed is the strength of the structure with the piezoelectric materials, as these materials known to have brittle nature. It is still unknown whether this material could sustain the deformation due to aerodynamic loading during the flight. Despite there were some researches concerning the strength of piezoelectric energy harvester, there is no investigation and means of evaluation for a flight application in the literature.

In the present research, several approaches are implemented to address those issues. Chapter 5 presents the evaluation of multiphase piezoelectric composite as an alternative to the bulk piezoelectric material. Chapter 6 discusses the application of multiphase piezoelectric composites on the aircraft wingbox concerning the trade-off between the weight, fuel and energy harvested. Chapter 7 presents a higher fidelity approach, so-called iterative finite element method, to evaluate the energy harvesting from the piezoelectric structure. This method is implemented to investigate lifting structures under aeroelastic condition. Furthermore, this iterative finite element method is applied for the aircraft wingbox analysis as presented in Chapter 8.

Chapter 5

Multiphase Piezoelectric Composites with Active Structural Fiber

In this chapter, the evaluation of the multiphase composite with active structural fiber (ASF) is discussed. The ASF is a multiphase fiber constructed of a core fiber which is a non-electro-active coated by a piezoelectric material. By combining a matrix material with the ASF, a so-called multiphase piezoelectric composite can be constructed. This type of multiphase composite is investigated as the alternative of bulk piezoelectric material for energy harvesting. From the literature, multiphase composites with ASF has proven able to provide better optimisation between actuating and load bearing capability compared to a pure piezoelectric material. However, application in energy harvesting purpose has not been found in the literature.

The estimation of the electro-elastic or electromechanical properties of the multiphase composite is discussed in this chapter. The Double-Inclusion model combined with the Mori-Tanaka method is implemented in a computational code to estimate the effective electro-elastic properties of the multiphase composite. The effective composite properties obtained via the present code are compared with the analytical, experimental and finite element results.

Some works and results presented in this chapter are parts of the author's published works in Composite Structures, Volume 202, 2018.

5.1 The Double-Inclusion model

In this section, the multiphase composite with electro-elastic constitutive matrix is concerned. The constitutive matrix of piezoelectric material is adopted to the multiphase composite. Two forms of the constitutive matrix, i.e., stress-charge, strain-charge,

are used. The stress-charge form is mainly used in The Double-Inclusion formulation. While the strain-charge form is applied in the energy harvester model. In contrast with the energy harvester model proposed in Chapter 3, the Double-Inclusion model evaluates the material in three dimensional form (3D). Based on the IEEE standard on piezoelectricity [74], the stress-charge form is expressed as

$$\mathbf{E}_{iJMn} = \begin{bmatrix} C_{11} & C_{12} & C_{13} & 0 & 0 & 0 & 0 & 0 & -e_{31} \\ C_{12} & C_{11} & C_{13} & 0 & 0 & 0 & 0 & 0 & -e_{31} \\ C_{13} & C_{13} & C_{33} & 0 & 0 & 0 & 0 & 0 & -e_{33} \\ 0 & 0 & 0 & C_{44} & 0 & 0 & 0 & -e_{15} & 0 \\ 0 & 0 & 0 & 0 & C_{44} & 0 & -e_{15} & 0 & 0 \\ 0 & 0 & 0 & 0 & 0 & C_{66} & 0 & 0 & 0 \\ 0 & 0 & 0 & 0 & e_{15} & 0 & \varepsilon_{11}^S & 0 & 0 \\ 0 & 0 & 0 & e_{15} & 0 & 0 & 0 & \varepsilon_{11}^S & 0 \\ e_{31} & e_{31} & e_{33} & 0 & 0 & 0 & 0 & 0 & \varepsilon_{33}^S \end{bmatrix} \quad (5.1)$$

and the strain-charge form is written as

$$\mathbf{F}_{AbiJ} = \begin{bmatrix} S_{11} & S_{12} & S_{13} & 0 & 0 & 0 & 0 & 0 & d_{31} \\ S_{12} & S_{11} & S_{13} & 0 & 0 & 0 & 0 & 0 & d_{31} \\ S_{13} & S_{13} & S_{33} & 0 & 0 & 0 & 0 & 0 & d_{33} \\ 0 & 0 & 0 & S_{44} & 0 & 0 & 0 & d_{15} & 0 \\ 0 & 0 & 0 & 0 & S_{44} & 0 & d_{15} & 0 & 0 \\ 0 & 0 & 0 & 0 & 0 & S_{66} & 0 & 0 & 0 \\ 0 & 0 & 0 & 0 & d_{15} & 0 & \varepsilon_{11}^T & 0 & 0 \\ 0 & 0 & 0 & d_{15} & 0 & 0 & 0 & \varepsilon_{11}^T & 0 \\ d_{31} & d_{31} & d_{33} & 0 & 0 & 0 & 0 & 0 & \varepsilon_{33}^T \end{bmatrix} \quad (5.2)$$

The contracted Voigt's notation (i.e., $11 \rightarrow 1$, $22 \rightarrow 2$, $33 \rightarrow 3$, $23 \rightarrow 4$, $13 \rightarrow 5$, $12 \rightarrow 6$, $41 \rightarrow 7$, $42 \rightarrow 8$, $43 \rightarrow 9$) is applied in Equations (5.1) and (5.1). The four subscripts define the row and column in a 9×9 matrix. Hence, for example E_{1111} denotes the first row - first column component of the \mathbf{E}_{iJMn} in a 9×9 matrix form, refer to the elasticity component C_{11} ; F_{2343} is the fourth row - ninth column component of the \mathbf{F}_{AbiJ} , refer to the piezoelectric coupling component d_{33} ; and so on. Important to note that in Equations (5.1) and (5.2), an orthotropic characteristic is assumed. Hence, the symmetries due to orthotropic, i.e., $C_{11} = C_{22}$, $d_{31} = d_{32}$, etc., are directly implemented. Equations (5.1) and (5.2) can be written in a compact form as

$$\mathbf{E}_{iJMn} = \begin{bmatrix} \mathbf{C} & -\mathbf{e}^t \\ (6 \times 6) & (6 \times 3) \\ \mathbf{e} & \boldsymbol{\varepsilon}^S \\ (3 \times 6) & (3 \times 3) \end{bmatrix} \quad (5.3)$$

$$\mathbf{F}_{\text{AbiJ}} = \begin{bmatrix} \mathbf{S} & \mathbf{d}^t \\ (6 \times 6) & (6 \times 3) \\ \mathbf{d} & \boldsymbol{\varepsilon}^T \\ (3 \times 6) & (3 \times 3) \end{bmatrix} \quad (5.4)$$

The stiffness/elasticity matrix and the compliance matrix are defined by \mathbf{C} and \mathbf{S} matrices. The \mathbf{e} and \mathbf{d} matrices define the piezoelectric coupling constants in stress-charge and strain-charge forms, respectively. In other formulations, the piezoelectric constant, \mathbf{d} , can also be called as the charge constant. The $\boldsymbol{\varepsilon}^S$ and $\boldsymbol{\varepsilon}^T$ represent the dielectric permittivity in stress-charge and strain-charge forms. The dielectric permittivity is often written in a non-dimensionalised form as the relative permittivity, its ratio with the vacuum permittivity, $\varepsilon_0 = 8.85 \times 10^{-12}$ F/m.

The relations between the stress-charge form and strain-charge form are defined as follows

$$\begin{aligned} \mathbf{C} &= \mathbf{S}^{-1} \\ \mathbf{e} &= \mathbf{d} \mathbf{S}^{-1} \\ \boldsymbol{\varepsilon}^S &= \boldsymbol{\varepsilon}^T - \mathbf{d} \mathbf{S}^{-1} \mathbf{d}^t \end{aligned} \quad (5.5)$$

Figure 5.1 illustrates an ASF made of a piezoelectric shell coated a carbon fiber which constructed a multiphase composite with the surrounding matrix. Herein, a long-cylindrical/ fibrous composite is focused. The long fibrous composite is a common type of composite used in the development of aircraft structure. The convention of the composite directions presented in [51] is adopted. The fiber direction is defined as direction 3. The ASF poling is taken in the transverse, 1 and 2, directions. This poling direction is aligned with the convention shown in Chapter 3, where direction 1 is the poling axis. However, to not be confused that often in a conventional composite model, the fiber direction is taken as direction 1 [86].

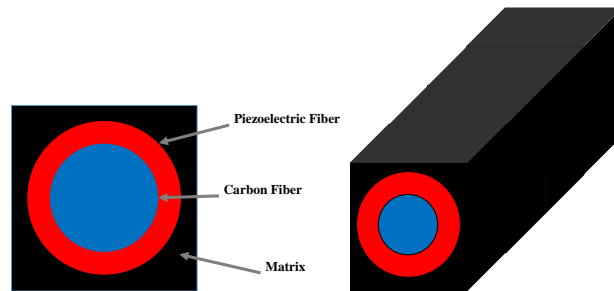


Figure 5.1: Multiphase composite with active structural fiber (ASF)

It is worth to mention that in the Double-Inclusion material, despite the fiber and matrix are not electro-active materials, they are still treated similar as the piezoelectric

material. Later in Section 5.3, it is shown that the fiber and matrix materials do not possess piezoelectric coupling constant. However, their permittivity are still considered. Despite these materials do not generate electrical charge, the electrical charges could still travel between the core fiber, the piezoelectric shell and the matrix. Hence, the overall multiphase composite is an electro-active structure.

In the Double-Inclusion model, the effective electro-elastic matrix of the overall composite, \mathbf{E}_{iJMn} , as a function of each phase properties is shown in Equation (5.6). The electro-elastic matrices of each phase; the core fiber, the piezoelectric shell, and the matrix are defined by \mathbf{E}_{iJMn}^c , \mathbf{E}_{iJMn}^p and \mathbf{E}_{iJMn}^m . In the following notations, the components of the matrix, the piezoelectric shell and the core fiber are denoted by the superscripts m , p and c , respectively.

$$\mathbf{E}_{iJMn} = (V^c \mathbf{E}_{iJMn}^c \mathbf{A}^c) + (V^p \mathbf{E}_{iJMn}^p \mathbf{A}^p) + (V^m \mathbf{E}_{iJMn}^m \mathbf{A}^m) \quad (5.6)$$

The volume fractions of each phase to the overall composite volume are defined by V^c , V^p and V^m . While the strain concentration tensors of each phase are denoted by \mathbf{A}^c , \mathbf{A}^p and \mathbf{A}^m , respectively.

The concentration tensors in the dilute limit is used by Lin and Sodano in [51] to obtain the effective electro-elastic properties of the multiphase composite. In the present work, instead of only using the dilute limit, the Mori-Tanaka's method is applied to evaluate the concentration tensors. It is expected with this approach, a better agreement with experimental and computational results can be achieved. The dilute and Mori-Tanaka's concentration tensors are estimated from the following formulations

$$\begin{aligned} \mathbf{A}_{dil}^c &= (\mathbf{I} + (\mathbf{S}_{MnAb}^p \mathbf{E}_{iJMn}^m)^{-1} \mathbf{E}_{iJMn}^{cm})^{-1} \\ \mathbf{A}_{dil}^p &= (\mathbf{I} + (\mathbf{S}_{MnAb}^c \mathbf{E}_{iJMn}^m)^{-1} \mathbf{E}_{iJMn}^{cp})^{-1} \\ \mathbf{A}_{MT}^m &= \mathbf{I} ((V^m \mathbf{I} + V^p \mathbf{A}_{dil}^p + V^c \mathbf{A}_{dil}^c)^{-1}) \\ \mathbf{A}_{MT}^p &= \mathbf{A}_{dil}^p ((V^m \mathbf{I} + V^p \mathbf{A}_{dil}^p + V^c \mathbf{A}_{dil}^c)^{-1}) \\ \mathbf{A}_{MT}^c &= \mathbf{A}_{dil}^c ((V^m \mathbf{I} + V^p \mathbf{A}_{dil}^p + V^c \mathbf{A}_{dil}^c)^{-1}) \end{aligned} \quad (5.7)$$

The concentration tensors in dilute limit, \mathbf{A}_{dil} , are calculated from Equation (5.7). These dilute concentration tensors are used to evaluate the Mori-Tanaka's concentration tensors, \mathbf{A}_{MT} , as given in Equation (5.8). In alignment with Equation (5.6), the concentration tensors $\mathbf{A} = \mathbf{A}_{MT}$. The identity matrix (9 x 9 size) is defined by \mathbf{I} . Meanwhile, the other components are obtained as $\mathbf{E}_{iJMn}^{cm} = \mathbf{E}_{iJMn}^c - \mathbf{E}_{iJMn}^m$ and $\mathbf{E}_{iJMn}^{cp} = \mathbf{E}_{iJMn}^p - \mathbf{E}_{iJMn}^c$.

The tensor defined by \mathbf{S}_{MnAb} is the piezoelectric analog of the Eshelby's tensor. The analytical form of this tensor is derived in detail by Dunn and Taya [55]. In the present work, the numerical form of \mathbf{S}_{MnAb} based on the work in [87] is applied.

Furthermore, for the case of circular cylindrical fibrous, if the fiber length is very large ($\rightarrow \infty$) compared to its radius, a simplified form of $\mathbf{S}_{\mathbf{MnAb}}$ [61, 88] can also be used.

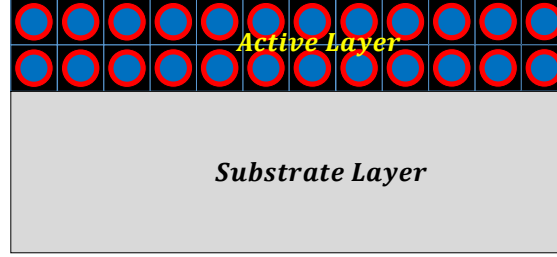


Figure 5.2: Cross-section of energy harvester beam with multiphase composite as an active layer

5.2 Evaluation procedure of the multiphase composite effective electro-elastic properties

The procedure to calculate the piezoelectric Eshelby's tensor, $\mathbf{S}_{\mathbf{MnAb}}$, is presented in this section. As previously explained in Section 5.1, if the $\mathbf{S}_{\mathbf{MnAb}}$ tensor is known, the concentration tensors can be calculated from Equations (5.7) and (5.8). Hence, the effective electro-elastic properties of the composite can be evaluated from Equation (5.6). Herein, the numerical form of $\mathbf{S}_{\mathbf{MnAb}}$ by applying Gauss integration procedure in [87] is adopted. The elastic part of $\mathbf{S}_{\mathbf{MnAb}}$ is expressed as

$$S_{MnAb} = \frac{E_{iJAb}}{8\pi} \sum_{p=1}^P \sum_{q=1}^Q (G_{MJin}^{pq} + G_{nJiM}^{pq}) W^p W^q \quad (5.9)$$

with $M = 1, 2, 3$;

and the electro-elastic part is given by

$$S_{MnAb} = \frac{E_{iJAb}^m}{4\pi} \sum_{p=1}^P \sum_{q=1}^Q (G_{MJin}^{pq}) W^p W^q \quad (5.10)$$

with $M = 4$

Where

$$\begin{aligned} G_{MJin}^{pq} &= z_i^{pq} z_n^{pq} (K_{MJ}^{pq})^{-1} \\ K_{MJ}^{pq} &= E_{iJMn}^m z_i^{pq} z_n^{pq} \end{aligned} \quad (5.11)$$

$i = 1, 2, 3; n = 1, 2, 3; J = 1, 2, 3, 4$

and

$$\begin{aligned} z_3^{pq} &= \xi_3^p/a_3 \\ z_1^{pq} &= \sqrt{1 - (\xi_1^p)^2} \cos \theta^q/a_1 \\ z_2^{pq} &= \sqrt{1 - (\xi_2^p)^2} \cos \theta^q/a_2 \end{aligned} \quad (5.12)$$

The contracted Voigt's notation (i.e., 11 \rightarrow 1, 22 \rightarrow 2, 33 \rightarrow 3, 23 \rightarrow 4, 13 \rightarrow 5, 12 \rightarrow 6, 41 \rightarrow 7, 42 \rightarrow 8, 43 \rightarrow 9) is also applied in Equations (5.9), (5.10) and (5.11).

The number of the integration points are defined by the capital letters, P and Q . Whereas the superscripts p and q are the numerical counters for the Gauss points, ξ_3^p and θ^q , and also for the weight coefficients, W^p and W^q . The ellipsoidal shape with the semiaxes, a_1 , a_2 and a_3 , is adopted as the inclusion shape [55]. In the longitudinal direction, the semiaxis length is defined by a_3 . Meanwhile, the semiaxis lengths in the transverse directions are a_1 and a_2 . Therefore, for example, if the inclusion is a sphere-shaped particle then all the semiaxis lengths are the same, $a_1 = a_2 = a_3$. In the other hand, if the inclusion is a long cylindrical fiber then the transverse semiaxis lengths are equal, $a_1 = a_2$, and the longitudinal length is assumed very long, $a_3 \gg a_1$.

The $\mathbf{S}_{\mathbf{MnAb}}$ tensor is calculated via the following procedure

1. The properties of the matrix material, $\mathbf{E}_{\mathbf{iJMn}}^{\mathbf{m}}$, and the shape aspect ratio a_2/a_1 and a_3/a_1 are used as the input. Then, the number of integration points P and Q are determined. Hence, the Gauss points, ξ_3^p and θ^q , and the weight coefficients, W^p and W^q can be obtained.
2. The z_3^{pq} , z_1^{pq} and z_2^{pq} components are evaluated for each combination of the Gauss points via Equation (5.12).
3. The K_{MJ}^{pq} matrix component is calculated for each combination of the Gauss points via Equation (5.11). Then, the inverse of K_{MJ}^{pq} is used to evaluate G_{MJin}^{pq} .
4. The S_{MnAb} matrix component is calculated via Equations (5.9) and (5.10).

A MATLAB[®] computational code is written to evaluate the $\mathbf{S}_{\mathbf{MnAb}}$ matrix and the effective electro-elastic properties, $\mathbf{E}_{\mathbf{iJMn}}$. The composite configuration is determined from the combination of the ASF volume fraction to the overall composite, V_f , and the aspect ratio of the piezoelectric shell thickness to the ASF radius, AR . In the case of long-infinite fiber, the shape aspect ratio of the fiber is assumed very large, $a_3/a_1 = 10^6$. In addition, in the present code, the linear summation of each phase density fraction is used to determine the average density, ρ , of the composite.

5.3 Case study and validation: Multiphase composite electro-elastic properties estimation

The present Double-Inclusion code is tested to estimate the effective properties of various composite configurations. Appendix D depicts an example of code to perform the evaluation discussed in Section 5.3.1. The main parts of the code are the inputs of material (piezoelectric, core fiber and matrix) properties and also the calculations of $\mathbf{S}_{\mathbf{MnAb}}$ matrix, concentration tensors (dilute and Mori-Tanaka's tensor), and the effective properties of the composite, $\mathbf{E}_{\mathbf{iJMn}}$.

The present results are validated against those obtained via analytical methods, experimental works and computational simulations in the literature. Moreover, the dynamic analyses of a lamina and a unimorph beam made of the multiphase composites are also conducted in the present work. The results of these works are discussed in this section.

The material properties used as piezoelectric shell, core fiber and matrix in the present analysis are depicted in Table 5.1, Table 5.2 and Table 5.3.

Table 5.1: Material Properties of Piezoelectric Materials

Property	PZT-7A [62]	PZT-5A [10]	BaTiO ₃ [89]
C_{11} (GPa)	148.0	120.3	150.4
C_{12} (GPa)	76.2	75.2	65.6
C_{13} (GPa)	74.2	75.1	65.9
C_{33} (GPa)	131	110.9	145.5
C_{44} (GPa)	25.4	21.0	43.9
C_{66} (GPa)	35.9	22.7	42.4
e_{31} (N/Vm)	-2.1	-5.2	-4.3
e_{33} (N/Vm)	9.5	15.9	17.3
e_{15} (N/Vm)	9.2	12.3	11.4
$\varepsilon_{11}^S/\varepsilon_0$	460	919.1	1115.1
$\varepsilon_{33}^S/\varepsilon_0$	235	826.6	1251.3
ρ (kg/m ³)	7600	7750	5700

5.3.1 Electro-elastic properties comparison against analytical model and experimental results

In the present case, the results of the Double-Inclusion code are compared against the analytical model and experimental works by Chan and Unsworth [60]. Chan and

Table 5.2: Material Properties of Core Fiber Materials

Property	Carbon Fiber [62]	SiC Fiber [62]	Glass Fiber [90]
C_{11} (GPa)	24.0	483.7	88.8
C_{12} (GPa)	9.7	99.1	29.6
C_{13} (GPa)	6.7	99.1	29.6
C_{33} (GPa)	243.7	483.7	88.8
C_{44} (GPa)	27.0	192.3	29.6
C_{66} (GPa)	11.0	192.3	29.6
e_{31} (N/Vm)	0	0	0
e_{33} (N/Vm)	0	0	0
e_{15} (N/Vm)	0	0	0
$\varepsilon_{11}^S/\varepsilon_0$	12.0	10.0	6.4
$\varepsilon_{33}^S/\varepsilon_0$	12.0	10.0	6.4
ρ (kg/m ³)	2000	4360	2550

Unsworth investigated single piezoelectric fiber composites in [60]. Hence, their model serves as an upper benchmark when the piezoelectric thickness becomes very dominant in the ASF.

In the work done by Chan and Unsworth [60], PZT-7A and Epoxy matrix are used to construct the single fiber composites. In the present work, carbon fiber is added as the core fiber of the ASF. The properties in Table 5.1, Table 5.2 and Table 5.3 are used. However, to be noted that Chan and Unsworth found the d_{33} of the tested PZT-7A was around 163-167 pm/V. Therefore, they used 167 pm/V in their analytical model [60]. Thus, in the present work, e_{33} is changed to 12.3 C/m², so that d_{33} is 167 pm/V and d_{31}, d_{32} are kept as -60 pm/V.

The stiffness, compliance and piezoelectric coupling components of the multiphase composite for various volume fraction, Vf, and aspect ratio, AR, are depicted in Figure 5.3. The results obtained from the present Double-Inclusion code are denoted by "Present Code - DI MT". Whereas "AR1", "AR2", "AR3" and "AR4" represent the results for 0.50, 0.60, 0.70 and 0.95 aspect ratios. Meanwhile, the solid black lines show the results of Chan-Unsworth's analytical model for single fiber composites.

It can be seen in Figure 5.3, the present code's results follow the similar trend with the Chan-Unsworth model. In addition, as expected, the pattern of the multiphase composite shifted closer to the results of single fiber model when the aspect ratio of the piezoelectric shell increases. It is clearly seen at AR 0.95, the results of multiphase composite and single fiber model are coincide. In this configuration, the ASF is made of 99.75% piezoelectric material. Therefore, the multiphase composite closely behaves

Table 5.3: Material Properties of Matrix Materials

Property	LaRC-SI [62]	Epoxy [90]
C_{11} (GPa)	8.1	8.0
C_{12} (GPa)	5.4	4.4
C_{13} (GPa)	5.4	4.4
C_{33} (GPa)	8.1	8.0
C_{44} (GPa)	1.4	1.4
C_{66} (GPa)	1.4	1.4
e_{31} (N/Vm)	0	0
e_{33} (N/Vm)	0	0
e_{15} (N/Vm)	0	0
$\varepsilon_{11}^S/\varepsilon_0$	2.8	4.2
$\varepsilon_{33}^S/\varepsilon_0$	2.8	4.2
ρ (kg/m ³)	1360	1150

like a single fiber composite.

Figure 5.3a depicts the stiffness component of the composite in the fiber direction. As the carbon fiber and PZT-7A stiffness components are larger than the epoxy matrix, the composite stiffness increases with the ASF volume fraction for the same aspect ratio. In contrast, as the carbon fiber stiffness is larger than PZT-7A, the composite stiffness decreases while the aspect ratio increases.

The piezoelectric constant of stress-charge form, e_{33} , is shown in Figure 5.3b. As the aspect ratio increases, the PZT-7A composition is larger. Hence, the piezoelectric constant of the composite increases. Whereas for the same aspect ratio, e_{33} increases with the volume fraction.

Figures 5.3c and 5.3d present the components in strain-charge form, i.e., compliance, S_{31} , and piezoelectric charge constant, d_{31} . Here, the negative (-) sign defines the cause and effect in opposite direction. For example, if d_{31} becomes more negative, hence, there is a larger deformation in negative direction (compression) exerted by a positive voltage.

It is interesting to note that for both S_{31} and d_{31} , the trend of the parameters for large volume fraction (above 50%) are almost no longer affected by the volume fraction. Hence, in relation to d_{31} , further increasing the volume fraction above 50% may not significantly increase the electrical response of the composite when a deformation is applied.

Figure 5.4 shows the variation of the other material properties, compliance, piezoelectric charge constants, dielectric permittivity and density of the composite. In addi-

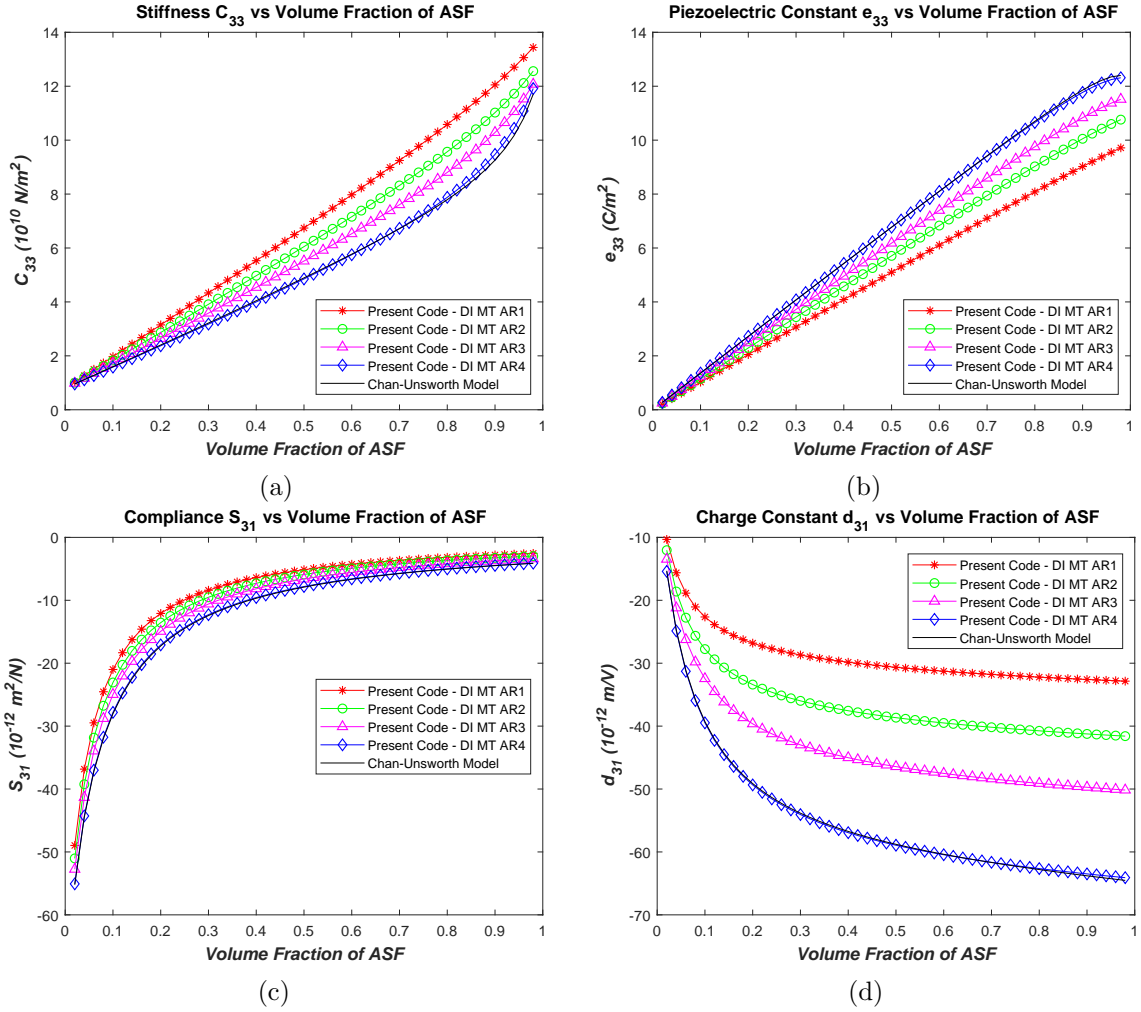


Figure 5.3: (a) Stiffness, C_{33} , (b) Piezoelectric Constant, e_{33} , (c) Compliance, S_{31} , and (d) Charge Constant, d_{31} , vs ASF Volume Fraction of PZT-7A - Carbon Fiber - Epoxy Composites

tion, Figure 5.4 depicts the experimental results of Chan-Unsworth [60]. Similarly with Figure 5.3, all the results obtained from the Double-Inclusion code follow the similar trend with Chan-Unsworth's results as displayed in Figure 5.4

It is clearly shown in Figures 5.4a and 5.4b that both the density, ρ , and the charge constant, d_{33} , of the composite at AR 0.95 are coincide with those estimated via Chan-Unsworth model. Furthermore, their values are in an excellent agreement with the experimental results. The density of the composite at the same aspect ratio increases linearly with the volume fraction due to the densities of the ASFs are larger than the matrix. Moreover, similarly to the trend of d_{31} depicted in Figure 5.3d, the charge constant, d_{33} , almost insensitive to the volume fraction increment at above 50% volume fraction.

The variation of the compliance components, $S_{11} + S_{12}$, is shown in 5.4c. Mathematically, by inverting the stiffness matrices, it is found the carbon fiber's compliance

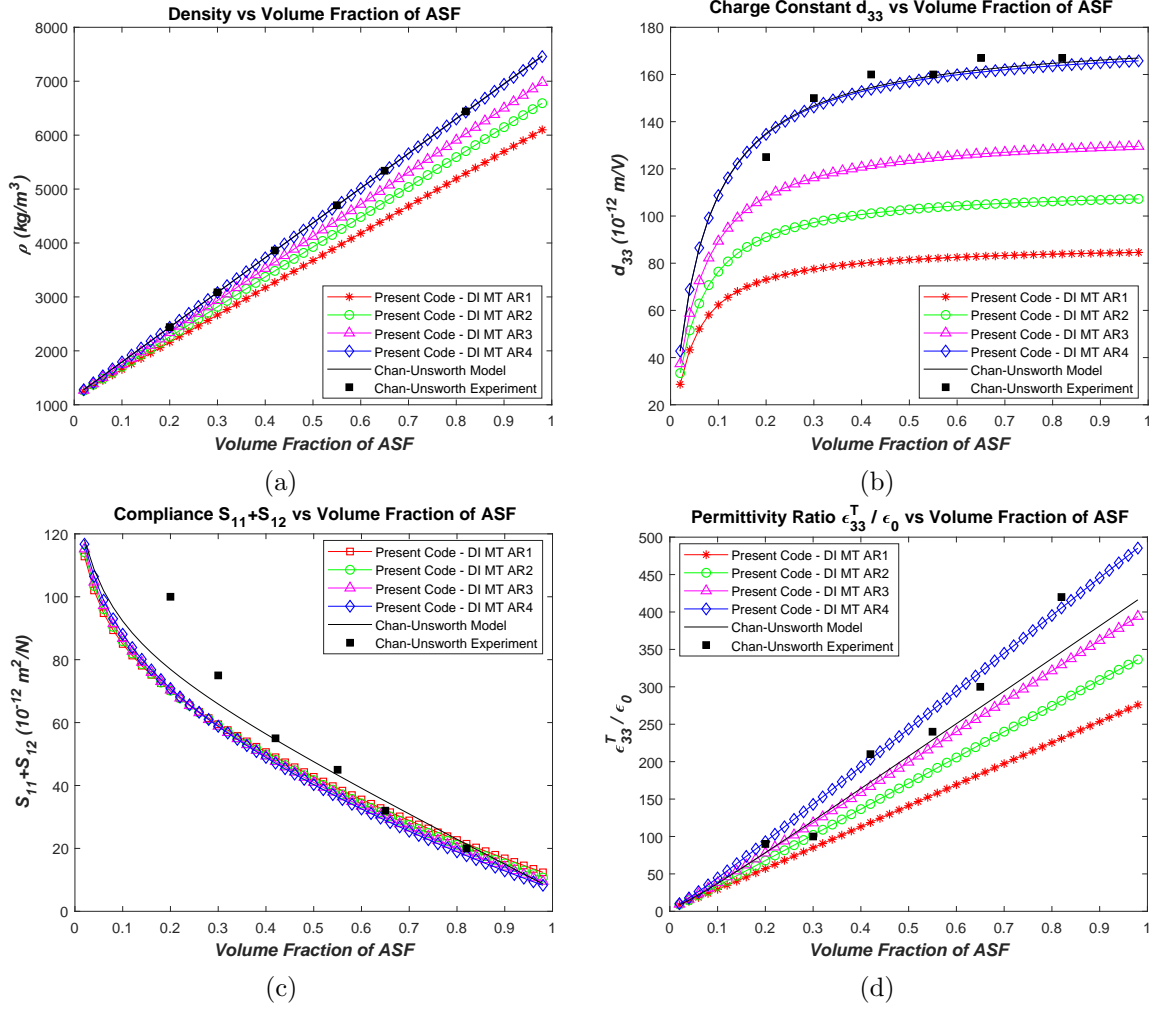


Figure 5.4: (a) Density, ρ , (b) Charge Constant, d_{33} , (c) Compliance, $S_{11} + S_{12}$, and (d) Dielectric Permittivity Ratio, $\frac{\epsilon_{33}^T}{\epsilon_0}$, vs ASF Volume Fraction of PZT-7A-Carbon Fiber-Epoxy Composites

at 11-direction, S_{11} , is more positive than the PZT-7A. In contrast, the compliance of carbon fiber at 12-direction, S_{12} , is more negative. Thus, the compliance components, S_{11} and S_{12} , of the ASF decrease and increase together with the increasing aspect ratio. This is aligned with the trend displayed in Figure 5.4c, the summation of S_{11} and S_{12} almost not affected by the variation of aspect ratio.

Despite the fact that most of the parameters obtained via the Double-Inclusion code are in good agreements Chan-Unsworth's results as depicted in Figures 5.3 and 5.4, some discrepancies are still evident. Chan and Unsworth in [60] explained that the differences occurred between the analytical model and the experimental results due to some properties of the tested materials had deviations with the supplied manufacturer data. For example, as explained earlier, the charge constant, d_{33} , for the present and Chan-Unsworth models need to be adjusted closer to the properties of the tested samples. However, the deviations data of other properties were not given in [60]; thus,

the other properties are kept the same.

In addition, the differences between both models may occur due to the models are derived from different approaches. The Chan-Unsworth model is derived based on the rule of mixture, in which the effective properties are a function of the volume fraction and fiber/matrix properties. Whereas the present model utilises the Eshelby's tensor with Mori-Tanaka method where the inclusion's shape is also considered.

Furthermore, Figure 5.4d shows the variation of the relative permittivity in strain-charge form, $\varepsilon_{33}^T/\varepsilon_0$. As the permittivity of PZT-7A is in a larger order than the carbon fiber and the epoxy matrix, the relative permittivity increases with the volume fraction and aspect ratio.

In contrast with earlier results, it can be seen at AR 0.95, the relative permittivity of the multiphase composite overestimate the single inclusion model. However, it is much closer to the experimental results. The analytical model of Chan-Unsworth is mainly influenced by the charge constant and the permittivity of the piezoelectric fiber. In contrast, the present code estimates the composite permittivity as the function of the permittivity of the core fiber, piezoelectric shell and matrix materials. Therefore, it is more comparable with the experimental results.

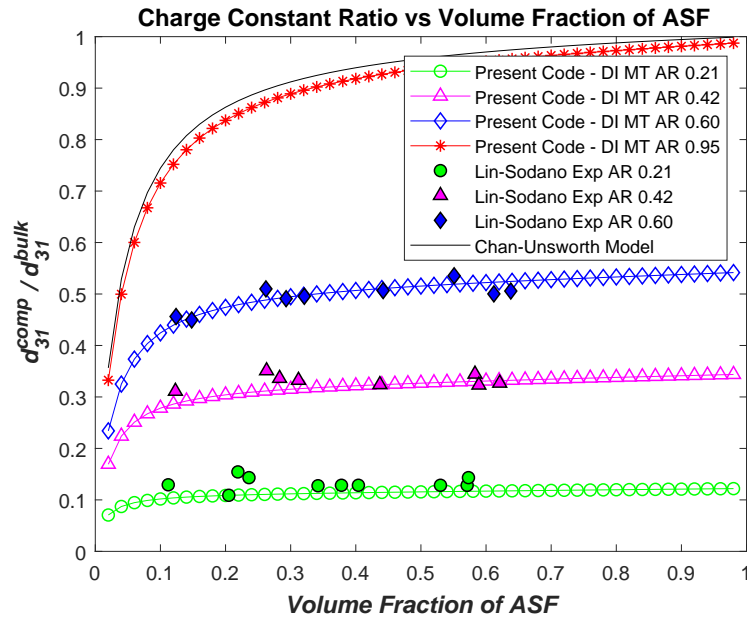


Figure 5.5: Charge Constant Ratio, $d_{31}^{\text{comp}}/d_{31}^{\text{bulk}}$, vs ASF Volume Fraction of BaTiO_3 - SiC - LaRC-SI Composites

In this section, a comparison against the experimental results of Lin and Sodano [50] is also presented. Figure 5.5 depicts the charge constant ratios of the multiphase composite to the bulk piezoelectric material, $d_{31}^{\text{comp}}/d_{31}^{\text{bulk}}$. The results from the present code, Lin-Sodano's experiment and Chan-Unsworth model are compared. The piezoelectric shell, core fiber, and matrix materials are BaTiO_3 , Silicon Carbide (SiC) and

LaRC-SI. Denoted by "Lin-Sodano Exp" is the experimental results of double inclusion composites investigate by Lin and Sodano in [50]. The single fiber model of Chan-Unsworth [60] is used as the upper bound benchmark. The composition of 0.21, 0.42 and 0.60 piezoelectric aspect ratios are evaluated.

In general, the present code results are in a good comparison with the experimental data. The charge constant ratio, $d_{31}^{\text{comp}}/d_{31}^{\text{bulk}}$, shows the similar trend as previously shown in Figure 5.3d for d_{31} component. It can be seen that the charge constant ratio shifted towards the single fiber model as the aspect ratio increases. Furthermore, similar characteristic with Figure 5.3d is observed. The charge constant ratio is almost insensitive to the volume fraction increment at above 50% volume fraction. In addition, at a small aspect ratio, 0.21, the charge constant ratio is almost constant.

The differences (Δ) between the present code and Lin-Sodano's model in [50] with the experimental results are depicted in Table 5.4. The maximum variances of both models occur at aspect ratio 0.21 with variances more than 20%. These variances arise due to some jumps in the experimental values as can be seen at AR 0.21 and Vf 23.6%.

Table 5.4: Comparison of The Present Model and Lin-Sodano Model against The Experimental Results

	AR	Min. Δ	Max. Δ	Average Δ
Lin -	0.21	0.01 %	21.9 %	9.8 %
Sodano	0.42	1.34 %	9.13 %	5.4 %
Model [50]	0.60	4.62 %	13.0 %	9.2 %
Present	0.21	0.01 %	29.17 %	14.47 %
Code	0.42	0.01 %	11.18 %	4.81 %
DI-MT	0.60	0.04 %	4.54 %	2.40 %

5.3.2 Electro-elastic properties comparison against finite element model

In the present work, as the multiphase composite is purposed for energy harvesting on aircraft structure, several stages of analyses are concerned to verify the present Double-Inclusion model. The static and dynamic analyses of single cell multiphase composites are discussed in this section. In addition, the multiphase composites are evaluated as a single cell lamina (similar to Figure 5.1) and also as a composite laminate structure (similar to Figure 5.2). The results of electromechanical analyses performed via FEM are also presented here.

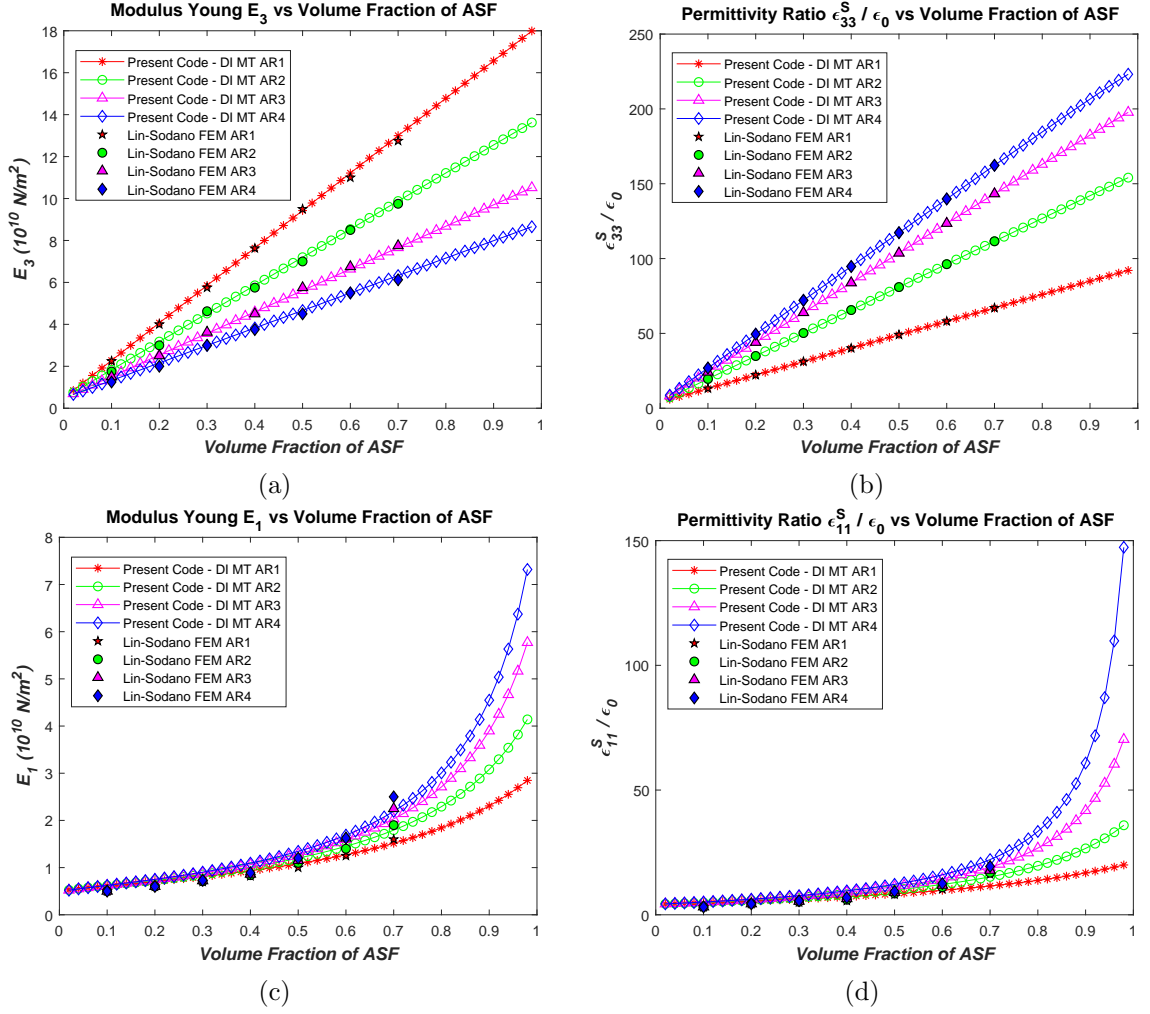


Figure 5.6: (a) Modulus Young, E_3 , (b) Relative Permittivity, $\epsilon_{33}^S/\epsilon_0$, (c) Modulus Young, E_1 , and (d) Relative Permittivity, $\epsilon_{11}^S/\epsilon_0$, vs ASF Volume Fraction of PZT-7A - Carbon Fiber - LaRC-SI Composites

5.3.2.1 Static analysis of single lamina composite

The results of Lin-Sodano [51] for the single cell multiphase composite is used as the first benchmark for the static analysis. The multiphase composites made of Carbon fiber, PZT-7A, and LaRC SI matrix were investigated by Lin and Sodano [51]. They applied eight unique electrical and mechanical boundary conditions to the single cell FEM model to evaluate each electro-elastic properties of the composite. Those unique properties are four stiffness components, two permittivity components, and two piezo-electric coupling components. Static load condition was applied. Therefore, for one composite configuration, eight static FEM simulations were required. In more details, those electro-mechanical boundary conditions can be found in [51, 62].

The modulus and relative permittivity at the transversal and longitudinal directions of the composites are depicted in Figure 5.6. The solid lines denotes the present code

results. Meanwhile, the FEM results from Lin-Sodano are depicted by the star, circle, triangle, and diamond symbols. "AR1", "AR2", "AR3" and "AR4" represent 0.2, 0.4, 0.6 and 0.8 aspect ratios.

The composite properties at longitudinal/fiber direction, E_3 and $\varepsilon_{33}^S/\varepsilon_0$ are shown in Figures 5.6a and 5.6b. It can be seen that the present code and FEM results possesses the same trends and the variances are insignificant. At the same aspect ratio, the Young's modulus, E_3 , increases linearly with the volume fraction. This can be explained as the composite becomes stiffer with larger fractions of carbon fiber and PZT-7A. In contrast, at the same volume fraction, the E_3 decreases as the aspect ratio increases. In this case, the carbon fiber fraction becomes smaller; hence the ASF stiffness is lesser. However, the relative permittivity, $\varepsilon_{33}^S/\varepsilon_0$, increases with both the aspect ratio and volume fraction. The PZT-7A has the largest permittivity compared to the carbon fiber and matrix. Therefore, more permittivity is gained with larger fraction of PZT-7A.

Figures 5.6c and 5.6d depict the composite properties at the transversal direction, E_1 and $\varepsilon_{11}^S/\varepsilon_0$. Important to note that orthotropic condition is assumed, thus, the properties at direction 1 and direction 2 are the same. In contrast with the longitudinal properties, at the transversal direction, the properties grow exponentially with the volume fraction. This characteristic occurs as the stiffness components of the PZT-7A at the transversal direction are in a larger magnitude than the carbon fiber, i.e., hundreds GPa compare to tens GPA. Hence, when the fraction of PZT-7A becomes larger, its stiffness rapidly dominates the effective stiffness of the overall composite. A similar condition also applied to the permittivity at transversal direction.

However, it can be seen there are some discrepancies occur between the FEM and the present code results for the transversal properties estimation. Both for E_1 and $\varepsilon_{11}^S/\varepsilon_0$, as the volume fraction increases, the FEM results show different increment rate with the present code results. The FEM results show a larger increment rate of E_1 at the large volume fraction (>50%). In contrast, for the relative permittivity, $\varepsilon_{11}^S/\varepsilon_0$, the FEM results have almost a steady increment rate with the increasing volume fraction.

These results aligned with the phenomena observed by Lin and Sodano in [51]. At AR 0.8 and Vf 70%, the maximum variance of E_1 was observed, their FEM model overestimated the Double-Inclusion model by 31%. Whereas at AR 0.2 and Vf 70%, the FEM model overestimated the $\varepsilon_{11}^S/\varepsilon_0$ value by 39%. Despite the maximum variances occur at the same composite configuration for the present code, a closer agreement is obtained with the FEM results. At AR 0.8 and Vf 70%, the E_1 estimation from the present code has 12% variance with the FEM results. Whereas at AR 0.2 and Vf 70%, the estimation of $\varepsilon_{11}^S/\varepsilon_0$ from the present code differs by 28% with the FEM's.

The second investigation for static analysis used the XFEM results of Koutsawa et

al. [91] as benchmark. The multiphase composite materials are PZT-7A, glass fiber and epoxy matrix. By means of XFEM, Koutsawa et al. modelled the different material regions and boundaries of the composite via enrichment functions and level set method. Thus, the finite element meshes are independent to the composite phases [91]. The comparison of the present code with their XFEM results is shown in Figure 5.7.

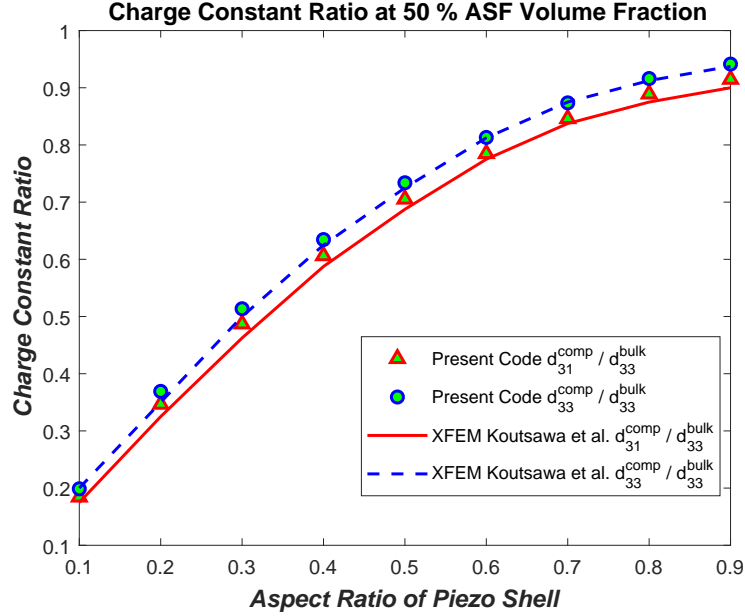


Figure 5.7: Charge Constant Ratio $d_{31}^{comp} / d_{31}^{bulk}$ & $d_{33}^{comp} / d_{33}^{bulk}$, vs Aspect Ratio of PZT-7A - Glass - Epoxy Composites

Excellent agreement between the present code and XFEM results can be seen in Figure 5.7. Both charge constant ratios at 33-directions and 31-directions show the same trend. At small aspect ratio, the charge constant ratio almost linearly increases with the aspect ratio. However, at a larger aspect ratio (>40%), the increment rate decreases. These trends aligned with the earlier results depicted in Figures 5.3d, 5.4b and 5.5. Table 5.5 shows the discrepancies of d_{31} ratios from both methods in more details.

5.3.2.2 Dynamic analysis of single lamina composite and unimorph beam

In this section, the dynamic analyses of single cell lamina and unimorph structure made of the multiphase composite are discussed. Two different models are used in the FEM simulations. The first model is a long cube/unit-cell constructed from different materials. The model consists of detailed and distinct 3D elements for each phase. In contrast, the second model is a simpler shape, only a long cube without any detail of each phase. The effective electro-elastic properties obtained from the Double-Inclusion code are the only material input. The analyses focused to compare the displacement

Table 5.5: Charge Constant Ratio Comparison: The Present Model vs XFEM - Kout-sawa et al.

AR	Charge Constant Ratio ($d_{31}^{comp}/d_{31}^{bulk}$)		
	Present Code	XFEM [91]	Δ (%)
0.1	0.19	0.18	5.56%
0.2	0.35	0.33	6.06%
0.3	0.49	0.46	6.52%
0.4	0.61	0.59	3.39%
0.5	0.71	0.69	2.90%
0.6	0.79	0.78	1.28%
0.7	0.85	0.84	1.19%
0.8	0.89	0.88	1.14%
0.9	0.91	0.90	1.11%

and voltage distributions of the lamina. Herein, the first and the second models are called as the "Detailed 3D FE" and the "homogenised FE" models, respectively.

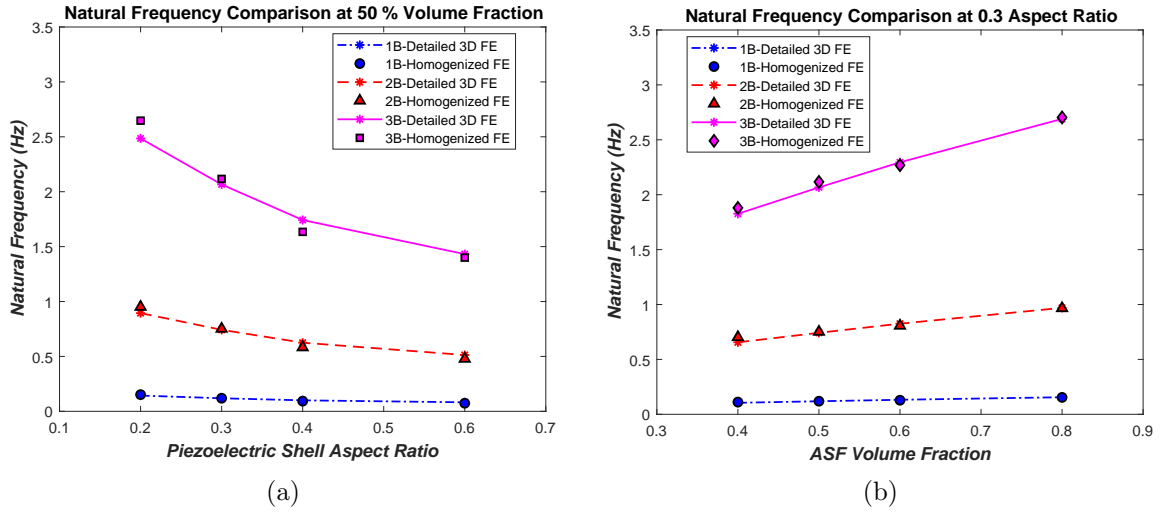


Figure 5.8: Natural Frequency Comparison of PZT-5A - Carbon - LaRC-SI Composites for (a) Different Aspect Ratio at 50% Volume Fraction (b) Different Volume Fraction at 0.3 Aspect Ratio

The FEM simulations are conducted using COMSOL Multiphysics[©] with the piezo-electric devices module. Due to the software limitation, only linear tetrahedral elements are used. The observed composites are made of PZT-5A, Carbon fiber, and LaRC-SI matrix. Fixed boundary conditions are applied at one end of the lamina. The FEM models are evaluated by means of modal analysis.

Figures 5.8a and 5.8b depict the natural frequencies of the composite at Vf 50% and

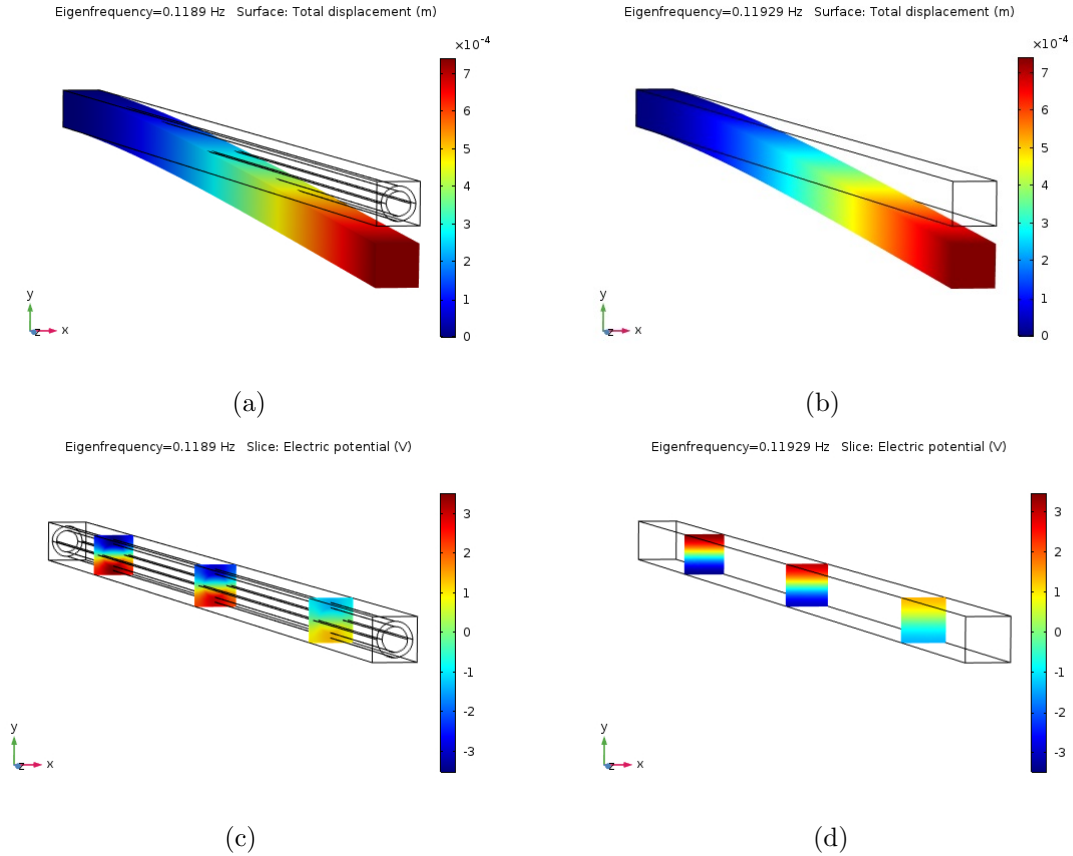


Figure 5.9: (a) Detailed 3D FE eigenvector (structural mode shape), (b) Homogenisation FE eigenvector (structural mode shape), (c) Detailed 3D FE eigenvector (voltage mode shape), and (d) Homogenisation FE eigenvector (voltage mode shape) of the first bending mode, PZT-5A - Carbon Fiber - LaRC-SI composites with Vf 50% and AR 0.3

AR 0.3, respectively. The notations of "1B", "2B" and "3B" represent the first, second and third bending modes. In Figure 5.8a, it is clearly seen that both the "Detailed 3D FE" and "homogenised FE" models are in a good comparison. The trend in Figure 5.8a shows the natural frequency decreases as the aspect ratio increases. This behaviour supports the trends displayed in Figures 5.6a and 5.4a. At the same volume fraction, the composite becomes heavier and less stiff when the aspect ratio increases.

At the same aspect ratio, the natural frequency increases with the volume fraction as displayed in Figure 5.8b. This trend aligns with the one displayed in Figure 5.6a, the composite's stiffness increases with the volume fraction. Despite the fact that the density also increases with the volume fraction, the Young's modulus increment rate is much higher than the density's. Table 5.6 shows the natural frequency comparison for different volume fraction in more details. It can be seen that the discrepancies between both FEM models are not significant ($<5\%$).

In relation to the energy harvesting ability, the natural frequencies with and without

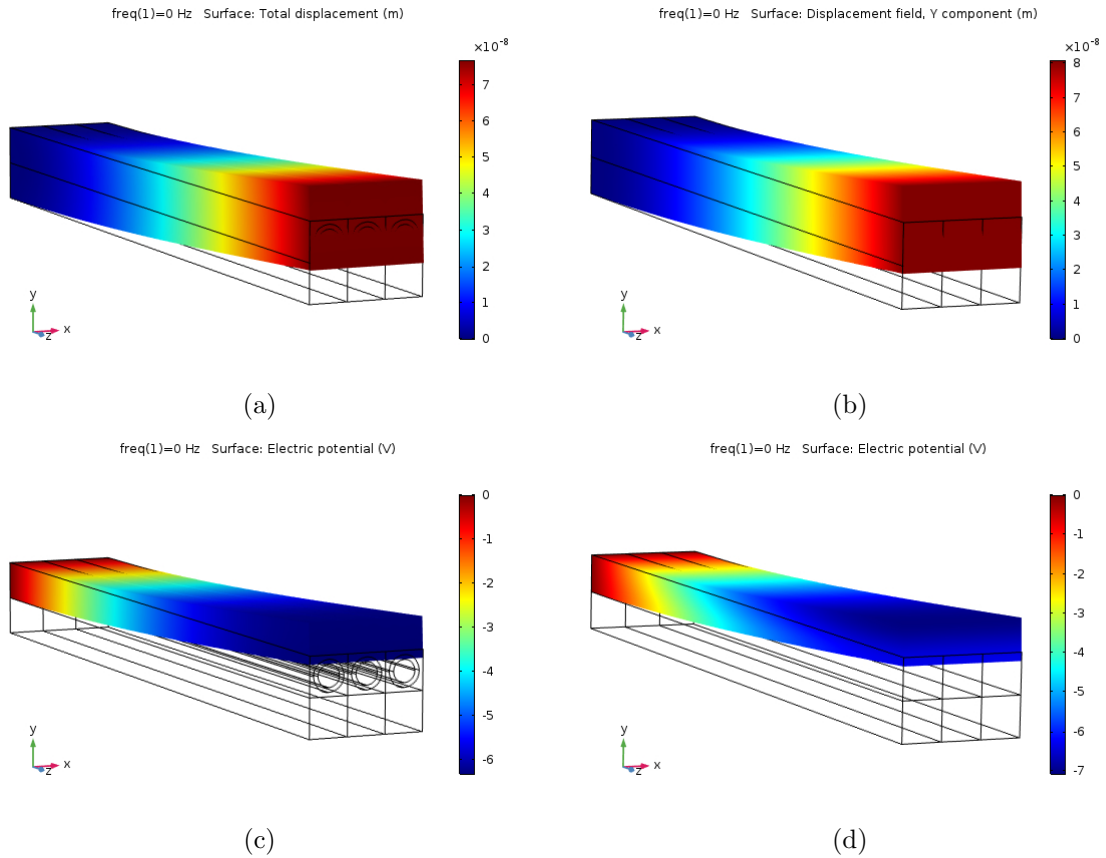


Figure 5.10: (a) Detailed 3D FE displacement, (b) Homogenisation FE displacement, (c) Detailed 3D FE voltage, and (d) Homogenisation FE voltage of the static bending response, PZT-5A - Carbon Fiber - LaRC-SI unimorph beam with Vf 50% - AR 0.3 and aluminium substrate

active piezoelectric effect are evaluated. The comparison between these two effects is shown in Table 5.7. The ones with pure mechanical effect (piezoelectric coupling inactive) are defined by "Pure Mech". Whereas "Elec-Mech" represents the model with active piezoelectric coupling. As depicted in Table 5.7, the natural frequencies of both models are in excellent agreement. Hence, in this case, the electro-mechanical coupling almost does not affect the bending natural frequencies.

Figure 5.9 depicts the example of the first bending mode shapes for displacement and voltage. The mode shapes for composite AR 0.3 and Vf 50% are shown. This combination is unique as the ASF is half of the composite and the ASF itself is half piezoelectric - half core fiber. As displayed in Figure 5.9, the displacement and voltage contours for both FEM models are well agreed. Following the first bending shape, the displacements are maximum at the tip as shown in Figures 5.9a and 5.9b.

Figures 5.9c and 5.9d depict the sliced contours of the voltage. From the voltage distributions, it can be seen the values are maximum near the root and decreases towards the tip. Moreover, from the cross-sectional slices, it is shown that the voltage

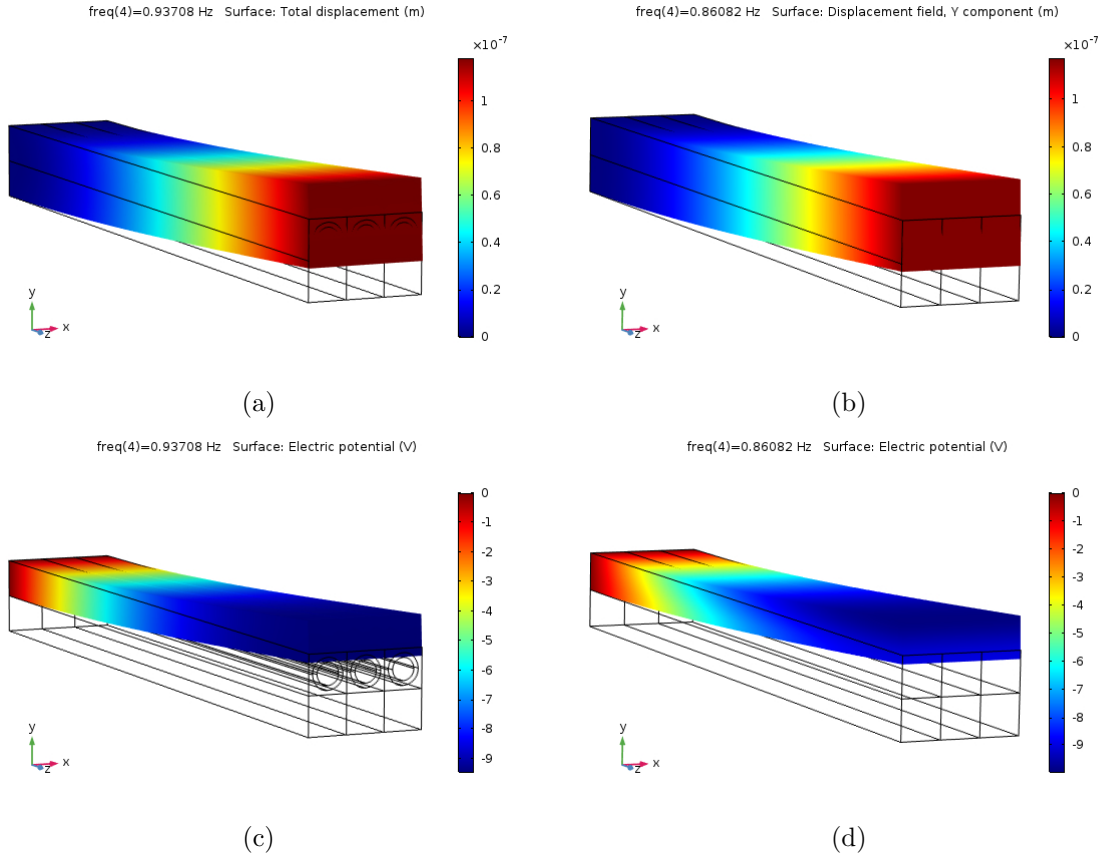


Figure 5.11: (a) Detailed 3D FE displacement, (b) Homogenisation FE displacement, (c) Detailed 3D FE voltage, and (d) Homogenisation FE voltage of the dynamic bending response at 0.6 frequency ratio, PZT-5A - Carbon Fiber - LaRC-SI unimorph beam with Vf 50% - AR 0.3 and aluminium substrate

of the bottom and top parts are in the opposite values. This is occurred as the bottom part exhibits compression and the top part exhibits tension. Whereas at the neutral axis, the voltage is zero.

The results from a unimorph beam analyses are also presented here. The unimorph beam commonly consisted of a piezoelectric material as the electro-active layer. In the present case, the bulk piezoelectric material is substituted with the multiphase composite.

In the present case, the active layer consisted of three multiphase composite lamina arranged in a row. The substrate (non-active) layer at the bottom is made of aluminium. Table 5.8 depicts the natural frequencies comparison of the unimorph modelled with the "Detailed 3D FE" and the "homogenised FE". The first bending, second bending and the first torsion modes are defined by "1B", "2B" and "1T". As shown in Table 5.8, the natural frequencies of both FEM models are reasonably agreed.

A sensor-like problem is evaluated in the dynamic response cases. An external mechanical load is given at the unimorph's tip. The responses at 0 Hz excitation frequency

Table 5.6: Natural Frequency Comparison for Different Volume Fraction at 0.3 Aspect Ratio of PZT-5A - Carbon - LaRC-SI Composites, Detailed 3D Finite Element vs Finite Element with Homogenization Properties

Vf	Mode	Natural frequency (Hz)		
		Detailed 3D	homogenised	Δ (%)
50%	1B	0.1189	0.1192	0.31%
	2B	0.7423	0.7513	1.32%
	3B	2.0662	2.1166	2.44%
60%	1B	0.1323	0.1281	3.14%
	2B	0.8254	0.8062	2.32%
	3B	2.2950	2.2684	1.16%
80%	1B	0.1556	0.1540	1.02%
	2B	0.9695	0.9657	0.40%
	3B	2.6902	2.7037	0.50%

(static condition) are shown in Figure 5.10. It is depicted that the deformation of the "Homogenised FE" model is slightly higher than the "Detailed 3D FE" model. This behaviour may occur due to the utilisation of the tetrahedral elements. The tetrahedral element is known to have a stiff character in a bending case. The mesh construction for the "Detailed 3D FE" model is much more difficult as the elements need to be carefully defined in each phase. Thus, despite that coarse meshes are used for both models, the "Detailed 3D FE" converges at a higher number of elements.

As the natural frequencies of both FEM models are slightly differing, a ratio of the excitation frequency to the first bending frequency is used to define the load. It is known that when the excitation is near the natural frequency, the resonance occurs, and the amplitude can be extremely amplified. Hence, it is considered reasonable to compare the responses at the excitation below the natural frequency. Figure 5.11 shows the unimorph responses for 0.6 frequency ratio. In the case of the "Detailed 3D FE", this ratio defines an excitation at 0.6×1.5618 Hz or 0.9371 Hz. It is shown in Figure 5.11 that the displacement and voltage amplitudes of both FEM models are in a good agreement.

5.3.3 Highlights on the effective electro-elastic properties concerning energy harvesting analysis

In relation to the energy harvested under dynamic bending, the following effective electro-elastic properties of the multiphase composite are highlighted.

Table 5.7: Natural Frequency Comparison of homogenised FE for Different Volume Fraction at 50% Volume Fraction of PZT-5A - Carbon - LaRC-SI Composites, Pure Mechanical Effect vs Activated Electro-mechanical Coupling

		Natural frequency (Hz)		
AR	Mode	Elec-Mech	Pure Mech	Δ (%)
0.2	1B	0.1521	0.1519	0.13%
	2B	0.9508	0.9452	0.59%
	3B	2.6470	2.6174	1.12%
0.3	1B	0.1192	0.1195	0.25%
	2B	0.7513	0.7468	0.60%
	3B	2.1166	2.0809	1.69%
0.4	1B	0.0926	0.0927	0.11%
	2B	0.5819	0.5780	0.67%
	3B	1.6345	1.6219	0.77%

Table 5.8: Natural Frequency Comparison for The Unimorph Beam, Detailed 3D Finite Element vs Finite Element with Homogenization Properties

Natural frequency (Hz)			
Mode	Detailed 3D	homogenised	Δ (%)
1B	1.5618	1.4347	8.13%
2B	7.8235	7.8421	0.24%
1T	8.5433	8.3114	2.71%

1. The Young's modulus at the longitudinal/fiber direction, E_3 , increases with increasing volume fraction and decreases with increasing aspect ratio. A similar fashion also observed for stiffness components at the longitudinal direction, C_{33} . Thus, large volume fraction and small aspect ratio mean stiffer composite, harder to deflect.
2. The charge constant, d_{31} , at volume fraction $>50\%$ almost insensitive to the increment of volume fraction at a particular aspect ratio. Hence, for a given structural deformation, the volume fraction increment insignificant to the increment rate of the electrical response.
3. The transverse permittivity at constant strain, ϵ_{11}^S , grows at a small rate with the volume fraction and aspect ratio. It is observed at high volume fraction, $>70\%$, the permittivity increases exponentially with the volume fraction. However, more than 80% volume fraction is considered not possible due to the geometrical con-

straint. Therefore, for all possible material composition, a low permittivity or a low capacitance in the structure is expected.

In addition, although the density is not explicitly shown in the governing energy harvester formulation, it influences the natural frequencies and dynamic response of the structure. Moreover, in the aircraft design case, density is a significant parameter in a weight-energy evaluation. The density increases with the volume fraction and aspect ratio. Hence, with larger volume fraction and aspect ratio, the structure is heavier and more fuel is required.

5.4 Summary

In this chapter, a method of evaluating electro-elastic properties of multiphase composites with active structural fiber has been presented. A computational code based on the Double-Inclusion model extended with the Mori-Tanaka method has been developed. The numerical code has been applied to estimate the effective electro-elastic properties of multiphase composites with various material compositions. The results of the present work have been well validated with the analytical, experimental and finite element results from the literature.

Static and dynamic electromechanical analyses for a single lamina and a unimorph beam via FEM has also been performed in the present work. The effective properties obtained from the present Double-Inclusion code has been verified with a detailed 3D FEM model. Therefore, the present Double-Inclusion model can be used as one of the preliminary tools to provide an estimation on the properties of multiphase composites for energy harvesting evaluation. Later in Chapter 6 and Chapter 8, the composites' properties evaluated here are utilised as the substitution of the bulk piezoelectric material in energy harvesting structures.

Chapter 6

Application of The Multiphase Composites on A Jet Aircraft Wingbox

In the present work, the multiphase composites with ASF are applied to a notional jet aircraft wingbox. The same wingbox presented in Chapter 4 is used for the investigation. The energy harvesting analysis of this wingbox is discussed in this chapter. The novel hybrid scheme presented in Chapter 3 is used. The Double-Inclusion model is implemented to evaluate the electro-elastic properties of the multiphase composites.

In addition, a new procedure is developed to investigate the trade-off between the aircraft weight, the fuel saving and the energy harvested for different composite configurations. A conceptual aircraft design approach concerning the aircraft weight breakdown is adopted for this procedure. The description and implementation of this procedure for the aircraft wingbox are presented in this chapter.

Some works and results presented in this chapter are parts of the author's published works in *Composite Structures*, Volume 202, 2018.

6.1 Aircraft weight breakdown in conceptual design

In this section an aircraft's weight breakdown is presented. The weight breakdown concerning a conceptual aircraft design stage [92] is adopted. This weight breakdown is used to establish the relationship due to the changes caused by the piezoelectric/multiphase composites to the aircraft weight. The main weight components concerned here can be classified as follows:

1. The empty weight, W_E , which consisted of the aircraft structure and the installed systems/equipments/interiors.

2. The crew weight, W_C , and the payload weight, W_P . The crews are the pilots, the flight attendants and any other staffs, i.e., engineers. The payloads are the passengers, the baggages and also the cargo. These components are usually a pre-determined requirements in the conceptual aircraft design.
3. The fuel weight, W_{fuel} , which consisted of the fuel to accomplish the flight mission with some extras, i.e., 5% reserve fuel. It is estimated based on the flight mission profile, i.e., take-off, climb, cruise, descent, landing.
4. The take-off weight, W_{TO} , which is the total of all the weight components as presented in Equation (6.1).

$$W_{TO} = W_E + W_C + W_P + W_{fuel} \quad (6.1)$$

In the conceptual aircraft design, the W_{TO} is initially estimated from a historical data or an empirical formulation. The ratio of W_E to the W_{TO} can be determined from the following empirical formulation.

$$\frac{W_E}{W_{TO}} = A W_{TO}^C K_{VS} \quad (6.2)$$

The constants A and C are defined based on the aircraft type. For a jet transport aircraft, $A = 1.02$ and $C = -0.06$. Whereas K_{VS} is the variable sweep constant, for a fixed-sweep wing, $K_{VS} = 1$, and for a variable-sweep wing, $K_{VS} = 1.04$. Hence, in the present case, Equation (6.2) can be rewritten as

$$\frac{W_E}{W_{TO}} = 1.02 W_{TO}^{-0.06} \quad (6.3)$$

However, it is important to note that the constants in Equation (6.3) are defined based on the historical data of conventional jet transport aircraft.

To the author's knowledge, composites have just started been used as main materials for the commercial aircraft in the past decade [93]. Hence, the historical data is not sufficient to develop an empirical weight function for a transport aircraft with composites. Therefore, for the study purpose, the weight fraction based on Equation (6.3) is applied to evaluate the aircraft with multiphase composite in the present work. However, in a more detailed design stage, some correction factors need to be applied to accomodate the influence of advanced composites. For reader's reference, some efforts have been reviewed in [94] concerning the prospect of composite implementation on future aircraft.

Commonly, an iterative procedure is required in the initial weight estimation as W_E , W_{fuel} and W_{TO} are unknown. Thus, Equation (6.1) and Equation (6.2) are solved iteratively. However, a reference aircraft is known in the present work. The W_E , W_{fuel} and W_{TO} components have been defined. Therefore, the concern is addressing the effects due to a material replacement. The detail of procedure to evaluate these effects is explained in the next section.

6.2 Evaluation procedure on the trade-off between aircraft weight and energy harvested

In this section, firstly, the increment or reduction of the aircraft weight due to a material replacement is discussed. Further, this modified weight is used to evaluate the trade off between the aircraft weight and the harvested energy. The empty weight, W_E , and the take-off weight, W_{TO} , are directly influenced by a material replacement as the structural weight changes. Thus, the aerodynamic load required to lift the aircraft will change, as well as the drag force that occurred due to lift and also the thrust required to move the aircraft forward. Hence, the fuel weight, W_{fuel} , is affected and a new aerodynamic load may be applied for the structural response and energy harvesting evaluations. The scheme to quantify these effects is given in Figure 6.1 and can be described as follows:

1. The weight components of a reference aircraft are defined. The superscript "Ref" in Figure 6.1 denotes these components.
2. The change in structural weight, $\Delta W_{Structural}$, due to material replacement is calculated.
3. The new empty weight, W_E^{New} , is obtained from the summation of the reference empty weight, W_E^{Ref} , and the $\Delta W_{Structural}$.
4. Once W_E^{New} is found, Equation (6.3) can be used to estimate the new take-off weight, W_{TO}^{New} .
5. In a steady level flight, a new lift cruise load may be defined equal to the W_{TO}^{New} .
6. There is no change in the payload and crew weights as these components are considered as requirements.
7. After the new weight components are obtained, the new fuel weight W_{fuel}^{New} is calculated via Equation (6.1).

In the current case study, the upper skin material of the aircraft wingbox is replaced (refer to Chapter 4). Important to note that the aircraft has two wings; hence, the $\Delta W_{Structural}$ is twice the weight change of a wingbox. In the present study, the electrical power harvested from the wingbox is associated with the APU generated power in order to have an equivalent parameter for the trade off between weight and energy. The scheme to estimate the fuel saving from the material replacement and the harvested power is depicted in Figure 6.2 and can be explained as follows:

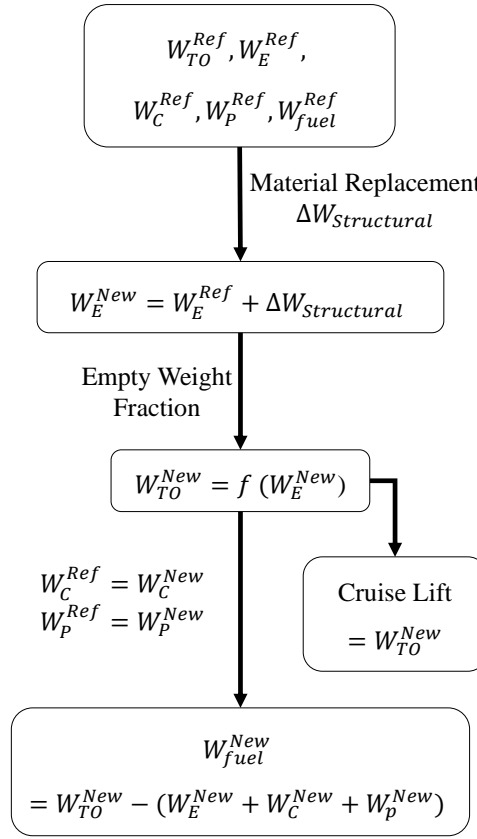


Figure 6.1: Schematic diagram of the weight change calculation

1. The power generated (kW) and the fuel consumption rate (kg/s or lbs/hour) of the APU are determined.
2. An operation time, t_{APU} , is defined. The energy generated by the APU, J_{APU} (Joule), and its consumed fuel consumed are estimated.
3. The ratio of the energy to the consumed fuel, J^* (Joule/kg-fuel or Joule/lbs-fuel), is calculated.
4. In relation to the hybrid scheme discussed in Chapter 4, a steady-state harmonic oscillation is assumed. Hence, the average power, P_{Ave} , can be defined as half the maximum harvested power P_{max} .
5. For a certain vibration time, $t_{Harvest}$, the energy generated by the harvester, $J_{Harvest}$ (Joule), is obtained from the integration of power to time.
6. The equivalent fuel saved due to the energy harvested, $\Delta W_{fuel-Pwr}$, is determined based on the J^* ratio.
7. The fuel change due to the direct effect of structural weight increment/reduction,

$\Delta W_{fuel-Str}$, is the difference between the new fuel weight, W_{fuel}^{New} , and the reference fuel weight, W_{fuel}^{Ref} .

8. The TOTAL ΔW_{fuel} , is the summation of $\Delta W_{fuel-Pwr}$ and $\Delta W_{fuel-Str}$.

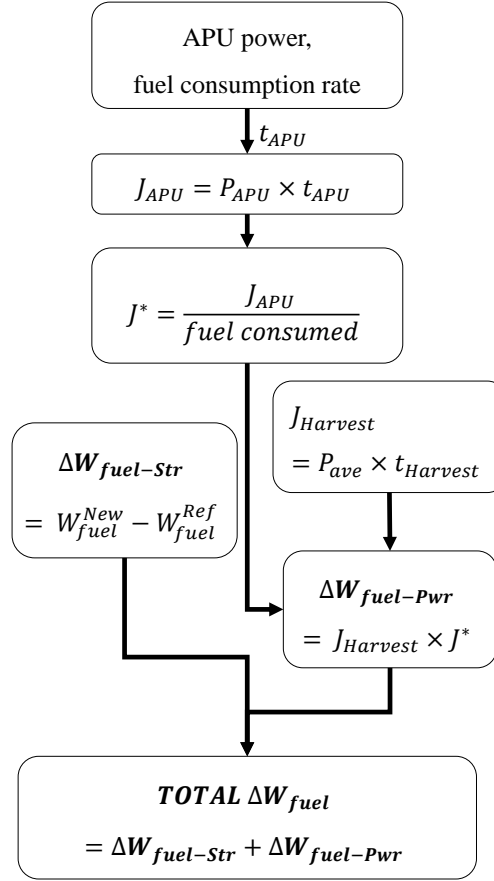


Figure 6.2: Schematic diagram of the fuel saving evaluation

To be noted that the formulation of maximum power in Chapter 3, Equation (3.32) is derived for one cantilever beam. In Chapter 4, one cantilever beam is associated with one aircraft wing. Hence, the total power harvested from the aircraft is twice the power harvested from a wing. Thus, P_{Ave} , needs to be considered for two wings.

6.3 Wingbox energy harvesting simulation with the multiphase composite

In this section, the investigation on the energy harvesting potential from the typical jet transport aircraft is presented. The same wingbox configuration discussed in Chapter 4 is evaluated. In addition to PZT-5A, multiphase composites with different configurations are analysed as the replacement material on the upper skin of the wingbox. The

similar composites evaluated in Chapter 5, Section 5.3.2.2 which consisted of PZT-5A, carbon fiber and LaRC SI matrix are used.

The fiber orientation is along the span of the wingbox, from the root to the tip. The material properties of the multiphase composites in 3D form is reduced to 2D form as input for the quadrilateral shell elements. The detailed transformation scheme of the properties is referred to [10]. Table 6.1 shows the wingbox weight with different bulk materials. Whereas, the wingbox weight with embedded multiphase composites are depicted in Tables 6.2 and 6.3. Here, the aerodynamic lift during cruise is assumed equal to the take-off weight, W_{TO} . Therefore, the lift load is dependent to the materials' weight.

Table 6.1: Wingbox Weight: Different Upper Skin Material

Material	Al-2219	PZT-5A
Weight (lbs)	2415	3929

Table 6.2: Wingbox Weight: Multiphase Composites Upper Skin, PZT-5A - Carbon - LaRC-SI 50% Volume Fraction

Aspect Ratio	0.2	0.4	0.6
Weight (lbs)	2373	2622	2800

Table 6.3: Wingbox Weight: Multiphase Composites Upper Skin, PZT-5A - Carbon - LaRC-SI 0.2 Aspect Ratio

Volume Fraction	50%	60%	70%
Weight (lbs)	2373	2457	2541

The W_{TO} and W_E of the aircraft is determined via Equation (6.1) and Equation (6.3) for each material configuration. Firstly, the weight components of a reference aircraft is calculated. The reference aircraft's W_{TO} is 170000 lbs with W_{fuel} is 41000 lbs [84]. Hence, it is found that the W_E is 84183 lbs. Therefore, the payload and crew weight, $W_C + W_P$ is 44817 lbs. In association with the scheme in Figure 6.1, these weight components are the ones with superscript "Ref". Hence, by following the procedure in Figure 6.1, the new aircraft weights for various material configurations can be calculated.

The W_{TO} and W_E for aircraft with different bulk materials are depicted in Table 6.4. Whereas Tables 6.5 and 6.6 show the W_{TO} and W_E for aircraft with different composites configurations. It is obviously seen in Table 6.4 the maximum W_E and

W_{TO} are obtained with bulk piezoelectric material. In contrast, the aircraft with the composite composition of the smallest volume fraction and aspect ratio, AR 0.2 and Vf 50%, gains the minimum W_E and W_{TO} .

Table 6.4: Aircraft Empty Weight and Take-Off Weight: Different Wingbox Upper Skin Material

Material	Al-2219	PZT-5A
W_E (lbs)	84183	87211
W_{TO} (lbs)	170000	176513

Table 6.5: Aircraft Empty Weight and Take-Off Weight: Multiphase Composite Wingbox Upper Skin, PZT-5A - Carbon - LaRC-SI 50% Volume Fraction

Aspect Ratio	0.2	0.4	0.6
W_E (lbs)	84099	84597	84593
W_{TO} (lbs)	169820	170890	171656

Table 6.6: Aircraft Empty Weight and Take-Off Weight: Multiphase Composite Wingbox Upper Skin, PZT-5A - Carbon - LaRC-SI 0.2 Aspect Ratio

Volume Fraction	50%	60%	70%
W_E (lbs)	84099	84267	84435
W_{TO} (lbs)	169820	170181	170542

Concerning the energy harvesting evaluation, the same loading condition as described in Chapter 4 is applied. The steady lift is modelled as a concentrated force acting on the wing. This force is used as the amplitude to form a harmonic load excitation. Initially, modal analyses is performed to the wingboxes. The natural frequencies are used to define the excitation frequencies acting on the structures. Similar to the one presented in Chapter 4, the excitation lower than the first bending natural frequency are also used here. Table 6.7 depicts the first bending frequencies for the wingboxes.

The first bending natural frequencies for the wingboxes are quite low, around 1.6-2.3 Hz. The frequency ratio defined in Chapter 4 is used. The loads with 0.5, 0.7, 0.9 frequency ratios are applied. In accordance to the implementation of the hybrid scheme in Chapter 4, the lift cruise load and a unit of moment are used as the actual and dummy loads. Appendix H shows the displacements of the wing with different composite configurations. The responses from the lift loads represent the displacement due to mechanical load. The responses from the dummy loads are used to obtain the reverse piezoelectric effect.

Table 6.7: 1st Bending Natural Frequency of The Wingbox for Different Multiphase Composite Composition

Vf	AR	Natural frequency (Hz)
0.5	0.2	2.21
0.5	0.4	1.99
0.5	0.6	1.76
0.6	0.2	2.32
0.7	0.2	2.35
Bulk	PZT-5A	1.61

Figure 6.3 shows the voltage amplitude responses for wingboxes with bulk PZT-5A and the multiphase composites at Vf 50%. The excitation at 0.5, 0.7, 0.9 frequency ratios are represented by "f1", "f2" and "f3", respectively. The trend of the voltage responses similar with shown earlier in Chapter 4. Initially, the voltage increases with the resistance load. However, at a particular point, it starts to undergo an asymptotic behaviour.

The wingbox with bulk PZT-5A has the small resistance load when the voltage starts to become asymptotic. In contrast, the wingbox with the composite at Vf 50% and AR 0.2 aspect ratio has the largest resistance load when the voltage starts to become asymptotic. Although a larger piezoelectric coupling comes with a higher aspect ratio, the voltage goes asymptotic at a smaller resistance; thus, it resulted in a smaller maximum voltage. Furthermore, in alignment with the discussion in Chapter 4, the largest excitation frequency provided the highest level of the maximum voltage as it exerts the highest displacement amplitude.

The power amplitude responses for wingboxes with bulk PZT-5A and the multiphase composites at Vf 50 % are depicted in Figure 6.4. Similar characteristics as presented in Chapter 4 are also observed. Initially, the power increases with the resistance load before it reaches a maximum point and starts to decline. An interesting characteristic is found as the powers from all configurations, including the bulk PZT-5A, could reach a similar maximum level as can be seen in Table 6.8. This finding could become a positive insight for the study on the energy harvesting material and its weight issue.

It is a positive value to remark as the multiphase composites are lighter than the bulk PZT and yet it can produce a similar level of power. In accordance with the findings highlighted in Chapter 5, Section 5.3.3, this behaviour may occur as the permittivity (capacitance) and the piezoelectric coupling constants of the composites are smaller than the bulk PZT. A smaller coupling constant may result in a smaller electrical field. However, a smaller capacitance may also result in a larger voltage for the

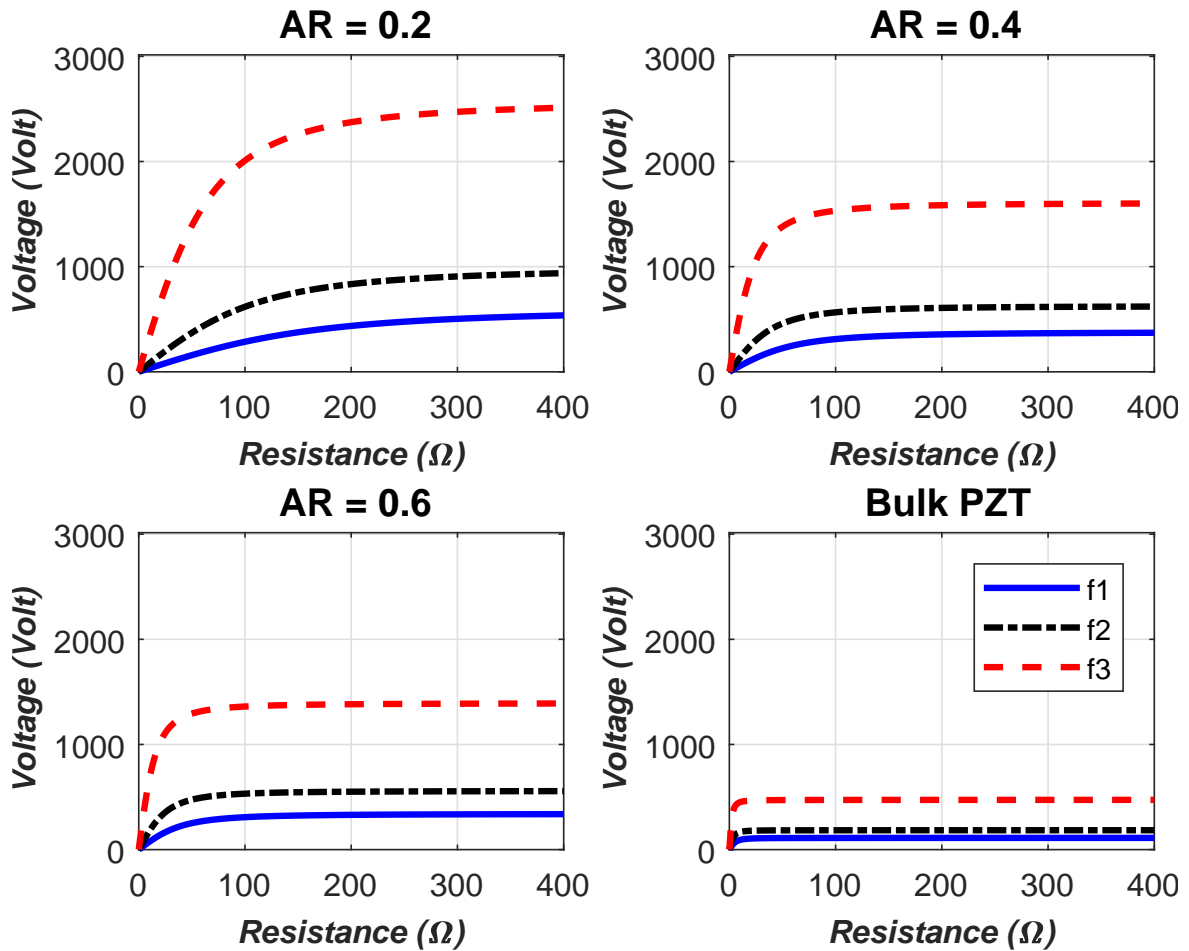


Figure 6.3: Variation of voltage amplitude to the resistance load for wingboxes with multiphase composite skin, AR 0.2, 0.4 & 0.6 at V_f 50%, and bulk PZT skin

same amount of charges.

In addition, Figure 6.5 shows the power amplitude responses for wingboxes with bulk PZT-5A and the composites at AR 0.2. It can be seen that the level of maximum power decreases as the volume fraction increases. This characteristic is caused by an increasing stiffness at the longitudinal/fiber direction for a composite at a higher volume fraction.

6.4 Aircraft fuel saving evaluation

In this section, the equivalent fuel saving from the implementation of the multiphase composites on the wingbox is discussed. The power responses obtained from the earlier section are equivalenced with the fuel used for an APU operation. The scheme presented in Figure 6.2 is applied.

The APU used as reference is a typical APU for a medium-long ranged jet transport aircraft, i.e., the B737 or the A320. Based on the data in [95,96], the APU can

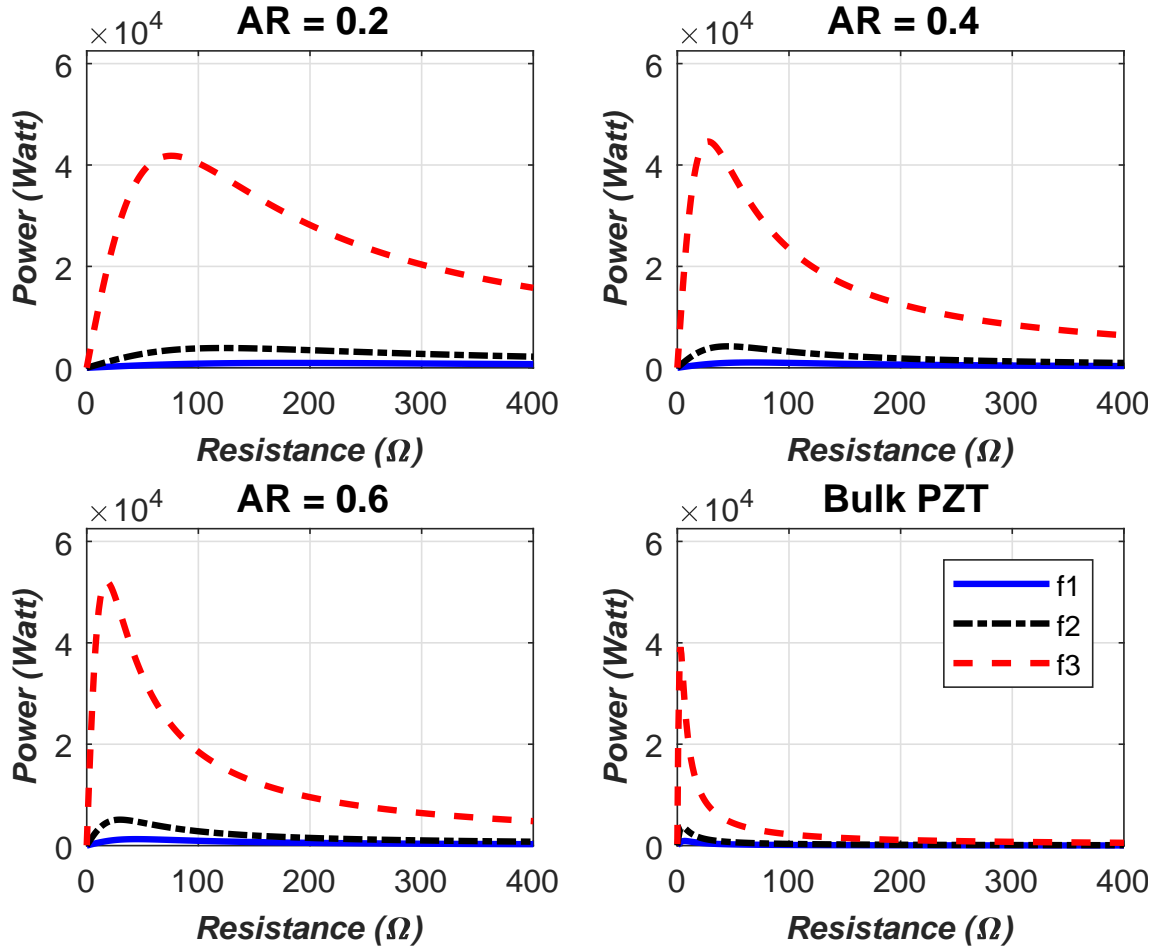


Figure 6.4: Variation of power amplitude to the resistance load for wingboxes with multiphase composite skin, AR 0.2, 0.4 & 0.6 at Vf 50%, and bulk PZT skin

support the aircraft normal electrical loads and taxiing system with 90kW by consuming 2kg/min of fuel. Therefore, for 1-hour APU operation, 324 Mega-Joule energy is produced and 264.5 lbs fuel is consumed (1220 kilo-Joule produced per pound fuel).

The evaluation on the fuel weight and the energy harvested for the wingbox with the bulk PZT is shown in Table 6.9. The terms " $\Delta W_{fuel-Str}$ ", " $\Delta W_{fuel-Pwr}$ " and " P_{Ave} " are referred to the scheme explained in Section 6.2. The positive/negative (+/-) signs define the increment/reduction of the fuel weight in comparison to the original weight of all Al-2219 aircraft.

The " $\Delta W_{fuel-Pwr}$ " is always negative as it defines a saved fuel. In contrast, the " $\Delta W_{fuel-Str}$ " can either be positive or negative depend on whether the structure is heavier or lighter. Therefore, the total change of the fuel weight, " $TOTAL \Delta W_{fuel}$ ", can also be positive or negative depend on whether the " $\Delta W_{fuel-Str}$ " support the fuel saving by " $\Delta W_{fuel-Pwr}$ " or against it.

Table 6.9 shows that by applying bulk PZT-5A resulted in almost 3500 lbs additional fuel is needed due to the increment of structural weight. The equivalent fuel

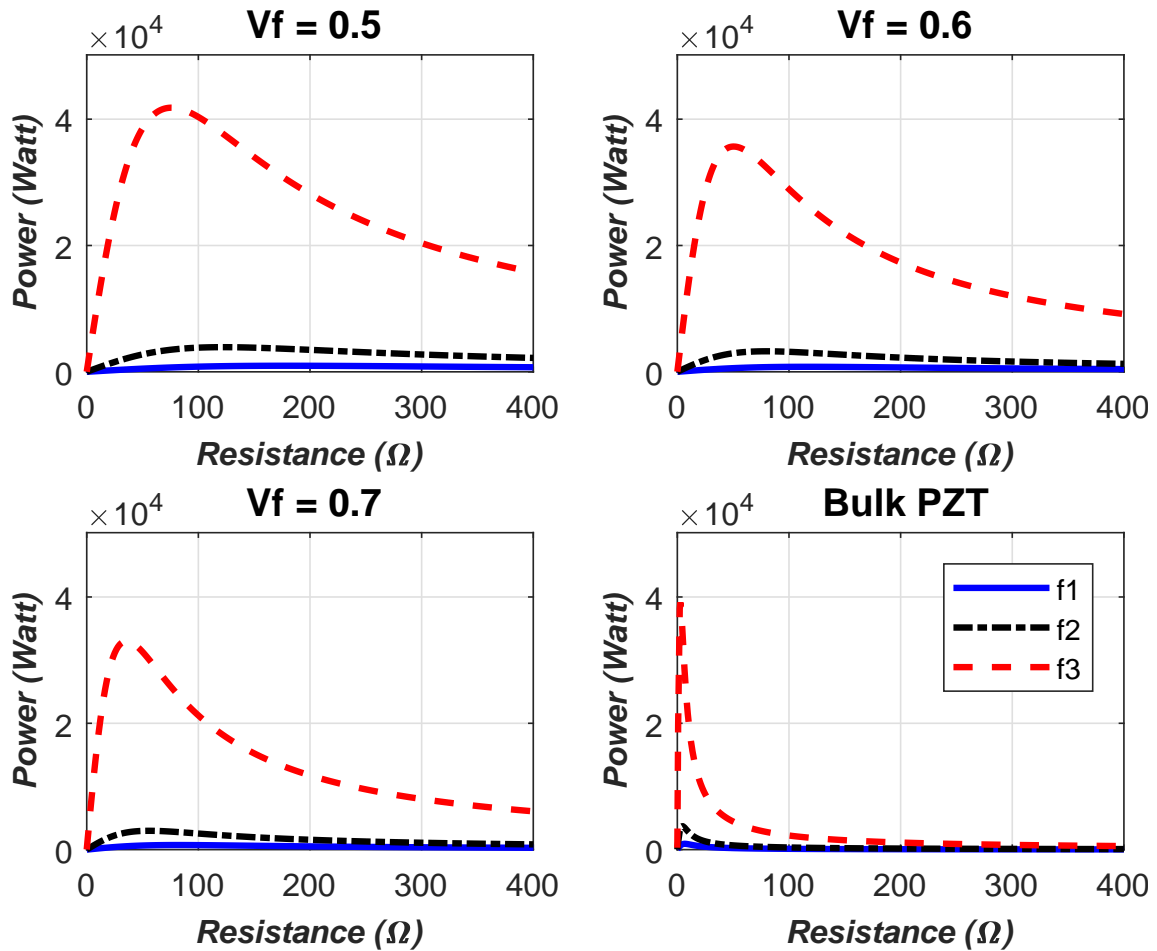


Figure 6.5: Variation of power amplitude to the resistance load for wingboxes with multiphase composite skin, Vf 50%, 60% & 70% at AR 0.2 and bulk PZT skin

saving from the power harvested even unable to overcome the effect of this increasing weight. Hence, the total addition of fuel around 3300-3500 lbs is required. However, the structural weight can be reduced significantly by substituting the bulk PZT with the multiphase composites.

Table 6.10 depicts the fuel saving evaluation by applying the multiphase composites. The fuel weight due to structural changes is reduced. The composite with Vf 50% and AR 0.2 gives the largest total fuel saved. The aircraft weight is lighter. Thus, it saves the fuel weight by almost 100 lbs due to the reduction in the structural weight. In addition, the equivalent fuel saving up to 240 lbs can be achieved. Hence, the total fuel saved is around 340 pounds and it is more than sufficient to support 1 hour APU operation.

Based on the results depicted in Table 6.10, a composite with large aspect ratio and volume fraction is not beneficial for aircraft operation as it may require more fuel. The composite with Vf 50% and AR 0.6 resulted in the heaviest structure, hence, it needs the most fuel. However, a large volume fraction may be optimised with small

Table 6.8: Maximum Power Amplitude and Resistance Load at Maximum Power of The Wingbox for Different Multiphase Composite Composition with 0.9 Frequency Ratio Excitation

Vf	AR	Max Power (kW)	R (Ω)
0.5	0.2	41.82	75.92
0.5	0.4	44.64	27.69
0.5	0.6	52.09	17.74
0.6	0.2	35.67	50.43
0.7	0.2	33.02	35.72
Bulk	PZT-5A	39.13	2.73

Table 6.9: Aircraft Fuel Saving Evaluation: Wingbox with Bulk PZT-5A Upper Skin

fr	$\Delta W_{fuel-Str}$ Structural (lbs)	P_{Ave} (kW)	$\Delta W_{fuel-Pwr}$ Power (lbs)	TOTAL ΔW_{fuel} (lbs)
0.5	+3485	0.92	- 2	+3483
0.7	+3485	3.72	- 12	+3473
0.9	+3485	39.1	-167	+3318

aspect ratio, thus, the harvested power can overcome the additional fuel weight from the structure. It is shown for the composite with Vf 60% and AR 0.2 at 0.9 frequency ratio (2.1 Hz excitation), the harvested power can overcome the additional fuel due to increasing structural weight. The total fuel saved is up to 120 lbs with this configuration, equivalent with 45% fuel needed for the APU operation. Moreover, a larger volume fraction may also be beneficial to add the structural strength.

6.5 Summary

A new investigation on the implementation of the multiphase composites for energy harvesting purpose has been conducted. In this chapter, analyses on the utilisation of different composite configurations for energy harvesting from aircraft wingbox has been presented. The results depict that a similar range of power to the bulk piezoelectric material is achievable via the multiphase composites.

A procedure to evaluate the trade-off between the energy harvested, aircraft weight and fuel has also been proposed. This procedure is beneficial in terms of the aircraft design process to establish a sense of the energy harvester design for the aircraft structure. The harvested power is associated with the fuel consumed for an APU operation. The results from the fuel-saving evaluation pointed out that the multiphase composites

Table 6.10: Aircraft Fuel Saving Evaluation: Wingbox with PZT-5A - Carbon - LaRC-SI Composite Upper Skin

Vf	AR	f_r	$\Delta W_{fuel-Str}$ (lbs)	P_{Ave} (kW)	$\Delta W_{fuel-Pwr}$ (lbs)	TOTAL ΔW_{fuel} (lbs)
		0.5	- 96	0.96	- 3	- 99
50%	0.2	0.7	- 96	3.90	- 18	- 114
		0.9	- 96	41.8	-244	- 340
		0.5	+476	1.05	- 3	+473
50%	0.4	0.7	+476	4.24	- 17	+362
		0.9	+476	44.6	-235	+241
		0.5	+886	1.28	- 3	+883
50%	0.6	0.7	+886	5.26	- 18	+868
		0.9	+886	52.1	-242	+644
		0.5	+ 97	0.79	- 3	+ 94
60%	0.2	0.7	+ 97	3.25	- 16	+ 81
		0.9	+ 97	35.7	-219	- 122
		0.5	+290	0.72	- 3	+287
70%	0.2	0.7	+290	2.98	- 14	+276
		0.9	+290	33.0	-205	+ 85

may result in the addition or reduction of the fuel required in the aircraft.

A composite with large volume fraction and aspect ratio may result in a dominant structural weight increment; hence, even the harvested power could not overcome this shortcoming. In contrast, a smaller volume fraction and aspect ratio is lighter and may still produce a similar level of power. Thus, the multiphase composites not only generate electrical energy but also construct a lightweight structure.

However, it is important to note that the assumption of load here, as previously discussed in Chapter 4, may only be applicable at an extreme and rare case. In practical condition, the oscillation happens during cruise flight may happen due to gust or turbulence, which normally does not sustain a continuous and similar level of amplitude. Moreover, some peaks of the disturbance, may only occur at a few occasions during the flight. Aerodynamic and structural coupling (aeroelastic condition) may also need to be considered to model a more realistic flight environment. A more advanced scheme, so-called iterative FEM, is discussed in Chapter 7. This iterative FEM scheme is used to address the aeroelastic coupling on a lifting structure concerning piezoelectric energy harvesting effect. Furthermore, in Chapter 8 the application of this iterative FEM to a similar wing under cruise and gust loads is discussed.

Chapter 7

Iterative Finite Element Method for Piezoelectric Energy Harvesting

In this chapter, a novel iterative finite element method (FEM) for energy harvesting purpose is presented. The development of this iterative FEM is purposed for further evaluation of the energy harvesting potential from the aircraft wing. Hence, aerodynamic loading and aero-structure coupling (aeroelasticity) are concerned. This iterative FEM may serve as a higher fidelity approach to verify the results from the hybrid computational/analytical scheme.

In this iterative FEM, the electromechanical coupling in the governing piezoelectric energy harvesting equation is separated into two parts. One part is an actuator-like problem and can be evaluated with ease via commercial software. The solution of the other part, for voltage generation, is obtained straightforward utilising the structural response of the earlier part. Hence, aero-structure and electro-mechanical couplings are evaluated. These two parts are solved iteratively until the convergence in voltage and structural responses is reached.

The new iterative FEM is implemented to solve the dynamic problems of piezoelectric-based energy harvester in the frequency and time domains. The frequency-domain scheme can be applied for a harmonic oscillation motion. Whereas the time-domain scheme can be used for much broader time-dependent cases. The application of the present iterative FEM to evaluate the piezoelectric energy harvesting of lifting structures under an aeroelastic condition, i.e., gust load, is shown in some details. The validation against other methods from the literature shows the robustness and capabilities of the iterative FEM.

Some works and results presented in this chapter are parts of the author's published works in *Composite Structures*, Volume 219, 2019.

7.1 The coupled electro-mechanical equations

In the present work, the piezoelectric electromechanical equilibrium in a dynamic problem is concerned. The governing equation of a coupled mechanical - electrical actuation problem for piezoelectric finite elements [97] is modified to obtain the energy harvesting solution. This actuation problem can be written as follows

$$\begin{bmatrix} \mathbf{M} & \mathbf{0} \\ \mathbf{0} & \mathbf{0} \end{bmatrix} \begin{Bmatrix} \ddot{\mathbf{U}} \\ \ddot{\mathbf{V}} \end{Bmatrix} + \begin{bmatrix} \mathbf{G} & \mathbf{0} \\ -\mathbf{K}_{\mathbf{vu}} & \mathbf{K}_{\mathbf{vv}} \end{bmatrix} \begin{Bmatrix} \dot{\mathbf{U}} \\ \dot{\mathbf{V}} \end{Bmatrix} + \begin{bmatrix} \mathbf{K}_{\mathbf{uu}} & \mathbf{K}_{\mathbf{uv}} \\ \mathbf{0} & \mathbf{0} \end{bmatrix} \begin{Bmatrix} \mathbf{U} \\ \mathbf{V} \end{Bmatrix} = \begin{Bmatrix} \mathbf{F} \\ \dot{\mathbf{Q}} \end{Bmatrix} \quad (7.1)$$

The sizes of the matrices in Equation (7.1) are defined by the number of degrees of freedom in mechanical, n_m , and electrical, n_e , domains [10]. The first and second derivatives with respect to the time are denoted by the dot, $[\dot{\quad}]$, and the double dots, $[\ddot{\quad}]$. Here, \mathbf{U} ($n_m \times 1$), \mathbf{V} ($n_e \times 1$), \mathbf{F} ($n_m \times 1$) and $\dot{\mathbf{Q}}$ ($n_e \times 1$), respectively, are the global nodal displacement, electrical voltage, mechanical force and electrical current vectors of the element. \mathbf{M} ($n_m \times n_m$) and \mathbf{G} ($n_m \times n_m$) represent the global mass and mechanical damping matrices. The global stiffness and damping matrices concerning the electromechanical system are denoted by $\mathbf{K}_{\mathbf{uu}}$ ($n_m \times n_m$), $\mathbf{K}_{\mathbf{uv}}$ ($n_m \times n_e$), $\mathbf{K}_{\mathbf{vu}}$ ($n_e \times n_m$) and $\mathbf{K}_{\mathbf{vv}}$ ($n_e \times n_e$). These global matrices are assembled from the associated element's matrices as follows [98]

$$\mathbf{K}_{\mathbf{uu}}^e = \int_{Vol} \mathbf{B}^T \mathbf{C} \mathbf{B} dVol \quad (7.2)$$

$$\mathbf{K}_{\mathbf{vv}}^e = \int_{Vol} \mathbf{B}_{\mathbf{E}}^T \boldsymbol{\varepsilon}^S \mathbf{B}_{\mathbf{E}} dVol \quad (7.3)$$

$$\mathbf{K}_{\mathbf{uv}}^e = \int_{Vol} \mathbf{B}^T \mathbf{e}^T \mathbf{B}_{\mathbf{E}} dVol \quad (7.4)$$

$$\mathbf{K}_{\mathbf{vu}}^e = \int_{Vol} \mathbf{B}_{\mathbf{E}}^T \mathbf{e} \mathbf{B} dVol \quad (7.5)$$

$$\mathbf{M}^e = \int_{Vol} \mathbf{N}^T \rho \mathbf{N} dVol \quad (7.6)$$

Equations (7.2-7.6) represent the element's volume integral of the electro-elastic properties of the material. The density of the material is defined as ρ . The superscript e denotes the matrix of an element. The structural stiffness matrix, $\mathbf{K}_{\mathbf{uu}}^e$, is constructed from the elasticity matrix. Whereas $\mathbf{K}_{\mathbf{vv}}^e$ is the capacitance of the piezoelectric element. The electromechanical coupling of the piezoelectric element is represented by $\mathbf{K}_{\mathbf{uv}}^e$ and $\mathbf{K}_{\mathbf{vu}}^e$ matrices. \mathbf{B} and $\mathbf{B}_{\mathbf{E}}$ involves the shape functions, \mathbf{N} , of the element based on the type of discretisation [99]. In the present work, the poling of the piezoelectric layer is assumed in the thickness direction. Hence, the component inside the integral of Equation (7.3) can be expressed as [10]

$$\mathbf{B}_E^T \boldsymbol{\varepsilon}^S \mathbf{B}_E = \frac{\varepsilon_{33}^S}{h^2} \quad (7.7)$$

In the present work, the polling of the piezoelectric layer is assumed in the thickness direction. In addition, the piezoelectric materials usually manufactured as a thin plate and sandwiched between very thin and conductive electrodes. Therefore, if the continuous electrodes are used on the whole surfaces, all elements can be assumed to generate the same voltage. Thus, vector \mathbf{V} reduces to a voltage V [10]. Hence,

$$\mathbf{K}_{uv} \mathbf{V} = \mathbf{K}_{uv} [1 \ 1 \dots 1]^T V = \mathbf{K}_{uv}^* V \quad (7.8)$$

where the size of the ones vector $[1 \ 1 \dots 1]^T$ is $n_e \times 1$, and the electromechanical coupling is now defined by the vector \mathbf{K}_{uv}^* ($n_m \times 1$).

To modify the actuation problem in Equation (7.1), the current, $\mathbf{I} = \dot{\mathbf{Q}}$, is defined not as an input, but, as the function of the voltage output from the piezoelectric harvester. The electrical load, however, comes from an external circuit connected to the structure as shown in Figure 3.7. In the present work, the resistance load, R , is applied as the the electrical load, thus, $\dot{\mathbf{Q}} = -\frac{V}{R}$. Therefore, Equation (7.1) can be written as

$$\mathbf{M}\ddot{\mathbf{U}} + \mathbf{G}\dot{\mathbf{U}} + \mathbf{K}_{uu}\mathbf{U} = \mathbf{F} - \mathbf{K}_{uv}^* V \quad (7.9)$$

, and

$$-\mathbf{K}_{vu}^* \dot{\mathbf{U}} + K_{vv} \dot{V} + \frac{V}{R} = 0 \quad (7.10)$$

where vector $\mathbf{K}_{vu}^* = \mathbf{K}_{uv}^{*T}$ and K_{vv} is the capacitance of the piezoelectric layer.

The idea of the present iterative FEM is to obtain the solution of the displacement vector \mathbf{U} of the structure and the voltage output, V , of the piezoelectric layer through an iterative process between Equations (7.9) and (7.10). This iteration process allows Equation (7.9) to be separately solved as if it is an "actuation" problem with the mechanical force, \mathbf{F} , and the voltage, V , as the actuating load to deform the structure. In the iteration process, Equation (7.10) will update the value of the voltage V on each iteration based on the displacement vector solved by Equation (7.9). A more detailed algorithm of the present iterative FEM is described in Section 7.2. In addition, the harvested power, P , is expressed as

$$P = \frac{V^2}{R} \quad (7.11)$$

For a harmonic oscillation motion, the displacement, voltage and force are assumed as the function of an excitation frequency, ω (rad/s) and can be written as

$$\begin{aligned} \mathbf{U} &= \bar{\mathbf{U}} e^{i\omega t} \\ \mathbf{F} &= \bar{\mathbf{F}} e^{i\omega t} \\ V &= \bar{V} e^{i\omega t} \end{aligned} \quad (7.12)$$

where $i = \sqrt{-1}$ and the bar above a parameter denotes the amplitude. Hence, Equations (7.9) and (7.10) become

$$-\omega^2 \mathbf{M} \bar{\mathbf{U}} + \mathbf{K}_{uu} \bar{\mathbf{U}} = \bar{\mathbf{F}} - \mathbf{K}_{uv}^* \bar{\mathbf{V}} \quad (7.13)$$

$$\bar{\mathbf{V}} = \frac{i\omega \mathbf{K}_{vu}^* \bar{\mathbf{U}}}{i\omega K_{vv} + \frac{1}{R}} \quad (7.14)$$

Therefore, in this case, the iteration process will involve Equations (7.13) and (7.14).

7.2 Computational scheme

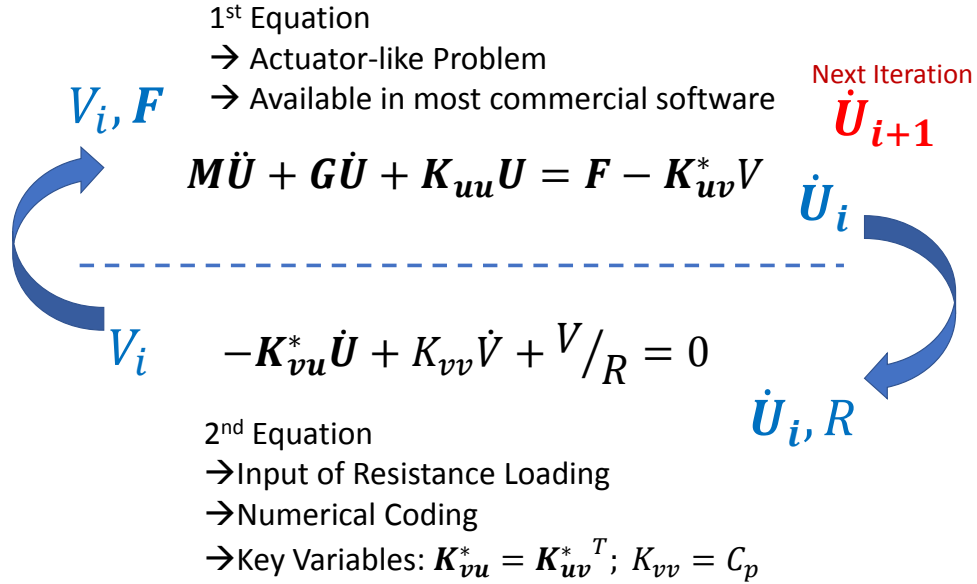


Figure 7.1: Illustration of the iterative FEM process

In the present iterative FEM, one of the unique features is the seclusion of Equation (7.9) to be solved as if it is an actuator problem. Figure 7.1 depicts the illustration of the iterative FEM process based on Equation (7.9) and Equation (7.10). The actuator problem is already a matured problem in the structural analysis field, and the module is readily available in many commercial finite element software, i.e., Abaqus, Ansys, MSC Nastran [100]. Therefore, the present iterative FEM provides excellent ease for utilising the standard commercial software. In addition, Equation (7.10) can be solved with minimum computational coding.

Moreover, the ease of solving Equation (7.9) via an already established computational software is that the mechanical force, \mathbf{F} , may have a wide range of form, i.e., concentrated force, pressure, relative motion, or combination of several load types.

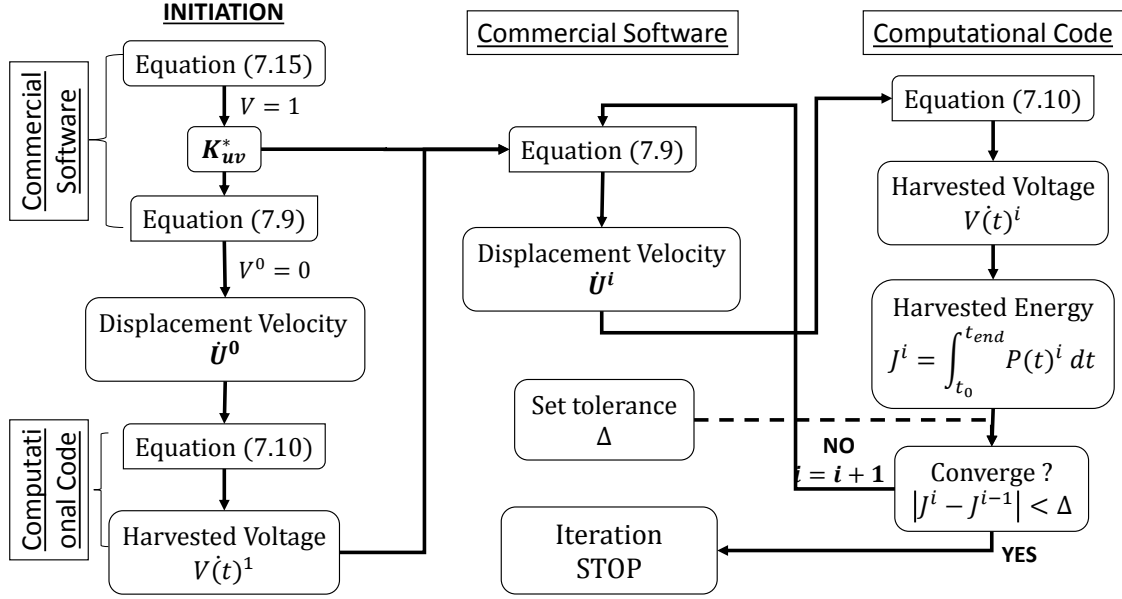


Figure 7.2: The algorithm of the iterative FEM for a time domain problem

Sections 7.3-7.6 present the works which demonstrate the implementation of base excitation motion and unsteady aerodynamic loads as the mechanical force. Moreover, the mechanical damping, \mathbf{G} , can also be modelled with various form [79], i.e., proportional to the structural stiffness matrix (structural damping), the linear combination of structural mass and stiffness matrix (Rayleigh damping), the function of natural frequency (modal damping).

However, it is worth to note that the procedure to solve the electromechanical problem for energy harvesting as depicted in Equations (7.9) and (7.10) is not limited to the present iterative process. Most notably, concerning unsteady aerodynamic loading, several works in [13, 24] solved the aeroelastic and electromechanical coupling by constructing a state-space matrix; thus, iterative process was not required. Despite this fact, their procedures require more elaborated effort in computational coding, i.e., numerical codes to evaluate the structure (FEM), unsteady aerodynamic and piezoaeroelastic coupling. Moreover, the selection of elements were limited to beam and planar (3-DoF) elements [13, 24].

Meanwhile, in the present iterative scheme, the need of computational code is minimum. The choice to maximise the utilisation of the commercial software is due to the focus of the present research which as a jet aircraft wing. This type of wing is much more complex and larger structure compared to the lifting structures evaluated in [13, 24]. Hence, it is expected that the construction of elements, aerodynamic loads and the aero-structure coupling could be handled by the commercial software with only concern on the computational coding is to incorporate the electromechanical effect.

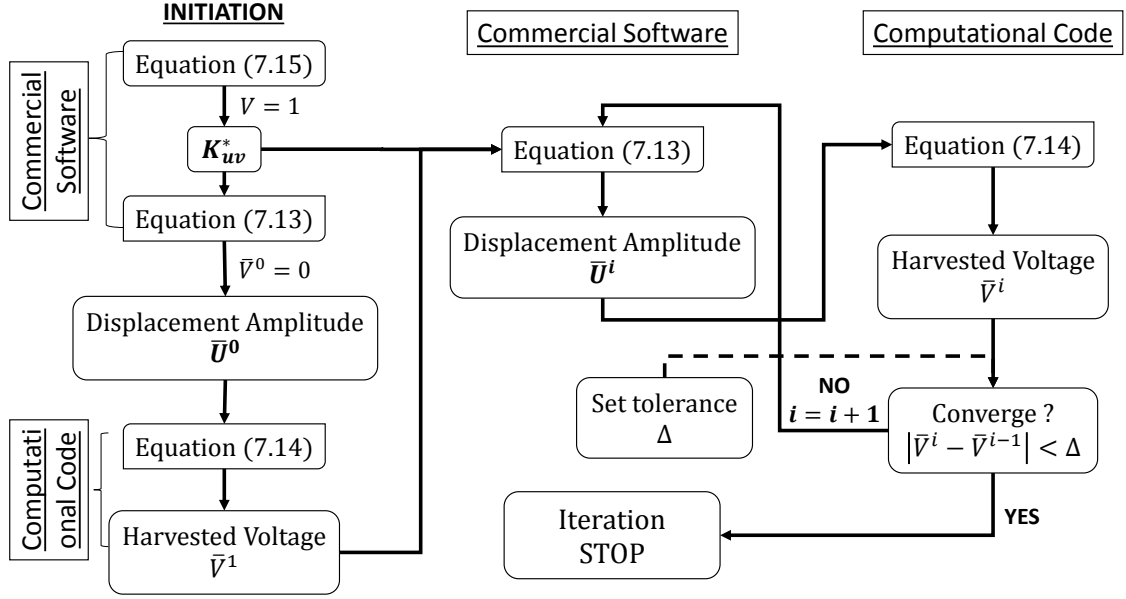


Figure 7.3: The algorithm of the iterative FEM for a frequency domain problem

Prior to entering the iteration process, one essential parameter to be obtained is the electromechanical coupling vector, K_{uv}^* . This vector can be extracted from the commercial software by solving first a dummy static actuator simulation with a unit voltage load, i.e., 1V, and no mechanical load. In the case of static analysis, Equation (7.9) reduces into

$$\mathbf{K}_{uu}\mathbf{U} = -\mathbf{K}_{uv}^*V \quad (7.15)$$

Hence, the commercial software will calculate a forcing vector on the nodes only as a function of \mathbf{K}_{uv}^* . This forcing vector can usually be found in the input file created by the software. To be noted, however, the negative sign on the right-hand side (RHS) of Equation (7.15) represents the internal force generated by the reverse piezoelectric effect. Therefore, as the commercial software treats the RHS as an external actuating force, the negative sign needs to be added to the extracted forcing vector or the input voltage of the software. This rule also applies when applying the voltage to the software during the iteration process.

In some software, electrical actuator solution is evaluated via the thermal actuator analogy [100]. The thermal expansion coefficient vector, α , is used to represent the piezoelectric charge constants, \mathbf{d} . Concerning the thermal forcing function, the analogy can be seen as follows [97]

$$\mathbf{RHS}_{\text{thermal}} = \int_{Vol} \mathbf{B}^T \mathbf{C} \alpha^T T dVol \quad (7.16)$$

$$\mathbf{K}_{uv}^*V = \int_{Vol} \mathbf{B}^T \mathbf{C} \tilde{\mathbf{d}}^T E dVol \quad (7.17)$$

where the electrical field is $E = V/h$ and the piezoelectric charge constants matrix \mathbf{d} (3×6) is collapsed to the vector $\tilde{\mathbf{d}}$ (1×6). This vector is expressed as

$$\tilde{\mathbf{d}}^T = [d_{31} \ d_{32} \ d_{33} \ 0 \ 0 \ 0]^T \quad (7.18)$$

which analogous to the thermal expansion coefficient vector as

$$\boldsymbol{\alpha}^T = [\alpha_1 \ \alpha_2 \ \alpha_3 \ \alpha_4 \ \alpha_5 \ \alpha_6]^T \quad (7.19)$$

Hence, in the case thermal actuator module is used, the piezoelectric charge constants per layer thickness are input as the thermal expansion coefficients, i.e., $d_{31}/h = \alpha_1$, and the voltage as the temperature, i.e., $V = T$, to the commercial software.

The algorithm of the time-domain iterative FEM is depicted in Figure 7.2. In the present work, the computational code to solve Equation (7.10) is built using MATLAB[®]. The ordinary differential equation (ODE) solver of MATLAB[®] is used to obtain the solution of $V(t)$ for each iteration. The iteration procedure can be described as follows:

1. Initially, Equation (7.9) is solved in the commercial software by assuming no voltage applied, $V^0 = 0$.
2. The initial value of velocity vector, $\dot{\mathbf{U}}^0$, is then used as input to the computational code to obtain the first solution of the harvested voltage, $V(t)^1$, via Equation (7.10).
3. This first solution, $V(t)^1$, is input to Equation (7.9) to obtain the new velocity vector of iteration.
4. This new velocity vector then inputs again to solve Equation (7.10). This process is repeated until the solution is converged.

In the present work, the convergence criteria for the time domain simulation is based on the variance of energy from the current iteration and the previous iteration, $J^i - J^{i-1} < \Delta$. In addition, the trend of the voltage function, $V(t)$, is also observed to ensure that the patterns are similar and in reasonable shape on each iteration.

The iteration process for the frequency domain is shown in Figure 7.3. In this case, Equations (7.13) and (7.14) are the main governing equations. In addition, the iterative variables for the frequency domain case are the amplitudes, $\bar{\mathbf{U}}$ and \bar{V} . Hence, the convergence criteria is also much simpler by comparing the variance of the voltage from each iteration, $V^i - V^{i-1} < \Delta$.

Appendices E and F show the examples of code to perform the frequency-domain and time-domain analyses. Both codes have similar segments to extract the data from

a commercial software to construct the coupling matrix, \mathbf{K}_{uv} , and the displacement amplitude vector, $\bar{\mathbf{U}}$, or the velocity vector, $\dot{\mathbf{U}}$. The frequency-domain code, as shown in Appendix E, calculates the voltage amplitude based on Equation (7.14). Meanwhile, the time-domain code, as depicted in Appendix F evaluates the voltage based on Equation (7.10).

In the present work, the commercial software used is MSC Nastran[©]. It can be seen in Appendices E and F, there are segments written for exchanging data between the codes and the commercial software for each iteration. The displacement vector or velocity vector is obtained from the analysis of dynamic responses via MSC Nastran[©]. The iterative process involves offline files exchange between the inputs and outputs from the code and the software. Appendix K depicts an example of input for gust analysis performed via MSC Nastran[©]. This Nastran input is used for the jet wingbox analysis presented in Chapter 8. The set of voltage input shown in Appendix K is obtained from the calculation performed in Appendix F. An example of velocity vector output from MSC Nastran[©] is shown in Appendix L. This data of velocity vector is used as input to the code in Appendix F.

7.3 Unimorph plate under base excitation

In this section, the energy harvesting evaluation of a unimorph exerted by base excitation is presented in [21]. The iterative FEM for frequency and time domain is utilised. Comparison against the result of Erturk-Inman's analytical model [21] is also shown in some details.

The unimorph plate consisted of a host structure (isotropic metal) and a piezoelectric layer (PZT-5A) covering the top surface of the plate similar to the configuration shown in Figure 3.7. The size of the plate is $100 \times 20 \times 0.9 \text{ mm}^3$ (length \times width \times thickness), with PZT covering 44% of the thickness. The details of the material properties for a beam-type formulation can be found in [21]. However, as solid and shell elements are used here, the 3D and 2D material properties of PZT-5A in [101] are utilised.

The verification of the unimorph structural models is performed using modal analysis. The unimorph is modelled by 25×5 elements, in the spanwise and the chordwise directions, respectively. For a solid model, each layer on thickness direction is made of their own respective material (PZT or metal). However, for the shell model, the laminated composite module is used to represent the lay-up sequence.

The natural frequencies and the mode shapes of the present structural models are depicted in Table 7.1. The results of Erturk-Inman's analytical model is displayed in the column "Analytical", while the present models' are shown in columns "Present-Solid"

and "Present-Shell". The first, second and third bending modes are denoted by "1B", "2B" and "3B", respectively. It can be seen that both solid and shell models natural frequencies are in a good agreement against analytical results in [21] with insignificant variances, $\Delta \leq 1\%$.

Table 7.1: Natural frequency comparison of the unimorph

Mode Shape	Natural Frequency (Hz)				
	Analytical [21]	Present - Solid	Δ	Present - Shell	Δ
1B	47.8	47.8	0.00%	47.5	0.63%
2B	299.6	299.3	0.10%	296.9	1.00%
3B	838.2	841.1	0.35%	831.9	0.75%

In the frequency domain investigation, $1\mu\text{m}$ amplitude of vertical displacement is applied at the root as the base excitation load. The excitation frequency is equal with the first bending natural frequency. Resistance load of $15\text{ k}\Omega$ is used as the external electrical load. As previously explained in Section 7.2, initially a pure structural dynamic response without voltage load is performed to start the iteration process. Following the iterative procedure in Section 7.2, on each iteration step, the voltage output and the structural responses are updated.

The voltage and relative tip amplitudes on each iteration step for both solid and shell models are depicted in Figures 7.4 and 7.5. The dotted line with green circles denote the results of the iterative FEM on each iteration step. The references' values denoted by the straight red line and the black dashed line are obtained via Erturk-Inman model [21] and the present hybrid analytical/computational scheme. However, with the hybrid scheme, only the voltage amplitude can be compared as the structural displacement after affected by voltage response could not be obtained from this approach.

It can be seen in Figures 7.4a and 7.5a, initial value of voltage amplitude, \bar{V} , is zero. This condition resulted in a pure mechanical structural response with relative tip displacement, \bar{Z}_{rel} , around 0.08 mm as depicted in Figures 7.4b and 7.5b. The first iteration updated these values with the existence of voltage output and a much lower tip displacement around 0.03 mm . The iteration histories shown in Figures 7.4 and 7.5 display the fluctuation on both voltage and tip displacement amplitudes around the references' values until they converge to some particular points.

The fluctuation happens as the electromechanical coupling tries to balance the responses exerted by the mechanical load and the reverse piezoelectric effect. Initially, a small voltage at an iteration step, i , resulted in a large displacement caused mainly by the mechanical load, $Z_{mech}^i \gg Z_{elec}^i$, hence, $Z_{total}^i \approx Z_{mech}^i$. However, large

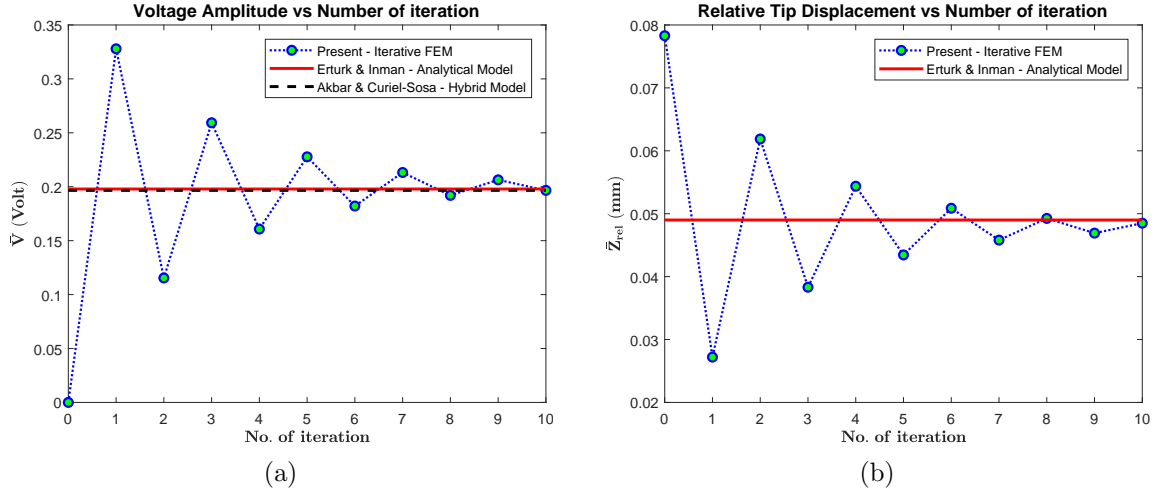


Figure 7.4: The iteration histories of (a) voltage and (b) relative tip displacement amplitudes of the unimorph modelled by solid elements

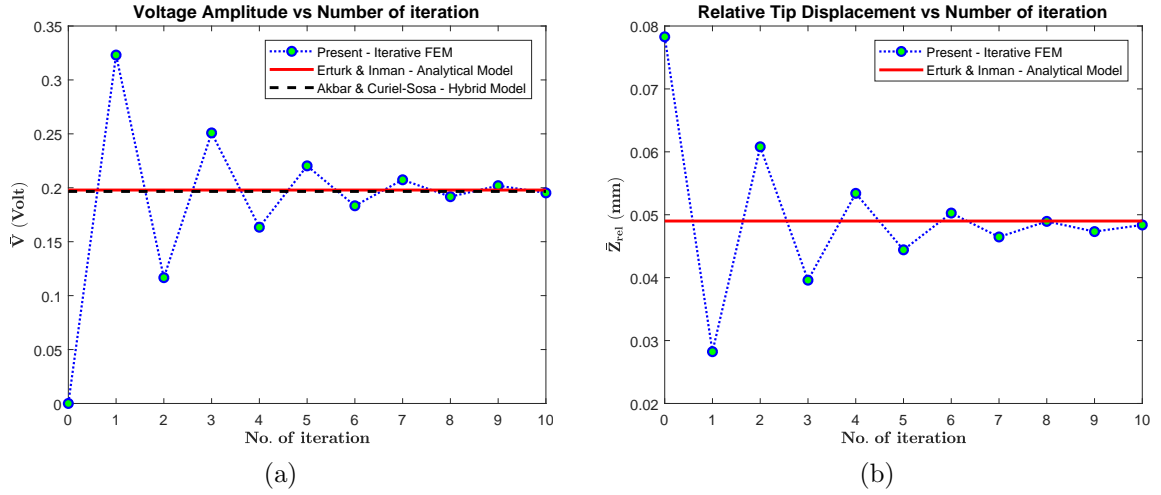


Figure 7.5: The iteration histories of (a) voltage and (b) relative tip displacement amplitudes of the unimorph modelled by shell elements

displacement means a larger voltage as the input for the next iteration, $i + 1$. Hence, the displacement due to electrical load will be larger, $Z_{elec}^{i+1} > Z_{elec}^i$. Due to reverse piezoelectric effect as explained in Section 7.2, as Z_{elec} is in the opposite direction of Z_{mech} , thus, the total displacement is reduced, $Z_{total}^{i+1} < Z_{total}^i$. On the next iteration, however, this means smaller voltage, hence, $Z_{elec}^{i+2} < Z_{elec}^{i+1}$, and $Z_{total}^{i+2} < Z_{total}^{i+1}$. The iteration process will go on in this cycle until the total displacement is consisted of proper amounts of Z_{elec} and Z_{mech} .

In more details, the iteration histories are shown in Tables 7.2 and 7.3. Initially, the iteration variances are more than 60% for both voltage and displacement amplitudes. However, only with ten iteration steps, the iteration variances significantly reduce to less than 5%. Table 7.4 depicted in detail the comparison of the present iterative fem

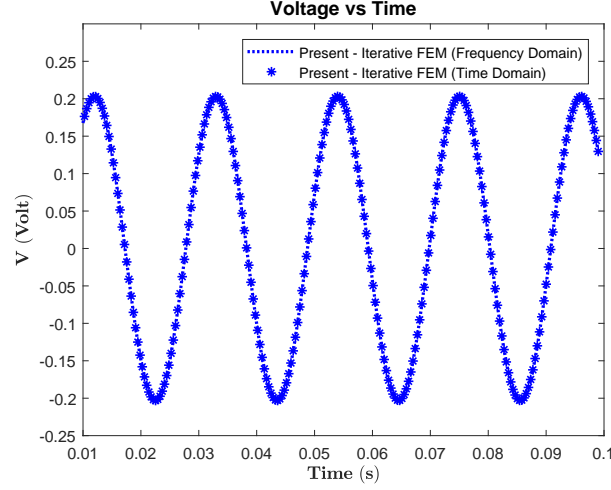


Figure 7.6: The voltage output time history of the unimorph modelled by solid elements

results with the references' values. The present results for both solid and shell models are in close comparison to the references' with variances only around 1%.

Table 7.2: Voltage amplitude for each iteration of the unimorph modelled by solid elements

Iteration	\bar{V} (Volt)	Variance
1	0.3279	
2	0.1154	$\Delta_{1-2} = 64.80\%$
9	0.2064	
10	0.1966	$\Delta_{9-10} = 4.75\%$

Table 7.3: Tip displacement amplitude for each iteration of the unimorph modelled by solid elements

Iteration	\bar{Z}_{rel} (mm)	Variance
0	0.0783	
1	0.0272	$\Delta_{0-1} = 65.26\%$
9	0.0469	
10	0.0485	$\Delta_{9-10} = 3.30\%$

For iterative FEM simulation in the time domain, the input of vertical displacement at the root is given at each time step following the harmonic oscillation motion, $Z(0, t) = \bar{Z}(0)e^{i\omega t}$. In the present case, a tabular input of the root displacement with 0.1 ms time step is applied. As explained in Section 7.2, in the time domain scheme, the voltage and velocity responses for each time step are updated on each time step. As expected, the final iteration results of the time domain scheme closely follow the

Table 7.4: Voltage and relative tip displacement amplitudes comparison of the uni-morph

Parameter	Erturk - Inman	Hybrid Scheme	Iterative FEM - Solid	Iterative FEM - Shell
\bar{V} (Volt)	0.1979	0.1966 $\Delta=0.66\%$	0.1966 $\Delta=0.66\%$	0.1952 $\Delta=1.36\%$
\bar{Z}_{rel} (mm)	0.0490	-	0.0485 $\Delta=1.02\%$	0.0484 $\Delta=1.22\%$

trend of the frequency domain's as shown in Figure 7.6. The iterative FEM in the time domain is further elaborated in the following sections.

7.4 Discrete 1-cosine gust and unsteady aerodynamic loads

The energy harvesting evaluation of piezoelectric embedded lifting surfaces/structures exposed to a freestream flow and gust wind are presented in this Section 7.5 and Section 7.6. Herein, only a brief introduction of the gust loading condition is described. The interested reader on gust and aeroelasticity loads is referred to a more detailed discussion in [102]. Figure 7.7 displays a general illustration of a discrete gust wind in the form of 1-cosine gust with a gust length, L_g .

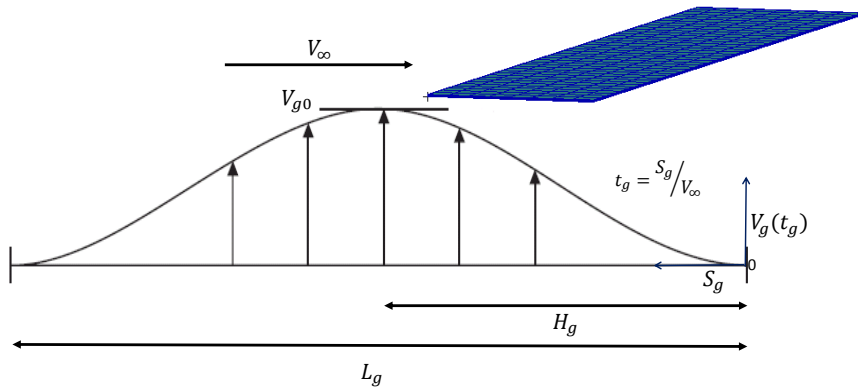


Figure 7.7: Illustration of a lifting surface exposed to a freestream flow with airspeed V_∞ and 1-cosine gust with maximum gust speed V_{g0}

In Figure 7.7, the lifting surface flies with speed, V_∞ entering the gust wind regime. The distance and time of the gust penetrating the lifting surface are denoted by S_g and t_g , respectively. The gust gradient distance, H_g , is the distance to reach the maximum gust speed, V_{g0} , in which $L_g = 2H_g$. The variation of the gust speed, V_g , to the time

t_g is defined as

$$V_g = \frac{V_{g_0}}{2} \left(1 - \cos \left(\frac{2\pi V_\infty t_g}{L_g} \right) \right) \quad (7.20)$$

To be noted, herein and hereafter, the letter V with subscripts " ∞ ", " g " and " g_0 " will be associated with speed. Therefore, it is important to note, the terms V_∞ , V_g and V_{g_0} always refer to airspeed and gust speed. Meanwhile, the terms V and \bar{V} always associated with voltage or voltage amplitude.

Evaluating Equation (7.9) in the electromechanical coupling equations, the equilibrium equation concerning the aerodynamic load due to freestream flow and gust wind can be written as

$$\mathbf{M}\ddot{\mathbf{U}} + \mathbf{G}\dot{\mathbf{U}} + \mathbf{K}_{\mathbf{uu}}\mathbf{U} = \mathbf{F}_\infty + \mathbf{F}_g - \mathbf{K}_{\mathbf{uv}}^*V \quad (7.21)$$

where \mathbf{F}_∞ and \mathbf{F}_g are the aerodynamic loads due to airspeed, V_∞ , and gust speed, V_g . Considering the coupling between the aerodynamic load and the structural deformation, \mathbf{F}_∞ can be written as the function of structural displacement, velocity and acceleration. Hence, \mathbf{F}_∞ can be written equivalent with the component of mass, damping and stiffness. Therefore, Equation (7.21) can be rearranged with the aerodynamic mass, \mathbf{M}_∞ , aerodynamic damping, \mathbf{G}_∞ , and aerodynamic stiffness, \mathbf{K}_∞ .

$$(\mathbf{M} - \mathbf{M}_\infty)\ddot{\mathbf{U}} + (\mathbf{G} - \mathbf{G}_\infty)\dot{\mathbf{U}} + (\mathbf{K}_{\mathbf{uu}} - \mathbf{K}_\infty)\mathbf{U} = \mathbf{F}_g - \mathbf{K}_{\mathbf{uv}}^*V \quad (7.22)$$

In the present work, the Doublet-Lattice Method (DLM) of Albano and Rodden [33] for subsonic flow is applied to model the aerodynamic loads acting on the lifting surface. The DLM of Albano and Rodden is a well-established approach and commonly implemented in the aircraft industries to evaluate the aeroelastic conditions for certification, i.e., flutter instability and gust loads [102]. In addition, this approach is readily available in commercial software, i.e., MSC Nastran [103].

In brief, Albano and Rodden [33] derived the aerodynamic force, \mathbf{F}_∞ , as a distributed pressure, \mathbf{p} , acting on the lifting surface. This pressure is evaluated numerically in matrix form as

$$\mathbf{p} = \mathbf{D}^{-1}\mathbf{w} \quad (7.23)$$

The DLM discretises the lifting surface into panels in which the aerodynamic forces modelled via doublets concentrated on the quarter chord line of each panel. The aerodynamic influence coefficient, \mathbf{D} , is obtained from the doublet strength of each panel and modelled as a function of the panel's geometry, location, and the flight condition. Meanwhile, the upwash velocity, \mathbf{w} , is evaluated from the structure's oscillatory mode shapes, ϕ .

$$\mathbf{w} = \frac{\partial \phi}{\partial x} + ik_r \phi \quad (7.24)$$

Thus, concerning Equation (7.24), the investigation of the mode shapes are essential to the aeroelastic evaluation. Moreover, the imaginary part of Equation (7.24) requires

the evaluation of the reduced frequency, k_r , which is defined as the ratio of excitation frequency and freestream airspeed times the lifting surface's half-chord.

7.5 Bimorph plate under gust load conditions

In this section, a plate-like wing with bimorph piezoelectric configuration in [24] is elaborated as the case study. The bimorph plate configuration is depicted in Figure 7.8. Piezoelectric layers are made of PZT-5A with each covering 30% of the length and 17% of the thickness. The host structure is made of Aluminum and sandwiched between the piezoelectric layers in the region near the root. The PZT-5A layers and Aluminum layers are represented with blue and red regions in Figure 7.8. The detailed material properties are given in [24].

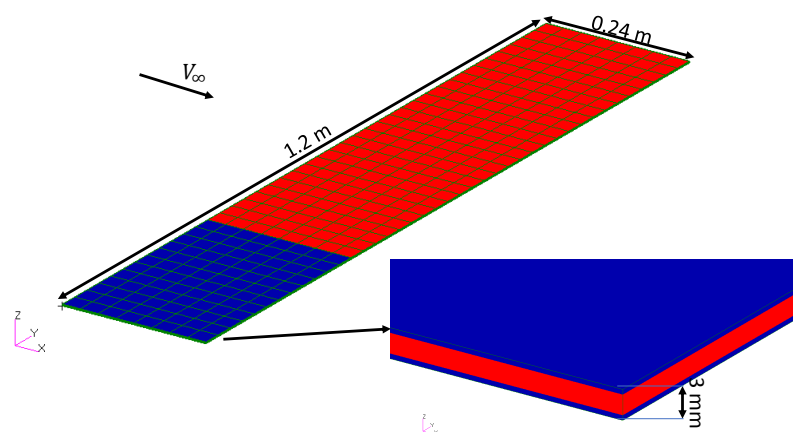


Figure 7.8: Configuration of the bimorph

The PZT-5A layers are combined in a series circuit with each poled in the thickness direction opposite to the other's. A resistance load of $10 \text{ k}\Omega$ is used to complete the electrical circuit. The whole bimorph plate is assumed as the lifting surface, exposed to a uniform freestream flow at the sea level condition with airspeed, V_∞ , parallel to the chordwise direction. The direction from the leading edge to trailing edge is defined as the x-positive direction.

Both solid and shell elements are also applied to model the bimorph plate. The solid finite element model of the bimorph is also shown in Figure 7.8. The configuration of 40×8 elements is used in spanwise and chordwise directions. The same division also applied to the shell model with the difference lies in the implementation of the laminated composite module to represent the lay-up sequence. In order to validate the structural model, the natural frequencies and mode shapes of the solid and shell models are compared against the results in [24] as depicted in Table 7.5.

Table 7.5: Natural frequency comparison of the bimorph

Mode Shape	Natural Frequency (Hz)				
	FEM [24]	Present - Solid	Δ	Present - Shell	Δ
1B	1.68	1.67	0.59%	1.66	0.60%
2B	10.46	10.43	0.29%	10.36	0.96%
1T	16.66	16.00	3.96%	15.90	4.56%
3B	27.74	27.74	0.00%	27.50	0.22%
2T	48.65	47.02	3.35%	46.67	4.07%

The present models' natural frequencies are well agreed with those obtained via full electromechanically-coupled shell elements in [24]. The variances are insignificant, varying from 0.0% to less than 5%. The bending modes are denoted by "1B", "2B" and "3B" while the torsion modes represented by "1T" and "2T". In order to evaluate aeroelastic loading condition with the freestream flow and gust wind, an unsteady aerodynamic model is coupled with the structural model.

Evaluation of the flutter instability is performed to verify the coupling of the finite elements and aerodynamic model via DLM in the present work. The results are compared with those obtained in [25] which evaluate the flutter condition of the same bimorph FEM model in [24].

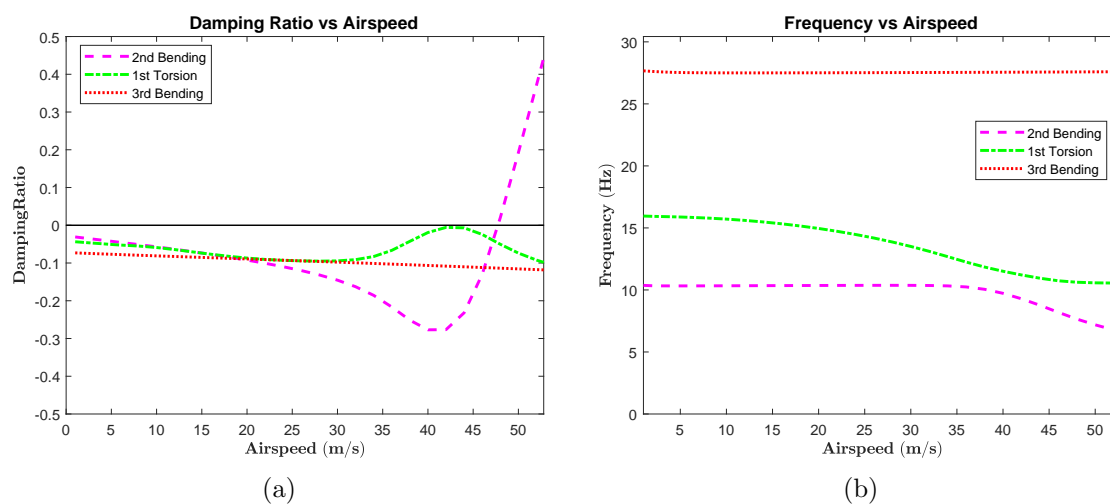


Figure 7.9: (a) Damping vs Airspeed, and (b) Frequency vs Airspeed graphs of the bimorph

Figure 7.9 displays the flutter summary of the bimorph modelled by solid elements. Five mode shapes mentioned in Table 7.5 are involved in the flutter analysis, the same as used in [25]. However, for clarity, only 3 modes are displayed in Figure 7.9. Figure 7.9a depicts the variation of the aeroelastic damping ratio to the airspeed. The damping

ratio shown here is the total damping ratio due to structural damping and aerodynamic damping. Hence, it changes with the airspeed. The consensus in aeroelasticity field is that negative damping ratio is the stable region, and the positive one is unstable.

Figure 7.9b shows the variation of the frequency of the aeroelastic system to the airspeed. Similar to the aeroelastic damping, the aeroelastic stiffness of the system also changes with the airspeed as the aerodynamic stiffness also gives addition/reduction to the structural stiffness. The critical instability point or the critical flutter speed is reached if the damping ratio of one of the modes become positive or if two or more modes' are coupled.

It can be seen in Figure 7.9a that the second bending mode crosses the positive region at around 48 m/s. However, in Figure 7.9b, the first torsion frequency is decreasing with the airspeed until it coalescences with the second bending frequency at around 40 m/s. Hence, it can be considered that the critical flutter speed is around 40 m/s. These phenomenons align with the conditions observed in [25], in which 40 m/s is the critical instability point where the second bending and the first torsion frequencies coalescence. In addition, identical conditions are also observed via the present shell model.

On the investigation presented in [24], the time-domain Vortex-Lattice Method (VLM) [32] was applied to model the aerodynamic forces. This method is a panel method similar to the DLM with the vortexes' strengths represent the aerodynamic forces. However, the VLM is a time-domain approach that is independent to the mode shapes nor modal analysis. The coupling with the structural model or FEM utilises an iterative procedure to perform a fluid-structure interaction (FSI). The information of the aerodynamic forces is transferred to structure, and the changed structural shape is passed to the aerodynamic model, and so on until the solution converges at a particular time step. It is worth to highlight, the FSI iteration involves only the structural and aerodynamic parts; thus, it is different from the present iterative scheme that is explained in Section 7.2.

A 3° angle of attack is applied to represent a vertical impulse gust [24]. This impulse gust is different from the illustration shown in Figure 7.7. The gust occurs in a very short time, i.e., the L_g is so small that the gust degenerates into an impulse as shown in Figure 7.10. Unfortunately, the detail of the total time nor time steps is not available in [24]. Hence, several time periods are tested, ranging from 0.1 ms to 0.001 ms. To be noted, 0.001 ms is the minimum tolerance of the commercial software used in this analysis. The maximum gust velocity, V_{g0} , is equal with 5.2% V_∞ considering the speed vertical component due to the 3° angle of attack. The gust speed is assumed zero at $t_g=0$ and suddenly reaches V_{g0} at a particular time, then suddenly drops to zero again.

Figure 7.11 shows the power responses for different time periods at 10 m/s airspeed

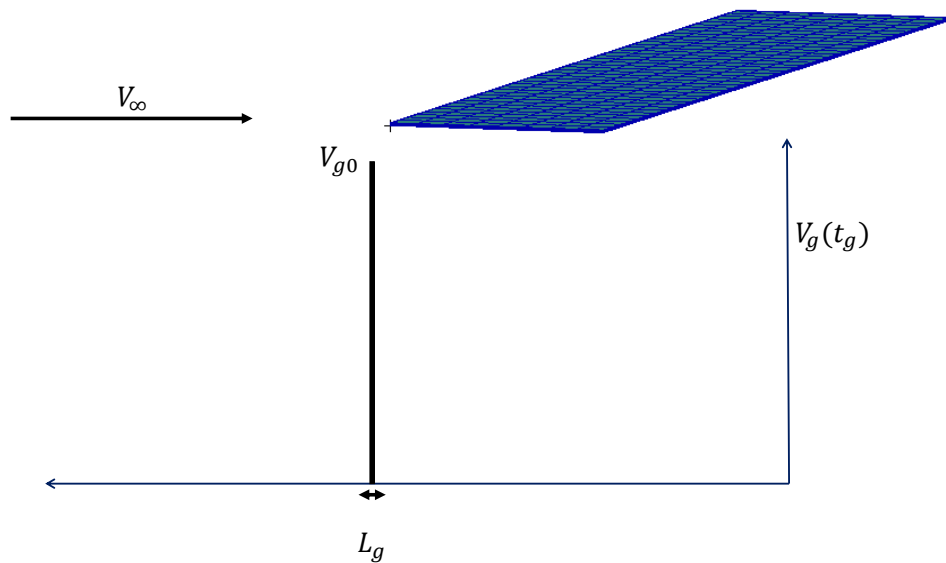


Figure 7.10: Illustration of a lifting surface exposed to a freestream flow with airspeed V_∞ and an impulse gust with maximum gust speed V_{g0}

obtained via shell elements. It is found that 0.01 ms period gives the closest results to the reference, total energy $0.0927 \mu\text{J}$ compared to $0.0865 \mu\text{J}$ in [24]. In contrast, 0.1 ms resulted in a more overestimated result, $0.0970 \mu\text{J}$, and 0.001 ms provides underestimated result with $0.0594 \mu\text{J}$. Therefore, for the current analysis, 0.01 ms is selected as the time period. Further, the comparison of the current results with the reference's is shown in Table 7.6.

Figures 7.12 and 7.13 depict time histories of the bimorph's tip displacements and harvested powers from the piezoelectric layers at 10 m/s and 30 m/s freestream conditions, respectively. The red dashed-dotted lines denote the results of De Marqui Jr. et al. [24]. The final iteration's results obtained via the present iterative FEM method by the shell and solid models are denoted by the black straight lines and the blue dotted lines. The iterative processes for both models rapidly converge in less than five iterations as the harvested voltages do not greatly affect the structural responses. This phenomenon aligns with the results in [24], in which the structural responses from the range of short circuit to open circuit are identical. Thus, showing that the displacement due to mechanical load is much more dominant than the one exerted by the electrical load.

The computational simulations are done via a standard office laptop with Intel Core i7 2.4 GHz and 4GB RAM. Less than 5 minutes are required for the aeroelastic evaluation and around 2-3 minutes for the electromechanical evaluation in MATLAB. Adding a couple of minutes for text editing of the aeroelastic result data to MATLAB,

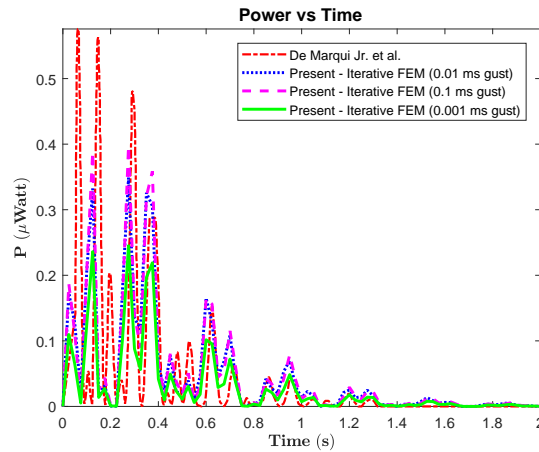


Figure 7.11: Time histories of the power output of the bimorph at 10 m/s airspeed for different gust period

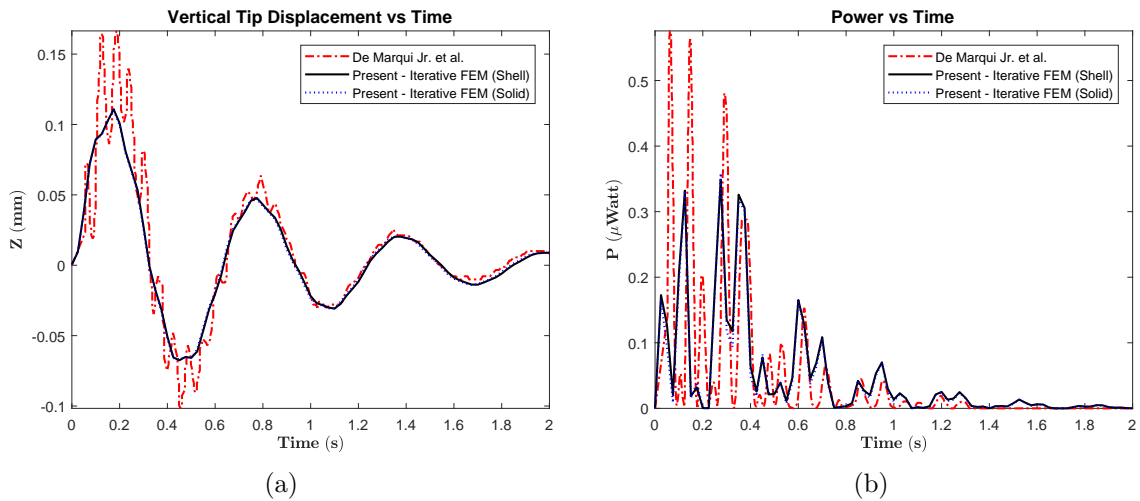


Figure 7.12: Time histories of (a) the tip displacement and (b) the power output of the bimorph at 10 m/s airspeed

in general, less than 10 minutes are needed for one iteration. Hence, for five iterations, the overall simulations to reach convergence is less than 1 hour. Unfortunately, there is no comparison data from the literature for the computational time. However, it is expected that more computational effort is required to develop numerical coding from the method proposed in the literature. In addition, the present iterative FEM is more flexible in its implementation, and there is no significant change required in the computational coding to accommodate for different structural models as the only input is the output data from aeroelastic analysis.

The 10 m/s airspeed condition provides small aerodynamic loads and structural displacement. The maximum tip displacement observed in Figure 7.12a is significantly in a lower order compared to those obtained at 30 m/s in Figure 7.13a. However, as larger damping occurs at 30 m/s, the response is rapidly damped after decreasing

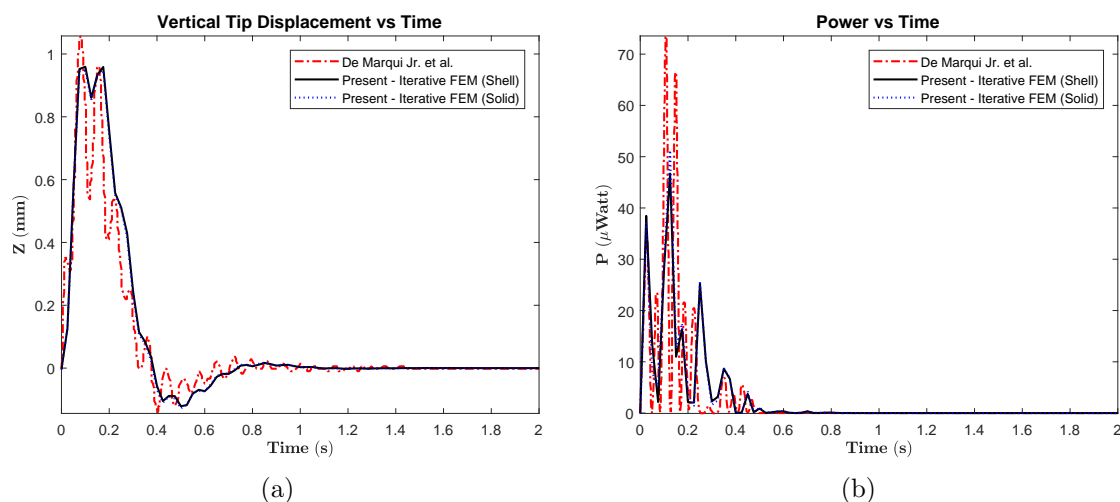


Figure 7.13: Time histories of (a) the tip displacement and (b) the power output of the bimorph 30 m/s airspeed

from the maximum point. In contrast, the one at 10 m/s still oscillating after the first maximum response, showing moderate damping of the system.

The harvested power responses are aligned with the trends of the tip displacements as shown in Figures 7.12b and 7.13b. The harvested power at 10 m/s still oscillating after the first maximum response. However, at 30 m/s, the power response quickly vanishes along with the damped structural response. The VLM simulation and both present models are all in agreement and show similar behaviours. However, it can be seen that the results of the VLM fluctuate with the time due to the FSI iterative process on each time step [32].

Table 7.6: Electrical energy comparison of the bimorph

Speed (m/s)	Energy (μJ)				
	FEM [10]	Present - Solid	Δ	Present - Shell	Δ
10	0.0865	0.0880	1.73%	0.0927	7.17%
30	5.5295	5.7258	3.55%	5.5838	0.98%

In more details, the energy harvested by the three approaches are compared in Table 7.6. Total time of 2s is used to calculate the energy harvested. The energies obtained from all approaches are in a good comparison. The present results only vary less than 10% to the results by De Marqui Jr. et al. [24], in which mostly vary between 1% to 4%. Nevertheless, for a preliminary engineering design phase, these variances are considered acceptable.

The displacement contours of the solid bimorph at $t_g = 0.175$ s are depicted in Figures 7.14a and 7.14b. At $t_g = 0.175$ s, the loads causes the maximum structural

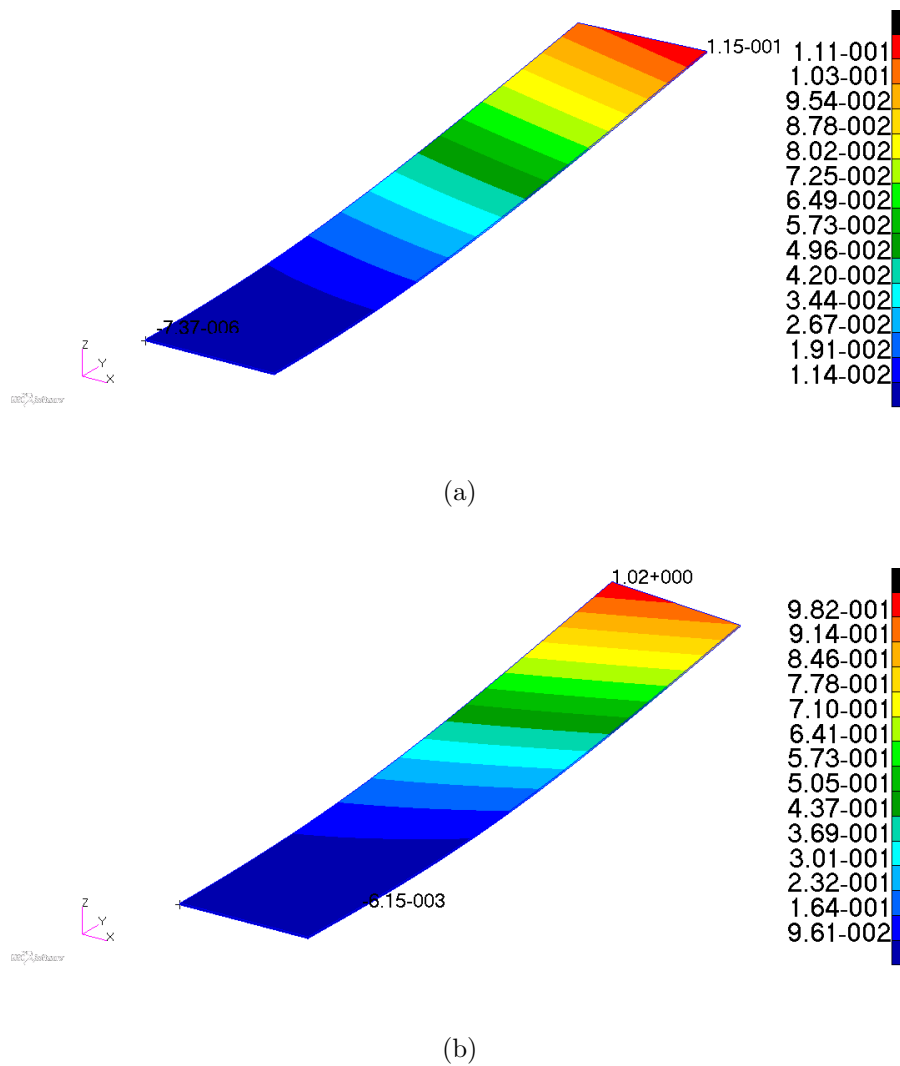


Figure 7.14: Displacement contours at $t_g = 0.175$ s of the bimorph with airspeeds (a) 10 m/s and (b) 30 m/s (displacement unit in mm)

responses for both airspeeds. It can be seen that the second bending mode is dominant in the response with a moderate effect from the torsion mode causes slight twisting to the plate.

7.6 UAV wingbox under gust load conditions

The energy harvesting evaluation of a UAV wingbox with a piezoelectric layer is presented in this section. The UAV wingbox configuration in [13] is utilised in the present case. Figure 7.15 displays the general configuration of the UAV wingbox, the structural model and the aerodynamic model.

In Figure 7.15, the blue frames depict the structural model via solid elements.

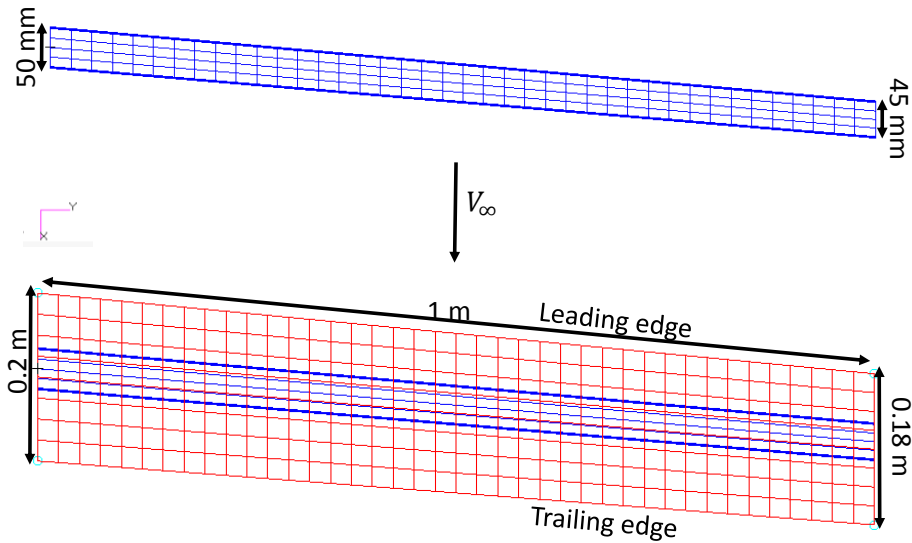


Figure 7.15: Topside view of the UAV wingbox configuration: Wingbox only - Structural model (top), Wingbox and wing surface - Structural model and aerodynamic panels (bottom)

The top picture only shows the structural model. Meanwhile, the bottom picture shows the finite elements and the aerodynamic panels of DLM, represented by the red frame. In the present case, the aerodynamic panels represent the lifting surface or the wing surface. However, the structural elements only represent the wingbox. The connection between aerodynamic loads and the structure is constructed via spline interpolation [104]. Modelling wing structure by wingbox is a common practice in aircraft wing's stress or aeroelasticity analyses as the wingbox is the primary load-bearing structure in the wing and constructed most of the wing's weight. Hence, if the wingbox can be assured safe, the wing can be assumed safe to carry the primary load, i.e., aerodynamic lift.

The wing has a 5° sweptback angle with 0.9 taper ratio and fixed at the root. The piezoelectric layer is made of PZT-5H, embedded on the top surface of the wingbox. It lies from the root until 10% of the span length. The host structure of the wingbox is aluminium alloy 7075. More detailed configuration parameters and material properties can be found in the article by Xiang et al. [13]. A flutter investigation of the UAV wing is also performed to validate the structural and aerodynamic models. In agreement with flutter observation in [13], sea level condition is assumed, and six mode shapes, i.e. four bending modes and two torsion modes, are involved in the analysis. Figure 7.16 depicted the flutter summary of the UAV wingbox. For clarity purpose, only three main modes coupled to the instability are shown.

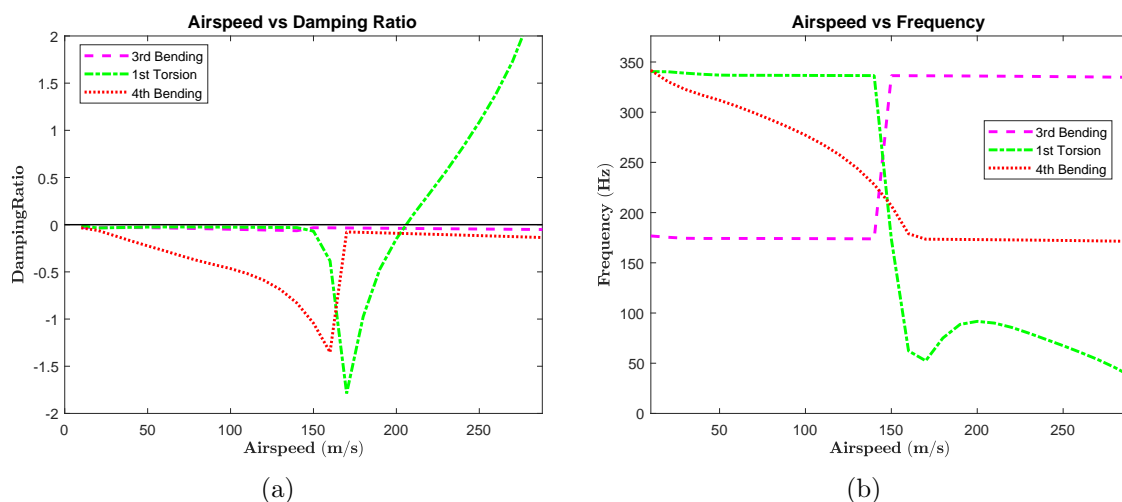


Figure 7.16: (a) Damping vs Airspeed, and (b) Frequency vs Airspeed graphs of the UAV wingbox

Figures 7.16a and 7.16a shows the variations of the damping ratio and frequency to the airspeed of the UAV wingbox. It can be seen that the first torsion crosses the positive damping (unstable) region at 220 m/s in Figure 7.16a. However, the frequency evolution in Figure 7.16b displays the three modes coalesce at around 140-150 m/s. Appendix I shows the flutter responses of the UAV wingbox at 150 m/s for different modes. The frequencies of the third and fourth bending coalesce first at 140 m/s followed by the other intersections. These complete intersections of the three frequencies may lead to violent instability. This case is also known as a hard flutter condition, while the one for the bimorph in Section 7.5 is called soft flutter as the frequencies only approach each other at a very short gap [102]. This condition agrees with the critical flutter speed at 150.2 m/s obtained by Xiang et al. [13].

For the gust load condition, the wing is observed at cruise state with $V_\infty = 100$ m/s and flight altitude 4000 m above sea level. The maximum gust velocity, V_{g0} , is 15 m/s. The gust gradient distance, H_g , is 12.5 mean aerodynamic chord (MAC). This typical gust gradient is one of the parameters set by FAR for time-dependant gust analysis as it normally gives the maximum structural response. Thus, the total gust time, t_g , is 0.0475 s. Extra 1 s observation time is given by Xiang et al. [13] to allow the dynamic response finishes. It can be seen, however, the displacement is completely damped after 0.2 s as shown in Figure 7.17a.

In Figures 7.17a and 7.17b the responses of both the present result and those obtained in [13] are in a good agreement at the beginning until it reaches the maximum responses. However, some discrepancies can be seen after the first maximum responses. The displacement obtained by Xiang et al. [13] is damped quickly without any oscillation after it reaches the first amplitude. In contrast, the present result shows at least

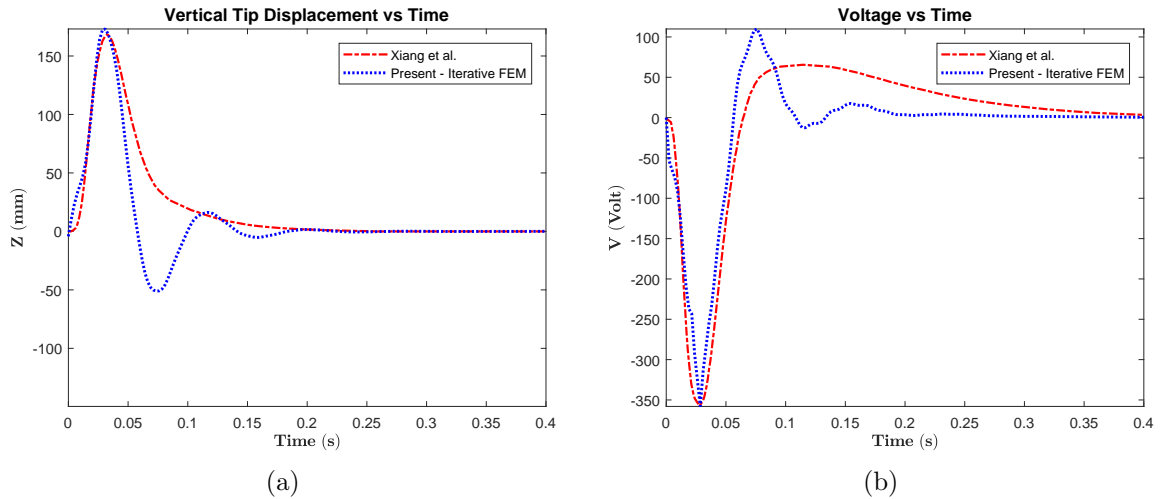


Figure 7.17: Time histories of (a) the tip displacement and (b) the voltage output of the UAV wingbox under 1-cosine gust

a few damped oscillations after the first amplitude.

This discrepancy may occur due to different structural and aerodynamic models used by both methods. Beam elements are utilised by Xiang et al. to model the structure. A step function is applied to discretise the mass. Moreover, the strip theory is used to model the unsteady aerodynamic load [13]. It has been discussed in the literature [103], in a classic aeroelastic benchmark of the BAH (Bisplinghoff-Ashley-Halfman) wing [9] shows the use of the strip theory may give an overdamped response compared to the one with DLM.

The strip theory divided the lifting surface into panels in the spanwise direction (strips) and was derived based on the 2-D (airfoil) aerodynamic force calculation of the Theodorsen Function [9]. In the strip theory, each strip does not interact with the other strips; hence, the aerodynamic force generated by each strip is independent of the other strips. In contrast, in DLM, each panel is influenced by the other panels; thus, larger aerodynamic force is expected. Therefore, DLM's equivalent aerodynamic damping force is larger than the strip theory. Mathematically, in relation to Equation (7.22), \mathbf{G}_∞ of the strip theory is smaller than \mathbf{G}_∞ of DLM. Hence, the overall system's damping is larger in the strip theory, and the response will be overdamped compare to those obtained via DLM.

In contrast, Figure 7.17b shows the result of Xiang et al. still produces voltage output even though the displacement is entirely damped. Meanwhile, the present voltage output is in agreement with the displacement response. The voltage output still oscillating after it reaches the first amplitude. This behaviour is much more consistent with those shown in Section 7.5, in which the electrical responses follow a similar trend with the displacement responses.

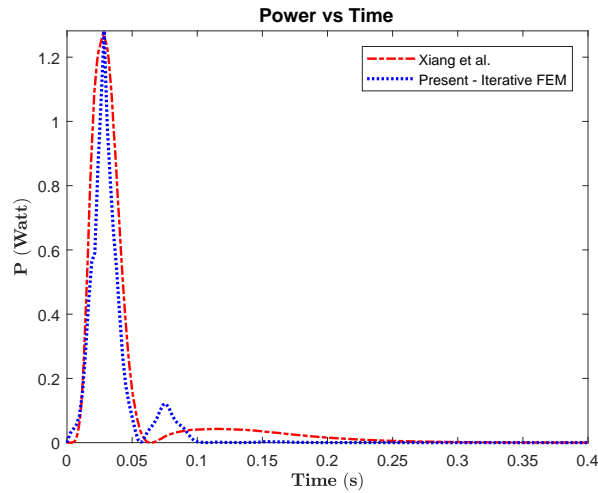


Figure 7.18: The power output time history

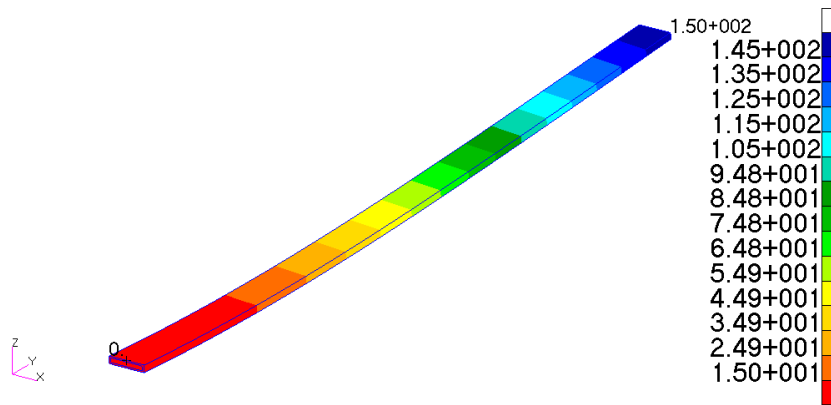


Figure 7.19: Displacement contour of the UAV wingbox at $t_g = 0.0285$ s (displacement unit in mm)

Figure 7.18 shows the power response of the present model still has fluctuations after the first maximum power although the second largest fluctuation only sustained around 0.05 s. Meanwhile, after the first amplitude, the result from Xiang et al. sustained a lower maximum power which sustained much longer, around 0.15 s. This behaviour resulted in a discrepancy of the total energy output. The present result only achieves 25.3 mJ compared to the one obtained by Xiang et al., 35.1 mJ.

A detailed displacement contour of the UAV wingbox at $t_g = 28.5$ ms is depicted in Figure 7.19. At $t_g = 28.5$ ms, the maximum displacement response is exerted by the combined mechanical and electrical loads. The displacement is mostly dominated by the first bending mode where the maximum is observed at the tip. Figure 7.20 shows the voltage contour on the wingbox. It is seen that the voltage only occurs at the thin top layer near the root in which the piezoelectric is located. An amount of 363 Volt

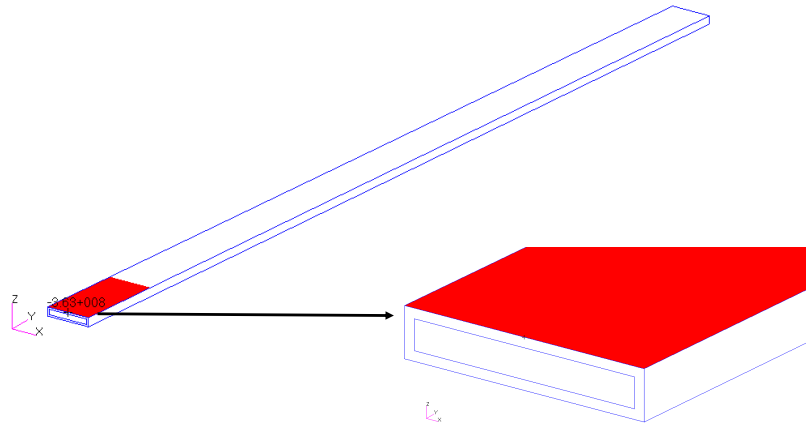


Figure 7.20: Voltage contour of the piezoelectric layer of the UAV wingbox at $t_g = 0.0285$ s (voltage unit in μV)

is observed at $t_g = 28$ ms. Meanwhile, the other parts of the wingbox do not produce the voltage as there is no electromechanical coupling.

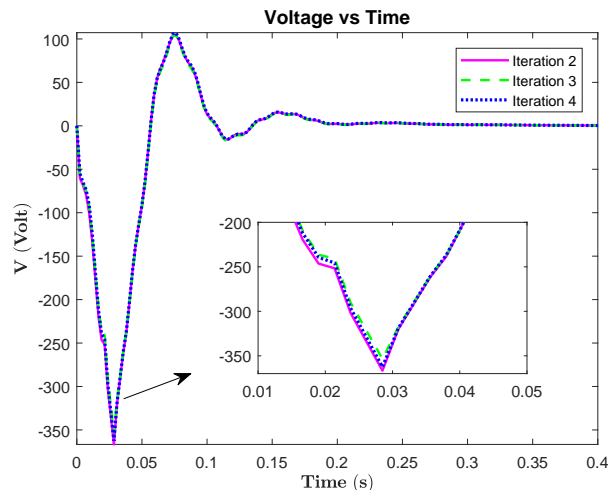


Figure 7.21: The voltage output time histories at different iteration steps

Figure 7.21 displays the voltage responses at different iteration steps. It can be seen that the responses for all the steps almost coincide. In the enlarged view, the result from the second iteration is shown slightly overestimates the other results. The third and the fourth iteration results, however, still almost coincide even in the enlarged view. In more details, the iterative process is shown in Table 7.7.

The harvested energy even only after the third iteration provided less than 5% iteration variance. After ten iterations, the iteration variance even lower, with a value less than 1%. This shows that the displacement due to electrical load is also insignificant to the one exerted by the mechanical load. This behaviour is similar to the results

observed in Section 7.5. In this case, it might be considered that the normal flight operation with active piezoelectric energy harvesting may not provide a significant change to the structural deformation while still may produce voltage response.

Table 7.7: Electrical energy output of the UAV wingbox on each iteration step

Iteration	Energy (J)	Variance
1	0.0250	
2	0.0263	$\Delta_{1-2} = 5.60\%$
3	0.0250	$\Delta_{2-3} = 4.94\%$
4	0.0256	$\Delta_{3-4} = 2.40\%$
9	0.0251	
10	0.0253	$\Delta_{9-10} = 0.79\%$

7.7 Summary

A novel iterative finite element method (FEM) for energy harvesting purpose has been developed. This iterative FEM scheme involves the utilisation of commercial software to create and evaluate the structure, aerodynamic, and aeroelastic models. A computational code based on this new iterative FEM has been built as the augmentation for the commercial software to solve the electromechanical coupling for energy harvesting case. Validation with the classical benchmark of piezoelectric energy harvester plate under base excitation shows an excellent agreement both in frequency and time domains.

Two different lifting structures, i.e., a plate-like wing and a UAV wingbox, with active energy harvesting layer(s) subjected to 1-cosine gusts have been investigated via the time-domain iterative FEM. Based on the case studies, the iterative processes are considerably fast, and convergences are achieved in less than ten iterations. The present results are all showing similar behaviours with the references' results.

From the observation on the iterative processes, an exciting finding is taken, the mechanically-exerted displacements dominate the responses of all the lifting structures. Thus, based on these results, the influences of the reverse piezoelectric effect are minimum. Hence, for normal flight operation, it may occur that the displacement is not significantly affected by the harvested voltage.

In the present work, the iterative FEM is further implemented to a notional jet aircraft wingbox exerted by gust and cruise loading. Chapter 8 discusses the energy harvesting evaluation of the wingbox for different gust load conditions.

Chapter 8

Iterative Finite Element Method with Implementation to An Aircraft Wingbox

In this chapter, the energy harvesting evaluation of a notional jet aircraft wingbox is presented. A similar wingbox as shown in Chapter 4 is used for the investigation. The energy harvesting potential of the wingbox due to the cruise and the 1-cosine gust loads is evaluated. In addition, for the first time, stress and failure analyses of the structure with an active energy harvesting layer are performed.

The power density of the present result is compared with those obtained by the other studies of piezoelectric energy harvester from lifting structure. Furthermore, an analysis of the aircraft flight performance with active energy harvesting is shown in some details.

Some works and results presented in this chapter have been published in *Composite Structures*, Volume 202, 2018 and submitted for publication in *Composite Structures*.

8.1 Jet aircraft wingbox under Gust Load Condition

The energy harvesting investigation for a notional civil jet aircraft wingbox is presented in this section. The typical 1-cosine gust is applied as the excitation load acting on the wingbox. The aircraft wingbox model used in the present work is based on the configuration shown in Section 4.1. However, some modifications are employed to have a more realistic configuration similar to those in a typical long-range flight aircraft. A 30° sweptback modification based on a typical jet aircraft wing in [84] is applied. The wingbox layout, including the structural and aerodynamic models from topside view,

is shown in Figure 8.1.

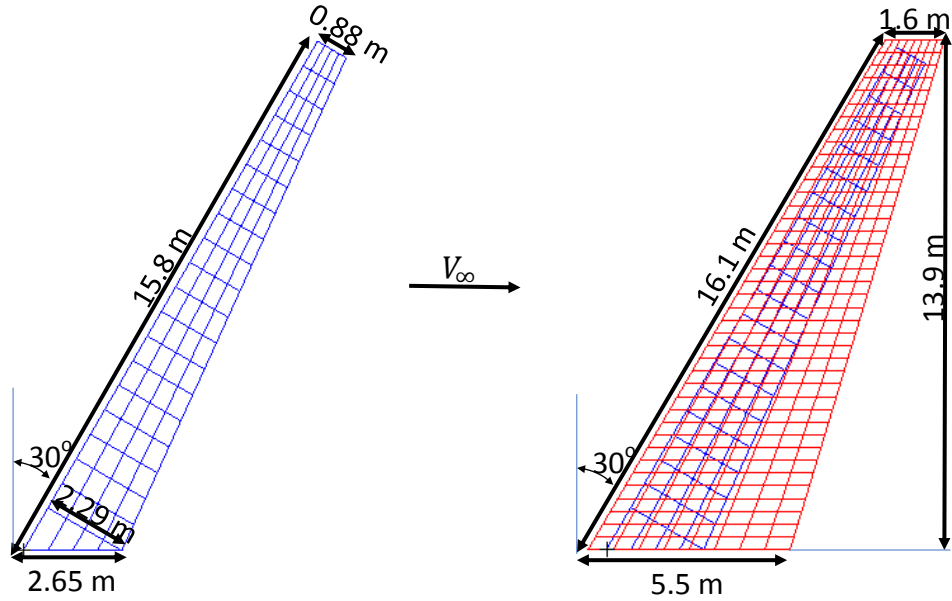


Figure 8.1: Topside view of the aircraft wingbox configuration: Wingbox only - Structural model (left), Wingbox and wing surface - Structural model and aerodynamic panels (right)

The blue frames on the left and right sides of Figure 8.1 represent the structural parts of the wingbox modelled via shell elements. The thickness for the ribs and the spars is 7.04 mm, while for the skins is 6.09 mm. Addition of an inner wingbox part as the connection to the fuselage is employed here to construct the swept configuration. In Section 4.1, the root chord was the one with 2.29 m chord length, and this is the location of the cantilevered boundary condition. However, in the current case, the fixed root is the one with 2.65 m chord length.

Initially, all of the wingbox materials are Aluminium Alloy, Al-2219, with density 2840 kg/m³ and Young's modulus 73.1 GPa. For energy harvesting purpose, the upper skin material is replaced by PZT-5A. The upper skin is modelled as unidirectional laminated via shell elements with piezoelectric 1-direction lies on the mid chord span. The wingbox configuration with PZT-5A as the upper skin has been shown to have a maximum energy harvesting potential around 40 kW in Section 4.2. However, the investigation in Section 4.2 assumed a harmonic load constructed from the steady aerodynamic cruise lift and excitation frequency near the first bending frequency. This loading scenario was very much simplified and may not represent a practical flight scenario. Therefore, in the present case, with the existence of gust load and the utilisation of commercial software to evaluate the unsteady aerodynamic loads, the investigation

on how much this harvesting potential can be achieved is discussed in a later part of this section.

The first bending natural frequency of the present wingbox is 1.72 Hz, slightly increasing from the one in Section 4.2 by 6.8% due to additional stiffness from the inner wingbox part at the root. Along with the first bending, other mode shapes of the wingbox are shown in Figure 8.2. The natural frequencies of the second bending and the first torsion shown in Figure 8.2 are 7.36 Hz and 23.47 Hz, respectively. The mix bending and torsion mode shown is the 7th mode of the wingbox at 31.50 Hz, following this mode, the higher modes are the combination of two or more basic modes. In the present case, flutter analysis is performed to observe the frequency and damping evolution as the functions of airspeed.

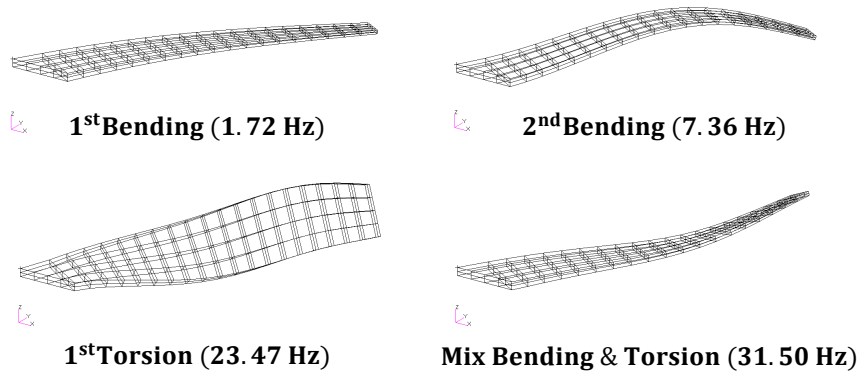


Figure 8.2: Mode shapes the aircraft wingbox

The red frame in Figure 8.1 depicts the wing surface divided into several aerodynamic panels. Similar to the case of UAV wingbox in Section 7.6, the aircraft wing represented by the aerodynamic panels covering a much larger surface than the structural elements. Ten modes are involved in the analysis to accommodate any influence from the high-frequency modes. The flutter analysis is performed at the cruise altitude, around 10000 m above sea level, with the speed of sound (Mach 1) is around 300 m/s. Therefore, the flutter analysis is limited to this speed as the DLM here is only applicable for the subsonic regime. The flutter summaries in the form of $V - g$ and $V - f$ graphs are shown in Figure 8.3.

It can be observed in both Figures 8.3a and 8.3b that neither the dampings nor the frequencies show any sign of instability, flutter does not occur at the subsonic regime. Although several behaviours can be observed going towards instability, i.e., the damping curve of the first bending starts going up just before 300 m/s, the first bending frequency approaching the second bending, and the first torsion frequency

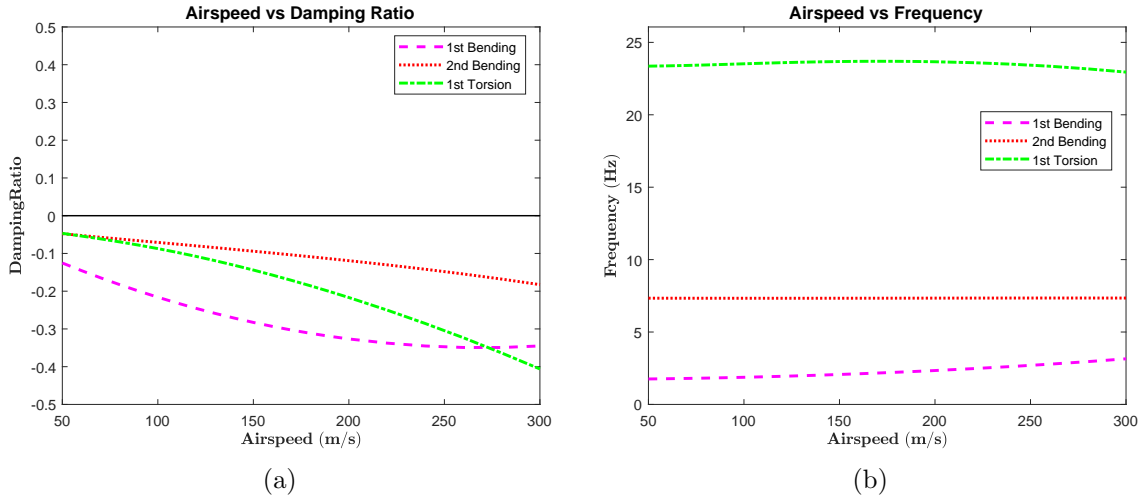


Figure 8.3: (a) Airspeed vs Damping ($V - g$), and (b) Airspeed vs Frequency ($V - f$) graphs of the aircraft wingbox

starts declining.

Nevertheless, concerning a typical long-ranged civil jet aircraft, i.e., B737-800, with around 0.8 Mach (240 m/s) cruise speed, it is understandable that the critical flutter speed will be beyond 300 m/s. To be noted that at high subsonic speed (> 0.8 Mach), locally at some points on the wing, the transonic flow could be developed and shock wave may occur. Hence, the aerodynamic calculation will require a more sophisticated model, i.e., Reynold-averaged Navier Stokes (RANS). In this case, it is assumed that at 0.8 Mach, there is no local transonic flow occurs on the wing; thus, the Doublet Lattice Method (DLM) can be used. According to FAR 25, the dive speed, which is the maximum aircraft speed limit on the flight envelope required to be 1.15 of the cruise speed. While the critical flutter speed is 1.15 of the dive speed, hence, the dive speed will be 276 m/s, and the minimum allowable critical flutter speed is 317 m/s (Mach 1.06).

In the gust loading simulation, the cruise condition and the discrete 1-cosine gust are applied. Based on FAR 25, the range of the gust gradient for discrete gust load evaluation are from 30 ft (9 m) to 350 ft (107 m). In the present case, three different gust gradient distances, H_g , 30 ft, 350 ft and a typical value of 12.5 MAC (43 m) are evaluated.

Concerning a maximum gust condition in the United Kingdom area [105], 15 m/s gust amplitude is observed, V_{g0} . Figure 8.4 displays the displacement and voltage responses for the three H_g conditions.

It can be seen in Figure 8.4a that the shortest distance gives the smallest amplitude while 12.5 MAC distance provides the largest amplitude. At $H_g = 9$ m, the disturbance only has a short time, 75 ms, to affect the structure. In contrast, at $H_g =$

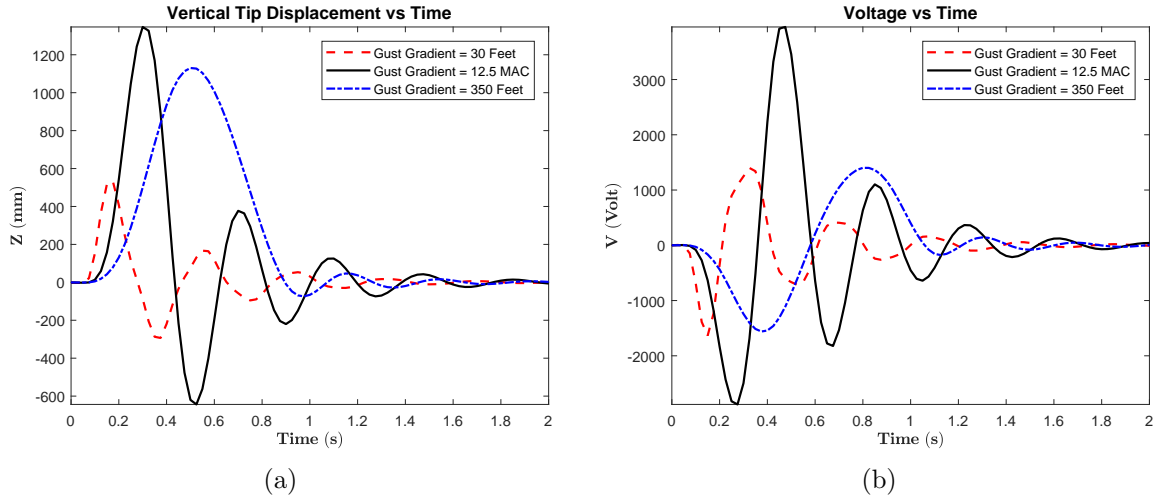


Figure 8.4: The time histories of (a) vertical tip displacement and (b) voltage output of the aircraft wingbox for different gust gradient distances with gust velocity 15 m/s

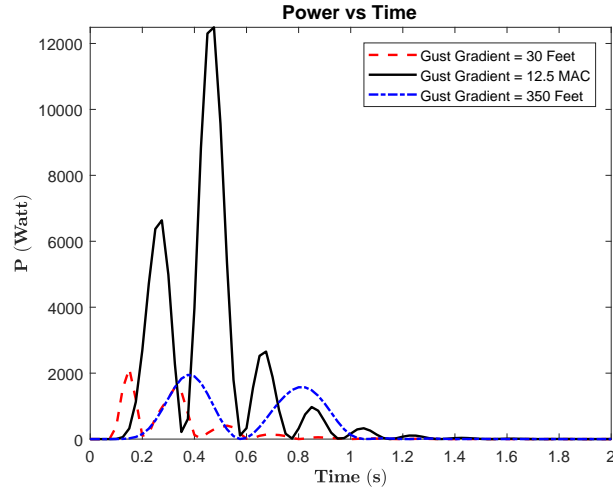


Figure 8.5: The power output time history of the aircraft wingbox for different gust gradient distance with gust velocity 15 m/s

107 m, the gust load penetrates the structure almost around 1 s, allowing a sloping displacement gradient or a low-velocity response. In this case, the dynamic effect is relatively small (almost like steady) compared to the other cases. However, at $H_g = 12.5$ MAC, the disturbance is sustained long enough to gives the maximum amplitude. While it still keeps a step displacement gradient or a high-velocity response; hence, it allows some oscillations after the gust ended. In a more detail, Appendix J displays the displacements of the wingbox at $H_g = 12.5$ MAC for different times, t_g .

In Figure 8.4b, it is interesting to see that the shortest and the longest distances resulted in a similar level of the maximum voltage. The shortest distance gives the smallest displacement amplitude; hence, small voltage. A sloping response exerted by the longest distance resulted in the smallest velocity amplitude; thus, small voltage as

well. Moreover, at $H_g = 12.5$ MAC, the maximum voltage amplitude is achieved as it gives the maximum displacement and velocity.

The power output as depicted in Figure 8.5 also reflected similar behaviours as the shortest and the longest distances give a similar level of amplitude, while at $H_g = 12.5$ MAC, the maximum power amplitude is obtained. As expected, the largest energy is harvested at $H_g = 12.5$ MAC as shown in Table 8.1.

Table 8.1: Electrical energy output of the aircraft wingbox for different gust gradient distance with gust velocity 15 m/s

H_g	Energy (kJ)
30 ft (9 m)	0.3767
12.5 MAC (43 m)	2.4921
350 ft (107 m)	0.7639

The voltage outputs at different iteration steps are shown in Figure 8.6. It can be seen that the responses from three iteration steps are hardly distinguished. In the enlarged view, the first iteration, denoted by the pink dashed line, slightly overestimates the second and third iterations. After the first iteration, the responses declined at the second iteration, and then slightly going up again at the third iteration.

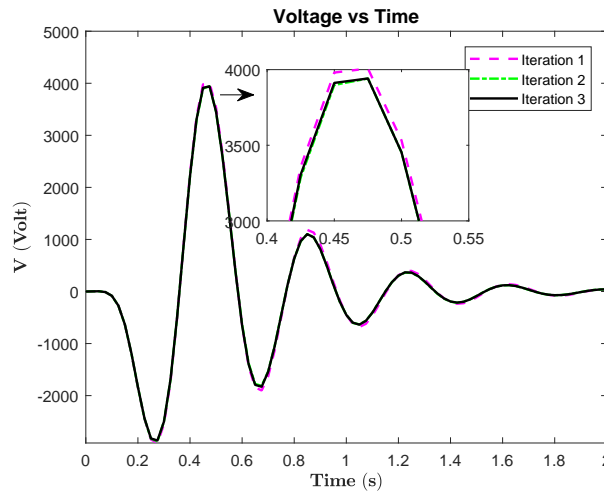


Figure 8.6: The voltage output time history of the aircraft wingbox with gust gradient distance 12.5 MAC at different iteration step

In more details, Table 8.2 displays the iteration process in terms of energy output. The first to the second iteration variance is only around 5%, followed by less than 1% variance after the third iteration. This trend is in agreement with the one shown in Section 7.6. In this case, the mechanical load dominated the displacement response, and the reverse piezoelectric effect may not be significant effects on the structural response.

Table 8.2: Electrical energy output of the aircraft wingbox on each iteration step

Iteration	Energy (kJ)	Variance
1	2.6093	
2	2.4752	$\Delta_{1-2} = 5.14\%$
3	2.4991	$\Delta_{2-3} = 0.97\%$
4	2.4884	$\Delta_{3-4} = 0.43\%$
5	2.4921	$\Delta_{4-5} = 0.15\%$

At $t_g = 0.3$ s, the gust loading exerted the maximum displacement response of the wingbox, and a maximum of 3.95 kV is generated at the upper skin made of PZT-5A. The maximum power achieved for $H_g = 12.5$ MAC and $V_{g0} = 15$ m/s, is around 12 kW. Considering a more extreme condition in the United Kingdom area, 30 m/s [105], is also observed as the V_{g0} . The displacement and voltage responses for the two different gust amplitudes are depicted in Figure 8.7.

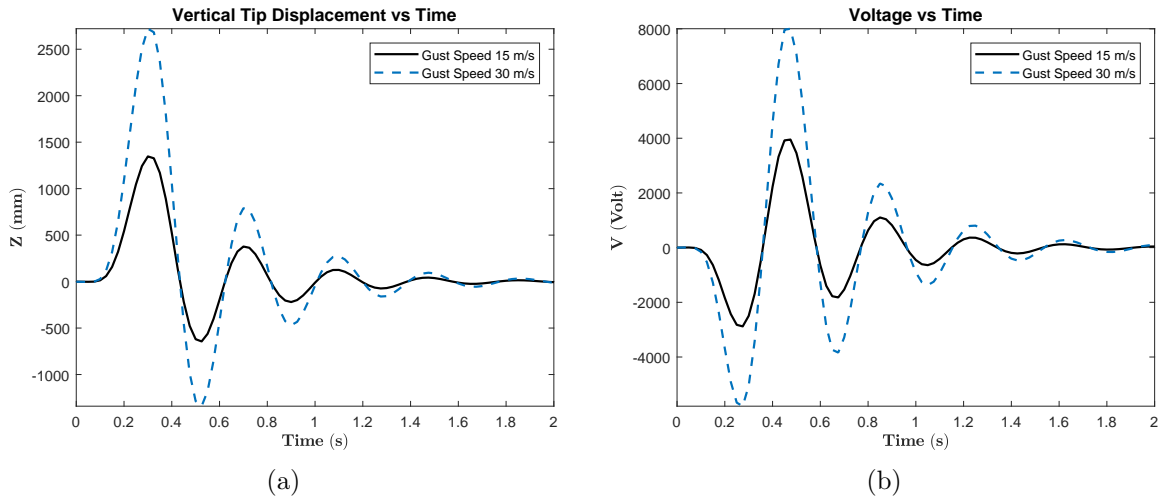


Figure 8.7: The time histories of (a) vertical tip displacement and (b) voltage output of the aircraft wingbox for different gust velocities with gust gradient distance 12.5 MAC

It is easily seen from Figure 8.7 that with the same gust gradient distance, both gust speeds possess a similar pattern of time histories. However, with a larger gust speed amplitude, 30 m/s, the amplitudes of the displacement and voltage are also higher. As displayed in Figure 8.8, In agreement with these trends, the power output for $V_{g0} = 30$ m/s is also higher than the one obtained for 15 m/s.

In the present work, concerning the structural strength, for the first time, the stress and failure analyses of the structure due to the flight condition and the harvested electrical power are performed. The present iterative FEM provides ease of commercial software utilisation; hence, several analysis modules can be explored to support the observation of the energy harvesting structure. In the present case, the gust and

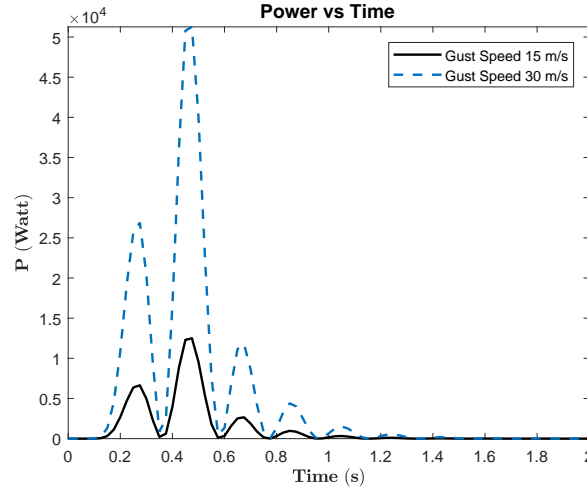


Figure 8.8: The power output time history of the aircraft wingbox for different gust velocity with gust gradient distance 12.5 MAC

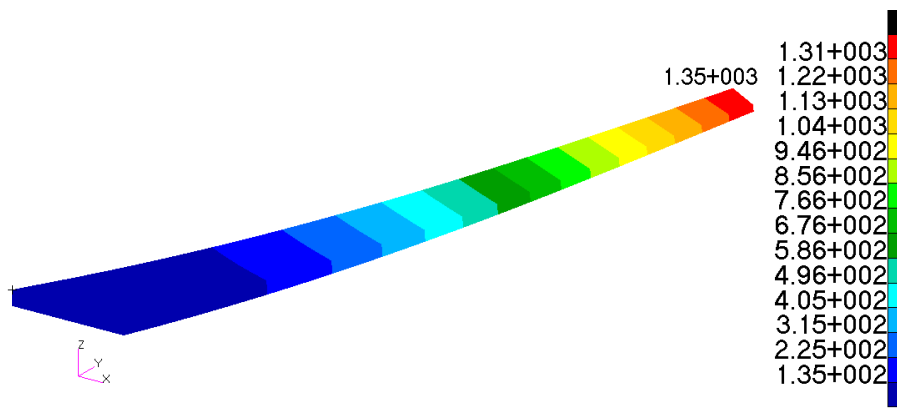
failure analysis modules can be used together via the commercial software; hence, the failure index of the wingbox with active energy harvesting during the gust loading can be observed.

Figures 8.9a and 8.9b show the vertical displacement contours of the wingbox for $V_{g_0} = 15$ m/s and $V_{g_0} = 30$ m/s. It can be seen that the displacements for both speed are mostly influenced by the first bending mode, with a slight twist as the effect from the torsion mode. The maximum displacements at the tip are 1.35 m and 2.73 m for $V_{g_0} = 15$ m/s and $V_{g_0} = 30$ m/s, respectively. The maximum principal stress contours in relation to these displacements can be seen in Figures 8.10a and 8.10b.

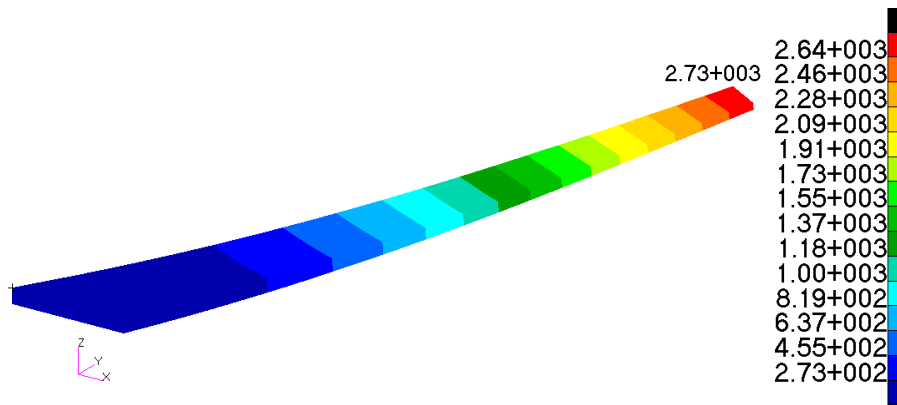
From the stress contours, compression at the upper skin and tension at the lower skin can be seen as the wingbox vertically bends upward. It can be seen that the stress concentrations occur at the lower skin' trailing edge near the root. The maximum stress is doubled from $V_{g_0} = 15$ m/s to 30 m/s as depicted from Figures 8.10a and 8.10b. Concerning the yield and ultimate strengths of Al-2219 are 352 MPa, and 455 MPa [106], the condition for both gust speeds are still in the regime of linear elastic. At 30 m/s gust, the maximum stress at the lower skin is 265 MPa which is lower than the yield strength of Al-2219. In addition, concerning the PZT-5A yield strength, 140 MPa [107], at 30 m/s gust, the upper skin is also still in linear elastic region at around 20 kPa to 60 kPa.

The failure analysis of the wingbox is performed using the Tsai-Wu theory. The convention of the failure index 0-1 is used. The yield and tensile strengths of the materials are concerned. To be noted that the PZT-5A is a brittle material; hence, the yield and tensile strengths are the same [107]. Index 0 shows there is no damage to the structure, while index 1 denotes a full failure.

Figures 8.11a and 8.11a depict that the maximum failure index for $V_{g_0} = 30$ m/s



(a)



(b)

Figure 8.9: Displacement contours of the aircraft wingbox for 12.5 MAC gust gradient distance with (a) 15 m/s and (b) 30 m/s gust velocities at $t_g = 0.3$ s (displacement unit: mm)

are four times the index for $V_{g_0} = 15$ m/s, from 0.143 to 0.575. Despite this fact, the maximum failure indices are still less than 1. Hence, even at an extreme condition, with 30 m/s gust amplitude, the wingbox structure is considered safe. In addition, the failure indices at the upper skin also relatively small, less than 0.1. Therefore, it can be assumed that the piezoelectric layer is in a very safe condition. However, despite the wing could withstand the loads while harvesting the energy, the displacements that occur are quite high, i.e., almost 10% of half span at 15 m/s gust amplitude. Hence, it is not practical in a routine flight.

Based on the data from ESDU [108], 15 m/s and 30 m/s gust amplitudes are quite extreme and very rare to occur during a normal flight. The data from ESDU [108], depicts empirical functions on the gust probability based on the altitude and

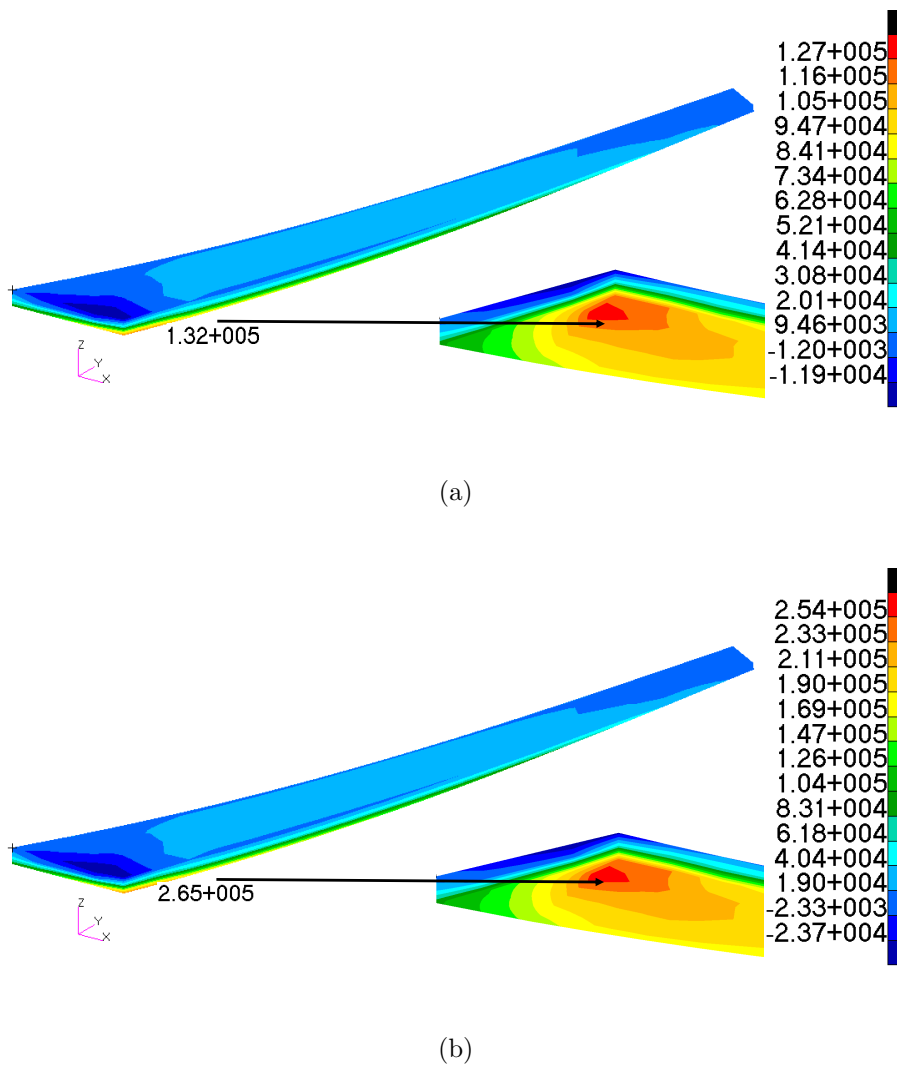


Figure 8.10: The stress contours with (a) $V_{g0} = 15$ m/s, (b) $V_{g0} = 30$ m/s of the aircraft wingbox for $H_g = 12.5$ MAC at $t_g = 0.3$ s (stress unit: kPa)

gust amplitude. At the altitude of 10000m, a 15 m/s gust only has 0.1 % chance to occur during an aircraft flight. Therefore, to evaluate more realistic cases, lower gust amplitudes, 5 m/s and 10 m/s, are observed.

It is important to note that the data in ESDU [108] are presented using Equivalent Air Speed (EAS) term, an equivalent speed concerning the dynamic pressure at sea-level density. In the following cases, 5 m/s, 10 m/s and 15 m/s are around 3 m/s EAS, 6 m/s EAS and 9 m/s EAS, respectively. A multiphase composite configuration which has been discussed in Chapter 6 is used as the upper skin. The composite is consisted of carbon fiber - PZT5A shell and epoxy matrix with aspect ratio 0.2 and 50% volume fraction.

A check on the time step used for evaluation is conducted. The results showed earlier in Figures 8.7 and 8.8 applied a time step of 25 ms. Figure 8.12 depicts the

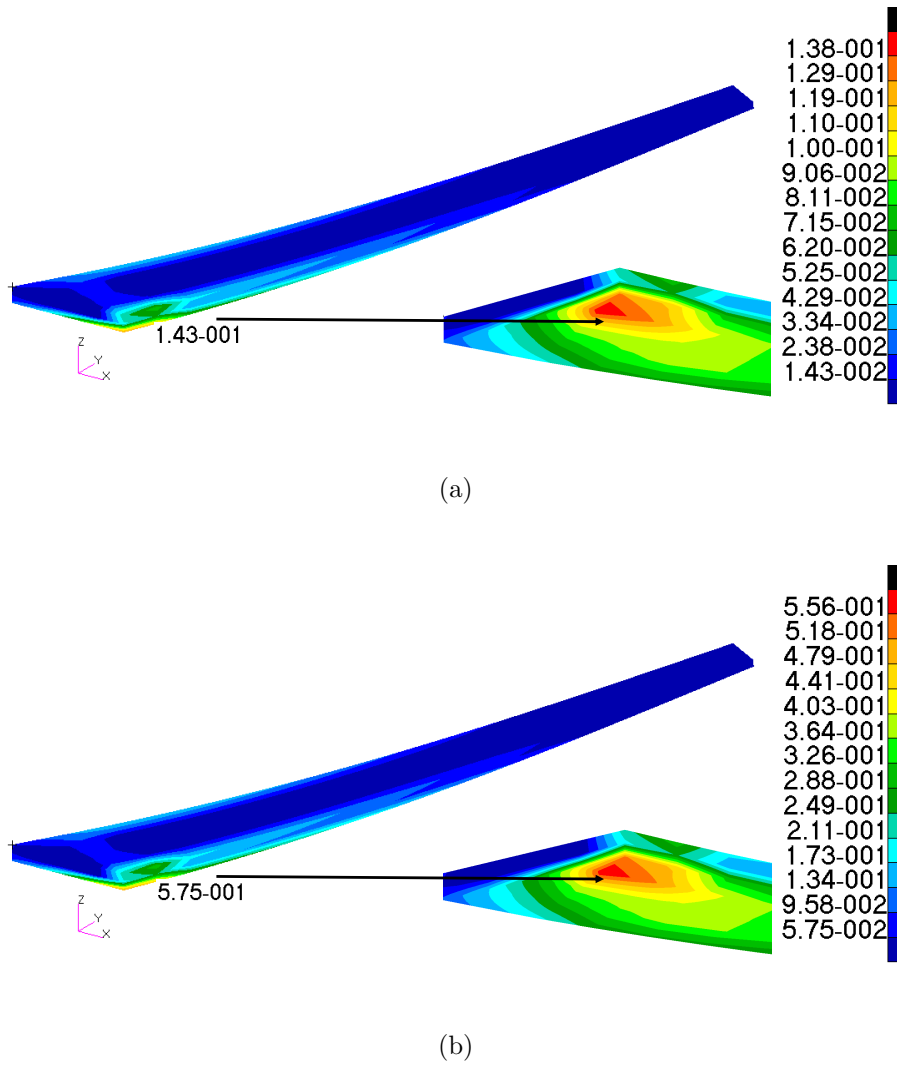


Figure 8.11: The failure indices with (a) $V_{g_0} = 15$ m/s, (b) $V_{g_0} = 30$ m/s of the aircraft wingbox for $H_g = 12.5$ MAC at $t_g = 0.3$ s

results using different time steps (dt) for the multiphase composite case. It can be seen that at time steps 25 ms, 12.5 ms and 6.25 ms the results coincide. For these time steps, the energy converges at around 2.39 kJ. Meanwhile at $dt = 50$ ms, despite the trends closely follow the ones with 25 ms, the energy is slightly underestimated with 2.37 kJ. However, using the largest time step, 100 ms, the responses are quite distinct. The power response despite does not reach the same maximum level with the others, the energy is overestimated with 2.41 kJ.

The voltage and power responses of the multiphase composites for different gust amplitudes are shown in Figure 8.13. As expected, lower gust amplitudes give smaller voltage and power outputs. For 15 m/s gust amplitude, the wing with multiphase composite can generate more voltage as the permittivity is much lower than the bulk piezoelectric material. This characteristic aligns with the discussions in Chapter 5 and

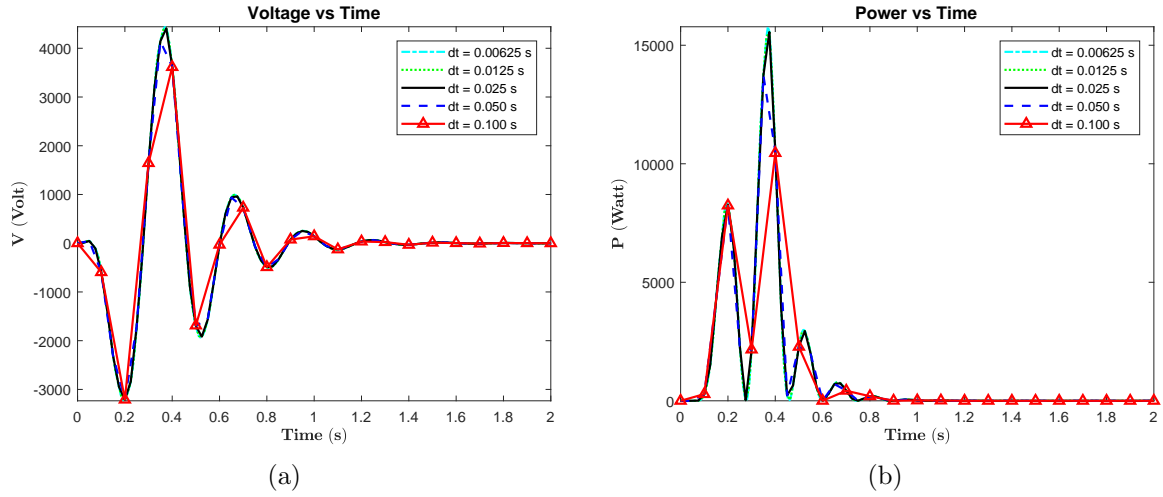


Figure 8.12: The time histories of (a) voltage output and (b) power output of the aircraft wingbox with multiphase composite for different time step

Chapter 6. However, similar to Figures 8.7 and 8.8, it can be seen that the responses during cruise speed are quickly damped.

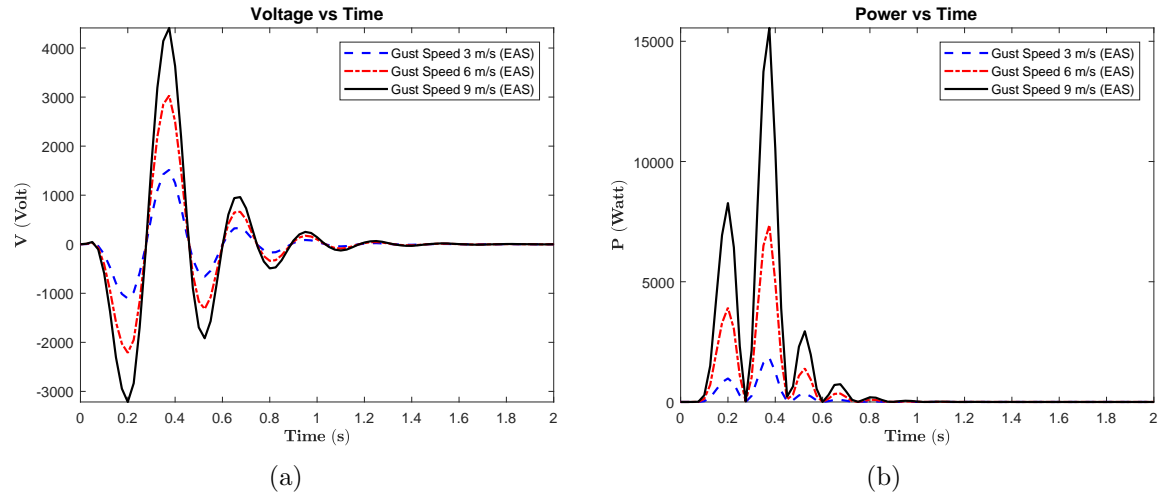


Figure 8.13: The time histories of (a) voltage output and (b) power output of the aircraft wingbox with multiphase composite for different gust velocities (U_p gust) with gust gradient distance 12.5 MAC

The electrical energies generated from each discrete gust amplitudes are 0.28 kJ, 1.13 kJ and 2.39 kJ for 3 m/s EAS, 6 m/s EAS and 9 m/s EAS, respectively. These outputs are much lower than those obtained in Chapter 6. It shows that the assumption used with harmonically oscillating cruise load resulted in overestimated responses and may happen only in a rare case, i.e., extreme (≥ 30 m/s) and continuous gust disturbance. Nevertheless, both the hybrid scheme and the iterative FEM have shown that it could successfully provide an estimation on the energy harvesting of a complex structure, i.e., wing. However, in a future study, it is essential to re-evaluate the loading

assumption for the application in the hybrid method. As an example, the amplitude of load may be corrected by considering a small amount of load as the oscillating part to represent the disturbance by gust; while the steady lift cruise load serves as a static pre-loaded case providing an initial deformation to the wing.

Based on the data from ESDU, the probability of gust at a specific amplitude not only could happen with an upward direction (up-gust) but also may happen with a downward direction (down-gust). Thus, similar gust amplitudes with downward direction are also evaluated. As it can be seen in Figure 8.14, the responses of the down-gust are similar to the up-gust with the only significant difference is the direction of the voltage.

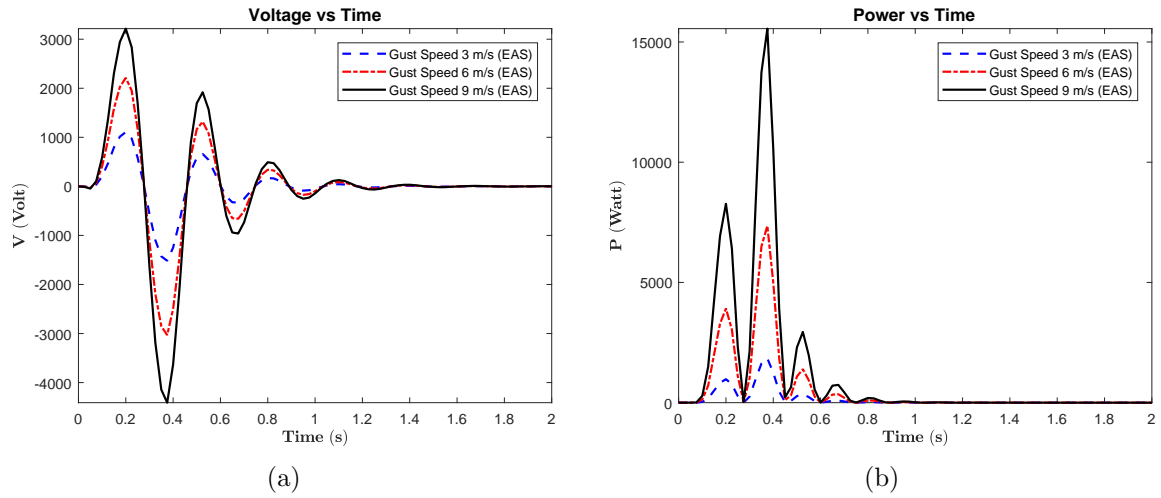


Figure 8.14: The time histories of (a) voltage output and (b) power output of the aircraft wingbox with multiphase composite for different gust velocities (Down gust) with gust gradient distance 12.5 MAC

8.2 Discussion on the power density and the flight performance

In this section, a comparison with the result from the references is depicted in Table 8.3. The selected cases provided studies on the different structural size with different flight/load condition, i.e., gust load, cruise flight, flutter. The maximum RMS or average power densities, power per volume of the piezoelectric layer(s), of different cases are compared. Table 8.3 ranked the power density from the lowest to the highest.

Table 8.3: Power Density Comparison from Different Case Studies

Case Study	Aircraft/Wing Structure	Piezoelectric Structure	Power Density kW/m ³
Anton & Inman [5]	RC Aircraft, 1.8m span, 23cm chord	MFC & PFC patches: (102×16×0.3)mm ³ , (145×15×0.3)mm ³	0.001 (MFC) 0.008 (PFC)
Wang & Inman [71]	Plate-like wing 700.5mm halfspan, 38mm chord	1 Packaged PZT-5A layer (45×25.4×0.5)mm ³	0.275
Tsushima & Su [16]	Tapered Wing, 200cm halfspan, 15cm meanchord	Piezo layers cover upper-lower surfaces, thickness=0.127mm	1.75
Present Work	Jet Aircraft Wing, 13.5m halfspan 3.55m MAC	Multiphase composite as the upper wingbox skin 24.5m ² × 0.006m	1.90
Erturk et al. [23]	2DoF Wing Section, 0.5m span, 25cm chord	Bimorph, Packaged PZT-5A 2×(45×25.4×0.5)mm ³	4.61
De Marqui Jr. et al. [24]	Plate-like wing, 1.2m halfspan 24cm meanchord	Bimorph, PZT-5A 2×(360×240×0.5)mm ³	8.68
Tsushima & Su [72]	Tapered Wing, 200cm halfspan, 15cm meanchord	Piezo layers cover upper-lower surfaces, thickness=0.127mm	75.62
Xiang et al. [13]	Tapered Wing, 1m halfspan, 19cm meanchord	1 layer PZT-5H at upper skin (100×40×0.255)mm ³	251.77

The current case study with multiphase composite (AR 0.2, Vf 50%) is right in the middle of the table, provides the fifth-highest power density. The case with 3 m/s gust amplitude is used in the comparison as it has the highest probability of occurrence amongst the other amplitudes. The first and the second highest power densities were obtained by a gust load case [13] and a post-flutter speed LCO case [72] which could reach hundreds and tens of kW/m³.

The study by Xiang et al. in [13] observed an extreme 15 m/s gust which is 15% of the cruise speed. Hence, it provided a large power output. However, based on the ESDU data [108], the occurrence of this gust is very unlikely, less than 0.1% probability. The work discussed by Tsushima and Su in [72] evaluated the responses from a Limit-Cycle Oscillation (LCO) at a post flutter speed. Theoretically, an LCO phenomenon exerts a sustained oscillation after the lifting structure pass the critical flutter point. However, as has been discussed earlier in Chapter 2, in a practical flight condition, flutter is a catastrophic phenomenon in which the structure may have been collapsed after the flutter point.

Meanwhile, Anton and Inman [5] obtained the smallest power density. They were the first researchers who did the flight experiment for piezoelectric energy harvesting. At the time they conducted the flight test, the mathematical/numerical model to estimate/design the energy harvester has not yet been developed. They used an already available piezoelectric patches in the market and did not optimise the design of the structure, the location of the piezoelectric nor the electrical load. Hence, it is understandable that they got significantly smaller order than the other studies compared in Table 8.3.

Wang and Inman implemented the most conventional approach in [71]. They approximated a cruise flight in a clear sky with a transient base excitation function. The aerodynamic load and aero-structure coupling were not modelled. The load was given as the base acceleration so that the tip displacement had a similar pattern to the response of a flight. They also obtained a small level of power density compared to the other's. It can be seen that the power density mostly varies from the order of 10^0 kW/m³ to 10^2 kW/m³. The variations are most likely influenced by the assumption taken to simulate the load acting on the wings.

Different gust types were observed in the literature, discrete 1-cosine gust [13] and Dryden gust/turbulence [16] resulted in different scale of power densities. The differences may also occur due to various resistance load. Despite the 1-cosine gust acting at a much slower speed than the Dryden gust, but the power density is more than a hundred times of the Dryden gust case. Most of the selected case study used the optimum resistance load; however, the studies in [16, 72] did not mention whether the optimum resistance load was used.

Moreover, the studies in [16] and [72] despite using the same wing structure, due to different loads, i.e., Dryden gust and post-flutter limit cycle oscillation (LCO) vibration, different level of power densities are obtained. The vibration amplitude due to the Dryden gust is not constant over time; however, at the flutter and LCO case, a persistent oscillation is expected. Hence, despite the author's effort to normalised the power by comparing the power densities as depicted in Table 8.3, it remains chal-

lenging to have an equivalent parametric comparison for the case of piezoaeroelastic energy harvesting. Nevertheless, Table 8.3 still provide an insight that the power estimated from the present work is still in a reasonable order compared to those from the literature.

Considering overall flight performance, for instance, a typical jet transport aircraft's mission profile with the weight fractions of each flight phase is shown in Figure 8.15. Meanwhile, an illustration of the mission profile with active energy harvesting is depicted in Figure 8.16. The range is initially assumed to be the same for both mission profiles. The same aircraft's velocity, specific fuel consumption, and lift to drag ratio are assumed. As W_{TO} is known and W_5 is assumed as the operational empty weight with 5% reserved fuel, hence W_2 and W_3 can be calculated. The range at cruise phase is evaluated using the Breguet's formula [92]. The range is proportional to the $\ln(W_2/W_3)$ based on the Breguet's formula.

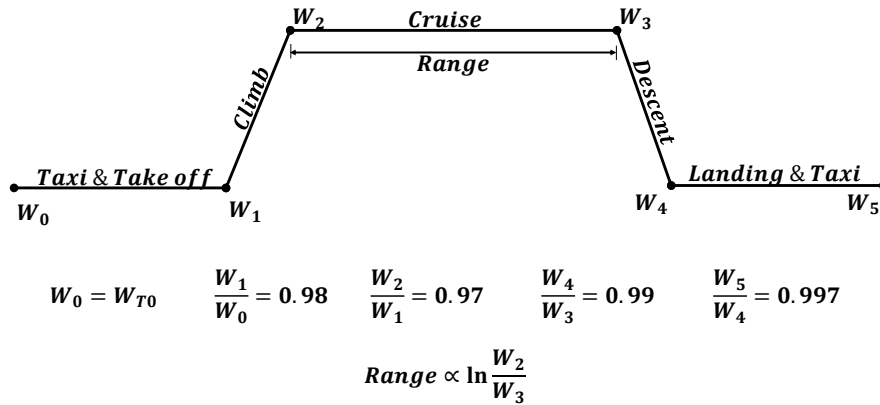
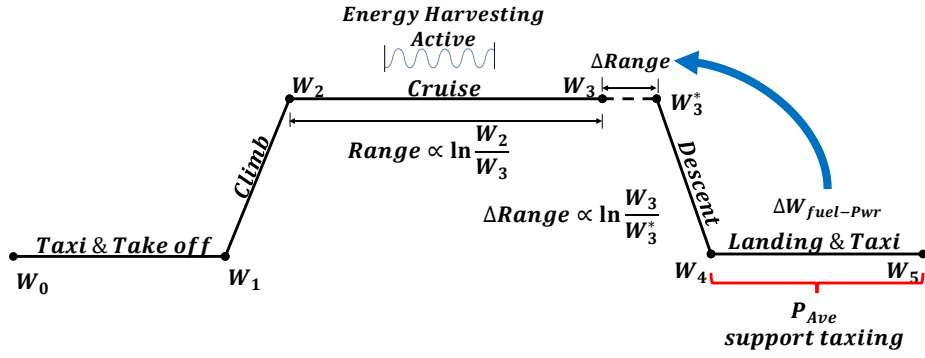


Figure 8.15: Mission profile of a typical jet transport aircraft

In the current case, the aircraft has the $W_{TO}=169820$ lbs and $W_E=84099$ lbs (refer to Chapter 6, Section 6.4). Hence, the weight breakdown for each phase can be found as follows:

- $W_1 = 166424$ lbs;
- $W_2 = 161431$ lbs;
- $W_3 = 89546$ lbs;
- $W_4 = 88651$ lbs;
- $W_5 = 88385$ lbs;
- $\ln(W_2/W_3) = 0.589$;



$$W_0 = W_{T0} \quad \frac{W_1}{W_0} = 0.98 \quad \frac{W_2}{W_1} = 0.97 \quad \frac{W_4}{W_3} = 0.99 \quad W_3^* = W_3 - \Delta W_{fuel-Pwr}$$

Figure 8.16: Mission profile with energy harvesting system and extended cruise range using the fuel saved

From the aircraft weight breakdown, then, it can be estimated that the fuel required during landing and taxi is 266 lbs. This amount of fuel is equivalent with 324 Mega-Joule of energy produced by the APU. If the energy harvesting ability is activated and the harvested power is used to support taxiing system, then the equivalent fuel saved from the harvested power can be used to extend the cruise range as shown in Figure 8.16.

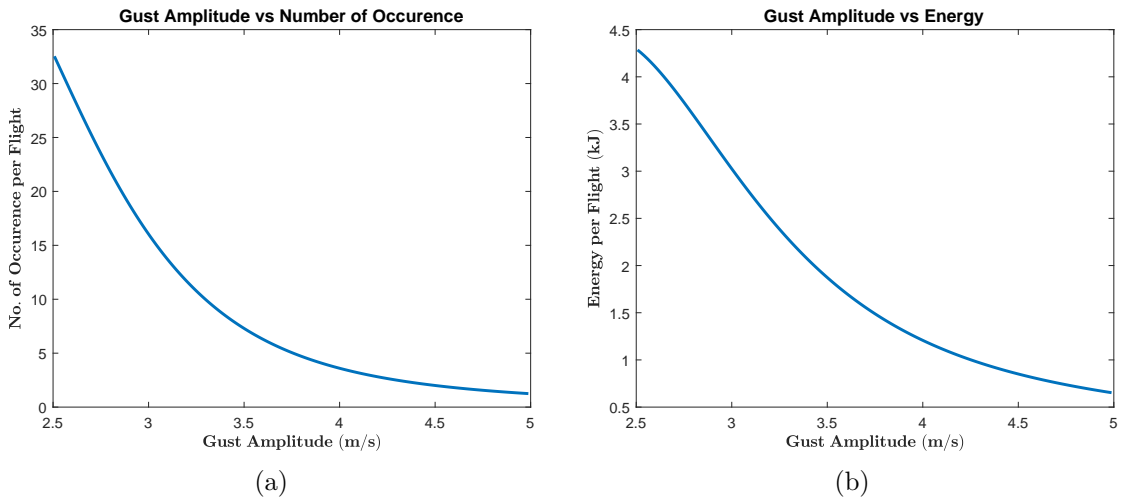


Figure 8.17: (a) The number of gust occurrence per flight, and (b) Total energy generated per flight as functions of the gust amplitude (V_{g0})

Based on the data from ESDU [108], considering an aircraft with cloud warning radar, at an altitude of 10000 m above sea level, the average distance flew to meet an up- or down- gust is around 2800 nautical miles or 5200 km. This average distance is equal to the cruising distance of a long-range aircraft with 240 m/s speed and 6 hours

cruise (for 7-8 hours flight time). The ratio of up-gust and down-gust at this altitude is around one [108]; thus, the chance to meet an up-gust or a down-gust is the same.

The probability of meeting a gust, however, is unique for a certain gust amplitude. The chances to encounter a 5 m/s (3 m/s EAS), 10 m/s (6 m/s EAS) and 15 m/s (9 m/s EAS) are 100%, 3% and 0.1%, respectively [108]. Therefore, there is only one chance to meet a gust with 5 m/s amplitude during a cruise flight of a typical jet aircraft observed in Section 8.1. Moreover, there are only three times a 10 m/s gust could be encountered in 100 flights and only one time a 15 m/s gust occurs in 1000 flights. Hence, the most realistic scenario between the three gusts is the one with 5 m/s gust amplitude.

Considering both wings of the aircraft generate the energy, then, around 0.56 kJ can be harvested during the flight if there is only a 5 m/s gust. If lower gust amplitude is concerned, there is a higher probability that the gust could occur more than once during this flight. Figure 8.17a depicts the number of occurrence for lower gust amplitudes based on the ESDU data [108]. It can be seen that the lowest gust amplitude, 2.5 m/s, could occur more than 30 times during this flight. Unfortunately, lower gust speed could not be evaluated as the data is not available, and extrapolating the data may lead to invalid result [108].

Figure 8.17b shows the variation of total energy per flight to the gust amplitude. It can be seen that lower gust amplitude does not necessary means lower energy during the flight. Smaller gust amplitude may result in higher number of encounter during the flight. Hence, may provide higher total energy per flight. However, despite this fact, the maximum energy harvested per flight is only around 4.3 kJ (from 2.5 m/s gusts). This amount of energy is still in a much lower order compared to the fuel-energy ratio of the APU, 1220 kJ per pound fuel. Therefore, the improvement in the flight performance, i.e., range, as shown in Figure 8.16 will not be significant or may even be negligible.

Nevertheless, the evaluation concerning discrete gust load disturbance during cruise flight provides more realistic results compared to the ones given in Chapter 6. The analyses based on the assumption of harmonically oscillating cruise load discussed in Chapter 6 lead to overestimated total energies. In a typical flight, as shown in the current analysis, the load does not continuously oscillate with the same amplitude, even when there is a disturbance, i.e., gust, the oscillation is quickly damped and each disturbance may occur only at a certain distance. In addition, the excitation near the first bending frequency as assumed in Chapter 6 may only valid to estimate the maximum power amplitude in such an extreme and rare case, i.e., very high gust amplitude.

8.3 Summary

Implementation of the iterative FEM scheme to a transport aircraft wingbox exerted by gust and cruise loads provide a more realistic approach to the flight loading condition. The analyses presented in this chapter have incorporated the aero-structure coupling with unsteady aerodynamics and structural dynamics models.

The utilisation of the commercial software in the iterative FEM has given the flexibility to evaluate several types of structural analysis, i.e., gust and failure modules. In the present work, the stress and failure analyses of the aircraft wingbox while subjected to the gust load and harvesting the energy have been conducted. The failure analysis depicts that the wingbox is safe even when it is subjected to an extreme load, 30 m/s gust amplitude while harvesting the energy. These results have shown that the multidisciplinary problems, i.e., aeroelastic vibration, energy harvesting and structural strength, as mentioned in the literature Chapter 4 can be overcome with this iterative FEM approach.

A more realistic load model concerning gust and cruise load has also shown a more grounded result. The responses exerted by the gust have shown that the structural vibration was quickly damped in a routine flight; thus, the maximum power was only attained at a very short time. Moreover, a gust with a particular amplitude may only occur once at a certain distance; hence, continuous vibration and power generation may not be feasible during a typical flight. Therefore, an earlier assumption of harmonically oscillating flight load as discussed in Chapter 4 and Chapter 6 may only apply to an extreme and rare condition; thus not realistic in a typical flight.

Nevertheless, a much simpler and faster approach as discussed in Chapter 4 and Chapter 6 can be beneficial to evaluate a conceptual design of energy harvesting implementation on an aircraft structure. The hybrid scheme may be used to provide more realistic investigation if the assumption of the loading condition considers much more constraints, i.e., level and occurrence of disturbance during flight. Hence, from the present work, two different approaches for evaluation of piezoelectric energy harvesting, namely the hybrid analytical/ computational scheme and the iterative FEM, can be utilised for different stages of design and engineering analyses.

A comparison with the power densities from other piezoeaeroelastic energy harvesting studies has also been conducted. The selected cases provided studies on different structural sizes and varied flight/load conditions. The result obtained from the present work reasonably falls in the range obtained from the literature.

The results presented in this chapter pointed out that the energy harvested during a normal cruise flight with gust disturbance is rather small compared to the energy provided by the aircraft system, i.e., the APU. Hence, it may not be recommended to consider the piezoelectric energy harvesting structure as an option to support the

main or auxiliary power system of the aircraft. The flight performance improvement, however, may be achieved if the harvested energy from the piezoelectric structure is used for improving the efficiency of other aircraft systems. As an example, it can be utilised to construct a self-powered actuating system for control surfaces or providing an active disturbance control, i.e., gust alleviation system. Thus, in the future works, it is worth to highlight that the research on the piezoelectric energy harvesting structure for aircraft can be focused on the evaluation of these kinds of systems.

Chapter 9

Conclusion

In the present research, for the first time, investigations on the potential of piezoelectric-based energy harvesting from a civil jet transport aircraft wing have been conducted. The piezoelectric-based structure has been proven could harvest the electrical energy from the structural vibration, i.e., aeroelastic vibration. Hence, it has the prospect to become an alternative energy source in aircraft flight as the aircraft always encountered aeroelastic vibration. From the literature, as has been discussed in Chapter 2, many researchers have done studies in piezoaeroelastic energy harvesting. However, there are not many who dedicated their research concerning normal flight loads. In addition, their focuses are limited to small-scale lifting structures, i.e., small plate, UAV wing. Therefore, the main questions on the piezoaeroelastic energy harvesting from large aircraft structure are rather basics yet has not been answered prior to the present research. Those questions are:

- how much energy can be harvested from an aircraft structure, and
- how this energy can be estimated.

Therefore, the essential part from the present research has been the development of computational methods to quantify the energy harvesting potential from an aircraft structure. The wing structure as the primary part in flight operation has been focused as the object of the present work. The wing also the part where the aeroelastic vibration is always concerned in the aircraft. Hence, the first computational method proposed in this research is based on one of the most common simplifications of a wing structure, i.e., a cantilevered beam.

Numerous researchers have studied beam-based piezoelectric energy harvesting. However, most of them either analytical or experimental. The base excitation model of Erturk and Inman [6] is one of the infamous analytical models in this subject. Despite this fact, there is no model which could handle the complexity of wing geometry. There is one electromechanical finite element model by De Marqui Jr. et al. [10] which has

the potential to be applied for wing analysis. However, the shell-based element will need a great effort on the coding development. Moreover, as previously said, there is even still a concern about how much energy the wing can generate. Therefore, the focus on this research has been on the early engineering analysis level.

The initial concept on the computational work in this research was always rooting on the utilisation of a commercial software as much as possible. The use of commercial software has been proven a significant benefit in this research, i.e., the ease of constructing wing structure and performing dynamic analyses. However, the commercial software readily available in the market are not capable of conducting electromechanical analysis for piezoelectric energy harvesting. Therefore, an augmentation from a manually built computational code was required in the current work. Namely, a novel hybrid analytical/ computational scheme has been proposed in the present research.

The so-called hybrid scheme combines the procedures from an analytically-solved electromechanical equation and a structural dynamic analysis done by commercial software. In the present work, a FEM-based commercial software was dedicated to the computational analysis. However, as has been presented in Chapter 3, it is also possible to provide information from an analytical solution or an advanced computational analysis, i.e., isogeometric analysis. This hybrid scheme has been successfully applied to estimate the energy harvesting potential from a typical jet aircraft wingbox as has been discussed in Chapter 4.

The results obtained via the hybrid scheme pointed out that the jet aircraft wingbox with 14.5 m half span could harvest as much as 40 kW of electrical power. This power came only from the implementation of a piezoelectric material as its upper skin. The level of power is indeed promising; however, there were some concerns found from this investigation. The weight of the piezoelectric material was one of the shortcomings found in the analysis. The wingbox weight increased significantly, thus, may result in additional fuel to consume. Secondly, the assumption of harmonic cruise load may not be suitable for a practical flight, i.e., concerning aero-structure coupling and disturbance occurrence during the flight. Moreover, the scaling of the load acted on the wingbox was only based on the bending frequency. Lastly, the strength of the wingbox exerted by flight loads while harvesting electrical energy was also one of the concerns.

In the current work, in order to address the weight issue, multiphase composites with active structural fiber (ASF) has been proposed as an alternative to the bulk piezoelectric materials. To this date, there has not been any study on the application of this type of multiphase composite for energy harvesting. Hence, several investigations were conducted to obtain insights on the characteristic of this composite concerning the energy harvesting analysis. Chapter 5 presented the Double-Inclusion model with

Mori Tanaka method as the approach to estimating the electromechanical properties of the multiphase composites. The investigations done employing the Double-Inclusion model have been well validated with the findings from other researchers. In addition, verification of the dynamic responses has been successfully conducted via FEM.

The similar investigation on the jet aircraft wingbox was then conducted by utilising the properties estimated via the Double-Inclusion model. The hybrid scheme was also applied. As presented in Chapter 6, various configurations of the multiphase composites have been tested. An interesting finding is that the wingboxes with multiphase composites could generate the same level of power compared to the one with the bulk piezoelectric material. Hence, by selecting a particular composition of the composite, a lightweight energy harvesting wing can be constructed. In the current case, with the combination of carbon fiber in the composite, not only lightweight but also an increase in strength can be expected.

In order to address a more realistic loading on the aircraft wing, another computational method has been developed in the present work. An iterative FEM has been proposed. Similar to the hybrid scheme, the idea of utilising commercial software was also the root of this iterative FEM. An interesting concept to separate the electromechanical coupling effect from piezoelectric structure was implemented. The commercial software was dedicated to solving the actuator-like part of the electromechanical coupling. In the other hand, a computational code was built to solve the part induced by the electrical resistance. These two parts were solved iteratively until the response from both parts converged.

Another ease of using commercial software was found during the investigation with the iterative FEM. Structural dynamic analysis, unsteady aerodynamic loads calculation and aero-structure coupling evaluation were done via a commercial software. A computational code was built and applied to evaluate the electromechanical coupling effect. Therefore, piezoaeroelastic energy harvesting concerning gust load analysis can be performed. Verification with the results from literature has been performed and depicted good agreements. The detail has been discussed in Chapter 7. The iterative FEM was then implemented to analyse the energy harvesting from the jet aircraft wing.

The investigations by means of iterative FEM have shown a level of maximum power similar to those obtained via the hybrid scheme is achievable. However, different natures on the gust load and harmonic cruise load proved to be the distinctive aspect. The analyses from discrete gust load conditions depicted a certain level of maximum power could not be sustained in the long term. As discussed in Chapter 8, a long flight hour may be needed to extract a considerable amount of energy. Nevertheless, via the iterative FEM, for the first time, failure analyses on piezoaeroelastic energy harvesting structure have been conducted. The failure index of the wingbox shown

that the structure could endure both the aerodynamics and electrical loads.

In addition, several notable findings and contributions of the present work are highlighted in the following sections.

9.1 On the hybrid piezoelectric energy harvester model

A mathematical model and computational scheme to evaluate a cantilevered piezoelectric energy harvester under dynamic bending to enable the hybrid analytical/ computational scheme have been proposed. The detailed derivation on the governing electromechanical equation and the algorithm of the hybrid scheme have been presented in Chapter 3.

The validation against the analytical base excitation model of Erturk and Inman [6], the experimental results of Erturk and Inman [22] and the electromechanical finite element model of De Marqui Jr. et al. [10] have been conducted and shown excellent agreements. In addition, the comparison against the electromechanical FEM has depicted significant benefits in terms of computational cost by means of the hybrid scheme (refer to Table 3.8 in Chapter 3, Section 3.5). Moreover, the robustness of the hybrid scheme has also been tested by replacing finite element analysis with isogeometric analysis.

A simulation for a notional civil jet aircraft wingbox with piezoelectric skin layer has been conducted in the present work. An assumption of a harmonic cruise loading was taken on the investigation. A steady cruise load equal to the weight of the aircraft was varied with different excitation frequencies. Excitation lower than the first bending frequency was considered. Based on the simulation results, the power responses could achieve the level of 10^2 to 10^4 watts. The estimated maximum power reached around 40 kW (refer to Figure 4.7 in Chapter 4, Section 4.2).

9.2 On the multiphase piezoelectric composite

The implementation of the multiphase composite with active structural fiber for energy harvesting structure has been proposed in the present work. The multiphase composite was designated as the substitute for the bulk piezoelectric material. This purpose was addressed to the weight issue which has been highlighted from the first study on the aircraft wingbox (refer to Chapter 4, Section 4.3).

The application of multiphase composites for energy harvesting has never been elaborated before the present work. Hence, a means of analysis was required to give

more understanding to the properties of the multiphase composite concerning the energy harvesting structure. A computational homogenisation method based on The Double-Inclusion model combined with the Mori-Tanaka method has been proposed in the present work. A computational code has also been built for the present Double-Inclusion model. The detailed derivation and computational procedure of this method have been presented in Chapter 5.

Benchmark analyses against the analytical model and experimental results of the piezoelectric-based single fiber composite by Chan and Unsworth [60] has been successfully conducted. Comparison against the finite element model of Lin and Sodano [50] and their experiment [51] have also shown a good agreement. Concerning the energy harvesting characteristic, dynamic analyses against detailed 3D FEM models have also been performed. The FEM models contained effective electro-elastic properties estimated via Double-Inclusion model were well agreed with the detailed 3D FEM models.

The hybrid scheme has also been applied to evaluate the energy harvesting potential from the jet aircraft wingbox embedded with the multiphase composite. The multiphase composites with various compositions have been applied to replace the bulk piezoelectric material as the wingbox upper skin. The results pointed out that different compositions of the composite were still able to generate similar level of maximum power with the bulk piezoelectric material (refer to Figure 6.4, Figure 6.5 and Table 6.8 in Chapter 6, Section 6.3).

Although the composites were able to harvest a similar order of power with the bulk material, different compositions may result in an increment or reduction of the structural weight. Hence, a specific composition has to be selected so that it could construct a lightweight structure while still able to harvest the energy. In order to satisfy this requirement, the composite needs to produce an equivalent electrical power which could save a considerable amount of fuel.

In the present work, a new procedure to investigate the trade-off between the aircraft weight, the fuel saved and the harvested energy has been developed. Based on the investigation results, 340 pounds of fuel potentially could be saved as the equivalence of the harvested power of the wingbox with a multiphase composite (refer to Table 6.10). Based on the comparison with a typical APU of a long-range aircraft, this amount of fuel saved may support an hour operation of the APU.

9.3 On the iterative FEM for piezoelectric energy harvesting

A novel iterative finite element method (FEM) for energy harvesting purpose has been developed in the present work. This iterative FEM was designated to resolve the

piezoelectric energy harvesting analysis considering aeroelastic condition. The main feature of this iterative FEM is the separation of the electromechanical coupling parts of the piezoelectric energy harvester. In which, one part is solved via a standard finite element software with the augmentation of a computational code to solve the other part. Iterative scheme to achieve convergence from both parts has been proposed. A computational code concerning the electromechanical coupling has been built and has been used together with a commercial software to conduct the iterative process. The mathematical background and computational scheme of this iterative FEM have been presented in Chapter 7.

The utilisation of commercial software has enabled the iterative FEM to assess aeroelastic problems conveniently. Three different lifting structures, i.e., a plate-like wing of De Marqui Jr. et al. [24], a UAV wingbox of Xiang et al. [13], and the jet transport aircraft wing, with active energy harvesting layer(s) subjected to 1-cosine gusts, have been investigated via the time-domain iterative FEM. Based on the study cases, the iterative processes are considerably fast, and convergences are achieved in less than ten iterations (refer to Figure 7.4, Figure 7.5, Figure 7.21, and Figure 8.6 in Chapter 7 and Chapter 8).

The energy harvesting analysis of the transport aircraft wing employing iterative FEM pointed out that the output up to 4.3 kJ could be achieved (refer to Chapter 8, Section 8.2). This result are much lower than the one obtained via the hybrid analytical/computational scheme. It is critical to remark that the response due to discrete gust were quickly damped during a cruise flight. Moreover, the occurrence probability of the gust is also an essential factor to be considered. A higher gust amplitude has a lower chance to be encountered. It was found that a gust with 15 m/s amplitude is very unlikely to happen (less than 0.1% chance), a gust with 5 m/s amplitude may occur only once during a cruise flight. Nevertheless, these results much more representing a practical flight condition than the assumption of harmonic cruise load as presented in Chapter 4.

In addition, the utilisation of the commercial software in the iterative FEM has given the flexibility to evaluate several types of structural analysis, i.e., gust and failure modules. In the present work, the stress and failure analyses of the aircraft wing while subjected to the gust load and harvesting the energy have been conducted. The failure index of the wing depicted that the structure is still safe even when subjected to cruise and gust loads while harvesting the electrical energy (refer to Figure 8.11a and Figure 8.11b). Therefore, the present iterative FEM has covered the multi-discipline analysis concerned in the early investigation of the current work. The hybrid scheme, nonetheless, was able to provide fast estimation on the energy harvesting potential; however, the iterative FEM enhanced the level of analysis for a more complex scope.

9.4 Future work

Continuation of the present work can be further developed in the manners of:

- A higher fidelity approach, i.e., a multiscale approach, can be considered for further verification of the effective electro-elastic properties. On a much complex configuration, in which a laminated composite consisted of thousands of fiber, the multiscale modelling approach could be much more efficient.
- In the current iterative FEM, to be noted that a continuous electrode is assumed, thus, uniform voltage distribution is expected. In a real case, manufacturing capability and materials availability may need to be considered. Hence, a discrete segmentation of the piezoelectric layer may be required.
- In relation to the flight operation, an evaluation on a continuous gust or turbulence disturbance may also be considered for the future works. The present work evaluated a discrete 1-cosine gust, which may represent a spike of atmospheric disturbance. However, it is also worth to investigate the effect of continuous disturbance during the flight which further can be used to verify the model of a discrete gust.
- Considering the failure analysis, fracture and delamination in the piezoelectric structure may need to be addressed in the future. Moreover, concerning a routine flight operation, apart from a failure due to maximum load condition, fatigue analysis is also important to be conducted in the future. It will be essential to see how the implementation of energy harvesting structure could affect the lifetime of an aircraft.
- A parametric scaling, i.e., non-dimensionalised parameters, are required in the future. Examples for these parameters are the Reynold number (aerodynamic analysis) and the Strouhal number (vortex-induced vibration case). These non-dimensional parameters could give senses to represent different scales of analysis for their respective cases. As depicted in Table 8.3, currently, it is still difficult to compare the piezoaeroelastic-based energy harvesting for various size of structures and different airspeed conditions. Hence, a scaled-down model for an experimental test could be done in the future.
- Lastly, employing the harvested energy for other applications in wing structure, i.e., control surface and morphing skin, might potentially enhance the aerodynamic efficiency, i.e., gust alleviation, drag reduction. Therefore, it could lead to other schemes to save fuel, instead of directly using the harvested power as an alternative to the primary power source.

Bibliography

- [1] L. Christodoulou and J. D. Venable, “Multifunctional material systems: The first generation,” *The Journal of The Minerals, Metals & Materials Society (TMS)*, vol. 55, no. 12, pp. 39–45, 2003.
- [2] R. F. Gibson, “A review of recent research on mechanics of multifunctional composite materials and structures,” *Composite Structures*, vol. 92, no. 12, pp. 2793 – 2810, 2010.
- [3] J. P. Thomas, M. Keennon, A. DuPasquier, M. A. Qidwai, and P. Matic, “Multifunctional structure-battery materials for enhanced performance in small unmanned air vehicles,” *American Society of Mechanical Engineers, Materials Division (Publication) MD*, vol. 98, pp. 289–292, 2003.
- [4] J. P. Thomas and M. A. Qidwai, “The design and application of multifunctional structure-battery materials systems,” *The Journal of The Minerals, Metals & Materials Society (TMS)*, vol. 57, no. 3, pp. 18–24, 2003.
- [5] S. R. Anton and D. J. Inman, “Vibration energy harvesting for unmanned aerial vehicles,” *Proceedings of SPIE - The International Society for Optical Engineering*, vol. 6928, p. 692824, 2008.
- [6] A. Erturk, S. R. Anton, and D. J. Inman, “Piezoelectric energy harvesting from multifunctional wing spars for UAVs - Part 1: Coupled modeling and preliminary analysis,” *Proceedings of SPIE - The International Society for Optical Engineering*, vol. 7288, p. 72880C, 2009.
- [7] S. R. Anton, A. Erturk, and D. J. Inman, “Piezoelectric energy harvesting from multifunctional wing spars for UAVs - Part 2: Experiments and storage applications,” *Proceedings of SPIE - The International Society for Optical Engineering*, vol. 7288, p. 72880D, 2009.
- [8] A. Abdelkefi, “Aeroelastic energy harvesting: A review,” *International Journal of Engineering Science*, vol. 100, pp. 112–135, 2016.

- [9] R. L. Bisplinghoff, H. Ashley, and R. L. Halfman, *Aeroelasticity*. Dover Publications, Inc., 1983.
- [10] C. De Marqui Jr., A. Erturk, and D. J. Inman, “An electromechanical finite element model for piezoelectric energy harvester plates,” *Journal of Sound and Vibration*, vol. 327, no. 1, pp. 9 – 25, 2009.
- [11] C. De Marqui Jr. and M. J. Maria, “Effect of piezoelectric energy harvesting on the response of a generator wing to a turbulence gust,” in *27th Congress of The International Council of The Aeronautical Sciences*, 2010.
- [12] C. De Marqui Jr. and A. Erturk, “Electroaeroelastic analysis of airfoil-based wind energy harvesting using piezoelectric transduction and electromagnetic induction,” *Journal of Intelligent Material Systems and Structures*, vol. 24, no. 7, pp. 846–854, 2013.
- [13] J. Xiang, Y. Wu, and D. Li, “Energy harvesting from the discrete gust response of a piezoaeroelastic wing: Modeling and performance evaluation,” *Journal of Sound and Vibration*, vol. 343, pp. 176–193, 2015.
- [14] C. Bruni, J. Gibert, G. Frulla, E. Cestino, and P. Marzocca, “Energy harvesting from aeroelastic vibrations induced by discrete gust loads,” *Journal of Intelligent Material System and Structure*, vol. 28, no. 1, pp. 47–62, 2017.
- [15] N. Tsushima and W. Su, “Modeling of highly flexible multifunctional wings for energy harvesting,” *Journal of Aircraft*, vol. 53, no. 4, pp. 1033–1044, 2016.
- [16] N. Tsushima and W. Su, “Concurrent active piezoelectric control and energy harvesting of highly flexible multifunctional wings,” *Journal of Aircraft*, vol. 54, no. 2, pp. 724–736, 2017.
- [17] J. P. Thomas, M. A. Qidwai, and J. C. Kellogg, “Energy scavenging for small-scale unmanned systems,” *Journal of Power Sources*, vol. 159, no. 2, pp. 1494 – 1509, 2006.
- [18] S. R. Anton and H. A. Sodano, “A review of power harvesting using piezoelectric materials (2003-2006),” *Smart Materials and Structures*, vol. 16, no. 3, p. R1, 2007.
- [19] K. V. Selvan and M. S. Mohamed Ali, “Micro-scale energy harvesting devices: Review of methodological performances in the last decade,” *Renewable and Sustainable Energy Reviews*, vol. 54, pp. 1035 – 1047, 2016.

- [20] A. Erturk and D. J. Inman, “Issues in mathematical modeling of piezoelectric energy harvesters,” *Smart Materials and Structures*, vol. 17, no. 6, p. 065016, 2008.
- [21] A. Erturk and D. J. Inman, “A distributed parameter electromechanical model for cantilevered piezoelectric energy harvesters,” *Journal of Vibration and Acoustics, Transactions of the ASME*, vol. 130, no. 4, p. 041002, 2008.
- [22] A. Erturk and D. J. Inman, “An experimentally validated bimorph cantilever model for piezoelectric energy harvesting from base excitations,” *Smart Materials and Structures*, vol. 18, no. 2, p. 025009, 2009.
- [23] A. Erturk, W. G. R. Vieira, C. De Marqui Jr., and D. J. Inman, “On the energy harvesting potential of piezoaeroelastic systems,” *Applied Physics Letters*, vol. 96, no. 18, p. 184103, 2010.
- [24] C. De Marqui Jr., A. Erturk, and D. J. Inman, “Piezoaeroelastic modeling and analysis of a generator wing with continuous and segmented electrodes,” *Journal of Intelligent Material Systems and Structures*, vol. 21, no. 10, pp. 983–993, 2010.
- [25] C. De Marqui Jr., W. G. R. Vieira, A. Erturk, and D. J. Inman, “Modeling and analysis of piezoelectric energy harvesting from aeroelastic vibrations using the doublet-lattice method,” *Journal of Vibration and Acoustics, Transactions of the ASME*, vol. 133, no. 1, p. 011003, 2011.
- [26] J. A. C. Dias, C. De Marqui Jr., and A. Erturk, “Three-degree-of-freedom hybrid piezoelectric-inductive aeroelastic energy harvester exploiting a control surface,” *AIAA Journal*, vol. 53, no. 2, pp. 394–404, 2015.
- [27] D. Li, Y. Wu, A. D. Ronch, and J. Xiang, “Energy harvesting by means of flow-induced vibrations on aerospace vehicles,” *Progress in Aerospace Sciences*, vol. 86, pp. 28 – 62, 2016.
- [28] A. B. Rostami and M. Armandei, “Renewable energy harvesting by vortex-induced motions: Review and benchmarking of technologies,” *Renewable and Sustainable Energy Reviews*, vol. 70, pp. 193 – 214, 2017.
- [29] C. Wei and X. Jing, “A comprehensive review on vibration energy harvesting: Modelling and realization,” *Renewable and Sustainable Energy Reviews*, vol. 74, pp. 1 – 18, 2017.
- [30] M. Bashir, P. Rajendran, and S. Khan, “Energy harvesting from aerodynamic instabilities: Current prospect and future trends,” *IOP Conference Series: Material Science*, vol. 290, p. 012054, 01 2018.

- [31] T. Theodorsen, “General theory of aerodynamic instability and mechanism of flutter,” Tech. Rep. 496, Langley Memorial Aeronautical Laboratory, NACA.
- [32] J. Katz and A. Plotkin, *Low Speed Aerodynamics*. Cambridge University Press, 2001.
- [33] E. Albano and W. P. Rodden, “A doublet-lattice method for calculating lift distributions on oscillating surfaces in subsonic flows,” *AIAA Journal*, vol. 7, no. 2, pp. 279–285, 1969.
- [34] Y. Amini, H. Emdad, and M. Farid, “Finite element modeling of functionally graded piezoelectric harvesters,” *Composite Structures*, vol. 129, pp. 165–176, 2015.
- [35] Y. Amini, P. Fatehi, M. Heshmati, and H. Parandvar, “Time domain and frequency domain analysis of functionally graded piezoelectric harvesters subjected to random vibration: Finite element modeling,” *Composite Structures*, vol. 136, pp. 384–393, 2016.
- [36] Y. Shindo and F. Narita, “Dynamic bending/torsion and output power of s-shaped piezoelectric energy harvesters,” *International Journal of Mechanics and Materials in Design*, vol. 10, pp. 305–311, Sep 2014.
- [37] H. Lee, N. Sharpes, H. Abdelmoula, A. Abdelkefi, and S. Priya, “Higher power generation from torsion-dominant mode in a zigzag shaped two-dimensional energy harvester,” *Applied Energy*, vol. 216, pp. 494 – 503, 2018.
- [38] A. G. Muthalif and N. D. Nordin, “Optimal piezoelectric beam shape for single and broadband vibration energy harvesting: Modeling, simulation and experimental results,” *Mechanical Systems and Signal Processing*, vol. 54-55, pp. 417 – 426, 2015.
- [39] Y. Chen, X. Mu, T. Wang, W. Ren, Y. Yang, Z. L. Wang, C. Sun, and A. Y. Gu, “Flutter phenomenon in flow driven energy harvester—a unified theoretical model for “stiff” and “flexible” materials,” *Scientific Reports*, vol. 6, October 2016.
- [40] A. I. Aquino, J. K. Calautit, and B. R. Hughes, “Evaluation of the integration of the wind-induced flutter energy harvester (wifeh) into the built environment: Experimental and numerical analysis,” *Applied Energy*, vol. 207, pp. 61 – 77, 2017.
- [41] E. Meiling Zhu, J. Worthington, and J. Njuguna, “Analyses of power output of piezoelectric energy-harvesting devices directly connected to a load resistor

- using a coupled piezoelectric-circuit finite element method,” *IEEE Transactions, Ultrasonics, and Ferroelectrics*, vol. 56, no. 7, pp. 1309–1318, 2009.
- [42] Y. Yang and L. Tang, “Equivalent circuit modeling of piezoelectric energy harvesters,” *Journal of Intelligent Material Systems and Structures*, vol. 20, no. 18, pp. 2223–2235, 2009.
- [43] P. H. Wu and Y. C. Shu, “Finite element modeling of electrically rectified piezoelectric energy harvesters,” *Smart Materials and Structures*, vol. 24, no. 9, p. 094008, 2015.
- [44] D. Gedeon and S. J. Rupitsch, “Finite element based system simulation for piezoelectric vibration energy harvesting devices,” *Journal of Intelligent Material Systems and Structures*, vol. 29, no. 7, pp. 1333–1347, 2018.
- [45] G. Gafforelli, R. Ardito, and A. Corigliano, “Improved one-dimensional model of piezoelectric laminates for energy harvesters including three dimensional effects,” *Composite Structures*, vol. 127, pp. 369 – 381, 2015.
- [46] I. Fattahi and H. R. Mirdamadi, “Novel composite finite element model for piezoelectric energy harvesters based on 3D beam kinematics,” *Composite Structures*, vol. 179, pp. 161 – 171, 2017.
- [47] Y. Amini, H. Emdad, and M. Farid, “An accurate model for numerical prediction of piezoelectric energy harvesting from fluid structure interaction problems,” *Smart Materials and Structures*, vol. 23, no. 9, p. 095034, 2014.
- [48] Y. Lin and H. A. Sodano, “Concept and model of a piezoelectric structural fiber for multifunctional composites,” *Composites Science and Technology*, vol. 68, no. 7, pp. 1911 – 1918, 2008.
- [49] Y. Lin and H. A. Sodano, “Fabrication and electromechanical characterization of a piezoelectric structural fiber for multifunctional composites,” *Advanced Functional Materials*, vol. 19, no. 4, pp. 592–598, 2009.
- [50] Y. Lin and H. A. Sodano, “Electromechanical characterization of a active structural fiber lamina for multifunctional composites,” *Composites Science and Technology*, vol. 69, no. 11, pp. 1825 – 1830, 2009.
- [51] Y. Lin and H. A. Sodano, “A double inclusion model for multiphase piezoelectric composites,” *Smart Materials and Structures*, vol. 19, no. 3, p. 035003, 2010.

- [52] M. L. Dunn and H. Ledbetter, “Elastic moduli of composites reinforced by multiphase particles,” *Journal of Applied Mechanics*, vol. 62, no. 4, pp. 1023–1028, 1995.
- [53] M. Hori and S. Nemat-Nasser, “Double-inclusion model and overall moduli of multi-phase composites,” *Mechanics of Materials*, vol. 14, no. 3, pp. 189 – 206, 1993.
- [54] M. Hori and S. Nemat-Nasser, “Double-inclusion model and overall moduli of multi-phase composites,” *Journal of Engineering Materials and Technology*, vol. 116, no. 3, pp. 305–309, 1994.
- [55] M. L. Dunn and M. Taya, “An analysis of piezoelectric composite materials containing ellipsoidal inhomogeneities,” *Proceedings of the Royal Society London A*, vol. 443, no. 1918, pp. 265–287, 1993.
- [56] J. Eshelby, “The determination of the field of an ellipsoidal inclusion and related problems,” *Proceedings of the Royal Society London*, vol. 241, pp. 376–396, 1957.
- [57] Z. Hashin, “The elastic moduli of heterogeneous materials,” *Journal of Applied Mechanics*, vol. 29, pp. 143 – 150, 1962.
- [58] T. Mori and K. Tanaka, “Average stress in matrix and average elastic energy of materials with misfitting inclusions,” *Acta Metallurgica*, vol. 21, no. 5, pp. 571 – 574, 1973.
- [59] N. A. Abdullah, J. L. Curiel-Sosa, and M. Akbar, “Aeroelastic assessment of cracked composite plate by means of fully coupled finite element and doublet lattice method,” *Composite Structures*, 2018.
- [60] H. L. W. Chan and J. Unsworth, “Simple model for piezoelectric ceramic/polymer 1-3 composites used in ultrasonic transducer applications,” *IEEE T Ultrason Ferr*, vol. 36, pp. 434–441, July 1989.
- [61] M. L. Dunn and M. Taya, “Micromechanics predictions of the effective electroelastic moduli of piezoelectric composites,” *International Journal of Solids and Structures*, vol. 30, no. 2, pp. 161 – 175, 1993.
- [62] G. Odegard, “Constitutive modeling of piezoelectric polymer composites,” *Acta Materialia*, vol. 52, no. 18, pp. 5315 – 5330, 2004.
- [63] R. Hashemi, G. Weng, M. Kargarnovin, and H. Shodja, “Piezoelectric composites with periodic multi-coated inhomogeneities,” *International Journal of Solids and Structures*, vol. 47, no. 21, pp. 2893 – 2904, 2010.

- [64] H.-Y. Kuo, “Multicoated elliptic fibrous composites of piezoelectric and piezomagnetic phases,” *International Journal of Engineering Science*, vol. 49, no. 7, pp. 561 – 575, 2011.
- [65] M. H. Malakooti and H. A. Sodano, “Multi-inclusion modeling of multiphase piezoelectric composites,” *Composites Part B: Engineering*, vol. 47, pp. 181 – 189, 2013.
- [66] J. Y. Li and M. L. Dunn, “Micromechanics of magneto-electro-elastic composite materials: Average fields and effective behavior,” *Journal of Intelligent Material Systems and Structures*, vol. 9, no. 6, pp. 404–416, 1998.
- [67] F. Dinzart and H. Sabar, “Magneto-electro-elastic coated inclusion problem and its application to magnetic-piezoelectric composite materials,” *International Journal of Solids and Structures*, vol. 48, no. 16, pp. 2393 – 2401, 2011.
- [68] H.-Y. Kuo and K. Bhattacharya, “Fibrous composites of piezoelectric and piezomagnetic phases,” *Mechanics of Materials*, vol. 60, pp. 159 – 170, 2013.
- [69] K. Zhou, H. J. Hoh, X. Wang, L. M. Keer, J. H. Pang, B. Song, and Q. J. Wang, “A review of recent works on inclusions,” *Mechanics of Materials*, vol. 60, pp. 144 – 158, 2013.
- [70] K. Sairajan, G. Aglietti, and K. Mani, “A review of multifunctional structure technology for aerospace applications,” *Acta Astronautica*, vol. 120, pp. 30 – 42, 2016.
- [71] Y. Wang and D. J. Inman, “Simultaneous energy harvesting and gust alleviation for a multifunctional composite wing spar using reduced energy control via piezoceramics,” *Journal of Composite Material*, vol. 47, no. 1, pp. 125–146, 2013.
- [72] N. Tsushima and W. Su, “Flutter suppression for highly flexible wings using passive and active piezoelectric effects,” *Aerospace Science Technology*, vol. 65, pp. 78 – 89, 2017.
- [73] A. Lenk, R. G. Ballas, R. Werthschützky, and G. Pfeifer, *Electromechanical Systems in Microtechnology and Mechatronics: Electrical, Mechanical and Acoustic Networks, their Interactions and Applications*. Microtechnology and MEMS, Springer Berlin Heidelberg, 2010.
- [74] Standards Committee of the IEEE Ultrasonics, Ferroelectrics, and Frequency Control Society, “IEEE Standard on Piezoelectricity,” *ANSI/IEEE Std 176-1987*, 1988.

- [75] A. Lenk, R. G. Ballas, R. Werthschützky, and G. Pfeifer, *Electromechanical Systems in Microtechnology and Mechatronics: Electrical, Mechanical and Acoustic Networks, their Interactions and Applications*, ch. 9, pp. 313–412. Microtechnology and MEMS, Springer Berlin Heidelberg, 2010.
- [76] R. G. Ballas, *Piezoelectric Multilayer Beam Bending Actuators: Static and Dynamic Behavior and Aspects of Sensor Integration*. Microtechnology and MEMS, Springer Berlin Heidelberg, 2007.
- [77] F. Lu, H. Lee, and S. Lim, “Modeling and analysis of micro piezoelectric power generators for micro-electromechanical-systems applications,” *Smart Materials and Structures*, vol. 13, no. 1, pp. 57–63, 2004.
- [78] S. Beeby, M. Tudor, and N. White, “Energy harvesting vibration sources for microsystems applications,” *Measurement Science and Technology*, vol. 17, no. 12, pp. R175–R195, 2006.
- [79] MSC Software Corporation, *MSC Nastran 2014 Dynamic Analysis User’s Guide*. Springer Berlin Heidelberg, 2014.
- [80] A. Erturk and D. J. Inman, *Piezoelectric Energy Harvesting*, ch. 3, pp. 49–96. John Wiley & Sons, 2011.
- [81] T. Hughes, J. Cottrell, and Y. Bazilevs, “Isogeometric analysis: CAD, finite elements, NURBS, exact geometry and mesh refinement,” *Computer Methods in Applied Mechanics and Engineering*, vol. 194, no. 39–41, pp. 4135 – 4195, 2005.
- [82] C. H. Thai, H. Nguyen-Xuan, N. Nguyen-Thanh, T.-H. Le, T. Nguyen-Thoi, and T. Rabczuk, “Static, free vibration, and buckling analysis of laminated composite Reissner-Mindlin plates using NURBS-based isogeometric approach,” *International Journal for Numerical Methods in Engineering*, vol. 91, no. 6, pp. 571–603, 2012.
- [83] Y. Kwon and H. Bang, *The Finite Element Method Using MATLAB, Second Edition*. Mechanical and Aerospace Engineering Series, CRC Press, 2000.
- [84] J. Ainsworth, C. Collier, P. Yarrington, R. Lucking, and J. Locke, “Airframe wingbox preliminary design and weight prediction,” in *69th Annual Conference on Mass Properties, Virginia Beach, Virginia*, p. 41, 05/2010 2010.
- [85] M. H. Sadraey, *Aircraft Design A System Engineering Approach*. John Wiley & Sons, 2013.

- [86] G. Voyiadjis and P. Kattan, *Mechanics of Composite Materials with MATLAB*. Springer Berlin Heidelberg, 2005.
- [87] J. Y. Li, “Magnetoelastoelectric multi-inclusion and inhomogeneity problems and their applications in composite materials,” *International Journal of Engineering Science*, vol. 38, no. 18, pp. 1993 – 2011, 2000.
- [88] Y. Mikata, “Determination of piezoelectric eshelby tensor in transversely isotropic piezoelectric solids,” *International Journal of Engineering Science*, vol. 38, no. 6, pp. 605 – 641, 2000.
- [89] H.-Y. Kuo and C.-Y. Peng, “Magnetolectricity in coated fibrous composites of piezoelectric and piezomagnetic phases,” *International Journal of Engineering Science*, vol. 62, pp. 70 – 83, 2013.
- [90] F. Dinzart and H. Sabar, “Electroelastic behavior of piezoelectric composites with coated reinforcements: Micromechanical approach and applications,” *International Journal of Solids and Structures*, vol. 46, no. 20, pp. 3556 – 3564, 2009.
- [91] Y. Koutsawa, S. Belouettar, A. Makradi, and S. Tiem, “X-FEM implementation of VAMUCH: Application to active structural fiber multi-functional composite materials,” *Composite Structures*, vol. 94, no. 4, pp. 1297 – 1304, 2012.
- [92] D. P. Raymer, *Aircraft Design: A Conceptual Approach*. AIAA Education Series, American Institute of Aeronautics and Astronautics, Inc., 1992.
- [93] M. Wagner and G. Norris, *Boeing 787 Dreamliner*. MBI Publishing Company, 2009.
- [94] O. Gohardani, M. C. Elola, and C. Elizetxea, “Potential and prospective implementation of carbon nanotubes on next generation aircraft and space vehicles: A review of current and expected applications in aerospace sciences,” *Progress in Aerospace Sciences*, vol. 70, pp. 42 – 68, 2014.
- [95] N. Yann, *eTAXI – Taxiing aircraft with engines stopped*, pp. 2–10. AIRBUS S.A.S., 01/2013 2013.
- [96] D. Scholz, “An optional APU for passenger aircraft,” in *5th Council of European Aerospace Societies Air and Space Conference: Challenges in European Aerospace, Delft*, 11/2015 2015.

- [97] B. D. Freed and V. Babuska, “Finite element modeling of composite piezoelectric structures with MSC/NASTRAN,” *Proceeding of SPIE*, vol. 3041, pp. 676–688, 1997.
- [98] F. Cote, P. Masson, N. Mrad, and V. Cotoni, “Dynamic and static modelling of piezoelectric composite structures using a thermal analogy with MSC/NASTRAN,” *Composite Structures*, vol. 65, no. 3, pp. 471 – 484, 2004.
- [99] S. Rao, *The Finite Element Method in Engineering*. Elsevier Butterworth Heine-
mann, 2005.
- [100] M. Staworko and T. Uhl, “Modeling and simulation of piezoelectric elements-
comparison of available methods and tools,” *Mechanics*, vol. 27, no. 4, pp. 161–
171, 2008.
- [101] A. Erturk and D. J. Inman, *Piezoelectric Energy Harvesting*. 2011.
- [102] J. R. Wright and J. E. Cooper, *Introduction to Aircraft Aeroelasticity and Loads*.
John Wiley & Sons, Ltd., 2007.
- [103] *MSC Nastran Version 68 Aeroelastic Analysis User’s Guide*. MSC Software Cor-
poration, 2002.
- [104] R. Harder and R. Desmarais, “Interpolation using surface splines,” *Journal of
Aircraft*, vol. 9, no. 2, pp. 189–191, 1972.
- [105] R. Hewston and S. R. Dorling, “An analysis of observed daily maximum wind
gusts in the uk,” *Journal of Wind Engineering and Industrial Aerodynamics*,
vol. 99, no. 8, pp. 845 – 856, 2011.
- [106] <http://asm.matweb.com/>, Accessed: June 2018.
- [107] S. R. Anton, A. Erturk, and D. J. Inman, “Bending strength of piezoelectric
ceramics and single crystals for multifunctional load-bearing applications,” *IEEE
Transactions, Ultrasonics and Ferroelectrics*, vol. 59, no. 6, pp. 1085 – 1092, 2012.
- [108] ESDU, “IHS ESDU 69023 Average gust frequencies subsonic transport aircraft,”
tech. rep., 1969.
- [109] J. Cottrell, A. Reali, Y. Bazilevs, and T. Hughes, “Isogeometric analysis of struc-
tural vibrations,” *Computer Methods in Applied Mechanics and Engineering*,
vol. 195, no. 41–43, pp. 5257 – 5296, 2006. John H. Argyris Memorial Issue.
Part II.

- [110] Y. Bazilevs, V. M. Calo, T. J. R. Hughes, and Y. Zhang, “Isogeometric fluid-structure interaction: theory, algorithms, and computations,” *Computational Mechanics*, vol. 43, no. 1, pp. 3–37, 2008.
- [111] J. Cottrell, T. Hughes, and Y. Bazilevs, *Isogeometric Analysis: Toward Integration of CAD and FEA*. Wiley, 2009.
- [112] D. Rypl and B. Patzák, “From the finite element analysis to the isogeometric analysis in an object oriented computing environment,” *Advances in Engineering Software*, vol. 44, no. 1, pp. 116 – 125, 2012.
- [113] R. Sevilla, S. Fernandez-Mendez, and A. Huerta, “NURBS-enhanced finite element method (NEFEM),” *International Journal for Numerical Methods in Engineering*, vol. 76, no. 1, pp. 56–83, 2008.
- [114] D. J. Benson, Y. Bazilevs, E. De Luycker, M.-C. Hsu, M. Scott, T. J. R. Hughes, and T. Belytschko, “A generalized finite element formulation for arbitrary basis functions: From isogeometric analysis to XFEM,” *International Journal for Numerical Methods in Engineering*, vol. 83, no. 6, pp. 765–785, 2010.
- [115] J. Kiendl, K.-U. Bletzinger, J. Linhard, and R. Wüchner, “Isogeometric shell analysis with Kirchhoff–Love elements,” *Computer Methods in Applied Mechanics and Engineering*, vol. 198, no. 49–52, pp. 3902 – 3914, 2009.
- [116] D. Benson, Y. Bazilevs, M. Hsu, and T. Hughes, “Isogeometric shell analysis: The Reissner–Mindlin shell,” *Computer Methods in Applied Mechanics and Engineering*, vol. 199, no. 5–8, pp. 276 – 289, 2010.
- [117] R. Echter, B. Oesterle, and M. Bischoff, “A hierarchic family of isogeometric shell finite elements,” *Computer Methods in Applied Mechanics and Engineering*, vol. 254, pp. 170 – 180, 2013.
- [118] S. Shojaee, N. Valizadeh, E. Izadpanah, T. Q. Bui, and T.-V. Vu, “Free vibration and buckling analysis of laminated composite plates using the NURBS-based isogeometric finite element method,” *Composite Structures*, vol. 94, no. 5, pp. 1677 – 1693, 2012.
- [119] S. Yin, T. Yu, T. Q. Bui, S. Xia, and S. Hirose, “A cutout isogeometric analysis for thin laminated composite plates using level sets,” *Composite Structures*, vol. 127, pp. 152 – 164, 2015.

- [120] T. Yu, S. Yin, T. Q. Bui, S. Xia, S. Tanaka, and S. Hirose, “NURBS-based isogeometric analysis of buckling and free vibration problems for laminated composites plates with complicated cutouts using a new simple FSDT theory and level set method,” *Thin-Walled Structures*, vol. 101, pp. 141 – 156, 2016.
- [121] V. P. Nguyen, C. Anitescu, S. P. Bordas, and T. Rabczuk, “Isogeometric analysis: An overview and computer implementation aspects,” *Mathematics and Computers in Simulation*, vol. 117, pp. 89 – 116, 2015.
- [122] G. Beer and S. Bordas, *Isogeometric Methods for Numerical Simulation*. CISM International Centre for Mechanical Sciences, Springer Vienna, 2015.
- [123] C. de Falco, A. Reali, and R. Vazquez, “GeoPDEs: A research tool for isogeometric analysis of PDEs,” *Advances in Engineering Software*, vol. 42, no. 12, pp. 1020 – 1034, 2011.
- [124] R. Vazquez, “A new design for the implementation of isogeometric analysis in Octave and Matlab: GeoPDEs 3.0,” *Computers and Mathematics with Applications*, vol. 72, no. 3, pp. 523 – 554, 2016.

APPENDIX A

A brief state-of-the-art of isogeometric analysis for structural analysis

Computational methods have become one of the major core on numerous engineering analysis. Research in both integral and differential equation based methods has grown over the past few decades. However, despite of these growth, there is always a gap between the engineering design geometry and the engineering analysis based on this geometry. In conventional engineering analysis, it is required to construct a discrete representation of the design geometry by some approximation objects, i.e. meshed elements. Thus, the accuracy of the engineering analysis result depends on how close this discrete representation approximate the design geometry. Hence, errors due to redundant geometry approximation is unavoidable. In order to bridge this concern, an alternate approach has been introduced by Hughes and colleagues [81], it is isogeometric analysis (IGA).

The concept of IGA integrates CAD (Computer Aided Design) process with computational engineering analysis by means of spline functions. Practically, in commercial CAD software, spline-based geometry construction technique has been established for engineering design and manufacturing. Hughes and colleagues utilised NURBS (Non-Uniform Rational B-splines) based geometry and applied the spline functions as the basis for engineering analysis [81]. Hence, the design geometry is directly applicable for engineering analysis.

Hughes and colleagues [81] NURBS-based IGA has been successfully implemented on a number of structural and fluid analyses. Furthermore, the extension of Hughes et. al work [81], can be seen in the works of Cotrell et. al [109] and Bazilevs et. al [110] with focuses on structural vibration problems and fluid-structure interaction problems. The reader is referred to [111] for more details of these works.

Rypl and Patzak [112] compare IGA and Finite Element Method (FEM) highlighting significant differences. Rypl and Patzak stated that one of the major differences is the ability of IGA to represent the exact geometry rather than to approximate the geometry. Thus, there is no interpolation between nodes as NURBS (or B-spline func-

tions) are used to construct the shape function. NURBS-based isogeometric element also proven to provide better accuracy compare to polynomial-based isoparametric element [113, 114].

IGA offers more flexibility on the use of a higher order methodology by simply elevating the orders of the basis functions [112]. A two dimensional (2D) IGA module for plane stress case is described by Rypl and Patzak [112]. Furthermore, in the field of IGA for 2D solid mechanics, aside of plane stress/strain problems, focus on the development of 2D shell/plate analysis has also been a great interest in recent years [115–117].

The development of IGA in plate analysis follows the development on the laminated composite analysis. One of the earliest articles on IGA for laminated composites was developed by means of the Classical Plate Theory [118]. Based on the classical plate theory, the IGA integrated with the level sets for capturing the defects or cutouts in the thin laminated composite plates have been presented in [119]. More recently the NURBS based IGA with level sets has also been applied tto buckling and vibration analysis of laminated composite plates with complicated cutouts, but using a new simple first-order shear deformation plate theory (FSDT) instead [120].

An overview of recent developments in the field of isogeometric analysis can be found in Nguyen et. al [121]. In this review, guidelines and development of an IGA computational code written in MATLAB[©] is described. The strategy applied to this computational code for extended isogeometric analysis (XIGA) has been detailed in [122]. To the author's knowledge, there are only a few published articles describing in details the guidelines for computational coding of IGA, e.g., see [123, 124].

APPENDIX B

Isogeometric analysis formulation for laminated composite

The isogeometric formulation for laminated composite based on First Shear Deformation Theory (FSDT) and Reissner-Mindlin Plate is presented here. In the isoparametric finite element formulation, a particular point in an element is associated with the shape functions and the locations of all the nodes.

$$R(x, y) = \sum_{A=1}^{nn} \bar{N}_A(t, s) R_A(x_A, y_A) \quad (\text{B.1})$$

where R is a point in the element with coordinate (x, y) . While, nn is the number of nodes in an element and $N_A(t, s)$ is the shape function of a particular node, R_A , associated with the point R .

In the NURBS-based isogeometric formulation, the surface or element, is also represented by the NURBS function. Hence, the shape functions, N_{ii} , are associated with the basis functions and the control points of the NURBS surface [82]. Considering a NURBS surface with control net B_A and weighting value w_A , the point R can be written as

$$R(t, s) = \sum_{A=1}^{(n+1) \times (m+1)} \bar{N}_A(t, s) B_A \quad (\text{B.2})$$

where the shape function ,

$$\bar{N}_A(t, s) = \frac{N_A(t, s) w_A}{w(t, s)} \quad (\text{B.3})$$

and

$$N_A(t, s) = N_{i,k}(t) M_{j,l}(s) \quad (\text{B.4})$$

Hence, the displacement at a particular point on the element is written as

$$\mathbf{u}(t, s) = \sum_{A=1}^{(n+1) \times (m+1)} \bar{N}_A(t, s) \mathbf{u}_A \quad (\text{B.5})$$

where $\mathbf{u} = [u_x \ u_y \ u_z \ \theta_{xz} \ \theta_{yz}]^T$ is the displacement associated with 3 translational and 2 rotational degree of freedoms.

Adopting the formulation of Reissner-Mindlin plate with FSDT assumption, the shape function derivatives for membrane, bending and shear component are written as

$$\mathbf{B}_A^m = \begin{bmatrix} \bar{N}_{A,x} & 0 & 0 & 0 & 0 \\ 0 & \bar{N}_{A,y} & 0 & 0 & 0 \\ \bar{N}_{A,x} & \bar{N}_{A,y} & 0 & 0 & 0 \end{bmatrix} \quad (\text{B.6})$$

$$\mathbf{B}_A^b = \begin{bmatrix} 0 & 0 & 0 & \bar{N}_{A,x} & 0 \\ 0 & 0 & 0 & 0 & \bar{N}_{A,y} \\ 0 & 0 & 0 & \bar{N}_{A,x} & \bar{N}_{A,y} \end{bmatrix} \quad (\text{B.7})$$

$$\mathbf{B}_A^s = \begin{bmatrix} 0 & 0 & \bar{N}_{A,x} & \bar{N}_A & 0 \\ 0 & 0 & \bar{N}_{A,y} & 0 & \bar{N}_A \end{bmatrix} \quad (\text{B.8})$$

The stiffness matrix of the plate element, \mathbf{K}^e , then obtained as

$$\begin{aligned} \mathbf{K}^e = & \int_{\Omega^e} (\mathbf{B}^m)^T \mathbf{A}_c \mathbf{B}^m d\Omega^e + \int_{\Omega^e} (\mathbf{B}^m)^T \mathbf{B}_c \mathbf{B}^b d\Omega^e + \\ & \int_{\Omega^e} (\mathbf{B}^b)^T \mathbf{B}_c \mathbf{B}^m d\Omega^e + \int_{\Omega^e} (\mathbf{B}^b)^T \mathbf{D}_c \mathbf{B}^b d\Omega^e + \\ & \int_{\Omega^e} (\mathbf{B}^s)^T \mathbf{H}_c \mathbf{B}^s d\Omega^e \end{aligned} \quad (\text{B.9})$$

where Ω^e is the domain of the element. The $\mathbf{A}_c, \mathbf{B}_c, \mathbf{D}_c$ and \mathbf{H}_c matrices are the elastic of the laminate properties which represent the in-plane, bending-extension coupling, bending and inter-laminar shear components. These matrices often called as one set, the A-B-D-H matrices, and are the function of the material constitutive matrix and the orientation of the lamina. Furthermore, the mass matrix of the element, \mathbf{M}^e , is written as

$$\mathbf{M}^e = \int_{\Omega^e} (\bar{N}_A)^T \mathbf{m} \bar{N}_A d\Omega^e \quad (\text{B.10})$$

with

$$\mathbf{m} = \rho \begin{bmatrix} h^e & 0 & 0 & 0 & 0 \\ 0 & h^e & 0 & 0 & 0 \\ 0 & 0 & h^e & 0 & 0 \\ 0 & 0 & 0 & h^{e3}/12 & 0 \\ 0 & 0 & 0 & 0 & h^{e3}/12 \end{bmatrix} \quad (\text{B.11})$$

where ρ and h^e are the material density and the thickness of the element.

For the free vibration analysis, the eigenvalue problem is written as

$$(\mathbf{K} - \omega_n^2 \mathbf{M}) \hat{\mathbf{u}} = 0 \quad (\text{B.12})$$

and for dynamic response problem,

$$(\mathbf{K} - \omega^2 \mathbf{M})\mathbf{u} = \mathbf{f} \quad (\text{B.13})$$

where \mathbf{K} , \mathbf{M} , ω_n , $\hat{\mathbf{u}}$ are the global stiffness matrix, global mass matrix, the natural frequency and the eigenvector. While \mathbf{u} is the displacement vector exerted by the force vector \mathbf{f} .

APPENDIX C

Example of MATLAB code for the hybrid computational/ analytical method

```
% Erturk-Inman bimorph with experimental validation
close all;
clear all;
clc;
%% Input Beam Layer Properties
nlay=3;%number of layers
layprop=zeros(7,nlay);%layer properties initiation
lb=(24.53e-3);%meter - beam length
wb=(6.4e-3);%meter - beam width
% Assume uniform cross section
for i=1:nlay
layprop(1,i)=lb;%meter - layers's length
layprop(2,i)=wb;%meter - layers's width
end
layprop(3,1)=0.265e-3;%meter - thickness - material 1 (PZT 5H)
layprop(3,2)=0.140e-3;%meter - thickness - material 2 (Aluminium)
layprop(3,3)=0.265e-3;%meter - thickness - material 3 (PZT 5H)
layprop(4,1)=(1/60.6)*1e-9;%m2/N - compliance (s11) - PZT 5H
layprop(4,2)=(1/105)*1e-9;%m2/N - compliance (s11) - Aluminium
layprop(4,3)=(1/60.6)*1e-9;%m2/N - compliance (s11) - PZT 5H
layprop(5,1)=0;% should be -274e-12 m/V;% - charge constant (d31) - PZT 5H
%...this is to avoid cancellation at sum of the voltage
%...effect of series or parallel connection with this layer
%...will be incorporated in electromechanical coupling calculation
layprop(5,2)=0;%m/V - charge constant (d31) - Aluminium
layprop(5,3)=-274e-12;%m/V - charge constant (d31) - PZT 5H
layprop(6,1)=0;% should be 3400*8.85*(10-12);%Farad/m - permitvty - PZT 5H
```

```

%...this is to avoid cancellation at sum of the voltage
%...effect of series or parallel connection with this layer
%...will be incorporated in electromechanical coupling calculation
layprop(6,2)=0;%Farad/m - permittvty - Aluminium
layprop(6,3)=3400*8.85*(10^-12);%Farad/m - permittvty - PZT 5H
layprop(7,1)=7500;%kg/(m^3) - density - PZT 5H
layprop(7,2)=9000;%kg/(m^3) - density - Aluminium
layprop(7,3)=7500;%kg/(m^3) - density - PZT 5H
%% Neutral axis, beam flexural stiffness and mpiezo calculations
l=zeros(1,nlay);%array of layers's length
w=zeros(1,nlay);%array of layers's width
h=zeros(1,nlay);%array of layers's thickness
s11=zeros(1,nlay);%array of layers's material compliance
d31=zeros(1,nlay);%array of layers's piezoelectric charge constant
eps33=zeros(1,nlay);%array of layers's permittivity (at constant stress)
rho=zeros(1,nlay);%array of layers's density
for i=1:nlay
l(i)=layprop(1,i);
w(i)=layprop(2,i);
h(i)=layprop(3,i);
s11(i)=layprop(4,i);
d31(i)=layprop(5,i);
eps33(i)=layprop(6,i);
rho(i)=layprop(7,i);
end
z1=0;hj=0;z2=0;z3=0;
for i=1:nlay
z1= z1+(w(i)*(h(i)^2)/s11(i));
hj= hj+h(i);
z2= z2+((w(i)*h(i)/s11(i))*hj);
z3= z3+(w(i)*h(i)/s11(i));
end
zbar=-((z1)-(2*z2))/(2*z3);%meter (measured from bottom) - neutral axis
clay=zeros(1,nlay);hu=0;
mlay=zeros(1,nlay);
for i=1:nlay
hu = hu+h(i);
hl = hu-h(i);

```

```

clay(i)=(w(i)/s11(i))*((3*h(i)*(zbar-hu)*(zbar-hl))+h(i)^3);
mlay(i)=(w(i)*d31(i)/(s11(i)*h(i)))*... ((2*zbar*h(i))-(2*h(i)*hu)+h(i)^2);
end
C=sum(clay)/3;%Nm^2 - Beam flexural stiffness
mpiezo=sum(mlay)/2;%Nm/V - internal moment due to piezo per unit volt
%% Dynamic bending modes and natural frequencies (clamped-free beam)
%%The first five solutions of characteristic equation
%%(not calculated here, taken from reference)
nmod=2;%number of modeshapes
kl=[1.8751 4.6941 7.8548 10.9955 14.137];
k=kl./lb;%1/m - characteristic solution per unit length
mass=0;
for i=1:nlay
mass=mass+(l(i)*w(i)*h(i)*rho(i));%kg - mass of the beam
end
miu=mass/lb;
for i=1:nmod
natomg(i)=((kl(i)^2)/(lb^2))*(sqrt(C/miu));%rad/s - angular natural freq
natfrq(i)=natomg(i)/(2*pi);%Hz - natural freq
end
%% Spanwise location
dx=1e-4;
x=(0:dx:lb)';%spanwise location along the beam
nx=numel(x);
%%Rayleigh function
ckx=(cosh(x*k)-cos(x*k))/2;
skx=(sinh(x*k)-sin(x*k))/2;
ckl=(cosh(kl)+cos(kl))/2;
skl=(sinh(kl)+sin(kl))/2;
for i=1:nmod
csl(i)=ckl(i)/skl(i);
Zmod(:,i)=ckx(:,i)-(skx(:,i)*csl(i));%mode shapes
end
for i=1:nmod
dz(:,i)=gradient(Zmod(:,i),dx);
dzl(i)=dz(nx,i);
am(i)=(sin(kl(i)).*sinh(kl(i)))./(sinh(kl(i))+sin(kl(i)));
kla(i)=kl(i).*am(i);

```

```

h11(i)=-4.*kla(i).*dzl(i)/((lb^2)*(miu));
end
%%Erturk - Technique
sigma = (sin(kl)-sinh(kl))./(cos(kl)+cosh(kl));
for i=1:nmod
Phimod(:,i)=sqrt(1/(miu*lb))*...
((cos(k(i)*x)-cosh(k(i)*x))+ (sigma(i)*(sin(k(i)*x)-sinh(k(i)*x))));
end
%%Slope of mode shapes along the span
for i=1:nmod
dphi(:,i)=gradient(Phimod(:,i),dx);
end
figure(1)
for i=1:nmod
plot((x*1000),(Zmod(:,i))*(-2)*sqrt(1/(miu*lb)), '*')
hold on
plot((x*1000),(Phimod(:,i)))
hold on
end
xlabel('x(mm)');
ylabel('Zmodes');
title('Mode Shapes');
grid on
%% Admittance matrix and dynamic response of base exc, m.Wo(omg^2) cos omg*t
zeta=[0.00874 0.00874 0.00874 0.00874 0.00874];%damping ratio
frq=natfrq(1);%Hz - input excitation frequency
omg=2*pi*frq;%rad/s - input angular excitation frequency
W0=1e-6;%meter - base displacement amplitude
j=sqrt(-1);
for i=1:nmod
Trtip(i)=abs(2*sigma(i)*(cos(kl(i))-cosh(kl(i)))+(sigma(i)*(sin(kl(i))-sinh(kl(i)))))...
/(kl(i)*((natomg(i)^2)-(omg^2)+(j*2*zeta(i)*natomg(i)*omg)));
end
%%Relative tip displacement(absolute value)
wrtip=W0*(omg^2)*sum(Trtip);
for i=1:nmod
for o=1:nx
if Phimod(o,i)~0

```

```

weight(o,i)=-1;
elseif Phimod(o,i)~=0
weight(o,i)=1;
elseif Phimod(o)==0
weight(o,i)=0;
end
Tr(o,i)=2*sigma(i)*((cos(k(i)*x(o))-cosh(k(i)*x(o)))+...
(sigma(i)*(sin(k(i)*x(o))-sinh(k(i)*x(o)))))...
/(kl(i)*((natomg(i)^2)-(omg^2)+(j*2*zeta(i)*natomg(i)*omg)));
Trm(o,i)=(Tr(o,i)).*weight(o,i);
end
end
%%Relative tip displacement along the span
for i=1:nx
wr(i,:)=-W0*(omg^2)*sum(Trm(i,:));
end
figure(2)
plot((x*1000),abs(wr)*1000)
xlabel('x (mm)');
ylabel('Tip Displacement (mm)');
title('Relative Tip Displacement Amplitude');
grid on
%%Slope of Relative tip displacement along the span
dwr=gradient(wr,dx);
%% Power Output Calculations
R=10:10:10000000;%Ohm - Resistance load
nR=numel(R);
A=lb*wb;
j=sqrt(-1);
hu=0;
for m=1:nlay
hu = hu+h(m);
hl = hu-h(m);
hu2hl2(m)=((zbar-hu)^2)-((zbar-hl)^2);
end
theta=(d31(m)*(h(m)+h(m-1))*wb)/(2*s11(m));% Series
Cp = (1/2)*A*(eps33(m)-((d31(m)^2)/s11(m)))/h(m);% Series
% theta=2*(d31(m)*hu2hl2(m)*wb)*(2)/(2*s11(m)*h(m));% Parallel

```

```

% Cp = 2*A*(eps33(m)-((d31(m)^2)/s11(m)))*(1/2)/h(m);% Parallel
% - From FEM - %
dwrFEb=3.552193E-05+((5.052968E-03)*j);%(rad) - tip displacement angle...
%... from FEM results for base excitation - 508.5 HZ
dwrFEb=3.384613E-07+((-8.776712E-05)*j);%(rad) - tip displacement angle...
%... from FEM results for bending moment excitation - 508.5 Hz
momentFE=1e-6;%(Nm) - bending moment excitation for FEM
h11FE=dwrFEb/momentFE;%(1/(Nm)) - Admittance matrix...
%... of angle - moment from FEM
ts=(-j)*omg*(theta*dwr(nx,1));
tsFE=(-j)*omg*(theta*dwrFEb);
for i=1:nmod
thetar(i)= theta*dphi(nx,i);
thesig(i)=(-j)*omg*(thetar(i)^2*sigma(i)*(sqrt(mass)))/...
(kl(i)*((natomg(i)^2)-(omg^2)+(j*2*zeta(i)*natomg(i)*omg)));
thethe(i)=(j)*omg*(thetar(i)*thetar(i))/...
((natomg(i)^2)-(omg^2)+(j*2*zeta(i)*natomg(i)*omg));
theh11(i)=(j)*omg*((theta^2)*h11(i))/...
((natomg(i)^2)-(omg^2)+(j*2*zeta(i)*natomg(i)*omg));
end
ksiA=sum(thesig);
ksiB=sum(thethe);
ksiC=sum(theh11);
ksiCFE=(j)*omg*((theta^2)*h11FE);
g=9.81;%(m/s^2) - gravitational acceleration for normalization
for n=1:nR
%Present model - Analytical
U1(n)= (ts/((1/(R(n)))+(j*omg*Cp)-(ksiC)));
Ug1(n) = U1(n)*g/(-W0*(omg^2));
Watt1(n)=((U1(n)).^2)/R(n);
Wattg1(n) = Watt1(n)*(g^2)/((-W0*(omg^2))^2);
%Present model - FEM
U1FE(n)= (tsFE/((1/(R(n)))+(j*omg*Cp)+(ksiCFE)));
Ug1FE(n) = U1FE(n)*g/(-W0*(omg^2));
Watt1FE(n)=((U1FE(n)).^2)/R(n);
Wattg1FE(n) = Watt1FE(n)*(g^2)/((-W0*(omg^2))^2);
%Erturk-Inman's model
U2(n)= (ksiA/((1./R(n))+(j*omg*Cp)+(ksiB)))*(-W0*(omg^2));

```

```

Ug2(n) = U2(n)*g/(-W0*(omg^2));
Watt2(n)=(U2(n).^2)/R(n);
Wattg2(n) = Watt2(n)*(g^2)/((-W0*(omg^2))^2);
end
%Erturk-Inman's experiment
Rexp = 1e3*[0.47 1.2 6.7 9.9 21.5 44.9 90.9 247.8 319.2 403.9 498.7 995.0];
Ugexp = [0.15 0.35 1.21 1.46 1.90 2.20 2.37 2.49 2.51 2.52 2.53 2.55];
Wattgexp = [4.72e-05 1.02e-04 2.17e-04 2.14e-04 1.68e-04 1.08e-04...
6.19e-05 2.51e-05 1.97e-05 1.57e-05 1.28e-05 6.53e-06];
figure(3)
subplot(1,1,1);
loglog((R)',(abs(Ug2))),'-k','linewidth',2)
hold on
loglog((R)',(abs(Ug1FE))),'-r','linewidth',2)
loglog((R)',(abs(Ug1))),'-g','linewidth',2)
loglog((Rexp)',(abs(Ugexp))),'ob','linewidth',2)
xlabel('Resistance (Ohm)');
ylabel('Voltage (V per g)');
title('Voltage Amplitude vs Resistance');
legend('Erturk-Inman Model','Present Model (FEM)','Present Model (Analytical)',...
'Erturk-Inman Experiment')
axis ([1e2 1e7 1e-3 1e2]);
grid off
annotation('rectangle',[0.40 0.60 0.05 0.05])
annotation('arrow',[0.45 0.55],[0.60 0.55])
axes('position',[.55, .25, .3, .3])
plot((R)',(abs(Ug2))),'-k','linewidth',2)
hold on
plot((R)',(abs(Ug1FE))),'-r','linewidth',2)
plot((R)',(abs(Ug1))),'-g','linewidth',2)
plot((Rexp)',(abs(Ugexp))),'ob','linewidth',2)
axis ([0.60*(10^4) 1.05*(10^4) 1.15*(10^0) 1.55*(10^0)]);
figure(4)
subplot(1,1,1);
loglog((R)',(abs(Wattg2)*1e6)),'-k','linewidth',2)
hold on
loglog((R)',(abs(Wattg1FE)*1e6)),'-r','linewidth',2)
loglog((R)',(abs(Wattg1)*1e6)),'-g','linewidth',2)

```

```
loglog((Rexp)',(abs(Wattgexp)*1e6)', 'ob', 'linewidth', 2)
xlabel('Resistance (Ohm)');
ylabel('Power (micro-Watts per g2)');
title('Power Amplitude vs Resistance');
legend('Erturk-Inman Model', 'Present Model (FEM)', 'Present Model (Analytical)', ...
'Erturk-Inman Experiment')
axis ([1e2 1e7 1e-1 1e4]);
grid off
annotation('rectangle', [0.4 0.625 0.05 0.05])
annotation('arrow', [0.425 0.425], [0.625 0.525])
axes('position', [.30, .225, .3, .3])
plot((R)', (abs(Wattg2)*1e6)', '-k', 'linewidth', 2)
hold on
plot((R)', (abs(Wattg1FE)*1e6)', '-r', 'linewidth', 2)
plot((R)', (abs(Wattg1)*1e6)', '-g', 'linewidth', 2)
plot((Rexp)', (abs(Wattgexp)*1e6)', 'ob', 'linewidth', 2)
axis ([0.60*(104) 1.05*(104) 2.10*(102) 2.25*(102)]);
grid off
```

APPENDIX D

Example of MATLAB code for the Double-Inclusion model with Mori-Tanaka method

```
% Chan - Unsworth: analytical and experimental validation
close all;
clear all;
clc;
%% Input piezo fiber and matrix properties
% Piezo Fiber: PZT-7A _ Chan - Unsworth
rho _ p = 7600;% kg/m3
C11 _ p = 148E09;% Pa
C12 _ p = 76.2E09;% Pa
C13 _ p = 74.2E09;% Pa
C21 _ p = 76.2E09;% Pa
C22 _ p = 148E09;% Pa
C23 _ p = 74.2E09;% Pa
C31 _ p = 74.2E09;% Pa
C32 _ p = 74.2E09;% Pa
C33 _ p = 131E09;% Pa
C44 _ p = 25.4E09;% Pa
C55 _ p = 25.4E09;% Pa
C66 _ p = 35.9E09;% Pa
C _ p = [C11 _ p C12 _ p C13 _ p 0 0 0;...
C21 _ p C22 _ p C23 _ p 0 0 0;...
C31 _ p C32 _ p C33 _ p 0 0 0;...
0 0 0 C44 _ p 0 0;...
0 0 0 0 C55 _ p 0;...
0 0 0 0 0 C66 _ p ];
S _ p = inv(C _ p);
e15 _ p = 9.2;% C/m2
```

```

e31_p = -2.1;% C/m2
e32_p = -2.1;% C/m2
e33_p = 12.3; %9.5;% C/m2
e_p = [0 0 0 0 e15_p 0;...
0 0 0 e15_p 0 0;...
e31_p e32_p e33_p 0 0 0];
d_p = e_p*S_p;
k0 = 8.85E-12;% C2/Nm2 - Standard Vacuum Permittivity
k1_p = 460 * k0;% C2/Nm2
k2_p = 460 * k0;% C2/Nm2
k3_p = 235 * k0;% C2/Nm2
k_p = [k1_p 0 0;...
0 k2_p 0;...
0 0 k3_p];
EiJMn_p = [C_p, -e_p';...
e_p, k_p];
% Matrix: Araldite - Epoxy
rho_m = 1150;% kg/m3
C11_m = 8.0E09;% Pa
C12_m = 4.4E09;% Pa
C13_m = 4.4E09;% Pa
C21_m = 4.4E09;% Pa
C22_m = 8.0E09;% Pa
C23_m = 4.4E09;% Pa
C31_m = 4.4E09;% Pa
C32_m = 4.4E09;% Pa
C33_m = 8.0E09;% Pa
C44_m = 1.8E09;% Pa
C55_m = 1.8E09;% Pa
C66_m = 1.8E09;% Pa
C_m = [C11_m C12_m C13_m 0 0 0;...
C21_m C22_m C23_m 0 0 0;...
C31_m C32_m C33_m 0 0 0;...
0 0 0 C44_m 0 0;...
0 0 0 0 C55_m 0;...
0 0 0 0 0 C66_m];
S_m = inv(C_m);
e15_m = 0.0;% C/m2

```

```

e31_m = 0.0;% C/m2
e32_m = 0.0;% C/m2
e33_m = 0.0;% C/m2
e_m = [0 0 0 0 e15_m 0;...
0 0 0 e15_m 0 0;...
e31_m e32_m e33_m 0 0 0];
k0 = 8.85E-12;% C2/Nm2 - Standard Vacuum Permittivity
k1_m = 4.2 * k0;% C2/Nm2
k2_m = 4.2 * k0;% C2/Nm2
k3_m = 4.2 * k0;% C2/Nm2
k_m = [k1_m 0 0;... 0 k2_m 0;... 0 0 k3_m];
EiJMn_m = [C_m, -e_m';...
e_m, k_m];
% Core Fiber: Graphite Carbon Fiber
rho_c = 2000;% kg/m3
C11_c = 24.0E09;% Pa
C12_c = 9.7E09;% Pa
C13_c = 6.7E09;% Pa
C21_c = 9.7E09;% Pa
C22_c = 24.0E09;% Pa
C23_c = 6.7E09;% Pa
C31_c = 6.7E09;% Pa
C32_c = 6.7E09;% Pa
C33_c = 243.7E09;% Pa
C44_c = 27.0E09;% Pa
C55_c = 27.0E09;% Pa
C66_c = 11.0E09;% Pa
C_c = [C11_c C12_c C13_c 0 0 0;...
C21_c C22_c C23_c 0 0 0;...
C31_c C32_c C33_c 0 0 0;...
0 0 0 C44_c 0 0;...
0 0 0 0 C55_c 0;...
0 0 0 0 0 C66_c];
S_c = inv(C_c);
e15_c = 0.0;% C/m2
e31_c = 0.0;% C/m2
e32_c = 0.0;% C/m2
e33_c = 0.0;% C/m2

```

```

e_c = [0 0 0 0 e15_c 0;...
0 0 0 e15_c 0 0;...
e31_c e32_c e33_c 0 0 0];
k0 = 8.85E-12;% C2/Nm2 - Standard Vacuum Permittivity
k1_c = 12 * k0;% C2/Nm2
k2_c = 12 * k0;% C2/Nm2
k3_c = 12 * k0;% C2/Nm2
k_c = [k1_c 0 0;... 0 k2_c 0;...
0 0 k3_c];
EiJMn_c = [C_c, -e_c';...
e_c, k_c];
EiJMn_pm = EiJMn_p - EiJMn_m;
EiJMn_cp = EiJMn_p - EiJMn_c;
EiJMn_cm = EiJMn_c - EiJMn_m;
%% Geometry of inclusion (fiber in the matrix) and concentration tensor
alfa = 1;% long-infinite cylindrical inclusion
V_cp = 0.02:0.02:0.98;% volume fraction of piezo+core fiber (ASF)
V_ASF = V_cp;
AR_p = [0.5, 0.6, 0.7, 0.95] ;% aspect ratio of piezo shell thickness
for i=1:numel(V_cp)
for j=1:numel(AR_p)
r_cASF(j) = 1-AR_p(j);% ratio of core radius to ASF radius
V_cASF(j) = (1-AR_p(j))^2;% volume fraction of core fiber to the ASF
V_pASF(j) = 1-V_cASF(j);% volume fraction of piezo to the ASF
V_m(i)= 1-V_cp(i);% volume fraction of matrix to the composite
V_c(i,j)= V_cASF(j)*V_cp(i);% volume fraction of core fiber to the composite
V_p(i,j)= 1-V_c(i,j)-V_m(i);% volume fraction of piezo to the composite
end
end
SMnAb_c = zeros(9,9);
SMnAb_p = zeros(9,9);
if alfa == 1
% Concentration Tensor for Piezo fiber
S1111_p = ((5*C11_m)+C12_m)/(8*C11_m);
S2222_p = S1111_p;
S1212_p = ((3*C11_m)-C12_m)/(8*C11_m);
S2121_p = S1212_p;
S1221_p = S1212_p;

```

$S_{2112_p} = S_{1212_p};$
 $S_{1313_p} = 1/4;$
 $S_{3131_p} = S_{1313_p};$
 $S_{1331_p} = S_{1313_p};$
 $S_{3113_p} = S_{1313_p};$
 $S_{2323_p} = S_{1313_p};$
 $S_{3232_p} = S_{1313_p};$
 $S_{2332_p} = S_{1313_p};$
 $S_{3223_p} = S_{1313_p};$
 $S_{1122_p} = ((3*C_{12_m})-C_{11_m})/(8*C_{11_m});$
 $S_{2211_p} = S_{1122_p};$
 $S_{1133_p} = C_{13_m}/(2*C_{11_m});$
 $S_{2233_p} = S_{1133_p};$
 $S_{1143_p} = e_{31_m}/(2*C_{11_m});$
 $S_{2243_p} = S_{1143_p};$
 $S_{4141_p} = 1/2;$
 $S_{4242_p} = S_{4141_p};$
 $S_{MnAb_p(1,1)} = S_{1111_p};$
 $S_{MnAb_p(1,2)} = S_{1122_p};$
 $S_{MnAb_p(1,3)} = S_{1133_p};$
 $S_{MnAb_p(1,9)} = S_{1143_p};$
 $S_{MnAb_p(2,1)} = S_{2211_p};$
 $S_{MnAb_p(2,2)} = S_{2222_p};$
 $S_{MnAb_p(2,3)} = S_{2233_p};$
 $S_{MnAb_p(2,9)} = S_{2243_p};$
 $S_{MnAb_p(4,4)} = S_{2323_p};$
 $S_{MnAb_p(5,5)} = S_{1313_p};$
 $S_{MnAb_p(6,6)} = S_{1212_p};$
 $S_{MnAb_p(7,7)} = S_{4141_p};$
 $S_{MnAb_p(8,8)} = S_{4242_p};$
 % Concentration Tensor for Core fiber
 $S_{1111_c} = ((5*C_{11_m})+C_{12_m})/(8*C_{11_m});$
 $S_{2222_c} = S_{1111_c};$
 $S_{1212_c} = ((3*C_{11_m})-C_{12_m})/(8*C_{11_m});$
 $S_{2121_c} = S_{1212_c};$
 $S_{1221_c} = S_{1212_c};$
 $S_{2112_c} = S_{1212_c};$
 $S_{1313_c} = 1/4;$

```

S3131_c = S1313_c;
S1331_c = S1313_c;
S3113_c = S1313_c;
S2323_c = S1313_c;
S3232_c = S1313_c;
S2332_c = S1313_c;
S3223_c = S1313_c;
S1122_c = ((3*C12_m)-C11_m)/(8*C11_m);
S2211_c = S1122_c;
S1133_c = C13_m/(2*C11_m);
S2233_c = S1133_c;
S1143_c = e31_m/(2*C11_m);
S2243_c = S1143_c;
S4141_c = 1/2;
S4242_c = S4141_c;
SMnAb_c(1,1) = S1111_c;
SMnAb_c(1,2) = S1122_c;
SMnAb_c(1,3) = S1133_c;
SMnAb_c(1,9) = S1143_c;
SMnAb_c(2,1) = S2211_c;
SMnAb_c(2,2) = S2222_c;
SMnAb_c(2,3) = S2233_c;
SMnAb_c(2,9) = S2243_c;
SMnAb_c(4,4) = S2323_c;
SMnAb_c(5,5) = S1313_c;
SMnAb_c(6,6) = S1212_c;
SMnAb_c(7,7) = S4141_c;
SMnAb_c(8,8) = S4242_c;
end
I=eye(9,9);
A_dil_c=inv(I+(SMnAb_p*inv(EiJMn_m)*EiJMn_cm));
A_dil_p=inv(I+(SMnAb_c*inv(EiJMn_m)*EiJMn_cp));
deltaS=SMnAb_c-SMnAb_p;
F_c = inv(EiJMn_cm)*EiJMn_m;
F_p = inv(EiJMn_pm)*EiJMn_m;
for i=1: numel(V_cp) for j=1: numel(AR_p)
A_MT_m(:,:,i,j)=I*inv((V_m(i)*I)+(V_p(i,j)*A_dil_p(:,:,:))+...
(V_c(i,j)*A_dil_c(:,:,:)));% Mori-Tanaka Concentration Tensor - matrix

```

```

A_MT_p(:,:,i,j)=A_dil_p(:,:,i,j)*inv((V_m(i)*I)+(V_p(i,j)*A_dil_p(:,:,i,j))+...
(V_c(i,j)*A_dil_c(:,:,i,j)));% Mori-Tanaka Concentration Tensor - piezo
A_MT_c(:,:,i,j)=A_dil_c(:,:,i,j)*inv((V_m(i)*I)+(V_p(i,j)*A_dil_p(:,:,i,j))+...
(V_c(i,j)*A_dil_c(:,:,i,j)));% Mori-Tanaka Concentration Tensor - carbon
EiJMn_MT(:,:,i,j)=(V_m(i)*EiJMn_m*A_MT_m(:,:,i,j))+...
(V_p(i,j)*EiJMn_p*A_MT_p(:,:,i,j))+(V_c(i,j)*EiJMn_c*A_MT_c(:,:,i,j));
C(:,:,i,j)=EiJMn_MT(1:6,1:6,i,j);
e(:,:,i,j)=EiJMn_MT(7:9,1:6,i,j);
k(:,:,i,j)=EiJMn_MT(7:9,7:9,i,j);
S(:,:,i,j)=inv(C(:,:,i,j));
d(:,:,i,j)=e(:,:,i,j)*S(:,:,i,j);
kt(:,:,i,j)=k(:,:,i,j)+(d(:,:,i,j)*C(:,:,i,j)*d(:,:,i,j)');
rho(i,j)=rho_m*V_m(i)+rho_p*V_p(i,j)+rho_c*V_c(i,j);
end
end
for i=1:numel(V_cp)
C33_AR1(i)=C(3,3,i,1);
C31_AR1(i)=C(3,1,i,1);
e33_AR1(i)=e(3,3,i,1);
e31_AR1(i)=e(3,1,i,1);
d33_AR1(i)=d(3,3,i,1);
d31_AR1(i)=d(3,1,i,1);
S33_AR1(i)=S(3,3,i,1);
S31_AR1(i)=S(3,1,i,1);
rho_AR1(i)=rho(i,1);
S11_AR1(i)=S(1,1,i,1);
S12_AR1(i)=S(1,2,i,1);
S11S12_AR1(i)=S11_AR1(i)+S12_AR1(i);
k33s_AR1(i)=k(3,3,i,1);
k33t_AR1(i)=kt(3,3,i,1);
C11_AR1(i)=C(1,1,i,1);
C33_AR2(i)=C(3,3,i,2);
C31_AR2(i)=C(3,1,i,2);
e33_AR2(i)=e(3,3,i,2);
e31_AR2(i)=e(3,1,i,2);
d33_AR2(i)=d(3,3,i,2);
d31_AR2(i)=d(3,1,i,2);
S33_AR2(i)=S(3,3,i,2);

```

$S_{31_AR2}(i) = S(3,1,i,2);$
 $\rho_{AR2}(i) = \rho(i,2);$
 $S_{11_AR2}(i) = S(1,1,i,2);$
 $S_{12_AR2}(i) = S(1,2,i,2);$
 $S_{11S_{12}_AR2}(i) = S_{11_AR2}(i) + S_{12_AR2}(i);$
 $k_{33s_AR2}(i) = k(3,3,i,2);$
 $k_{33t_AR2}(i) = kt(3,3,i,2);$
 $C_{11_AR2}(i) = C(1,1,i,2);$
 $C_{33_AR3}(i) = C(3,3,i,3);$
 $C_{31_AR3}(i) = C(3,1,i,3);$
 $e_{33_AR3}(i) = e(3,3,i,3);$
 $e_{31_AR3}(i) = e(3,1,i,3);$
 $d_{33_AR3}(i) = d(3,3,i,3);$
 $d_{31_AR3}(i) = d(3,1,i,3);$
 $S_{33_AR3}(i) = S(3,3,i,3);$
 $S_{31_AR3}(i) = S(3,1,i,3);$
 $\rho_{AR3}(i) = \rho(i,3);$
 $S_{11_AR3}(i) = S(1,1,i,3);$
 $S_{12_AR3}(i) = S(1,2,i,3);$
 $S_{11S_{12}_AR3}(i) = S_{11_AR3}(i) + S_{12_AR3}(i);$
 $k_{33s_AR3}(i) = k(3,3,i,3);$
 $k_{33t_AR3}(i) = kt(3,3,i,3);$
 $C_{11_AR3}(i) = C(1,1,i,3);$
 $C_{33_AR4}(i) = C(3,3,i,4);$
 $C_{31_AR4}(i) = C(3,1,i,4);$
 $e_{33_AR4}(i) = e(3,3,i,4);$
 $e_{31_AR4}(i) = e(3,1,i,4);$
 $d_{33_AR4}(i) = d(3,3,i,4);$
 $d_{31_AR4}(i) = d(3,1,i,4);$
 $S_{33_AR4}(i) = S(3,3,i,4);$
 $S_{31_AR4}(i) = S(3,1,i,4);$
 $\rho_{AR4}(i) = \rho(i,4);$
 $S_{11_AR4}(i) = S(1,1,i,4);$
 $S_{12_AR4}(i) = S(1,2,i,4);$
 $S_{11S_{12}_AR4}(i) = S_{11_AR4}(i) + S_{12_AR4}(i);$
 $k_{33s_AR4}(i) = k(3,3,i,4);$
 $k_{33t_AR4}(i) = kt(3,3,i,4);$
 $C_{11_AR4}(i) = C(1,1,i,4);$

```

% Chan and Unsworth Model (1989)
cv(i) = C_p(1,1)+C_p(1,2)+((V_ASF(i)*(C_m(1,1)+C_m(1,2)))/(1-V_ASF(i)));
sv(i) =(V_ASF(i)*S_m(1,1))+ ((1-V_ASF(i))*(S_p(3,3)));
c33v(i) = (V_ASF(i)*(C_p(3,3)-(2*((C_p(1,3)-C_m(1,2))^2)/cv(i))))+...
((1-V_ASF(i))*C_m(1,1));
e33v(i) = V_ASF(i)*(e_p(3,3)-(2*e_p(3,1)*(C_p(1,3)-C_m(1,2))/cv(i)));
c31v(i) = ((C_m(1,2)*(C_p(1,1)+C_p(1,2)))+...
(V_ASF(i)*C_p(1,3)*(C_m(1,1)+C_m(1,2))/(1-V_ASF(i))))/cv(i);
e31v(i) = e_p(3,1)*(1-((C_p(1,1)+C_p(1,2))/cv(i)));
s31v(i) = ((S_p(3,3)*S_m(1,2)*(1-V_ASF(i)))+...
(V_ASF(i)*S_m(1,1)*S_p(1,3)))/sv(i);
s33v(i) = S_m(1,1)*S_p(3,3)/sv(i);
d33v(i) = V_ASF(i)*S_m(1,1)*d_p(3,3)/sv(i);
d31v(i) = (V_ASF(i)*d_p(3,1))-((V_ASF(i)*(1-V_ASF(i))*d_p(3,3)*...
(S_p(1,3)-S_m(1,2)))/sv(i));
rhov(i) = rho_m*V_m(i)+rho_p*(1-V_m(i));
s11s12v(i) = (V_ASF(i)*(S_p(1,1)+S_p(1,2)))+...
((1-V_ASF(i))*(S_m(1,1)+S_m(1,2)))-...
((2*V_ASF(i)/sv(i))*(1-V_ASF(i))*((S_m(1,3)-S_p(1,2))^2));
k33tv(i) = (V_ASF(i)*425*k0)-(V_ASF(i)*(1-V_ASF(i))*d_p(3,3)^2/sv(i))+...
((1-V_ASF(i))*(k_m(1,1)));
end
expdata=[0.2, 0.3, 0.42, 0.55, 0.65, 0.82;...
90, 100, 210, 240, 300, 420;...
125, 150, 160, 160, 167, 167;...
100, 75, 55, 45, 32, 20;...
2440, 3085, 3860, 4700, 5340, 6440;];
figure (1)
plot (V_cp,C33_AR1*1E-10,'r-*, V_cp,C33_AR2*1E-10,'g-o',...
V_cp,C33_AR3*1E-10,'m-^',V_cp,C33_AR4*1E-10,'b-d',...
V_cp,c33v*1E-10,'k-')
xlabel('Volume Fraction of ASF');
ylabel('C_33 (10^10 N/m^2)');
title('Stiffness C_33 vs Volume Fraction of ASF');
legend('Present Code - DI MT AR1','Present Code - DI MT AR2',...
'Present Code - DI MT AR3','Present Code - DI MT AR4',...
'Chan-Unsworth Model','Location','Best')
figure (2)

```

```

plot (V_cp,C31_AR1*1E-10,'r-*',V_cp,C31_AR2*1E-10,'g-o',...
V_cp,C31_AR3*1E-10,'m-^',V_cp,C31_AR4*1E-10,'b-d',...
V_cp,c31v*1E-10,'k-')
xlabel('Volume Fraction of ASF');
ylabel('C_31 (10^10 N/m^2)');
title('Stiffness C_31 vs Volume Fraction of ASF');
legend('Present Code - DI MT AR1','Present Code - DI MT AR2',...
'Present Code - DI MT AR3','Present Code - DI MT AR4',...
'Chan-Unsworth Model','Location','Best')
figure (3)
plot (V_cp,e33_AR1,'r-*',V_cp,e33_AR2,'g-o',...
V_cp,e33_AR3,'m-^',V_cp,e33_AR4,'b-d',...
V_cp,e33v,'k-')
xlabel('Volume Fraction of ASF');
ylabel('e_33 (C/m^2)');
title('Piezoelectric Constant e_33 vs Volume Fraction of ASF');
legend('Present Code - DI MT AR1','Present Code - DI MT AR2',...
'Present Code - DI MT AR3','Present Code - DI MT AR4',...
'Chan-Unsworth Model','Location','Best')
figure (4)
plot (V_cp,e31_AR1,'r-*',V_cp,e31_AR2,'g-o',...
V_cp,e31_AR3,'m-^',V_cp,e31_AR4,'b-d',...
V_cp,e31v,'k-')
xlabel('Volume Fraction of ASF');
ylabel('e_31 (C/m^2)');
title('Piezoelectric Constant e_31 vs Volume Fraction of ASF');
legend('Present Code - DI MT AR1','Present Code - DI MT AR2',...
'Present Code - DI MT AR3','Present Code - DI MT AR4',...
'Chan-Unsworth Model','Location','Best')
figure (5)
plot (V_cp,d33_AR1*1E12,'r-*',V_cp,d33_AR2*1E12,'g-o',...
V_cp,d33_AR3*1E12,'m-^',V_cp,d33_AR4*1E12,'b-d',...
V_cp,d33v*1E12,'k-')
hold on
plot(expdata(1,:),expdata(3,:), 'ks','MarkerFaceColor','k')
xlabel('Volume Fraction of ASF');
ylabel('d_33 (10^-12 m/V)');
title('Charge Constant d_33 vs Volume Fraction of ASF');

```

```

legend('Present Code - DI MT AR1','Present Code - DI MT AR2',...
'Present Code - DI MT AR3','Present Code - DI MT AR4',...
'Chan-Unsworth Model','Chan-Unsworth Experiment','Location','Best')

```

figure (6)

```

plot (V_cp,d31_AR1*1E12,'r-*',V_cp,d31_AR2*1E12,'g-o',...
V_cp,d31_AR3*1E12,'m-^',V_cp,d31_AR4*1E12,'b-d',...
V_cp,d31v*1E12,'k-')
xlabel('Volume Fraction of ASF');
ylabel('d_31 (10^-12 m/V)');
title('Charge Constant d_31 vs Volume Fraction of ASF');
legend('Present Code - DI MT AR1','Present Code - DI MT AR2',...
'Present Code - DI MT AR3','Present Code - DI MT AR4',...
'Chan-Unsworth Model','Location','Best')

```

figure (7)

```

plot (V_cp,S33_AR1*1E12,'r-*',V_cp,S33_AR2*1E12,'g-o',...
V_cp,S33_AR3*1E12,'m-^',V_cp,S33_AR4*1E12,'b-d',...
V_cp,s33v*1E12,'k-')
xlabel('Volume Fraction of ASF');
ylabel('S_33 (10^-12 m^2/N)');
title('Compliance S_33 vs Volume Fraction of ASF');
legend('Present Code - DI MT AR1','Present Code - DI MT AR2',...
'Present Code - DI MT AR3','Present Code - DI MT AR4',...
'Chan-Unsworth Model','Location','Best')

```

figure (8)

```

plot (V_cp,S31_AR1*1E12,'r-*',V_cp,S31_AR2*1E12,'g-o',...
V_cp,S31_AR3*1E12,'m-^',V_cp,S31_AR4*1E12,'b-d',...
V_cp,s31v*1E12,'k-')
xlabel('Volume Fraction of ASF');
ylabel('S_31 (10^-12 m^2/N)');
title('Compliance S_31 vs Volume Fraction of ASF');
legend('Present Code - DI MT AR1','Present Code - DI MT AR2',...
'Present Code - DI MT AR3','Present Code - DI MT AR4',...
'Chan-Unsworth Model','Location','Best')

```

figure (9)

```

plot (V_cp,rho_AR1,'r-*',V_cp,rho_AR2,'g-o',...
V_cp,rho_AR3,'m-^',V_cp,rho_AR4,'b-d',...
V_cp,rhov,'k-')
hold on

```

```

plot(expdata(1,:),expdata(5,:), 'ks', 'MarkerFaceColor', 'k')
xlabel('Volume Fraction of ASF');
ylabel('Density (kg/m^3)');
title('Density vs Volume Fraction of ASF');
legend('Present Code - DI MT AR1', 'Present Code - DI MT AR2', ...
'Present Code - DI MT AR3', 'Present Code - DI MT AR4', ...
'Chan-Unsworth Model', 'Chan-Unsworth Experiment', 'Location', 'Best')
figure (10)
plot (V_cp,S11_AR1*1E12, 'r-*', V_cp,S11_AR2*1E12, 'g-o', ...
V_cp,S11_AR3*1E12, 'm-^', ...
V_cp,S11_AR4*1E12, 'b-d')
xlabel('Volume Fraction of ASF');
ylabel('S_11 (10^-12 m^2/N)');
title('Compliance S_11 vs Volume Fraction of ASF');
legend('Present Code - DI MT AR1', 'Present Code - DI MT AR2', ...
'Present Code - DI MT AR3', 'Present Code - DI MT AR4', 'Location', 'Best')
figure (11)
plot (V_cp,C11_AR1*1E-10, 'r-*', V_cp,C11_AR2*1E-10, 'g-o', ...
V_cp,C11_AR3*1E-10, 'm-^', ...
V_cp,C11_AR4*1E-10, 'b-d')
xlabel('Volume Fraction of ASF');
ylabel('C_11 (10^10 m^2/N)');
title('Stiffness C_11 vs Volume Fraction of ASF');
legend('Present Code - DI MT AR1', 'Present Code - DI MT AR2', ...
'Present Code - DI MT AR3', 'Present Code - DI MT AR4', 'Location', 'Best')
figure (12)
plot (V_cp,S11S12_AR1*1E12, 'r-s', V_cp,S11S12_AR2*1E12, 'g-o', ...
V_cp,S11S12_AR3*1E12, 'm-^', V_cp,S11S12_AR4*1E12, 'b-d', ...
V_cp,s11s12v*1E12, 'k-')
hold on
plot(expdata(1,:),expdata(4,:), 'ks', 'MarkerFaceColor', 'k')
xlabel('Volume Fraction of ASF');
ylabel('S_11+S_12 (10^-12 m^2/N)');
title('Compliance S_11+S_12 vs Volume Fraction of ASF');
legend('Present Code - DI MT AR1', 'Present Code - DI MT AR2', ...
'Present Code - DI MT AR3', 'Present Code - DI MT AR4', ...
'Chan-Unsworth Model', 'Chan-Unsworth Experiment', 'Location', 'Best')
figure (13)

```

```

plot (V_cp,k33t_AR1*(1/k0),'r-*',V_cp,k33t_AR2*(1/k0),'g-o',...
V_cp,k33t_AR3*(1/k0),'m-^',V_cp,k33t_AR4*(1/k0),'b-d',...
V_cp,k33tv*(1/k0),'k-')
hold on
plot (expdata(1,:),expdata(2:),'ks','MarkerFaceColor','k')
xlabel('Volume Fraction of ASF');
ylabel('\epsilon_33^T / \epsilon_0');
title('Permittivity Ratio \epsilon_33^T / \epsilon_0 vs Volume Fraction of ASF');
legend('Present Code - DI MT AR1','Present Code - DI MT AR2',...
'Present Code - DI MT AR3','Present Code - DI MT AR4',...
'Chan-Unsworth Model','Chan-Unsworth Experiment','Location','Best')
%% Output 2D Plane Stress Constitutive
for i=1: numel(V_cp)
for j=1: numel(AR_p)
C11_2D(i,j) = C(1,1,i,j) - ((C(1,3,i,j)^2)/C(3,3,i,j));
C12_2D(i,j) = C(1,2,i,j) - ((C(1,3,i,j)*C(2,3,i,j))/C(3,3,i,j));
C22_2D(i,j) = C(2,2,i,j) - ((C(2,3,i,j)^2)/C(3,3,i,j));
C66_2D(i,j) = C(6,6,i,j);
C_2D(:,:,i,j) = [C11_2D(i,j) C12_2D(i,j) 0;...
C12_2D(i,j) C22_2D(i,j) 0;... 0 0 C66_2D(i,j)];
S_2D(:,:,i,j) = inv(C_2D(:,:,i,j));
e31_2D(i,j) = e(3,1,i,j) - ((C(1,3,i,j)*e(3,3,i,j))/C(3,3,i,j));
e32_2D(i,j) = e(3,2,i,j) - ((C(2,3,i,j)*e(3,3,i,j))/C(3,3,i,j));
e_2D(:,:,i,j) = [e31_2D(i,j) e32_2D(i,j) 0];
d_2D(:,:,i,j) = e_2D(:,:,i,j)*S_2D(:,:,i,j);
k3_2D(i,j) = k(3,3,i,j) + ((e(3,3,i,j)^2)/C(3,3,i,j));
k_2D(i,j) = k3_2D(i,j);
EiJMn_2D(:,:,i,j) = [C_2D(:,:,i,j), -e_2D(:,:,i,j)];...
e_2D(:,:,i,j), k_2D(i,j)];
end
end
end

```

APPENDIX E

Example of MATLAB code for the Iterative FEM in frequency domain

```
% Marqui unimorph base excitation - solid element
close all
clear all
clc
%% Input read XLS from Nastran PCH
j=sqrt(-1);
Kuv(:,1)=-xlsread('marqui _ uni3d _ pch','FX','B:B');
nnod=length(Kuv);
Kuv(nnod+1:2*nnod,1)=-xlsread('marqui _ uni3d _ pch','FY','B:B');
Kuv((2*nnod)+1:3*nnod,1)=-xlsread('marqui _ uni3d _ pch','FZ','B:B');
U(:,1)=xlsread('marqui _ uni3d _ pch','UX _ r0','B:B')+...
(j*xlsread('marqui _ uni3d _ pch','UX _ i0','B:B')); % mm
U(nnod+1:2*nnod,1)=xlsread('marqui _ uni3d _ pch','UY _ r0','B:B')+...
(j*xlsread('marqui _ uni3d _ pch','UY _ i0','B:B')); % mm
U((2*nnod)+1:3*nnod,1)=xlsread('marqui _ uni3d _ pch','UZ _ r0','B:B')+...
(j*xlsread('marqui _ uni3d _ pch','UZ _ i0','B:B')); % mm
%% Input geometry and material properties
n _ lay=2;%number of layers
lay _ prop=zeros(7,n _ lay);%layer properties initiation
lb=(100);%mm - beam length
wb=(20);%mm - beam width
% Assume uniform cross section
for i=1:n _ lay
lay _ prop(1,i)=lb;%mm - layers's length
lay _ prop(2,i)=wb;%mm - layers's width
end
lay _ prop(3,1)=0.5;%mm - thickness - material 1 (metal)
```

```

lay_prop(3,2)=0.4;%mm - thickness - material 2 (PZT 5A)
lay_prop(4,1)=(1/100)*1e-6;%mm.s/kg - compliance (s_11) - metal
lay_prop(4,2)=(1/66)*1e-6;%mm.s/kg - compliance (s_11) - PZT 5A
lay_prop(5,1)=0;% C/(kg.mm/s2) - charge constant (d_31) - metal
lay_prop(5,2)=-190e-15;% C/(kg.mm/s2) - charge constant (d_31) - PZT 5A
lay_prop(6,1)=0;%Farad/mm - permittivity - metal
lay_prop(6,2)=2069*8.85*(10^-15);%Farad/mm - permittivity - PZT 5A
lay_prop(7,1)=7800e-9;%kg/(mm^3) - density - metal
lay_prop(7,2)=7165e-9;%kg/(mm^3) - density - PZT 5A
%% neutral axis, beam flexural stiffness and m_piezo calculations
l=zeros(1,n_layer);%array of layers's length
w=zeros(1,n_layer);%array of layers's width
h=zeros(1,n_layer);%array of layers's thickness
s_11=zeros(1,n_layer);%array of layers's material compliance
d_31=zeros(1,n_layer);%array of layers's piezoelectric charge constant
eps_33=zeros(1,n_layer);%array of layers's permittivity (at constant stress)
rho=zeros(1,n_layer);%array of layers's density
for i=1:n_layer
l(i)=lay_prop(1,i);
w(i)=lay_prop(2,i);
h(i)=lay_prop(3,i);
s_11(i)=lay_prop(4,i);
d_31(i)=lay_prop(5,i);
eps_33(i)=lay_prop(6,i);
rho(i)=lay_prop(7,i);
end
z1=0;hj=0;z2=0;z3=0;
for i=1:n_layer
z1= z1+(w(i)*(h(i)^2)/s_11(i));
hj= hj+h(i);
z2= z2+((w(i)*h(i)/s_11(i))*hj);
z3= z3+(w(i)*h(i)/s_11(i));
end
z_bar=-((z1)-(2*z2))/(2*z3);%meter (measured from bottom) - neutral axis
c_layer=zeros(1,n_layer);hu=0;
m_layer=zeros(1,n_layer);
for i=1:n_layer
hu = hu+h(i);

```

```

hl = hu-h(i);
c_lay(i)=(w(i)/s_11(i))*((3*h(i)*(z_bar-hu)*(z_bar-hl))+h(i)^3);
m_lay(i)=(w(i)*d_31(i)/(s_11(i)*h(i)))*...
((2*z_bar*h(i))-(2*h(i)*hu)+h(i)^2);
end
C=sum(c_lay)/3;%Nm^2 - Beam flexural stiffness
m_piezo=sum(m_lay)/2;%Nm/V - internal moment due to piezo per unit volt
A=lb*wb;
Cp = A*(eps_33(2)-((d_31(2)^2)/s_11(2)))/h(2);% unimorph
%% Dynamic bending modes and natural frequencies (clamped-free beam)
%%The first five solutions of characteristic equation
%%(not calculated here, taken from reference)
n_mod=5;%number of modeshapes
kl = [1.8751 4.6941 7.8548 10.9955 14.137];%dimensionless
k =kl./lb;%1/m - characteristic solution per unit length
mass=0;
for i=1:n_lay
mass = mass+(l(i)*w(i)*h(i)*rho(i));%kg - mass of the beam
end
miu=mass/lb;
for i=1:n_mod
natomg(i)= ((kl(i)^2)/(lb^2))*(sqrt(C/miu));%rad/s - angular natural freq
natfrq(i)= natomg(i)/(2*pi);%Hz - natural freq
end
%% Electrical Equation - Iteration 0
R = 15000; % Ohm
Volt1=j*natomg(1)*(Kuv'*U)*(1/((j*natomg(1)*Cp)+(1/R)));
%% Electrical Equation - Iteration 1
Uiter1(:,1)=xlsread('marqui_uni3d_pch','UX_r1','B:B')+...
(j*xlsread('marqui_uni3d_pch','UX_i1','B:B')); % mm
Uiter1(nnod+1:2*nnod,1)=xlsread('marqui_uni3d_pch','UY_r1','B:B')+...
(j*xlsread('marqui_uni3d_pch','UY_i1','B:B')); % mm
Uiter1((2*nnod)+1:3*nnod,1)=xlsread('marqui_uni3d_pch','UZ_r1','B:B')+...
(j*xlsread('marqui_uni3d_pch','UZ_i1','B:B')); % mm
Volt2=j*natomg(1)*(Kuv'*Uiter1)*(1/((j*natomg(1)*Cp)+(1/R)));
%% Electrical Equation - Iteration 2
Uiter2(:,1)=xlsread('marqui_uni3d_pch','UX_r2','B:B')+...
(j*xlsread('marqui_uni3d_pch','UX_i2','B:B')); % mm

```

```

Uiter2(nnod+1:2*nnod,1)=xlsread('marqui _ uni3d _ pch','UY _ r2','B:B')+...
(j*xlsread('marqui _ uni3d _ pch','UY _ i2','B:B')); % mm
Uiter2((2*nnod)+1:3*nnod,1)=xlsread('marqui _ uni3d _ pch','UZ _ r2','B:B')+...
(j*xlsread('marqui _ uni3d _ pch','UZ _ i2','B:B')); % mm
Volt3=j*natomg(1)*(Kuv'*Uiter2)*(1/((j*natomg(1)*Cp)+(1/R)));
%% Electrical Equation - Iteration 3
Uiter3(:,1)=xlsread('marqui _ uni3d _ pch','UX _ r3','B:B')+...
(j*xlsread('marqui _ uni3d _ pch','UX _ i3','B:B')); % mm
Uiter3(nnod+1:2*nnod,1)=xlsread('marqui _ uni3d _ pch','UY _ r3','B:B')+...
(j*xlsread('marqui _ uni3d _ pch','UY _ i3','B:B')); % mm
Uiter3((2*nnod)+1:3*nnod,1)=xlsread('marqui _ uni3d _ pch','UZ _ r3','B:B')+...
(j*xlsread('marqui _ uni3d _ pch','UZ _ i3','B:B')); % mm
Volt4=j*natomg(1)*(Kuv'*Uiter3)*(1/((j*natomg(1)*Cp)+(1/R)));
%% Electrical Equation - Iteration 4
Uiter4(:,1)=xlsread('marqui _ uni3d _ pch','UX _ r4','B:B')+...
(j*xlsread('marqui _ uni3d _ pch','UX _ i4','B:B')); % mm
Uiter4(nnod+1:2*nnod,1)=xlsread('marqui _ uni3d _ pch','UY _ r4','B:B')+...
(j*xlsread('marqui _ uni3d _ pch','UY _ i4','B:B')); % mm
Uiter4((2*nnod)+1:3*nnod,1)=xlsread('marqui _ uni3d _ pch','UZ _ r4','B:B')+...
(j*xlsread('marqui _ uni3d _ pch','UZ _ i4','B:B')); % mm
Volt5=j*natomg(1)*(Kuv'*Uiter4)*(1/((j*natomg(1)*Cp)+(1/R)));
%% Electrical Equation - Iteration 5
Uiter5(:,1)=xlsread('marqui _ uni3d _ pch','UX _ r5','B:B')+...
(j*xlsread('marqui _ uni3d _ pch','UX _ i5','B:B')); % mm
Uiter5(nnod+1:2*nnod,1)=xlsread('marqui _ uni3d _ pch','UY _ r5','B:B')+...
(j*xlsread('marqui _ uni3d _ pch','UY _ i5','B:B')); % mm
Uiter5((2*nnod)+1:3*nnod,1)=xlsread('marqui _ uni3d _ pch','UZ _ r5','B:B')+...
(j*xlsread('marqui _ uni3d _ pch','UZ _ i5','B:B')); % mm
Volt6=j*natomg(1)*(Kuv'*Uiter5)*(1/((j*natomg(1)*Cp)+(1/R)));
%% Electrical Equation - Iteration 6
Uiter6(:,1)=xlsread('marqui _ uni3d _ pch','UX _ r6','B:B')+...
(j*xlsread('marqui _ uni3d _ pch','UX _ i6','B:B')); % mm
Uiter6(nnod+1:2*nnod,1)=xlsread('marqui _ uni3d _ pch','UY _ r6','B:B')+...
(j*xlsread('marqui _ uni3d _ pch','UY _ i6','B:B')); % mm
Uiter6((2*nnod)+1:3*nnod,1)=xlsread('marqui _ uni3d _ pch','UZ _ r6','B:B')+...
(j*xlsread('marqui _ uni3d _ pch','UZ _ i6','B:B')); % mm
Volt7=j*natomg(1)*(Kuv'*Uiter6)*(1/((j*natomg(1)*Cp)+(1/R)));
%% Electrical Equation - Iteration 7

```

```

Uiter7(:,1)=xlsread('marqui _ uni3d _ pch','UX _ r7','B:B')+...
(j*xlsread('marqui _ uni3d _ pch','UX _ i7','B:B')); % mm
Uiter7(nnod+1:2*nnod,1)=xlsread('marqui _ uni3d _ pch','UY _ r7','B:B')+...
(j*xlsread('marqui _ uni3d _ pch','UY _ i7','B:B')); % mm
Uiter7((2*nnod)+1:3*nnod,1)=xlsread('marqui _ uni3d _ pch','UZ _ r7','B:B')+...
(j*xlsread('marqui _ uni3d _ pch','UZ _ i7','B:B')); % mm
Volt8=j*natomg(1)*(Kuv'*Uiter7)*(1/((j*natomg(1)*Cp)+(1/R)));
%% Electrical Equation - Iteration 8
Uiter8(:,1)=xlsread('marqui _ uni3d _ pch','UX _ r8','B:B')+...
(j*xlsread('marqui _ uni3d _ pch','UX _ i8','B:B')); % mm
Uiter8(nnod+1:2*nnod,1)=xlsread('marqui _ uni3d _ pch','UY _ r8','B:B')+...
(j*xlsread('marqui _ uni3d _ pch','UY _ i8','B:B')); % mm
Uiter8((2*nnod)+1:3*nnod,1)=xlsread('marqui _ uni3d _ pch','UZ _ r8','B:B')+...
(j*xlsread('marqui _ uni3d _ pch','UZ _ i8','B:B')); % mm
Volt9=j*natomg(1)*(Kuv'*Uiter8)*(1/((j*natomg(1)*Cp)+(1/R)));
%% Electrical Equation - Iteration 9
Uiter9(:,1)=xlsread('marqui _ uni3d _ pch','UX _ r9','B:B')+...
(j*xlsread('marqui _ uni3d _ pch','UX _ i9','B:B')); % mm
Uiter9(nnod+1:2*nnod,1)=xlsread('marqui _ uni3d _ pch','UY _ r9','B:B')+...
(j*xlsread('marqui _ uni3d _ pch','UY _ i9','B:B')); % mm
Uiter9((2*nnod)+1:3*nnod,1)=xlsread('marqui _ uni3d _ pch','UZ _ r9','B:B')+...
(j*xlsread('marqui _ uni3d _ pch','UZ _ i9','B:B')); % mm
Volt10=j*natomg(1)*(Kuv'*Uiter9)*(1/((j*natomg(1)*Cp)+(1/R)));
%% Electrical Equation - Iteration 10
Uiter10(:,1)=xlsread('marqui _ uni3d _ pch','UX _ r10','B:B')+...
(j*xlsread('marqui _ uni3d _ pch','UX _ i10','B:B')); % mm
Uiter10(nnod+1:2*nnod,1)=xlsread('marqui _ uni3d _ pch','UY _ r10','B:B')+...
(j*xlsread('marqui _ uni3d _ pch','UY _ i10','B:B')); % mm
Uiter10((2*nnod)+1:3*nnod,1)=xlsread('marqui _ uni3d _ pch','UZ _ r10','B:B')+...
(j*xlsread('marqui _ uni3d _ pch','UZ _ i10','B:B')); % mm
Volt11=j*natomg(1)*(Kuv'*Uiter10)*(1/((j*natomg(1)*Cp)+(1/R)));
%% Plot Umax and Volt vs No. Iter.
Iter = 0:1:10;
Volt = [0 Volt1 Volt2 Volt3 Volt4 Volt5 Volt6 Volt7 Volt8 Volt9 Volt10];
Volt _ EIM = ones(1,11)*0.1979;
Volt _ ACS = ones(1,11)*0.1966;
Umax = [max(abs(U)) max(abs(Uiter1)) max(abs(Uiter2)) max(abs(Uiter3)) ...
max(abs(Uiter4)) max(abs(Uiter5)) max(abs(Uiter6)) max(abs(Uiter7))...

```

```

max(abs(Uiter8)) max(abs(Uiter9)) max(abs(Uiter10));% mm
Umax _ EIM = ones(1,11)*49e-3;% mm
figure(1)
plot(Iter,abs(Volt),':ob','linewidth',1.5,'MarkerFaceColor','g')
hold on
plot(Iter,Volt _ EIM,'-r','linewidth',2)
plot(Iter,Volt _ ACS,'-k','linewidth',2)
xlabel('No. of iteration', 'interpreter','latex');
ylabel('V̄ (Volt)', 'interpreter','latex');
title('Voltage Amplitude vs Number of iteration');
legend('Present - Iterative FEM','Erturk and Inman - Analytical Model',...
'Akbar and Curiel-Sosa - Hybrid Model')
figure(2)
plot(Iter,Umax,':ob','linewidth',1.5,'MarkerFaceColor','g')
hold on
plot(Iter,Umax _ EIM,'-r','linewidth',2)
% plot(Iter,Umax _ ACS,'-k','linewidth',2)
xlabel('No. of iteration', 'interpreter','latex');
ylabel('Z̄rel (mm)', 'interpreter','latex');
title('Relative Tip Displacement vs Number of iteration');
legend('Present - Iterative FEM','Erturk and Inman - Analytical Model',...
'Akbar and Curiel-Sosa - Hybrid Model')

```

APPENDIX F

Example of MATLAB code for the Iterative FEM in time domain

```
% Jet aircraft wing PZT-5A gust load - shell element
close all
clear all
clc
%% Input read XLS from Nastran PCH
j=sqrt(-1);
Kuv(:,1)=-xlsread('SAWEswept _ pzt5a _ pch','FX','B:B');
nnod=length(Kuv);
Kuv(nnod+1:2*nnod,1)=-xlsread('SAWEswept _ pzt5a _ pch','FY','B:B');
Kuv((2*nnod)+1:3*nnod,1)=-xlsread('SAWEswept _ pzt5a _ pch','FZ','B:B');
Kuv((3*nnod)+1:4*nnod,1)=-xlsread('SAWEswept _ pzt5a _ pch','MX','B:B');
Kuv((4*nnod)+1:5*nnod,1)=-xlsread('SAWEswept _ pzt5a _ pch','MY','B:B');
Kuv((5*nnod)+1:6*nnod,1)=-xlsread('SAWEswept _ pzt5a _ pch','MZ','B:B');
nt=200;% no of increment + 1, from Nastran BDF
dt=2.500000E-02;% time step, from Nastran BDF
nonzero=find(Kuv ==0);
nnzeronod=length(nonzero)/2;
Kuv _ red=Kuv(nonzero);
% F06 needs to be modified, delete all lines before and after the displacement results
ni=nt/50;% iteration parameter, 50 is total numeric lines in 1 page of SOL 146 F06
for i=1:ni*nnzeronod
    datah43(:,i,1)=dlmread('saweswept _ pzt5a _ sol146 _ h43 _ vel _ 0.txt','...',
    [(7*i)+(50*(i-1)) 0 ((7*i)-1)+(50*i) 0]);% Time data
    datah43(:,i,2)=dlmread('saweswept _ pzt5a _ sol146 _ h43 _ vel _ 0.txt','...',
    [(7*i)+(50*(i-1)) 1 ((7*i)-1)+(50*i) 1]);% Velocity x data
    datah43(:,i,3)=dlmread('saweswept _ pzt5a _ sol146 _ h43 _ vel _ 0.txt','...',
    [(7*i)+(50*(i-1)) 2 ((7*i)-1)+(50*i) 2]);% Velocity y data
```

```

% 50 is total numeric lines in 1 page of SOL 146 F06
% 7 is total non-numeric lines in 1 page of SOL 146 F06
end
time=(reshape(datah9(:,1),[nt,nnzeronod]));% Time data, (nnzeronod x nt) size
Uh43(:,1)=(reshape(datah43(:,2),[nt,nnzeronod]));...
% Velocity x, (nnzeronod x nt) size
Uh43(nnzeronod+1:2*nnzeronod,:)=(reshape(datah43(:,3),[nt,nnzeronod]));...
% Velocity y, (nnzeronod x nt) size
%% Material and beam properties
L = 14480;%mm - halfspan length
h = 6.096;%mm - piezo layer thickness
A = 24.5243*(10^6);%mm^2 - piezo layer surface area
b = 1587.5;%mm - piezo layer average width
s_11 = 16.4e-09;%mm.s/kg - piezo material compliance (E_11 = 1/s_11)
d_31 = -171e-15;%C/(kg.mm/s^2) - piezoelectric charge constant
eps_33 = 15051.8e-15;%Farad/mm - permittivity at constant stress
Cp = A*(eps_33-((d_31^2)/s_11))/h;% unimorph
%% Electrical Equation - Iteration 0
R = 1250; % Ohm
tspan=[0 4.975000E+00];
KUth43=Kuv_red'*Uh43;
[t1h43,V1h43] = ode45(@(t1h43,V1h43) ((-V1h43/R) +...
interp1(time(1,:),KUth43,t1h43))/Cp, tspan, 0);
% t1, V1 will not have the same length with nt, because automatically
% calculated by the ode45.
Volt1h43 = interp1(t1h43,V1h43,time(1,:));% interpolate V1, so,...
% size Volt1 = nt x 1
P1h43=(Volt1h43.^2)*(1/R);
tVolt1h43(1,1:2:2*nt) = time(1,:);
tVolt1h43(1,2:2:2*nt) = Volt1h43;
tVolt1h43=reshape(tVolt1h43,8,[]);
% dlmwrite('tVolt1h43.dat',tVolt1h43,'precision','%4f')
%% Electrical Equation - Iteration 1
for i=1:ni*nnzeronod
data1h43(:,i,1)=dlmread('saweswept_ptz5a_sol146_h43_vel_1.txt',',...
[(7*i)+(50*(i-1)) 0 ((7*i)-1)+(50*i) 0]);% Time data
data1h43(:,i,2)=dlmread('saweswept_ptz5a_sol146_h43_vel_1.txt',',...
[(7*i)+(50*(i-1)) 1 ((7*i)-1)+(50*i) 1]);% Velocity x data

```

```

data1h43(:,i,3)=dlmread('saweswept_ptz5a_sol146_h43_vel_1.txt',',...
[(7*i)+(50*(i-1)) 2 ((7*i)-1)+(50*i 2)];% Velocity y data
% 50 is total numeric lines in 1 page of SOL 146 F06
% 7 is total non-numeric lines in 1 page of SOL 146 F06
end
U1h43(:,:)= (reshape(data1h43(:,:),[nt,nnzeronod]));...
% Velocity x, (nnzeronod x nt) size
U1h43(nnzeronod+1:2*nnzeronod,:)= (reshape(data1h43(:,:),[nt,nnzeronod]));...
% Velocity y, (nnzeronod x nt) size
KUt1h43=Kuv_red'*U1h43;
[t2h43,V2h43] = ode45(@(t2h43,V2h43) ((-V2h43/R) +...
interp1(time(1,:),KUt1h43,t2h43))/Cp, tspan, 0);
Volt2h43 = interp1(t2h43,V2h43,time(1,:));% interpolate V1, so,...
% size Volt1 = nt x 1
P2h43=(Volt2h43.^2)*(1/R);
tVolt2h43(1,1:2:2*nt) = time(1,:);
tVolt2h43(1,2:2:2*nt) = Volt2h43;
tVolt2h43=reshape(tVolt2h43,8,[]);
% dlmwrite('tVolt2h43.dat',tVolt2h43,'precision','%4f')
%% Electrical Equation - Iteration 2
for i=1:ni*nnzeronod
data2h43(:,i,1)=dlmread('saweswept_ptz5a_sol146_h43_vel_2.txt',',...
[(7*i)+(50*(i-1)) 0 ((7*i)-1)+(50*i 0)];% Time data
data2h43(:,i,2)=dlmread('saweswept_ptz5a_sol146_h43_vel_2.txt',',...
[(7*i)+(50*(i-1)) 1 ((7*i)-1)+(50*i 1)];% Velocity x data
data2h43(:,i,3)=dlmread('saweswept_ptz5a_sol146_h43_vel_2.txt',',...
[(7*i)+(50*(i-1)) 2 ((7*i)-1)+(50*i 2)];% Velocity y data
% 50 is total numeric lines in 1 page of SOL 146 F06
% 7 is total non-numeric lines in 1 page of SOL 146 F06 end
U2h43(:,:)= (reshape(data2h43(:,:),[nt,nnzeronod]));...
% Velocity x, (nnzeronod x nt) size
U2h43(nnzeronod+1:2*nnzeronod,:)= (reshape(data2h43(:,:),[nt,nnzeronod]));...
% Velocity y, (nnzeronod x nt) size
KUt2h43=Kuv_red'*U2h43;
[t3h43,V3h43] = ode45(@(t3h43,V3h43) ((-V3h43/R) +...
interp1(time(1,:),KUt2h43,t3h43))/Cp, tspan, 0);
Volt3h43 = interp1(t3h43,V3h43,time(1,:));% interpolate V1, so,...
% size Volt1 = nt x 1

```

```

P3h43=(Volt3h43.^2)*(1/R);
tVolt3h43(1,1:2:2*nt) = time(1,:);
tVolt3h43(1,2:2:2*nt) = Volt3h43;
tVolt3h43=reshape(tVolt3h43,8,[]);
% dlmwrite('tVolt3h43.dat',tVolt3h43,'precision','%4f')
%% Electrical Equation - Iteration 3
for i=1:ni*mnzeronod
data3h43(:,i,1)=dlmread('saweswept_ptz5a_sol146_h43_vel_3.txt',",...
[(7*i)+(50*(i-1)) 0 ((7*i)-1)+(50*i) 0]);% Time data
data3h43(:,i,2)=dlmread('saweswept_ptz5a_sol146_h43_vel_3.txt',",...
[(7*i)+(50*(i-1)) 1 ((7*i)-1)+(50*i) 1]);% Velocity x data
data3h43(:,i,3)=dlmread('saweswept_ptz5a_sol146_h43_vel_3.txt',",...
[(7*i)+(50*(i-1)) 2 ((7*i)-1)+(50*i) 2]);% Velocity y data
% 50 is total numeric lines in 1 page of SOL 146 F06
% 7 is total non-numeric lines in 1 page of SOL 146 F06
end
U3h43(:,:)=(reshape(data3h43(:,:,2),[nt,mnzeronod]));...
% Velocity x, (mnzeronod x nt) size
U3h43(mnzeronod+1:2*mnzeronod,:)=(reshape(data3h43(:,:,3),[nt,mnzeronod]));...
% Velocity y, (mnzeronod x nt) size
KUt3h43=Kuv_red*U3h43;
[t4h43,V4h43] = ode45(@(t4h43,V4h43) ((-V4h43/R) +...
interp1(time(1,:),KUt3h43,t4h43))/Cp, tspan, 0);
Volt4h43 = interp1(t4h43,V4h43,time(1,:));% interpolate V1, so,...
% size Volt1 = nt x 1
P4h43=(Volt4h43.^2)*(1/R);
tVolt4h43(1,1:2:2*nt) = time(1,:);
tVolt4h43(1,2:2:2*nt) = Volt4h43;
tVolt4h43=reshape(tVolt4h43,8,[]);
% dlmwrite('tVolt4h43.dat',tVolt4h43,'precision','%4f')
%% Electrical Equation - Iteration 4
for i=1:ni*mnzeronod
data4h43(:,i,1)=dlmread('saweswept_ptz5a_sol146_h43_vel_4.txt',",...
[(7*i)+(50*(i-1)) 0 ((7*i)-1)+(50*i) 0]);% Time data
data4h43(:,i,2)=dlmread('saweswept_ptz5a_sol146_h43_vel_4.txt',",...
[(7*i)+(50*(i-1)) 1 ((7*i)-1)+(50*i) 1]);% Velocity x data
data4h43(:,i,3)=dlmread('saweswept_ptz5a_sol146_h43_vel_4.txt',",...
[(7*i)+(50*(i-1)) 2 ((7*i)-1)+(50*i) 2]);% Velocity y data

```

```

% 50 is total numeric lines in 1 page of SOL 146 F06
% 7 is total non-numeric lines in 1 page of SOL 146 F06 end
U4h43(:,:)= (reshape(data4h43(:,:),2,[nt,nnzeronod]));...
% Velocity x, (nnzeronod x nt) size
U4h43(nnzeronod+1:2*nnzeronod,:)= (reshape(data4h43(:,:),3,[nt,nnzeronod]));...
% Velocity y, (nnzeronod x nt) size
KU4h43=Kuv _ red'*U4h43;
[t5h43,V5h43] = ode45(@(t5h43,V5h43) ((-V5h43/R) +...
interp1(time(1,:),KU4h43,t5h43))/Cp, tspan, 0);
Volt5h43 = interp1(t5h43,V5h43,time(1,:));% interpolate V1, so,...
% size Volt1 = nt x 1
P5h43=(Volt5h43.^2)*(1/R);
tVolt5h43(1,1:2:2*nt) = time(1,:);
tVolt5h43(1,2:2:2*nt) = Volt5h43;
tVolt5h43=reshape(tVolt5h43,8,[]);
% dlmwrite('tVolt5h43.dat',tVolt5h43,'precision','%4f')
%% Plot results and references
for i=1:ni
wzh43(:,i,1)=dlmread('saweswept _ ptz5a _ sol146 _ h43 _ wz _ 4.txt','',...
[(7*i)+(50*(i-1)) 3 ((7*i)-1)+(50*i) 3]);% Tip Displacement z data
% 50 is total numeric lines in 1 page of SOL 146 F06
% 7 is total non-numeric lines in 1 page of SOL 146 F06
end
wzh43=(reshape(wzh43,[nt,1]));% Disp z, (1 x nt) size
figure(1)
plot(time(1,:),wzh43,'-k','linewidth',1.5')
xlabel('Time (s)', 'interpreter','latex');
ylabel('Z (mm)', 'interpreter','latex');
title('Vertical Tip Displacement vs Time');
legend('Gust Gradient = 12.5 MAC','Location','northeast')
axis ([0 2 -inf inf])
figure(2)
plot(ttime(1,:),Volt5h43,'-k','linewidth',1.5')
xlabel('Time (s)', 'interpreter','latex');
ylabel('V (Volt)', 'interpreter','latex');
title('Voltage vs Time');
legend('Gust Gradient = 12.5 MAC','Location','northeast')
axis ([0 2 -inf inf])

```

```

figure(3)
plot(time(1,:),P5h43,'-k','linewidth',1.5')
xlabel('Time (s)', 'interpreter','latex');
ylabel('P (Watt)', 'interpreter','latex');
title('Power vs Time');
legend('Gust Gradient = 12.5 MAC','Location','northeast')
axis ([0 2 -inf inf])
figure(4)
plot(time(1,:),Volt1h43,'-m',time(1,:),Volt2h43,'-g',time(1,:),Volt3h43,'-k',...
'linewidth',1.5')
xlabel('Time (s)', 'interpreter','latex');
ylabel('V (Volt)', 'interpreter','latex');
title('Voltage vs Time');
legend('Iteration 1','Iteration 2','Iteration 3','Location','northeast')
axis ([0 2 -inf 5000])
annotation('arrow',[0.33 0.38],[0.80 0.80])
axes('position', [.40, .55, .3, .3])
plot(time(1,:),Volt1h43,'-m',time(1,:),Volt2h43,'-g',time(1,:),Volt3h43,'-k',...
'linewidth',1.5')
axis ([0.40 0.55 3000 4000]);
figure(5)
plot(time(1,:),P1h43,'-m',time(1,:),P2h43,'-g',time(1,:),P3h43,'-k','linewidth',1.5')
xlabel('Time (s)', 'interpreter','latex');
ylabel('P (Watt)', 'interpreter','latex');
title('Power vs Time');
legend('Iteration 1','Iteration 2','Iteration 3','Location','northeast')
axis ([0 2 -inf inf])
annotation('arrow',[0.35 0.45],[0.75 0.70])
axes('position', [.5, .4, .3, .3])
plot(time(1,:),P1h43,'-m',time(1,:),P2h43,'-g',time(1,:),P3h43,'-k','linewidth',1.5')
axis ([0.40 0.55 11000 13000]);

```

APPENDIX G

Example of dynamic analysis results for wingbox with bulk PZT

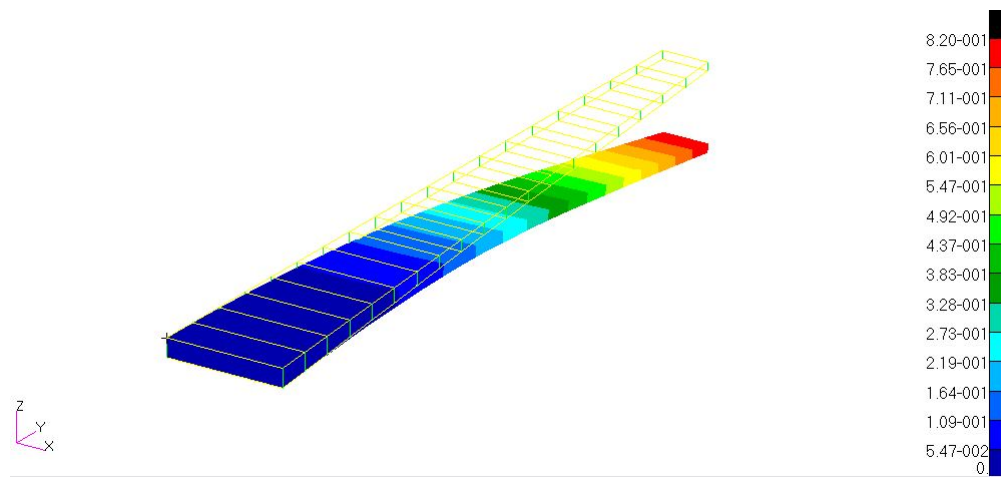


Figure G.1: The first bending mode of the jet aircraft wingbox with PZT-5A as upper skin material

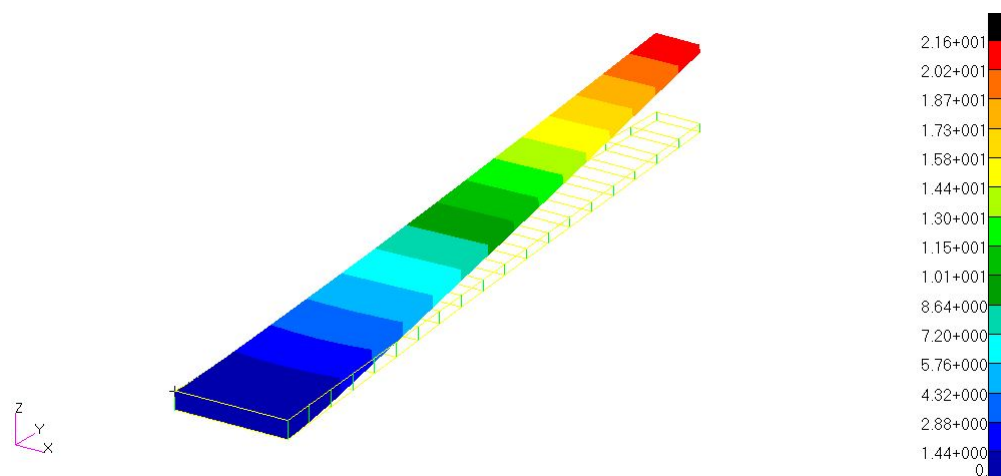


Figure G.2: The dynamic response at 0.5 frequency ratio of the jet aircraft wingbox with PZT-5A as upper skin material (displacement unit: inch)

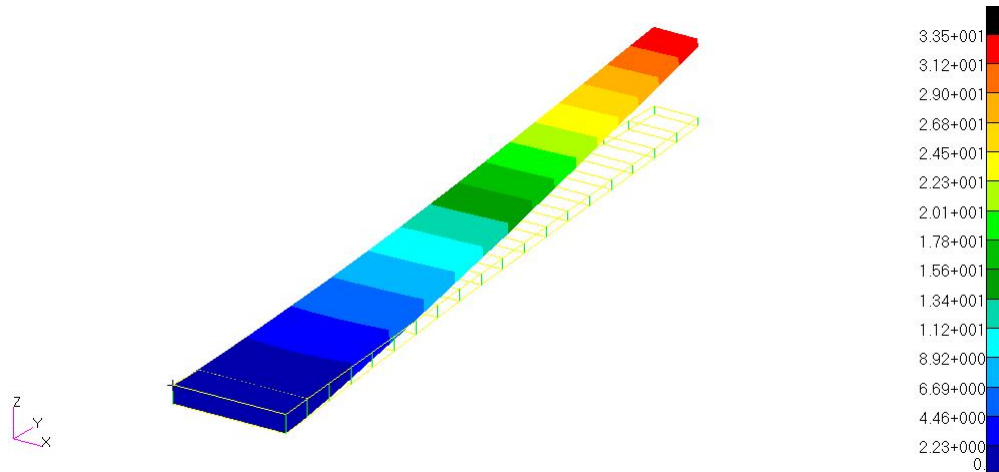


Figure G.3: The dynamic response at 0.7 frequency ratio of the jet aircraft wingbox with PZT-5A as upper skin material (displacement unit: inch)

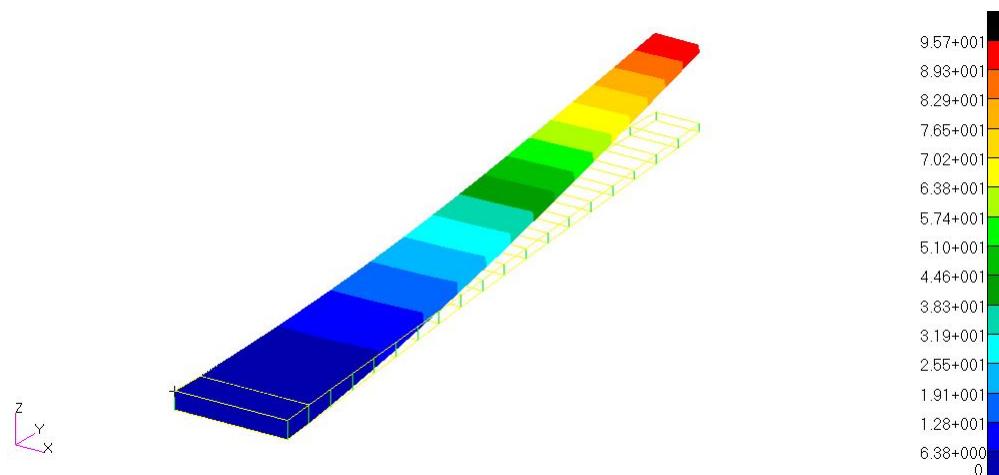


Figure G.4: The dynamic response at 0.9 frequency ratio of the jet aircraft wingbox with PZT-5A as upper skin material (displacement unit: inch)

APPENDIX H

Example of dynamic analysis results for wingbox with multiphase composite

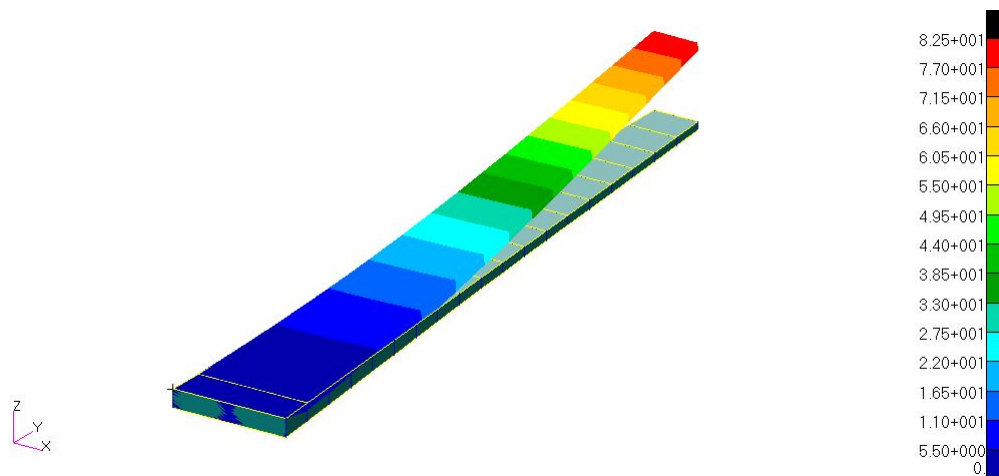


Figure H.1: The dynamic response at 0.9 frequency ratio of the jet aircraft wingbox with multiphase composite at Vf 50% and AR 0.2 (displacement unit: inch)

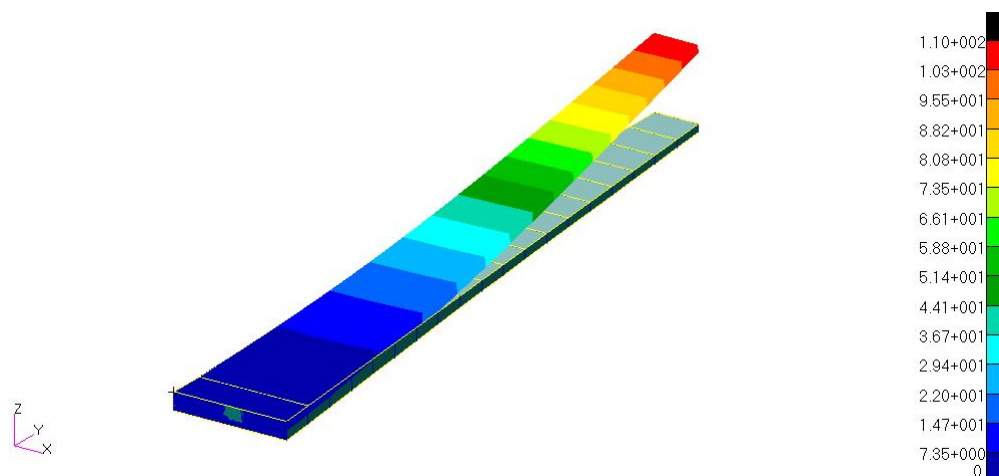


Figure H.2: The dynamic response at 0.9 frequency ratio of the jet aircraft wingbox with multiphase composite at Vf 50% and AR 0.6 (displacement unit: inch)

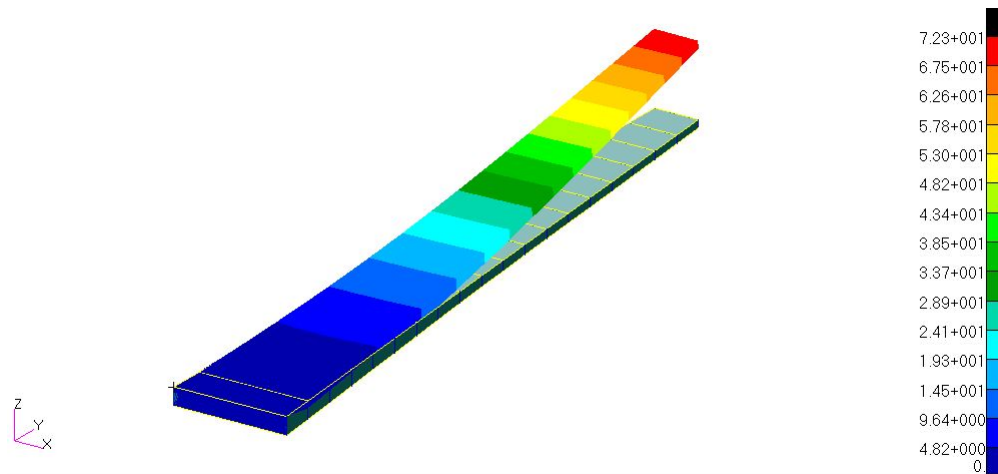


Figure H.3: The dynamic response at 0.9 frequency ratio of the jet aircraft wingbox with multiphase composite at Vf 60% and AR 0.2 (displacement unit: inch)

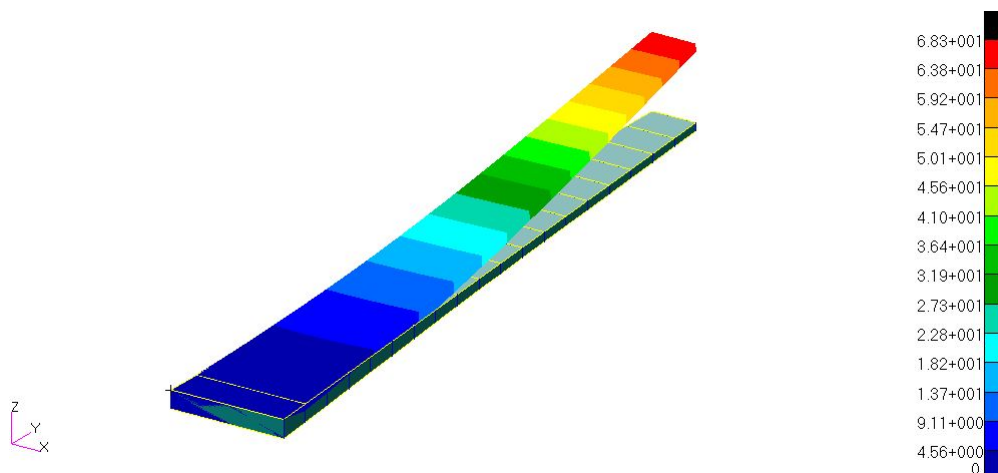


Figure H.4: The dynamic response at 0.9 frequency ratio of the jet aircraft wingbox with multiphase composite at Vf 70% and AR 0.2 (displacement unit: inch)

APPENDIX I

Example of flutter analysis results

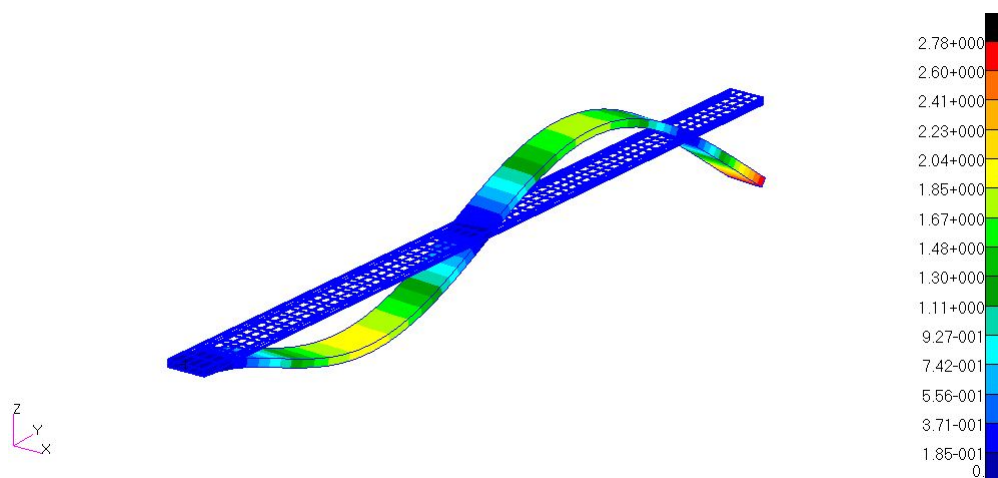


Figure I.1: The flutter response of Xiang et al. UAV wingbox associated with the third bending eigenvector at airspeed 150 m/s and frequency 174 Hz

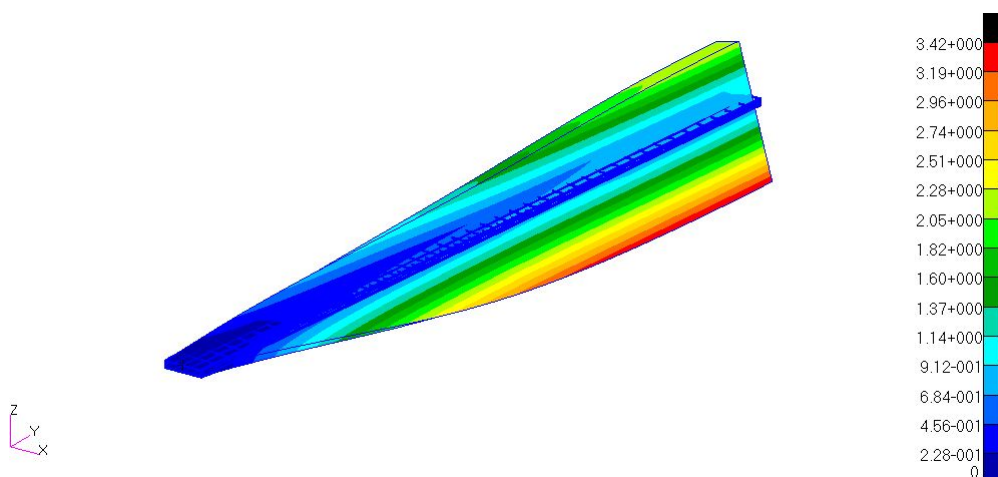


Figure I.2: The flutter response of Xiang et al. UAV wingbox associated with the first torsion eigenvector at airspeed 150 m/s and frequency 207 Hz

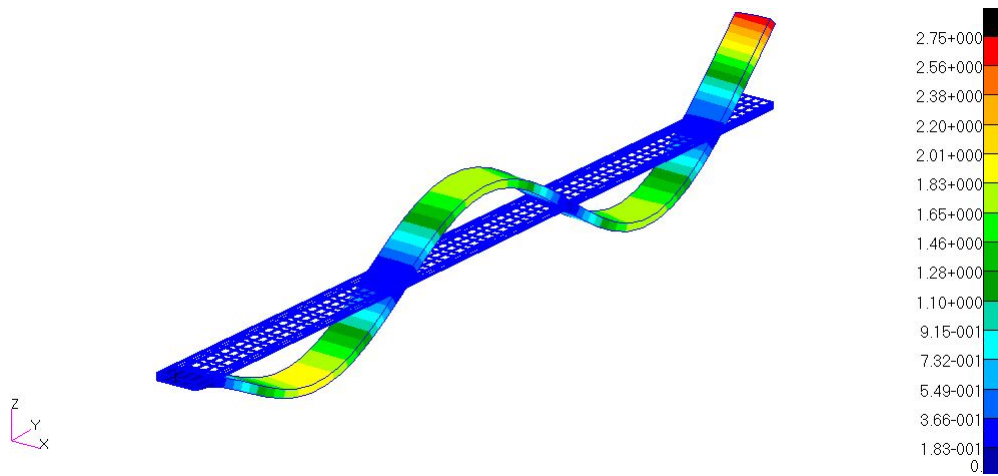


Figure I.3: The flutter response of Xiang et al. UAV wingbox associated with the fourth bending eigenvector at airspeed 150 m/s and frequency 336 Hz

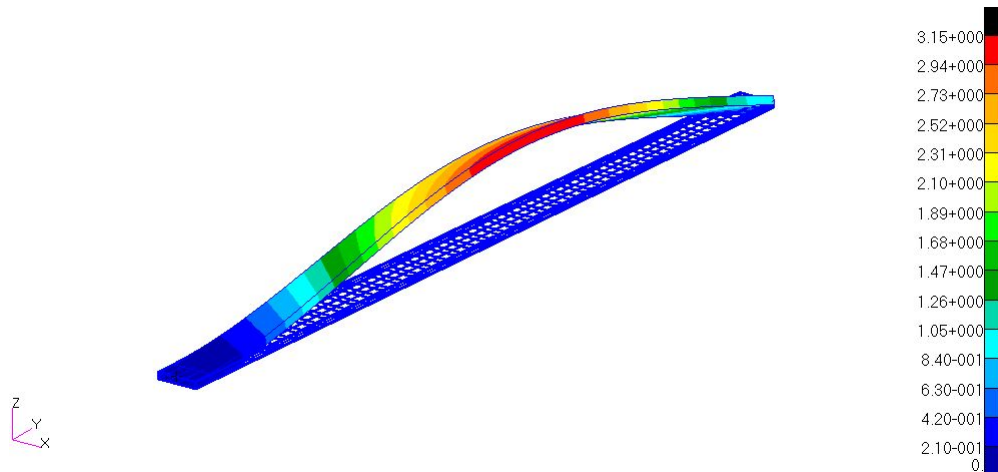


Figure I.4: The flutter response of Xiang et al. UAV wingbox associated with the mixed eigenvector (bending and torsion modes already coalesced) at airspeed 210 m/s and frequency 90 Hz

APPENDIX J

Example of gust analysis results

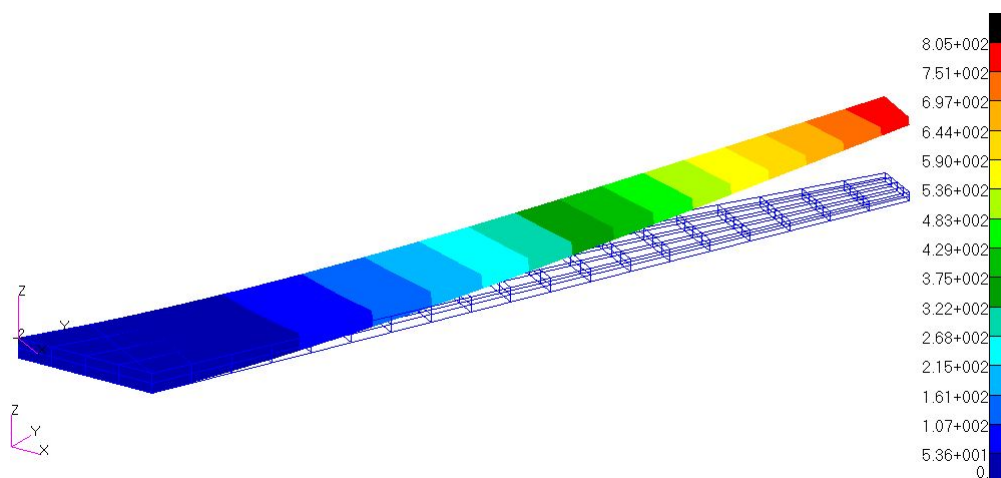


Figure J.1: Displacement contour of the aircraft wingbox for 12.5 MAC gust gradient distance with gust velocities at $t_g = 0.225$ s (displacement unit: mm)

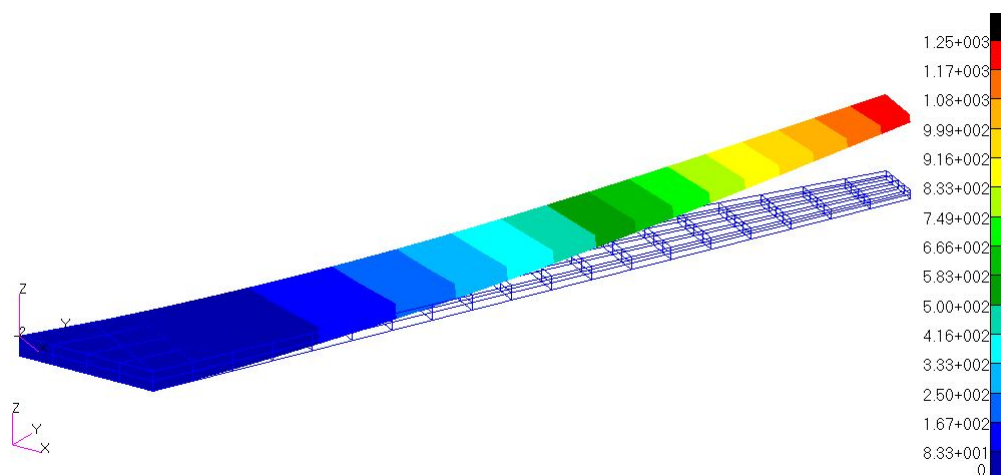


Figure J.2: Displacement contour of the aircraft wingbox for 12.5 MAC gust gradient distance with gust velocities at $t_g = 0.275$ s (displacement unit: mm)

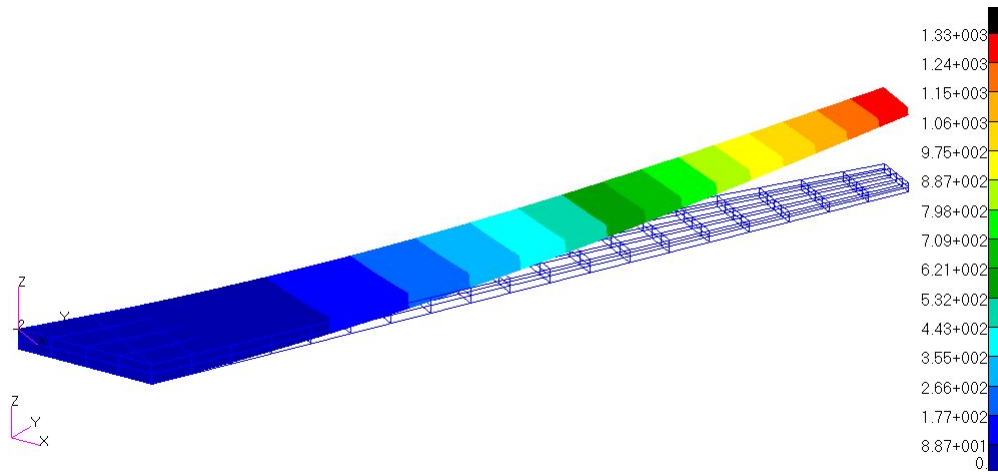


Figure J.3: Displacement contour of the aircraft wingbox for 12.5 MAC gust gradient distance with gust velocities at $t_g = 0.325$ s (displacement unit: mm)

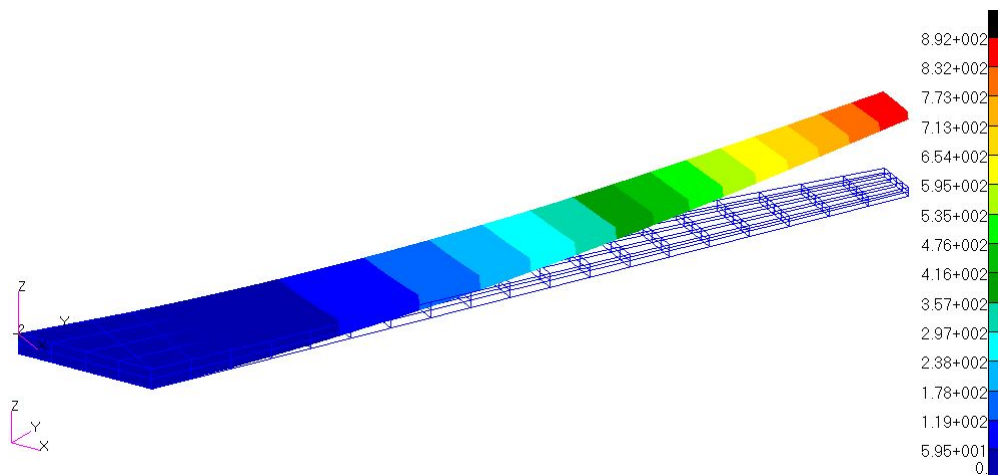


Figure J.4: Displacement contour of the aircraft wingbox for 12.5 MAC gust gradient distance with gust velocities at $t_g = 0.375$ s (displacement unit: mm)

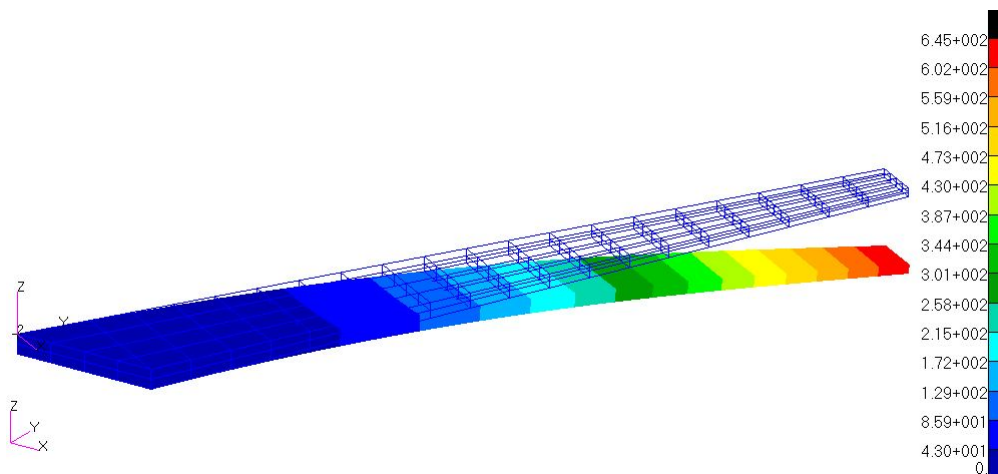


Figure J.5: Displacement contour of the aircraft wingbox for 12.5 MAC gust gradient distance with gust velocities at $t_g = 0.525$ s (displacement unit: mm)

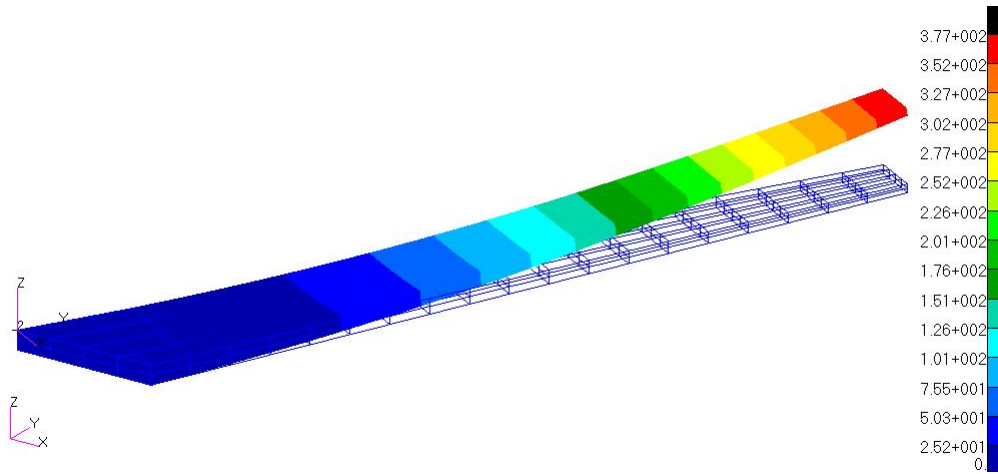


Figure J.6: Displacement contour of the aircraft wingbox for 12.5 MAC gust gradient distance with gust velocities at $t_g = 0.225$ s (displacement unit: mm)

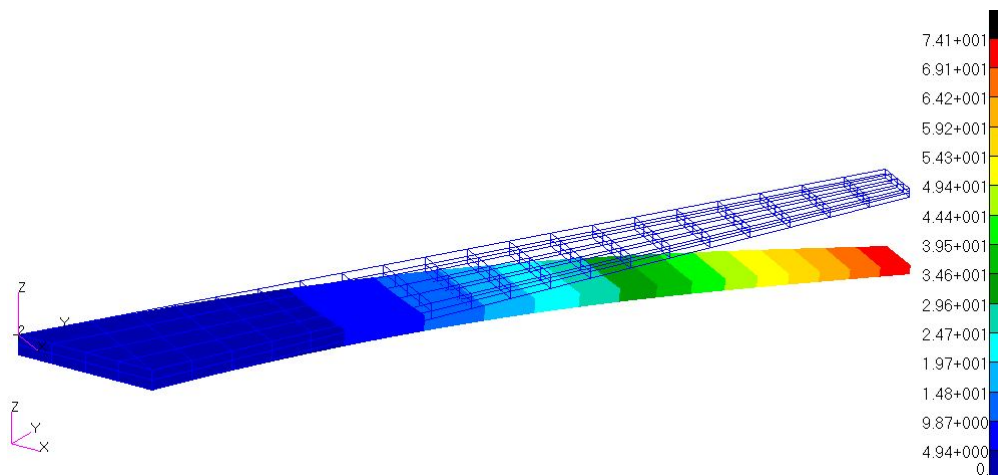


Figure J.7: Displacement contour of the aircraft wingbox for 12.5 MAC gust gradient distance with gust velocities at $t_g = 1.275$ s (displacement unit: mm)

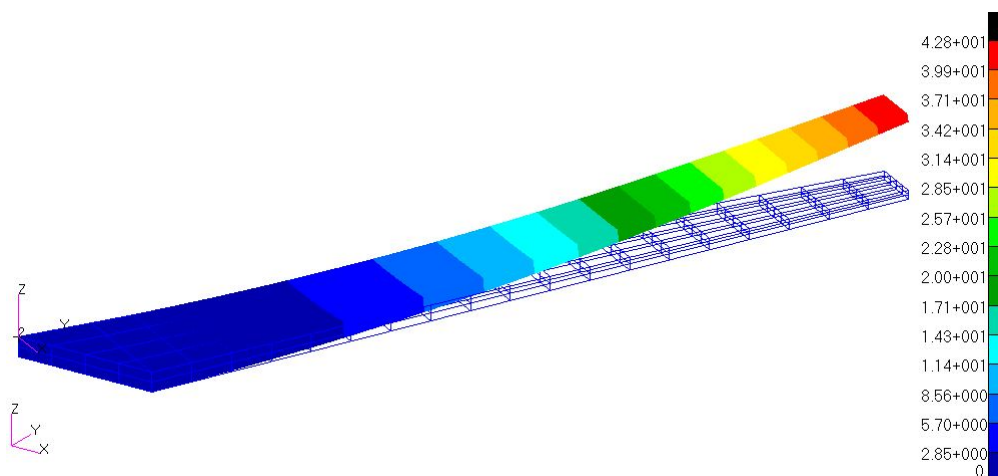


Figure J.8: Displacement contour of the aircraft wingbox for 12.5 MAC gust gradient distance with gust velocities at $t_g = 1.475$ s (displacement unit: mm)

APPENDIX K

Example of NASTRAN input for gust analysis with voltage load

The following pages show the NASTRAN input for gust analysis with additional voltage load. The main input for the unsteady aerodynamic/ gust analysis and voltage load are depicted. However, for displaying purpose only in this appendix, the FEM structural input has been shortened.

SOL 146

CEND

\$ Direct Text Input for Global Case Control Data

TITLE = WINGBOX_GUST

SUBTI = CANTILEVERED, DOUBLET-LATTICE AERODYNAMICS

LABEL = 1-COSINE GUST

ECHO = BOTH

LOADSET = 1

SPC = 1 \$ FUSELAGE CONSTRAINT

SDAMP = 2000 \$ STRUCTURAL DAMPING

METHOD= 1 \$ LANCZOS METHOD

SVEC = NONE \$ PRINT VIBRATION MODES

GUST = 1000 \$ AERODYNAMIC LOADING (1-COS GUST)

DLOAD = 999 \$ COMBINED LOAD

FREQ = 40 \$ FREQUENCY LIST

TSTEP = 41 \$ SOLUTION TIME STEPS

SET 999 = 1 THRU 10

MODESELECT = 999

OUTPUT

SET 1 = 1 THRU 104

VELOCITY = 1 \$ VELOCITY RESPONSE FOR GRID IN SET 1

\$ DISP = ALL \$ PRINT GUST RESPONSE

BEGIN BULK

\$ Direct Text Input for Bulk Data

TEMPD 4 0

PARAM GRDPNT 0

PARAM POST 1

PARAM PRTMAXIM YES

\$ * * STRUCTURAL DAMPING * *

\$ THE PARAMETER KDAMP DETERMINES THE MANNER OF INCLUSION
 \$ OF STRUCTURAL DAMPING IN EQUATIONS OF MOTION (SEE HANDBOOK
 \$ FOR DYNAMIC ANALYSIS, SECT. 3.2.2). IF SET TO -1, MODAL
 \$ DAMPING IS PUT INTO COMPLEX STIFFNESS MATRIX AS STRUCTURAL
 \$ DAMPING.

PARAM	N	V1	V2
KDAMP	+1		

\$ THE TABDMP1 ENTRY DEFINES MODAL DAMPING AS A TABULAR
 \$ FUNCTION OF FREQUENCY. THE DAMPING LEVELS ARE LINEAR
 \$ BETWEEN THE FREQUENCY AND DAMPING PAIRS AND ARE EXTRAP-
 \$ OLATED OUTSIDE THE TABULATED FREQUENCY RANGE.

TABDMP1	ID	F1	G1	F2	G2	ETC	ENDT
2000							
+T2000	0.0	0.02	1000.	0.02	ENDT		

\$ * * * AERODYNAMIC DATA * * *

(SNAIL-IN-SEC SYSTEM)

* * ELEMENT GEOMETRY * *

\$ THE AERO ENTRY SPECIFIES THE AERO COORDINATE SYSTEM, THE
 \$ VELOCITY (USED FOR DATA RECOVERY), THE REFERENCE CHORD
 \$ AND FLUID DENSITY, PLUS SYMMETRY KEYS. SYMXZ=1 INDICATES
 \$ THAT THE MODEL IS MOUNTED WITH A ROOT REFLECTION PLANE;
 \$ SYMXY = 0 INDICATES THAT THE MODEL IS MOUNTED FAR ENOUGH
 \$ FROM THE FLOOR SO THAT REFLECTION EFFECTS ARE NEGLIGIBLE.

\$234567 1234567 1234567 1234567 1234567 1234567 1234567

\$ ACSID VELOCITY REFC RHOREF SYMXZ SYMXY

AERO 0 24000. 3500. .4615E-9 1

\$ THE CAERO1 ENTRY IS USED FOR DOUBLET-LATTICE AERODYNAMICS.
 \$ LISTED ARE ITS PAERO ENTRY ID AND THE COORDINATE SYSTEM
 \$ FOR LOCATING THE INBOARD AND OUTBOARD LEADING EDGE POINTS
 \$ (1 AND 4). NSPAN AND NCHORD, OR LSPAN AND LCHORD, ARE
 \$ USED TO PARTITION THE WING INTO AERODYNAMIC BOXES, THE
 \$ FORMER FOR UNIFORMLY SPACED BOXES AND THE LATTER FOR
 \$ NON-UNIFORMLY SPACED BOXES. IGID IS THE ID OF ITS
 \$ ASSOCIATED INTERFERENCE GROUP. THE CONTINUATION ENTRY
 \$ DEFINES POINTS 1 AND 2, THE ROOT CHORD AND THE TIP CHORD.
 \$ THE BOXES FORMED BY THE GRID LINES WILL BE NUMBERED
 \$ BEGINNING WITH EID, SO A NUMBER SHOULD BE CHOSEN THAT IS
 \$ UNIQUE, AND IS GREATER THAN ALL STRUCTURAL GRID, SCALAR
 \$ AND EXTRA POINT IDS.

CAERO1	EID	PID	CP	NSPAN	NCHORD	LSPAN	LCHORD	IGID
3001	1000	0	40	8				1

\$234567 1234567 1234567 1234567 1234567 1234567 1234567 1234567 1234567 +CC1

\$ (FWD INBOARD POINT) ROOTCHORD (FWD OUTBOARD POINT) TIP CHORD

SAWEswept_ptz5a_sol146_H43_vel_4
 +CC1 -500. 0.0 0.0 5500. 7600. 13880. 0.0 1600.0

THE PAERO ENTRY IS REQUIRED EVEN THOUGH IT IS NON-FUNCTIONAL
 (BECAUSE THERE ARE NO ASSOCIATED BODIES IN THIS EXAMPLE).

PAERO1 1000

* * SPLINE FIT ON THE LIFTING SURFACES * *

* LINEAR SPLINE FIT ON THE WING *

THE SPLINE2 ENTRY SPECIFIES A BEAM SPLINE FOR INTERPOLATION OVER THE REGION OF THE CAERO ENTRY (ID1 AND ID2 ARE THE FIRST AND LAST BOXES IN THIS REGION). SETG REFERS TO A SET1 ENTRY WHERE THE STRUCTURAL GRID POINTS ARE DEFINED. DZ AND DTOR ARE SMOOTHING CONSTANTS FOR LINEAR ATTACHMENT AND TORSIONAL FLEXIBILITIES. DTHX AND DTHY ARE ROTATIONAL ATTACHMENT FLEXIBILITIES. CID IDENTIFIES THE SPLINE AXIS.

***** Aerodynamics Model *****

	EID	CAERO	BOX1	BOX2	SETG	DZ	METH	USAGE
SPLINE1	3001	3001	3001	3320	3001	0.0		
SET1	3001	1	THRU	104				

* * * SOLUTION SPECIFICATIONS * * *

* VIBRATION SOLUTION PARAMETERS *

THE EIGR ENTRY SPECIFIES THE METHOD OF EXTRACTING THE EIGENSOLUTIONS OF THE STRUCTURE IN A VACUUM, IN THIS CASE THE LANCZOS METHOD. TEN MODES ARE DESIRED, NORMALIZED ON THE MAXIMUM DISPLACEMENTS.

	SID	V1	V2	ND
EIGRL	1			10

* AERODYNAMIC CONDITIONS *

ALL COMBINATIONS OF MACH NUMBER AND REDUCED FREQUENCY LISTED ON THE MKAERO1 ENTRY AND ITS CONTINUATION CARD WILL BE USED TO GENERATE GENERALIZED AERO FORCE MATRICES. IF MORE THAN EIGHT MACH NOS OR REDUCED FREQUENCIES ARE REQUIRED A SECOND MKAERO1 ENTRY IS NECESSARY.

	M1	M2	M3	ETC	K1	K2	K3	K4	K5	ETC
MKAERO1	0.800									
+MK	0.02	0.1	0.5	1.0	2.0	3.0	4.0	5.0		
+MK1	10.0	15.0	20.0	25.0	50.0	75.0	100.0	150.0		

THE TLOAD1 ENTRY DEFINES A TIME DEPENDENT DYNAMIC LOAD OR AN ENFORCED MOTION. LISTED ARE THE IDS OF A DAREA ENTRY, A DELAY ENTRY, THE TYPE OF DYNAMIC EXCITATION AND THE TABLED ID.

	SID	LSEQ	DELAY	TYPE	TID
TLOAD1	5	6			1
LSEQ	1	6		4	
TEMP	4	1	1. +6	2	1. +6 3 1. +6
TEMP	4	4	1. +6	5	1. +6 6 1. +6
TEMP	4	7	1. +6	8	1. +6 9 1. +6
TEMP	4	10	1. +6	11	1. +6 12 1. +6
TEMP	4	13	1. +6	14	1. +6 15 1. +6
TEMP	4	16	1. +6	17	1. +6 18 1. +6
TEMP	4	19	1. +6	20	1. +6 21 1. +6
TEMP	4	22	1. +6	23	1. +6 24 1. +6
TEMP	4	25	1. +6	26	1. +6 27 1. +6
TEMP	4	28	1. +6	29	1. +6 30 1. +6
TEMP	4	31	1. +6	32	1. +6 33 1. +6
TEMP	4	34	1. +6	35	1. +6 36 1. +6
TEMP	4	37	1. +6	38	1. +6 39 1. +6
TEMP	4	40	1. +6	41	1. +6 42 1. +6
TEMP	4	43	1. +6	44	1. +6 45 1. +6
TEMP	4	46	1. +6	47	1. +6 48 1. +6
TEMP	4	49	1. +6	50	1. +6 51 1. +6
TEMP	4	52	1. +6	53	1. +6 54 1. +6
TEMP	4	55	1. +6	56	1. +6 57 1. +6
TEMP	4	58	1. +6	59	1. +6 60 1. +6

SAWEswept_ptz5a_sol 146_H43_vel_4

TEMP	4	61	1.+6	62	1.+6	63	1.+6
TEMP	4	64	1.+6	65	1.+6	66	1.+6
TEMP	4	67	1.+6	68	1.+6	69	1.+6
TEMP	4	70	1.+6	71	1.+6	72	1.+6
TEMP	4	73	1.+6	74	1.+6	75	1.+6
TEMP	4	76	1.+6	77	1.+6	78	1.+6
TEMP	4	79	1.+6	80	1.+6	81	1.+6
TEMP	4	82	1.+6	83	1.+6	84	1.+6
TEMP	4	85	1.+6	86	1.+6	87	1.+6
TEMP	4	88	1.+6	89	1.+6	90	1.+6
TEMP	4	91	1.+6	92	1.+6	93	1.+6
TEMP	4	94	1.+6	95	1.+6	96	1.+6
TEMP	4	97	1.+6	98	1.+6	99	1.+6
TEMP	4	100	1.+6	101	1.+6	102	1.+6
TEMP	4	103	1.+6	104	1.+6		

\$

INCLUDE 'tVol t4h43.dat'

\$

* * * * *

\$

* * DYNAMIC LOAD AND RESPONSE DATA * *

\$

GUST DEFINES A STATIONARY VERTICAL GUST. LISTED ARE T/LOAD ENTRY ID, GUST ANGLE OF ATTACK (I.E., THE RATIO OF GUST VELOCITY TO THE VEHICLE VELOCITY), LOCATION OF THE GUST WITH RESPECT TO THE ORIGIN OF THE AERO COORDINATE SYSTEM, AND THE VEHICLE VELOCITY.

\$234567	1234567	1234567	1234567	1234567	1234567	1234567	1234567	\$
GUST	SID	DLOAD	WG	X0	V			
	1000	1001	.0625	0.	240000.			

\$

TLOAD1 DEFINES A TIME DEPENDENT DYNAMIC LOAD OR ENFORCED MOTION. LISTED ARE THE ID, DAREA ID, DELAY ID, TYPE OF DYNAMIC EXCITATION, AND TABELDi ID.

TLOAD1	SID	DAREA	DELAY	TYPE	TID
	1001	1002			1003

\$

DAREA DEFINES THE DOF WHERE THE LOAD IS APPLIED AND A SCALE FACTOR. NOTE: THIS IS JUST DUMMY CARD REQUIRED BY TLOAD CARD BUT NOT AFFECTING THE ACTUAL LOAD

DAREA	SID	P	C	A
	1002	11	1	0.

\$

TABLED1 DEFINES A TABULAR FUNCTION OF A TIME-DEPENDENT LOAD.

TABLED1	SID									
	1003									+TAB1
+TAB1	X1	Y1	X2	Y2	X3	Y3	X4	Y4		+TAB2
	0.	0.	0.03646	.09549	0.07292	.34549	0.10938	.65451		
+TAB2	X5	Y5	Xn...	Yn...						+TAB3
	0.14584	.90451	0.1823	1.	0.21876	.90451	0.25522	.65451		
+TAB3	X9	Y9	Xn...	Yn...						
	0.29168	.34549	0.32814	.09549	0.3646	0.	ENDT			
\$234567	1234567	1234567	1234567	1234567	1234567	1234567	1234567	1234567	1234567	\$

\$

PARAM, GUSTAERO, -1 IS REQUIRED IF GUST LOADS ARE TO BE COMPUTED.

PARAM GUSTAERO -1

\$

PARAM, MACH SPECIFIES MACH NUMBER.

PARAM MACH 0.800

\$

PARAM, Q SPECIFIES DYNAMIC PRESSURE.

PARAM Q 13.291

\$

PARAM, LMODES, N SPECIFIES THAT N MODES ARE TO BE USED IN THE GUST ANALYSIS.

PARAM LMODES 10

\$

FREQ1 DEFINES THE SET OF FREQUENCIES USED TO OBTAIN THE FREQUENCY RESPONSE SOLUTION. LISTED ARE THE STARTING FREQUENCY, FREQUENCY INCREMENT AND NUMBER OF INCREMENTS.

\$234567	1234567	1234567	1234567	1234567	1234567	1234567	1234567	1234567	\$
FREQ1	SID	F1	DF	NDF					
	40	0.	0.2	350					

\$

TSTEP DEFINES TIME STEP INTERVALS AT WHICH THE TRANSIENT RESPONSES ARE DESIRED. LISTED ARE THE NUMBER OF STEPS, THE TIME INTERVAL AND SKIP FACTOR FOR OUTPUT.
T = 1/DF

\$

```

$      SID      N      DT      NO
TSTEP 41      199    .025    1
$
$
DLOAD  999    1.    1.    5    1.    1001
$
$ ALL THE STRUCTURAL MODEL FROM FEM IS COPIED BELOW
$ Elements and Element Properties for region : skin_upper
$ Composite Property Reference Material : piezo_comp
$ Composite Material Description :
PCOMP  1
2      .01    0.    YES    1    6.09    0.    YES
$ Pset: "skin_upper" will be imported as: "pcomp.1"
CQUAD4 1      1      1      2      6      5
CQUAD4 2      1      2      3      7      6
CQUAD4 3      1      3      4      8      7
CTRIA3 4      1      4      9      8
CQUAD4 5      1      5      6      11     10
CQUAD4 6      1      6      7      12     11
CQUAD4 7      1      7      8      13     12
CQUAD4 8      1      8      9      14     13
CQUAD4 9      1      10     11     16     15
CQUAD4 10     1      11     12     17     16
CQUAD4 11     1      12     13     18     17
CQUAD4 12     1      13     14     19     18
CQUAD4 13     1      15     16     21     20
CQUAD4 14     1      16     17     22     21
CQUAD4 15     1      17     18     23     22
CQUAD4 16     1      18     19     24     23
CQUAD4 17     1      20     21     26     25
CQUAD4 18     1      21     22     27     26
CQUAD4 19     1      22     23     28     27
CQUAD4 20     1      23     24     29     28
CQUAD4 21     1      25     26     31     30
CQUAD4 22     1      26     27     32     31
CQUAD4 23     1      27     28     33     32
CQUAD4 24     1      28     29     34     33
CQUAD4 25     1      30     31     36     35
CQUAD4 26     1      31     32     37     36
CQUAD4 27     1      32     33     38     37
CQUAD4 28     1      33     34     39     38
CQUAD4 29     1      35     36     41     40
CQUAD4 30     1      36     37     42     41
CQUAD4 31     1      37     38     43     42
CQUAD4 32     1      38     39     44     43
CQUAD4 33     1      40     41     46     45
CQUAD4 34     1      41     42     47     46
CQUAD4 35     1      42     43     48     47
CQUAD4 36     1      43     44     49     48
CQUAD4 37     1      45     46     51     50
CQUAD4 38     1      46     47     52     51
CQUAD4 39     1      47     48     53     52
CQUAD4 40     1      48     49     54     53
CQUAD4 41     1      50     51     56     55
CQUAD4 42     1      51     52     57     56
CQUAD4 43     1      52     53     58     57
CQUAD4 44     1      53     54     59     58
CQUAD4 45     1      55     56     61     60
CQUAD4 46     1      56     57     62     61
CQUAD4 47     1      57     58     63     62
CQUAD4 48     1      58     59     64     63
CQUAD4 49     1      60     61     66     65
CQUAD4 50     1      61     62     67     66
CQUAD4 51     1      62     63     68     67
CQUAD4 52     1      63     64     69     68
CQUAD4 53     1      65     66     71     70
CQUAD4 54     1      66     67     72     71
CQUAD4 55     1      67     68     73     72
CQUAD4 56     1      68     69     74     73
CQUAD4 57     1      70     71     76     75
CQUAD4 58     1      71     72     77     76
CQUAD4 59     1      72     73     78     77
CQUAD4 60     1      73     74     79     78
CQUAD4 61     1      75     76     81     80
CQUAD4 62     1      76     77     82     81
CQUAD4 63     1      77     78     83     82
CQUAD4 64     1      78     79     84     83
CQUAD4 65     1      80     81     86     85
CQUAD4 66     1      81     82     87     86
CQUAD4 67     1      82     83     88     87
CQUAD4 68     1      83     84     89     88
CQUAD4 69     1      85     86     91     90
CQUAD4 70     1      86     87     92     91
CQUAD4 71     1      87     88     93     92
CQUAD4 72     1      88     89     94     93

```

tVol t4h43

TABLED1, 1,
, 0. 0000, 0. 0000, 0. 0250, 2. 3135, 0. 0500, 4. 6804, 0. 0750, -10. 9943
, 0. 1000, -82. 7196, 0. 1250, -271. 9634, 0. 1500, -634. 8188, 0. 1750, -1186. 3383
, 0. 2000, -1836. 8734, 0. 2250, -2427. 6053, 0. 2500, -2822. 6709, 0. 2750, -2870. 3971
, 0. 3000, -2490. 7074, 0. 3250, -1694. 6164, 0. 3500, -510. 8557, 0. 3750, 860. 3047
, 0. 4000, 2210. 3075, 0. 4250, 3281. 2748, 0. 4500, 3881. 5671, 0. 4750, 3920. 8258
, 0. 5000, 3432. 0364, 0. 5250, 2573. 5400, 0. 5500, 1481. 2408, 0. 5750, 350. 9155
, 0. 6000, -654. 4099, 0. 6250, -1396. 1086, 0. 6500, -1794. 9457, 0. 6750, -1819. 9479
, 0. 7000, -1538. 4317, 0. 7250, -1046. 6470, 0. 7500, -445. 1146, 0. 7750, 146. 2349
, 0. 8000, 639. 6721, 0. 8250, 974. 4865, 0. 8500, 1110. 1262, 0. 8750, 1044. 1474
, 0. 9000, 821. 0892, 0. 9250, 497. 6614, 0. 9500, 139. 5043, 0. 9750, -187. 3755
, 1. 0000, -444. 8861, 1. 0250, -595. 9391, 1. 0500, -634. 5928, 1. 0750, -561. 2838
, 1. 1000, -406. 5495, 1. 1250, -206. 9737, 1. 1500, -0. 8384, 1. 1750, 175. 0979
, 1. 2000, 303. 1245, 1. 2250, 363. 1700, 1. 2500, 359. 4439, 1. 2750, 298. 4442
, 1. 3000, 194. 3961, 1. 3250, 73. 7661, 1. 3500, -42. 9718, 1. 3750, -135. 6717
, 1. 4000, -194. 4653, 1. 4250, -214. 6643, 1. 4500, -198. 3722, 1. 4750, -152. 0631
, 1. 5000, -87. 5385, 1. 5250, -17. 3102, 1. 5500, 46. 9647, 1. 5750, 93. 8178
, 1. 6000, 118. 5986, 1. 6250, 122. 7137, 1. 6500, 105. 8869, 1. 6750, 74. 2883
, 1. 7000, 34. 5582, 1. 7250, -5. 3924, 1. 7500, -38. 8338, 1. 7750, -61. 4827
, 1. 8000, -71. 0196, 1. 8250, -68. 1684, 1. 8500, -55. 1468, 1. 8750, -34. 6222
, 1. 9000, -11. 2215, 1. 9250, 11. 0186, 1. 9500, 28. 2893, 1. 9750, 38. 6265
, 2. 0000, 41. 3660, 2. 0250, 37. 3086, 2. 0500, 27. 8909, 2. 0750, 15. 1204
, 2. 1000, 1. 7412, 2. 1250, -10. 3028, 2. 1500, -19. 2165, 2. 1750, -23. 6610
, 2. 2000, -23. 5290, 2. 2250, -19. 8979, 2. 2500, -13. 4615, 2. 2750, -5. 8007
, 2. 3000, 1. 8375, 2. 3250, 8. 3088, 2. 3500, 12. 4832, 2. 3750, 14. 1057
, 2. 4000, 13. 1182, 2. 4250, 10. 2666, 2. 4500, 6. 1982, 2. 4750, 1. 6780
, 2. 5000, -2. 5115, 2. 5250, -5. 8019, 2. 5500, -7. 6635, 2. 5750, -8. 0508
, 2. 6000, -7. 0462, 2. 6250, -5. 0707, 2. 6500, -2. 5389, 2. 6750, 0. 0420
, 2. 7000, 2. 3058, 2. 7250, 3. 8761, 2. 7500, 4. 6013, 2. 7750, 4. 5020
, 2. 8000, 3. 6919, 2. 8250, 2. 3922, 2. 8500, 0. 8787, 2. 8750, -0. 5595
, 2. 9000, -1. 7214, 2. 9250, -2. 4403, 2. 9500, -2. 6843, 2. 9750, -2. 4828
, 3. 0000, -1. 8812, 3. 0250, -1. 0639, 3. 0500, -0. 1859, 3. 0750, 0. 6035
, 3. 1000, 1. 1947, 3. 1250, 1. 5085, 3. 1500, 1. 5437, 3. 1750, 1. 3287
, 3. 2000, 0. 9207, 3. 2250, 0. 4233, 3. 2500, -0. 0769, 3. 2750, -0. 5026
, 3. 3000, -0. 7826, 3. 3250, -0. 8968, 3. 3500, -0. 8593, 3. 3750, -0. 6880
, 3. 4000, -0. 4262, 3. 4250, -0. 1272, 3. 4500, 0. 1504, 3. 4750, 0. 3679
, 3. 5000, 0. 4917, 3. 5250, 0. 5203, 3. 5500, 0. 4663, 3. 5750, 0. 3438
, 3. 6000, 0. 1783, 3. 6250, 0. 0030, 3. 6500, -0. 1473, 3. 6750, -0. 2537
, 3. 7000, -0. 3017, 3. 7250, -0. 2980, 3. 7500, -0. 2487, 3. 7750, -0. 1636
, 3. 8000, -0. 0612, 3. 8250, 0. 0413, 3. 8500, 0. 1244, 3. 8750, 0. 1766
, 3. 9000, 0. 1948, 3. 9250, 0. 1821, 3. 9500, 0. 1447, 3. 9750, 0. 0885
, 4. 0000, 0. 0231, 4. 0250, -0. 0394, 4. 0500, -0. 0886, 4. 0750, -0. 1169
, 4. 1000, -0. 1245, 4. 1250, -0. 1145, 4. 1500, -0. 0886, 4. 1750, -0. 0508
, 4. 2000, -0. 0056, 4. 2250, 0. 0390, 4. 2500, 0. 0759, 4. 2750, 0. 1030
, 4. 3000, 0. 1193, 4. 3250, 0. 1248, 4. 3500, 0. 1200, 4. 3750, 0. 1030
, 4. 4000, 0. 0751, 4. 4250, 0. 0400, 4. 4500, 0. 0003, 4. 4750, -0. 0429
, 4. 5000, -0. 0894, 4. 5250, -0. 1366, 4. 5500, -0. 1797, 4. 5750, -0. 2110
, 4. 6000, -0. 2251, 4. 6250, -0. 2169, 4. 6500, -0. 1816, 4. 6750, -0. 1094
, 4. 7000, 0. 0062, 4. 7250, 0. 1681, 4. 7500, 0. 3683, 4. 7750, 0. 5998
, 4. 8000, 0. 8495, 4. 8250, 1. 0897, 4. 8500, 1. 2950, 4. 8750, 1. 4333
, 4. 9000, 1. 4548, 4. 9250, 1. 3558, 4. 9500, 1. 1871, 4. 9750, 1. 1924
, ENDT

APPENDIX L

Example of NASTRAN output for gust analysis with voltage load

The following pages show the NASTRAN output for gust analysis with additional voltage load. The output defines voltage responses for a node (point) at 6-DoF (3 translations and 3 rotations) within a time range. This output used as input in the MATLAB code for the iterative FEM. However, for displaying purpose only in this appendix, the data has been shortened.

1 TESTPLATE_FLUTTER
Nastran 11/13/14 PAE 76
CANTILEVERED, DOUBLET-LATTICE AERODYNAMICS AT MACH NO. 0.0

0 1-COSINE UST

POINT-ID = 1

VELOCITY VECTOR

TIME	T1	T2	T3	R1	R2
R3					
0.0	0.0	0.0	0.0	0.0	0.0
0.0					
2.500000E-02	0.0	0.0	0.0	0.0	0.0
0.0					
5.000000E-02	0.0	0.0	0.0	0.0	0.0
0.0					
7.500000E-02	0.0	0.0	0.0	0.0	0.0
0.0					
1.000000E-01	0.0	0.0	0.0	0.0	0.0
0.0					
1.250000E-01	0.0	0.0	0.0	0.0	0.0
0.0					
1.500000E-01	0.0	0.0	0.0	0.0	0.0
0.0					
1.750000E-01	0.0	0.0	0.0	0.0	0.0
0.0					
2.000000E-01	0.0	0.0	0.0	0.0	0.0
0.0					
2.250000E-01	0.0	0.0	0.0	0.0	0.0
0.0					
2.500000E-01	0.0	0.0	0.0	0.0	0.0
0.0					
2.750000E-01	0.0	0.0	0.0	0.0	0.0
0.0					
3.000000E-01	0.0	0.0	0.0	0.0	0.0
0.0					
3.250000E-01	0.0	0.0	0.0	0.0	0.0
0.0					
3.500000E-01	0.0	0.0	0.0	0.0	0.0
0.0					
3.750000E-01	0.0	0.0	0.0	0.0	0.0
0.0					
4.000000E-01	0.0	0.0	0.0	0.0	0.0
0.0					
4.250000E-01	0.0	0.0	0.0	0.0	0.0
0.0					
4.500000E-01	0.0	0.0	0.0	0.0	0.0
0.0					
4.750000E-01	0.0	0.0	0.0	0.0	0.0
0.0					
5.000000E-01	0.0	0.0	0.0	0.0	0.0
0.0					
5.250000E-01	0.0	0.0	0.0	0.0	0.0
0.0					
5.500000E-01	0.0	0.0	0.0	0.0	0.0
0.0					
5.750000E-01	0.0	0.0	0.0	0.0	0.0
0.0					
6.000000E-01	0.0	0.0	0.0	0.0	0.0
0.0					
6.250000E-01	0.0	0.0	0.0	0.0	0.0
0.0					
6.500000E-01	0.0	0.0	0.0	0.0	0.0
0.0					
6.750000E-01	0.0	0.0	0.0	0.0	0.0
0.0					
7.000000E-01	0.0	0.0	0.0	0.0	0.0
0.0					
7.250000E-01	0.0	0.0	0.0	0.0	0.0
0.0					
7.500000E-01	0.0	0.0	0.0	0.0	0.0
0.0					
7.750000E-01	0.0	0.0	0.0	0.0	0.0
0.0					
8.000000E-01	0.0	0.0	0.0	0.0	0.0
0.0					
8.250000E-01	0.0	0.0	0.0	0.0	0.0
0.0					
8.500000E-01	0.0	0.0	0.0	0.0	0.0
0.0					
8.750000E-01	0.0	0.0	0.0	0.0	0.0
0.0					
9.000000E-01	0.0	0.0	0.0	0.0	0.0
0.0					

saweswept_ptz5a_sol 146_h43_vel_4

0.0	9.250000E-01	0.0	0.0	0.0	0.0	0.0
0.0	9.500000E-01	0.0	0.0	0.0	0.0	0.0
0.0	9.750000E-01	0.0	0.0	0.0	0.0	0.0
0.0	1.000000E+00	0.0	0.0	0.0	0.0	0.0
0.0	1.025000E+00	0.0	0.0	0.0	0.0	0.0
0.0	1.050000E+00	0.0	0.0	0.0	0.0	0.0
0.0	1.075000E+00	0.0	0.0	0.0	0.0	0.0
0.0	1.100000E+00	0.0	0.0	0.0	0.0	0.0
0.0	1.125000E+00	0.0	0.0	0.0	0.0	0.0
0.0	1.150000E+00	0.0	0.0	0.0	0.0	0.0
0.0	1.175000E+00	0.0	0.0	0.0	0.0	0.0
0.0	1.200000E+00	0.0	0.0	0.0	0.0	0.0
0.0	1.225000E+00	0.0	0.0	0.0	0.0	0.0

1 TESTPLATE_FLUTTER JULY 8, 2018 MSC

Nastran 11/13/14 PAE 77
 CANTILEVERED, DOUBLET-LATTICE AERODYNAMICS AT MACH NO. 0.0

0 1-COSINE UST

POINT-ID = 1

VELOCITY VECTOR

R3	TIME	T1	T2	T3	R1	R2
0.0	1.250000E+00	0.0	0.0	0.0	0.0	0.0
0.0	1.275000E+00	0.0	0.0	0.0	0.0	0.0
0.0	1.300000E+00	0.0	0.0	0.0	0.0	0.0
0.0	1.325000E+00	0.0	0.0	0.0	0.0	0.0
0.0	1.350000E+00	0.0	0.0	0.0	0.0	0.0
0.0	1.375000E+00	0.0	0.0	0.0	0.0	0.0
0.0	1.400000E+00	0.0	0.0	0.0	0.0	0.0
0.0	1.425000E+00	0.0	0.0	0.0	0.0	0.0
0.0	1.450000E+00	0.0	0.0	0.0	0.0	0.0
0.0	1.475000E+00	0.0	0.0	0.0	0.0	0.0
0.0	1.500000E+00	0.0	0.0	0.0	0.0	0.0
0.0	1.525000E+00	0.0	0.0	0.0	0.0	0.0
0.0	1.550000E+00	0.0	0.0	0.0	0.0	0.0
0.0	1.575000E+00	0.0	0.0	0.0	0.0	0.0
0.0	1.600000E+00	0.0	0.0	0.0	0.0	0.0
0.0	1.625000E+00	0.0	0.0	0.0	0.0	0.0
0.0	1.650000E+00	0.0	0.0	0.0	0.0	0.0
0.0	1.675000E+00	0.0	0.0	0.0	0.0	0.0
0.0	1.700000E+00	0.0	0.0	0.0	0.0	0.0
0.0	1.725000E+00	0.0	0.0	0.0	0.0	0.0
0.0	1.750000E+00	0.0	0.0	0.0	0.0	0.0
0.0	1.775000E+00	0.0	0.0	0.0	0.0	0.0
0.0	1.800000E+00	0.0	0.0	0.0	0.0	0.0
0.0	1.825000E+00	0.0	0.0	0.0	0.0	0.0

Nastran 11/13/14 PAE 125
 CANTILEVERED, DOUBLET-LATTICE AERODYNAMICS AT MACH NO. 0.0

0 1-COSINE UST

POINT-ID = 13

VELOCITY VECTOR

TIME	T1	T2	T3	R1	R2
R3					
1. 250000E+00	3. 018021E-01	8. 914543E-01	-2. 888492E+00	-4. 913677E-03	1. 665195E-03
-3. 359958E-04					
1. 275000E+00	8. 877153E-02	1. 155595E-01	-3. 545005E-01	-6. 718423E-04	3. 785901E-04
-4. 561735E-05					
1. 300000E+00	-1. 223534E-01	-5. 788389E-01	1. 938026E+00	3. 169167E-03	-8. 158363E-04
2. 209204E-04					
1. 325000E+00	-3. 025409E-01	-1. 131719E+00	3. 854096E+00	6. 320012E-03	-1. 795745E-03
4. 247121E-04					
1. 350000E+00	-4. 113624E-01	-1. 454886E+00	5. 006360E+00	8. 194306E-03	-2. 394885E-03
5. 341288E-04					
1. 375000E+00	-4. 284621E-01	-1. 484951E+00	5. 109393E+00	8. 370501E-03	-2. 498593E-03
5. 335273E-04					
1. 400000E+00	-3. 661546E-01	-1. 236316E+00	4. 210274E+00	6. 939012E-03	-2. 125072E-03
4. 434834E-04					
1. 425000E+00	-2. 573636E-01	-8. 056436E-01	2. 659308E+00	4. 471546E-03	-1. 442272E-03
3. 054965E-04					
1. 450000E+00	-1. 271670E-01	-3. 292407E-01	1. 021461E+00	1. 795806E-03	-6. 579097E-04
1. 370932E-04					
1. 475000E+00	3. 215468E-03	1. 091150E-01	-4. 269446E-01	-6. 288690E-04	8. 245922E-05
-3. 444303E-05					
1. 500000E+00	1. 174433E-01	4. 692566E-01	-1. 578425E+00	-2. 597314E-03	7. 102106E-04
-1. 840826E-04					
1. 525000E+00	1. 994102E-01	7. 328935E-01	-2. 463925E+00	-4. 069112E-03	1. 179349E-03
-2. 777597E-04					
1. 550000E+00	2. 412568E-01	8. 608315E-01	-2. 942354E+00	-4. 826362E-03	1. 425715E-03
-3. 105939E-04					
1. 575000E+00	2. 404300E-01	8. 230457E-01	-2. 843774E+00	-4. 653131E-03	1. 398350E-03
-2. 932292E-04					
1. 600000E+00	1. 977613E-01	6. 371763E-01	-2. 182087E+00	-3. 600478E-03	1. 113966E-03
-2. 348866E-04					
1. 625000E+00	1. 237009E-01	3. 673314E-01	-1. 197876E+00	-2. 033526E-03	6. 730634E-04
-1. 438171E-04					
1. 650000E+00	3. 921142E-02	8. 971892E-02	-2. 335192E-01	-4. 508116E-04	2. 052376E-04
-3. 498167E-05					
1. 675000E+00	-3. 395760E-02	-1. 547981E-01	5. 601961E-01	8. 880699E-04	-2. 091430E-04
6. 060499E-05					
1. 700000E+00	-8. 644745E-02	-3. 431142E-01	1. 146403E+00	1. 887968E-03	-5. 307549E-04
1. 269509E-04					
1. 725000E+00	-1. 218678E-01	-4. 616550E-01	1. 542002E+00	2. 544439E-03	-7. 461493E-04
1. 646513E-04					
1. 750000E+00	-1. 411848E-01	-4. 944018E-01	1. 689832E+00	2. 776473E-03	-8. 286189E-04
1. 798798E-04					
1. 775000E+00	-1. 368041E-01	-4. 390366E-01	1. 524904E+00	2. 505644E-03	-7. 608862E-04
1. 677081E-04					
1. 800000E+00	-1. 032517E-01	-3. 168100E-01	1. 087741E+00	1. 800223E-03	-5. 634433E-04
1. 210885E-04					
1. 825000E+00	-5. 108851E-02	-1. 580824E-01	5. 005932E-01	8. 537362E-04	-2. 927354E-04
5. 400764E-05					
1. 850000E+00	-1. 452706E-03	2. 521327E-03	-5. 727227E-02	-6. 198284E-05	-2. 102941E-05
-8. 695444E-06					
1. 875000E+00	3. 296999E-02	1. 406697E-01	-4. 940124E-01	-7. 923287E-04	2. 058966E-04
-5. 003075E-05					
1. 900000E+00	5. 574218E-02	2. 361913E-01	-7. 802777E-01	-1. 281118E-03	3. 670648E-04
-7. 663096E-05					
1. 925000E+00	7. 399895E-02	2. 796990E-01	-9. 300632E-01	-1. 537032E-03	4. 562878E-04
-9. 791497E-05					
1. 950000E+00	8. 423702E-02	2. 736187E-01	-9. 424017E-01	-1. 555310E-03	4. 686965E-04
-1. 082069E-04					
1. 975000E+00	7. 626593E-02	2. 272394E-01	-7. 981332E-01	-1. 315526E-03	4. 026972E-04
-9. 404814E-05					
2. 000000E+00	4. 906438E-02	1. 529777E-01	-5. 211948E-01	-8. 624854E-04	2. 739423E-04
-5. 493709E-05					
2. 025000E+00	1. 582801E-02	6. 095287E-02	-1. 750975E-01	-3. 023870E-04	1. 129281E-04
-1. 145806E-05					
2. 050000E+00	-9. 048259E-03	-3. 285731E-02	1. 416910E-01	2. 152304E-04	-4. 193599E-05
1. 783951E-05					
2. 075000E+00	-2. 353648E-02	-1. 096115E-01	3. 712469E-01	5. 986382E-04	-1. 636158E-04
3. 255460E-05					
2. 100000E+00	-3. 490832E-02	-1. 538016E-01	5. 013138E-01	8. 236037E-04	-2. 401674E-04
4. 545476E-05					
2. 125000E+00	-4. 587012E-02	-1. 629479E-01	5. 458346E-01	9. 038811E-04	-2. 704811E-04
6. 013416E-05					
2. 150000E+00	-4. 978830E-02	-1. 468430E-01	5. 155519E-01	8. 530853E-04	-2. 583958E-04
6. 477133E-05					
2. 175000E+00	-4. 008333E-02	-1. 147921E-01	4. 058519E-01	6. 703204E-04	-2. 072791E-04

saweswept_ptz5a_sol 146_h43_vel_4

4. 942548E-05						
2. 200000E+00	-2. 045420E-02	-7. 098755E-02	2. 328671E-01	3. 863435E-04	-1. 265431E-04	
2. 052640E-05						
2. 225000E+00	-1. 801986E-03	-1. 736390E-02	3. 422764E-02	6. 360714E-05	-3. 237332E-05	
-4. 019993E-06						
2. 250000E+00	9. 185501E-03	3. 689863E-02	-1. 386320E-01	-2. 187521E-04	5. 375959E-05	
-1. 515225E-05						
2. 275000E+00	1. 543346E-02	7. 782198E-02	-2. 549198E-01	-4. 132127E-04	1. 169169E-04	
-1. 954737E-05						
2. 300000E+00	2. 198924E-02	9. 555425E-02	-3. 104720E-01	-5. 100389E-04	1. 502392E-04	
-2. 722243E-05						
2. 325000E+00	2. 823124E-02	9. 192727E-02	-3. 134783E-01	-5. 195563E-04	1. 560855E-04	
-3. 701960E-05						
2. 350000E+00	2. 837986E-02	7. 664351E-02	-2. 748842E-01	-4. 562252E-04	1. 391233E-04	
-3. 774947E-05						
2. 375000E+00	1. 980279E-02	5. 600881E-02	-1. 970816E-01	-3. 269890E-04	1. 029895E-04	
-2. 438041E-05						
2. 400000E+00	7. 138335E-03	3. 073279E-02	-9. 347762E-02	-1. 557663E-04	5. 387238E-05	
-4. 838585E-06						
2. 425000E+00	-2. 698327E-03	-1. 373258E-04	1. 704285E-02	2. 486289E-05	-9. 216393E-08	
7. 962350E-06						
2. 450000E+00	-7. 231271E-03	-3. 089691E-02	1. 089446E-01	1. 746970E-04	-4. 671577E-05	
1. 070907E-05						
2. 475000E+00	-9. 781658E-03	-5. 196571E-02	1. 660354E-01	2. 697745E-04	-7. 793179E-05	
1. 106820E-05						

1 TESTPLATE_FLUTTER JULY 8, 2018 MSC

Nastran 11/13/14 PAE 126
CANTI LEVERED, DOUBLET-LATTICE AERODYNAMICS AT MACH NO. 0.0

0 1-COSINE UST

POINT-ID = 13

VELOCITY VECTOR

TIME	T1	T2	T3	R1	R2
R3					
2. 500000E+00	-1. 341345E-02	-5. 755111E-02	1. 867187E-01	3. 065565E-04	-9. 081404E-05
1. 591674E-05					
2. 525000E+00	-1. 681938E-02	-5. 036348E-02	1. 753934E-01	2. 912364E-04	-8. 785409E-05
2. 254940E-05					
2. 550000E+00	-1. 592185E-02	-3. 841492E-02	1. 421456E-01	2. 369763E-04	-7. 302592E-05
2. 190387E-05					
2. 575000E+00	-9. 496507E-03	-2. 590689E-02	9. 077088E-02	1. 513983E-04	-4. 895806E-05
1. 139393E-05					
2. 600000E+00	-1. 277074E-03	-1. 202385E-02	3. 027400E-02	5. 064575E-05	-1. 956666E-05
-1. 762314E-06					
2. 625000E+00	3. 946489E-03	5. 303766E-03	-2. 994814E-02	-4. 801622E-05	1. 046822E-05
-8. 097372E-06					
2. 650000E+00	5. 137724E-03	2. 284320E-02	-7. 744919E-02	-1. 250256E-04	3. 478522E-05
-6. 767819E-06					
2. 675000E+00	5. 510922E-03	3. 369194E-02	-1. 037448E-01	-1. 687968E-04	4. 948876E-05
-5. 231175E-06					
2. 700000E+00	7. 636522E-03	3. 392768E-02	-1. 089840E-01	-1. 790620E-04	5. 345930E-05
-8. 801099E-06					
2. 725000E+00	1. 013523E-02	2. 640421E-02	-9. 583440E-02	-1. 595926E-04	4. 845513E-05
-1. 415112E-05					
2. 750000E+00	9. 290924E-03	1. 783409E-02	-7. 120925E-02	-1. 192237E-04	3. 703995E-05
-1. 328050E-05					
2. 775000E+00	4. 243002E-03	1. 117998E-02	-3. 836487E-02	-6. 445217E-05	2. 162064E-05
-4. 686019E-06					
2. 800000E+00	-1. 504565E-03	4. 341206E-03	-3. 647980E-03	-6. 395997E-06	4. 660537E-06
4. 635616E-06					
2. 825000E+00	-3. 898834E-03	-5. 519086E-03	2. 798661E-02	4. 556305E-05	-1. 144537E-05
6. 975249E-06					
2. 850000E+00	-2. 962929E-03	-1. 613454E-02	5. 110154E-02	8. 301870E-05	-2. 383600E-05
3. 270081E-06					
2. 875000E+00	-2. 357708E-03	-2. 169941E-02	6. 253965E-02	1. 019216E-04	-3. 047483E-05
1. 201534E-06					
2. 900000E+00	-4. 301113E-03	-1. 938800E-02	6. 234631E-02	1. 023668E-04	-3. 075369E-05
4. 922122E-06					
2. 925000E+00	-6. 657049E-03	-1. 262069E-02	5. 139206E-02	8. 570462E-05	-2. 592411E-05
9. 841403E-06					
2. 950000E+00	-5. 676170E-03	-7. 255834E-03	3. 391360E-02	5. 729835E-05	-1. 794233E-05
8. 464491E-06					
2. 975000E+00	-1. 221289E-03	-4. 751477E-03	1. 346745E-02	2. 313665E-05	-8. 569339E-06
7. 204950E-07					
3. 000000E+00	2. 770664E-03	-1. 743792E-03	-5. 549086E-03	-9. 119816E-06	9. 223670E-07
-5. 808555E-06					
3. 025000E+00	3. 035591E-03	4. 534454E-03	-2. 129972E-02	-3. 513824E-05	9. 437264E-06
-5. 087867E-06					
3. 050000E+00	9. 489715E-04	1. 146647E-02	-3. 218146E-02	-5. 240535E-05	1. 554929E-05
-2. 196403E-07					
3. 075000E+00	4. 871726E-04	1. 386899E-02	-3. 691742E-02	-5. 997596E-05	1. 824166E-05
1. 023174E-06					
3. 100000E+00	2. 825374E-03	1. 033701E-02	-3. 495668E-02	-5. 740245E-05	1. 725974E-05

POINT-ID =

104

V E L O C I T Y V E C T O R

TIME	T1	T2	T3	R1	R2
R3					
3. 750000E+00	3. 195991E-02	-2. 052107E-02	9. 144466E-02	1. 480380E-05	-6. 432360E-06
-3. 882778E-06					
3. 775000E+00	2. 872361E-01	-1. 585655E-01	-3. 399534E-01	-2. 278181E-05	2. 712839E-05
-3. 501218E-05					
3. 800000E+00	1. 704479E-01	-8. 459052E-02	-6. 793213E-01	-6. 324151E-05	4. 660745E-05
-2. 035578E-05					
3. 825000E+00	-1. 563228E-01	1. 066188E-01	-8. 590188E-01	-9. 126713E-05	4. 849045E-05
2. 015978E-05					
3. 850000E+00	-2. 665188E-01	1. 696859E-01	-8. 619423E-01	-9. 267431E-05	4. 262465E-05
3. 379988E-05					
3. 875000E+00	-2. 355909E-02	2. 725387E-02	-7. 264923E-01	-7. 029758E-05	3. 830412E-05
3. 662041E-06					
3. 900000E+00	2. 509679E-01	-1. 343785E-01	-5. 127407E-01	-4. 262735E-05	3. 394094E-05
-3. 043947E-05					
3. 925000E+00	2. 017643E-01	-1. 105395E-01	-2. 610786E-01	-2. 255467E-05	2. 122426E-05
-2. 458094E-05					
3. 950000E+00	-1. 026348E-01	5. 924448E-02	7. 499449E-03	-6. 134869E-06	-9. 631411E-07
1. 270125E-05					
3. 975000E+00	-2. 678051E-01	1. 487879E-01	2. 640849E-01	1. 690030E-05	-2. 215617E-05
3. 271375E-05					
4. 000000E+00	-8. 745309E-02	4. 105816E-02	4. 593306E-01	4. 455392E-05	-3. 095563E-05
1. 019899E-05					
4. 025000E+00	1. 966733E-01	-1. 237156E-01	5. 489387E-01	6. 142191E-05	-2. 778364E-05
-2. 484382E-05					
4. 050000E+00	2. 163467E-01	-1. 342064E-01	5. 291392E-01	5. 730867E-05	-2. 319973E-05
-2. 711175E-05					
4. 075000E+00	-4. 724709E-02	1. 909298E-02	4. 347475E-01	3. 922313E-05	-2. 354622E-05
5. 464358E-06					
4. 100000E+00	-2. 480887E-01	1. 365661E-01	3. 040114E-01	2. 282438E-05	-2. 336912E-05
3. 019810E-05					
4. 125000E+00	-1. 286805E-01	7. 056681E-02	1. 509815E-01	1. 400785E-05	-1. 426322E-05
1. 556059E-05					
4. 150000E+00	1. 513786E-01	-8. 686364E-02	-2. 257291E-02	4. 969327E-06	2. 178083E-06
-1. 867354E-05					
4. 175000E+00	2. 303163E-01	-1. 284842E-01	-1. 992796E-01	-1. 251741E-05	1. 530538E-05
-2. 809735E-05					
4. 200000E+00	1. 328749E-02	-9. 957608E-04	-3. 425493E-01	-3. 438179E-05	1. 827542E-05
-1. 248478E-06					
4. 225000E+00	-2. 126808E-01	1. 300722E-01	-4. 233594E-01	-4. 777685E-05	1. 553950E-05
2. 651976E-05					
4. 250000E+00	-1. 565715E-01	9. 793471E-02	-4. 435534E-01	-4. 609960E-05	1. 572000E-05
1. 954990E-05					
4. 275000E+00	1. 030413E-01	-5. 147516E-02	-4. 267159E-01	-3. 651198E-05	2. 057882E-05
-1. 235764E-05					
4. 300000E+00	2. 279808E-01	-1. 236060E-01	-3. 892858E-01	-3. 114907E-05	2. 367662E-05
-2. 764114E-05					
4. 325000E+00	6. 085704E-02	-2. 852717E-02	-3. 256041E-01	-3. 196169E-05	1. 916279E-05
-7. 094159E-06					
4. 350000E+00	-1. 773425E-01	1. 063022E-01	-2. 235016E-01	-2. 895216E-05	9. 187196E-06
2. 203379E-05					
4. 375000E+00	-1. 800225E-01	1. 050586E-01	-8. 853387E-02	-1. 399587E-05	1. 640557E-06
2. 216542E-05					
4. 400000E+00	4. 955968E-02	-2. 946150E-02	5. 504843E-02	7. 589428E-06	7. 597289E-07
-6. 126533E-06					
4. 425000E+00	2. 100646E-01	-1. 236941E-01	1. 882280E-01	2. 328112E-05	1. 825256E-06
-2. 581812E-05					
4. 450000E+00	9. 602978E-02	-6. 019597E-02	3. 156094E-01	2. 963177E-05	-3. 247071E-06
-1. 185401E-05					
4. 475000E+00	-1. 407424E-01	7. 312045E-02	4. 517425E-01	3. 589924E-05	-1. 542380E-05
1. 702251E-05					
4. 500000E+00	-1. 946238E-01	1. 010371E-01	5. 915315E-01	5. 051499E-05	-2. 650806E-05
2. 342351E-05					
4. 525000E+00	-2. 076759E-03	-1. 182051E-02	7. 035817E-01	6. 871821E-05	-3. 015162E-05
-3. 045990E-07					
4. 550000E+00	1. 827056E-01	-1. 187903E-01	7. 534439E-01	7. 797959E-05	-2. 993055E-05
-2. 301285E-05					
4. 575000E+00	1. 218864E-01	-8. 352202E-02	7. 261918E-01	7. 256576E-05	-3. 404317E-05
-1. 564216E-05					
4. 600000E+00	-1. 009016E-01	4. 581758E-02	6. 167808E-01	5. 744177E-05	-4. 185558E-05
1. 160793E-05					
4. 625000E+00	-1. 954223E-01	1. 031724E-01	4. 088509E-01	3. 830896E-05	-4. 443343E-05
2. 325238E-05					
4. 650000E+00	-4. 220985E-02	2. 086093E-02	7. 109596E-02	1. 259657E-05	-3. 500421E-05
4. 632816E-06					
4. 675000E+00	1. 583661E-01	-8. 569200E-02	-4. 193067E-01	-2. 800680E-05	-1. 615577E-05
-1. 974162E-05					
4. 700000E+00	1. 512873E-01	-7. 023248E-02	-1. 055757E+00	-8. 884124E-05	6. 840753E-06
-1. 849989E-05					
4. 725000E+00	-4. 435500E-02	5. 571879E-02	-1. 800161E+00	-1. 660403E-04	3. 306436E-05

saweswept_ptz5a_sol 146_h43_vel_4

6. 113950E-06						
4. 750000E+00	-1. 666747E-01	1. 407199E-01	-2. 595703E+00	-2. 471692E-04	6. 495756E-05	
2. 183972E-05						
4. 775000E+00	-5. 343694E-02	9. 044844E-02	-3. 380996E+00	-3. 195818E-04	1. 077864E-04	
8. 668092E-06						
4. 800000E+00	1. 520215E-01	-1. 383798E-02	-4. 074815E+00	-3. 823109E-04	1. 585389E-04	
-1. 578365E-05						
4. 825000E+00	1. 913422E-01	-2. 510236E-02	-4. 562643E+00	-4. 388892E-04	2. 085523E-04	
-1. 969794E-05						
4. 850000E+00	2. 415948E-02	7. 606084E-02	-4. 688665E+00	-4. 741055E-04	2. 367621E-04	
1. 395856E-06						
4. 875000E+00	-1. 269008E-01	1. 585610E-01	-4. 332330E+00	-4. 523290E-04	2. 529605E-04	
2. 023599E-05						
4. 900000E+00	-6. 853218E-02	1. 100816E-01	-3. 410939E+00	-3. 825924E-04	2. 218790E-04	
1. 224584E-05						
4. 925000E+00	1. 090501E-01	-1. 529681E-02	-2. 077428E+00	-3. 355566E-04	3. 771772E-05	
-1. 296418E-05						
4. 950000E+00	1. 435650E-01	-6. 493582E-02	-1. 286726E+00	-3. 865468E-04	-5. 247009E-04	
-2. 819376E-05						
4. 975000E+00	-4. 971029E-02	4. 613657E-02	-3. 939311E+00	-2. 766407E-04	-7. 760281E-04	
-7. 778375E-06						